UNIVERSIDAD POLITÉCNICA DE MADRID

Escuela Técnica Superior de Ingeniería Aeronáutica y del Espacio

Tesis Doctoral / *PhD Thesis:*

“DEVELOPMENT OF A MULTIFUNCTIONAL COMPOSITE STRUCTURE WITH SELF-SENSING PROPERTIES”

Autor: Xoan Xosé Fernández Sánchez-Romate

Programa de Doctorado en Ingeniería Aeroespacial

Madrid, 2019

AGRADECIMIENTOS / *ACKNOWLEDGEMENTS*

En primer lugar, quiero comenzar agradeciendo a los Prof. Alejandro Ureña Fernández y Jesús Alfredo Güemes Gordo por haberme dado la oportunidad de realizar esta Tesis en colaboración entre la Universidad Politécnica de Madrid y la Universidad Rey Juan Carlos, así como por su confianza ciega en mi desempeño.

A su vez, quiero agradecer a la Comunidad de Madrid por el proyecto *Multimat Challenge* (P2013/MIT-2862) gracias al cual pude comenzar la Tesis. También al Ministerio de Economía y Competitividad del Gobierno de España por otros proyectos como *Sensorgraph* (MAT2013-46695-C3-1-R) o *Multiadit* (MAT2016-78825-C2-1-R) de los que también he formado parte.

De manera especial, quiero agradecer a todos los compañeros y amigos que han ido acompañándome y soportándome a lo largo de estos años:

En particular, a Sonia, por haber sido un gran apoyo, una gran amiga, desde el principio. Por haber compartido conmigo tantos momentos de alegría y de frustraciones y por saber que, pase lo que pase, siempre nos tendremos como apoyo para los buenos y los no tan buenos momentos. Y porque nuestros caminos siempre se han ido cruzando y espero que así siga siendo durante muchos años. Ahora estamos al final de una etapa, pero esto es sólo el comienzo. Ah, y porque el año que viene…

A Nuria, porque desde que llegó, hace algo más de dos años, ha sido alguien muy importante para mí dentro de este sitio y porque siempre tendremos muchos puntos de vista en común. Y por esas palmeras rellenas tan ricas. A Najib, quien siempre ha estado ahí para escuchar y para poner el toque de cordura cuando lo he necesitado. Y por hacerme esa tabla de ejercicios que nunca he llevado a cabo.

A Alejandro Cortés, Juan Pablo y Osiris, porque hemos compartido muy buenos momentos en la antesala, ahora fragmentada, y por esos viernes de relax a la hora de la comida. De la misma manera, también quiero dedicarles unas palabras a todos aquellos que han pasado por allí, porque siempre se ha hecho grupo ahí dentro.

No podría olvidarme de Alberto, quien ha sido no sólo un mentor para mí, un espejo en el que mirarme, sino también un gran amigo, un gran apoyo y alguien con quien desahogarme. A veces nos cuesta reconocer el talento y el esfuerzo aunque lo tengamos delante de nosotros todo el tiempo, pero estoy convencido de que llegarás lo más alto posible y que todas estas vicisitudes de plazas bloqueadas, de talento bloqueado, serán un mal sueño dentro de unos años. Y ahí estaré yo para verlo. Gracias por haberme ayudado tanto estos años.

A Rocío, porque siempre ha sido mi otra mitad nano aquí dentro y quien me inició en la monitorización y porque en sus últimos meses aquí nos hemos compenetrado a la perfección. Siempre me dará mucha pena que te fueras, pero espero que en Sevilla cumplas todos tus sueños. Y también estaré ahí para verlos porque no solo has sido una gran compañera sino también una amiga.

Al resto del área de Ciencia e Ingeniería de Materiales y, en especial, al grupo de polímeros. Particularmente, a Silvia, porque he aprendido mucho de ti, sobre todo en estos últimos meses, por tu integridad y por tu capacidad de trabajo en equipo. A María, por haber iniciado la línea fundamental de mi Tesis y haberme dado la oportunidad de participar en proyectos tan interesantes como *Fuselage*. Y a Mónica, porque últimamente hemos empezado a trabajar juntos y estoy muy a gusto contigo.

Por supuesto, a Maribel, por ayudarme tanto en el laboratorio y hacerme siempre la vida más fácil (nunca nadie me ha encontrado tantas cosas) y por esas charlas sobre la vida. Dentro de unos años nos estaremos riendo de todo en nuestra isla privada. Y a Fabio, porque entramos juntos, porque eres un gran tío y porque me encanta mantener el contacto contigo.

I would like to acknowledge Claudio, for giving me the opportunity of working with you. I have learnt a lot of things and I really admire your working capacity and your knowledge. My regards also to Mauro, who has helped me very much during my tests at Politecnico di Milano; and to all the rest of the people from the laboratories.

Many thanks also to Prof. Claus-Peter Fritzen, who supervised me during my research stay in Siegen. It was a pleasure to take part of your group and I really enjoyed my stay there. I would like to acknowledge Volkan and Jens. You, guys, were a really good support for me, by helping me with my tests but also by introducing me in the German lifestyle. You were not only colleagues but also friends.

Por supuesto, quiero agradecer a todas esas personas que, fuera de la universidad, han sido un apoyo, un soporte para mí. A Fran, un amigo y hermano, escuchándome y aguantando mi mal genio muchas veces desde tiempos inmemoriales. A Gabi, porque además de también soportarme, siempre me has sacado una sonrisa con tus historias en el colegio. A Dani, porque fuimos cuasi gemelos durante la carrera y ahora lo hemos sido durante el doctorado. A Javi, porque cada fin de semana compartimos juegos de mesa, comidas y cenas y por ser un apoyo desde siempre. A Bolty y a Floren, porque, sin ellos, esos findes de ocio no serían lo que son.

Al Indio, por esos viajes a Kenia y al Calderón. A Albano, por haber estado siempre ahí y porque espero que sea mi compañero aerodinámico en unos meses. A Charlie, por los debates futboleros y de reggaetón. *Urban culture*.

A los Clásicos foráneos: Andrea, Álex, Isaac y Ramón; porque sé que siempre estaréis ahí y porque se os echa mucho de menos. Por esas quedadas que no se deben perder.

A Lu, porque, aunque nuestros caminos se hayan separado, siempre te tendré un cariño muy especial y me acordaré de nuestras charlas infinitas y nuestros debates sobre la vida.

Y para finalizar; acordarme de la gente más importante para mí, la que me define como persona y la que ha estado, está y siempre estará ahí: mi familia. Mi madre, mi padre, mi hermano y Gis. Vosotros me hacéis mejor persona cada día. Esto va para vosotros, para que lo disfrutéis, porque ha sido un trabajo y un esfuerzo de todos. Os quiero.

Y también para mí, porque me lo merezco.

RESUMEN

El amplio uso de los materiales compuestos junto con la creciente complejidad de las estructuras haces necesario el desarrollo de adecuadas técnicas de inspección. A día de hoy, hay muchos métodos diferentes como la fibra óptica o la emisión de ondas elásticas guiadas. Sin embargo, normalmente no ofrecen una visión global de la salud de la estructura y presentan limitaciones para la monitorización del crecimiento de grieta o desencolado.

En este sentido, este trabajo presente explorar las capacidades para la monitorización de la salud estructural (SHM) de materiales compuestos reforzados con nanotubos de carbono (CNT). Para ello, primero se han analizado en detalle las propiedades electromecánicas de los nanocompuestos derivados mediante un nuevo modelo analítico que correlacione la dispersión de los CNT con sus propiedades eléctricas.

La sensibilidad aumenta mejorando la técnica de dispersión debido a un efecto más pronunciado de los mecanismos de conducción tipo túnel frente a las propiedades intrínsecas de los CNT. A su vez, la geometría y ondulación de las nanopartículas juega un papel crucial aumentando el umbral de percolación, definido como el punto en el que el material aislante se convierte en conductor.

Por otro lado, las capacidades de SHM de compuestos reforzados con CNT han sido ampliamente investigadas en uniones adhesivas, donde hay una falta de procesos de inspección adecuados que garanticen la fiabilidad de dichas uniones. Para ello, se ha propuesto un novedoso adhesivo film modificado con CNT y su capacidad de sensorización de deformaciones y crecimiento de grieta se han demostrado tanto a nivel probeta como subelemento.

Se han ensayado uniones a solape simple, Modo I y Modo II de energía de fractura mientras se registraba su respuesta eléctrica probándose una gran sensibilidad y correspondencia entre la respuesta eléctrica y el crecimiento de grieta, sin afectar negativamente a las propiedades mecánicas, siendo posible distinguir entre propagación uniforme o inestable.

Los subelementos rigidizados mostraron un comportamiento similar con una buena correlación entre respuesta eléctrica y mecánica. Por lo tanto, la técnica propuesta ha demostrado ser de gran aplicabilidad para aplicaciones de SHM.

ABSTRACT

The widely extended use of composite materials together with the increasing complexity of structures makes necessary the development of adequate inspection techniques. Nowadays, there are a lot of different methods addressing these concerns such as fiber optics or guided waves. However, they do not offer sometimes a global overview of the health of the structure and present some limitations for crack and debonding monitoring.

In this regard, this work aims to explore structural health monitoring (SHM) capabilities of carbon nanotube (CNT) reinforced composites. First, electromechanical properties of CNT nanocomposites were deeply investigated by proposing a novel analytical model correlating CNT dispersion state to electrical properties of nanocomposites.

The sensitivity was found to be higher by improving the dispersion technique because of a more prevalent effect of tunneling mechanisms over intrinsic properties which remain invariable. Moreover, CNT geometry and waviness plays a significant role by increasing the percolation threshold, that is, the volume fraction where the material becomes electrically conductive and, thus, affecting the inter-particle distance and tunneling mechanisms.

On the other hand, SHM capabilities of CNT doped composites were also investigated in adhesive joints where there is a lack of proper inspection techniques ensuring their reliability. To achieve this purpose, a novel CNT reinforced adhesive film was proposed and its sensing and crack propagation monitoring capabilities were deeply analyzed at both coupon and skin-stringer sub-element level.

Single Lap Shear, Mode-I and Mode-II tests were carried out while the electrical response was measured. It was found that there is a good agreement between the measured crack length and the corresponding electrical resistance without significant detriment on mechanical properties. It was possible to identify different crack propagation mechanisms such as a uniform crack growth or stick-slip behavior.

Skin-stringer sub-element test showed a similar behavior with a proper correlation between electrical and mechanical performances. Therefore, the proposed technique showed a high applicability for SHM purposes.

Table of contents

CHAPTER 1: INTRODUCTION

Chapter 1: Introduction

1.1 Advanced composite materials

Composite materials are constituted by two or more distinguishing materials with different properties that, when combined, promote a new material with a combination of properties that is not possible to achieve separately.

Although composite materials can be also referred to metal matrix (MMC), intermetallic matrix (IMC) or ceramic matrix composites (CMC), it is particularly interesting to focus on Fiber Reinforced Polymers (FRPs) due to their importance in a lot of industries. Here, there are generally two constituents: the reinforcement, which could be in the form of short, long fibers or particulates and gives the mechanical and some physical properties such as electrical conductivity in the in-plane direction (in case of long fibers); and the polymeric matrix, in charge of load transferring between the fibers and provides the mechanical and physical properties in the out-of-plane direction [1]. In this case, we will be focusing on long fiber reinforcements.

Nowadays, FRPs are attracting the interest in many fields. For example, there is an increasing effort in developing composite parts for automotive industry [2]. Since the first *Corvette* series, there have been several improvements concerning the manufacturing and curing processes which gives an optimistic point of view about a more extensive use in the future [3] and even the use of nanostructured composites for automotive applications is being also explored [4].

Another example, and probably the most important, is the aircraft industry. In the last decades, the use of composite material structures has significantly increased [5], as can be seen in the chart of Figure 1.1 where the evolution of aerospace materials among the different aircraft models in the last decades is shown. It is particularly interesting to point out that composite materials constitute more than a 50 % of the total weight of the whole aircraft in the last models manufactured by Boeing and Airbus: A350 and Boeing 787. Their use is nowadays extensive in structural parts where they should meet strict requirements [6].

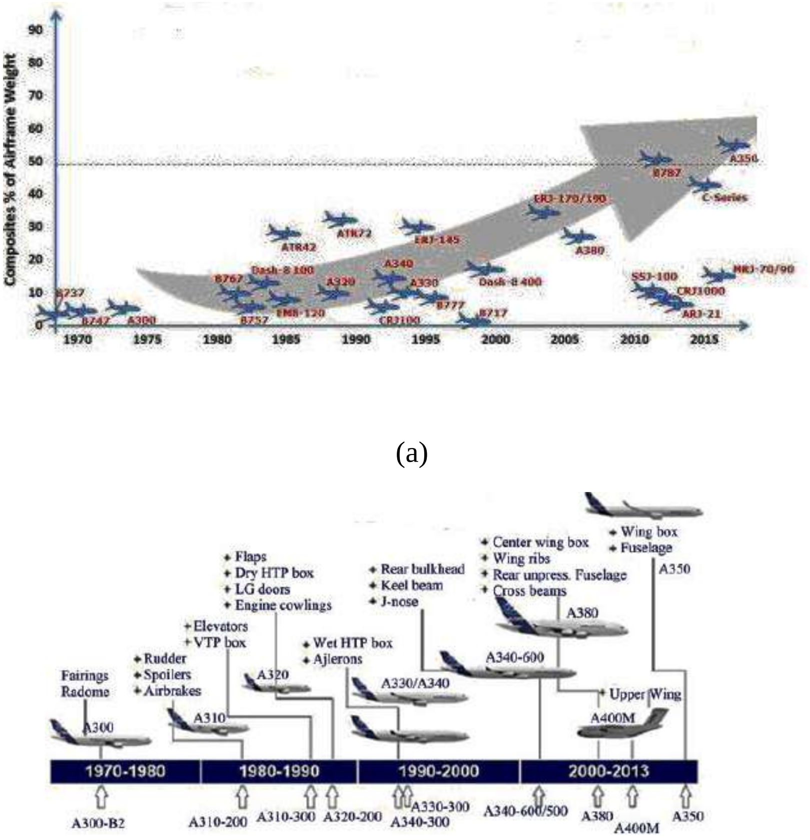

(a)

(b)

Figure 1.1: Evolution of composite materials in aircraft industry showing (a) the % of composites over the total weight and (b) specific applications in aircrafts.

In this context, Carbon Fiber Reinforced Polymers (CFRPs) seem to be a good alternative to conventional alloys for structural purposes. This is explained based on the fact that CFRP materials have very high specific properties, especially, when compared to aluminum or titanium alloys and steel. In fact, high modulus CFRPs have a Young Modulus over twice conventional aluminum alloys and a density in the range of 1.5 g/cm^3, much lower than 2.7 g/cm^3 of aluminum [7]. For this reason, CFRP plates and bars have been widely used for strengthening steel bridges [8,9].

However, they also have some disadvantages when comparing to conventional alloys. For example, their electrical conductivity in the transversal direction is affected mainly by the physical properties of the matrix, which is not electrically conductive. Therefore, it is a limitation for their use in some applications such as lightning strike, where a high conductivity is needed to provide electrical pathways.

Moreover, they present complex failure modes due to the nature of the constituent materials: matrix and fiber cracking or delamination due to crack propagation in the fiber-matrix interface [10]. Therefore, their inspection is nowadays a challenging aspect.

In addition to that, the increasingly complexity of composite structures, make it also necessary the development of adequate joining techniques. In this context, there are several efforts in the use of adhesives which will be one of the main objectives of the present work.

1.2 Adhesive joints

Adhesive joints differ from mechanical ones by the use of an adhesive layer uniformly distributed along the joint while mechanical joining consisting of a discrete distribution of rivets and fasteners. In this regard, the main advantages of bonded joints are the following [11]:

- Avoid stress concentrations around the bolt holes that could lead to a prompt failure of the joint.
- Excellent fatigue strength.
- Weight saving due to the fasteners removal.
- Seals the joint.
- Elimination of corrosion problems as there are no metal materials involved.

But, their implementation in composite structures has not widely extended yet due to some limitations such as:

- Necessity of an adequate surface treatment to strengthen the joint.
- They are limited to lower continuous operating temperature (usually below 200 ºC) due to the polymer nature of the adhesive.
- Difficulty for inspection and detection of possible debonding leading to an unknown prognosis of the life of the structure in composite repairs.
- Lack of adequate reliability unless quite strict manufacturing procedures are kept. For this reason, their use in repairs have strong limitations in aerospace industry.

The effect of surface treatment on adhesive bonds has been widely studied, showing that it could significantly affect the mechanical and physical properties of the joint. L. Sorrentino et al. [12] investigated the effect of sanding, grit-blasting and peel-ply treatment on Lap Shear Strength (LSS) of CFRP bonded joints by using different adhesives. A detriment of more than 30 % in the LSS was observed for peel-ply treatment in two of the adhesives tested. However, the other one, which was an adhesive film, showed a slight increase when comparing to grit-blasting and sanding treatments. S.G. Prolongo et al. [13] showed that the roughness of the substrate surface plays an important role, but there are more effects affecting the interface strength, such as the creation of an energy activated surface by methods such as plasma treatment. W.S. Johnson et al. [14] observed also that surface treatment also plays a crucial role in the fatigue strength of metal-metal adhesive joints and M. Davis et al. [15] explains the lower use of adhesive bonding in repairs because the enormous variability of strength due to surface treatment in comparison to mechanical joint despite its superior performance.

In fact, surface treatment has a strong influence in the way adhesive joints fail. These failure modes can be divided in three types [11]:

- Adhesive failure: it takes place when crack propagates in the interface between adhesive and substrate. The fracture surface typically shows the presence of adhesive in only one side of the joint. It is due to a poor interfacial strength usually explained by a non-adequate surface treatment of the adherends.
- Cohesive failure: it takes place when crack propagates inside the adhesive joint. The fracture surface shows the presence of adhesive in both sides. In this case, the total strength of the joint is given mainly by the strength of the adhesive.

- Failure of the substrate: it consists on the breakage or delamination of the substrate. It means that the strength of the adhesive is higher than the strength of the substrate. It usually means that both the adhesive and the surface treatment are adequate but it can be also due to defects inside the substrate.

In addition to that, there are another multiple failure modes such as near-interface failure, suggesting that both adherend and adhesive are influencing each other or dissipative after a large absorption of energy [16]. The correct failure identification in bonded joints is critical to know how the overall strength of the joint can be improved (Figure 1.2).

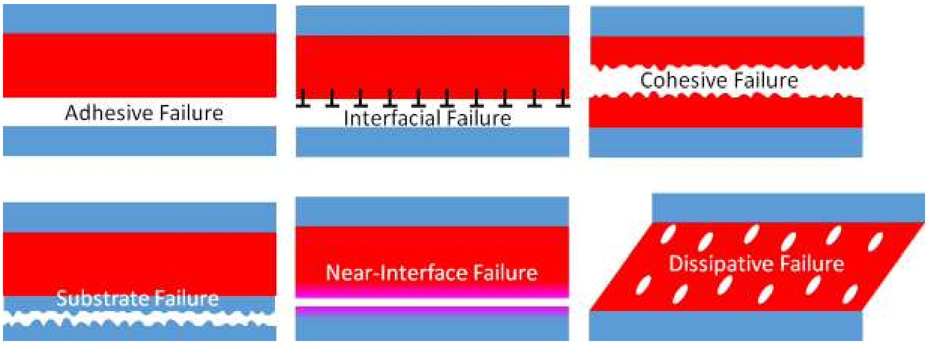

Figure 1.2: Schematic of typical failure modes in adhesive joining [16].

The assessment of the influence of defects inside the joint has been always of wide interest. M. Elhannani et al. [17,18] did a numerical analysis of the effect of bonding defects on the shear stress distribution in a Single Lap Shear (SLS) joint. They observed that a higher number of defects inside the joint lead to an increase of shear stresses. In addition, the influence of defects is more prevalent when they are located near the edges, where the highest shear stresses are achieved. R.S. Trask et al. [19] analyzed the influence of defects during process in composite T-joints. It was found that a reduction on the deltoid area of the T-joint induced a significant decrease (around 33 %) of load carrying capacity. F. Heirdarpour et al. [20] investigated the influence of the shape and size of defects in a lap joint. They concluded that 3D defects have a stronger influence on the decrease of tensile strength properties, having circular shapes a lower influence due to lower stress concentrations than rectangular or triangular ones. The influence of defects on strength and damage growth assessment in CFRP bonded joints was also analyzed by F.M.F. Ribeiro et al. [21] highlighting the difficulty to make predictions in damaged adhesive joints.

Therefore, the difficulty for inspection is a crucial factor to be overcome to make the adhesive joining as an extensive structural joining technique in composite components. For this reason, there are several efforts in developing novel non-destructive testing (NDT) techniques to ensure the reliability of bonded joints.

In this context, the aim is not only to have proper NDT techniques but also to reduce maintenance costs which suppose a 14 % of hull loss [22]. A way to achieve that purpose would be the development of on-line systems giving us a complete information about the health of the constituents of the structure during their whole life.

1.3 Structural Health Monitoring

1.3.1 Definition

The commented motivation constitutes the basis for Structural Health Monitoring (SHM) applications. It has been observed that the integration of suitable SHM systems addressing the previously concerns, would cause a drastic reduction in the inspection time on aircrafts where a reduction of nearly 50 % in time inspection could be achieved. In fact, the assessment of SHM techniques is now being used in a wide range of non-aircraft applications such as offshore structures [23], bridges [24] or to investigate the health of a structure after an accident [25]. An example of the increasing use of SHM tools in aircraft industry is the addition of a Comparative Vacuum Monitoring as an alternative inspection technique for the front spar fitting of Boeing 737.

The proposed SHM systems must address the following four levels of damage identification, defined by A. Rytter et al. [26]

- Level 1: Determination that a damage is present in the structure
- Level 2: Localization of the damage in the structure
- Level 3: Quantification of the damage size.
- Level 4: Prediction or *prognosis* of the remaining life of the structure

A parallelism between human activity monitoring and SHM systems has been proposed. A central processor is needed as well as several sensors distributed around the structure in a similar way as the brain and nervous system in humans, as shown in Figure 1.3. The idea is to replicate this behavior by creating a whole sensing structure.

Therefore, SHM on bonded joints is now attracting the attention of many researchers, due to the previously commented difficulty for their inspection.

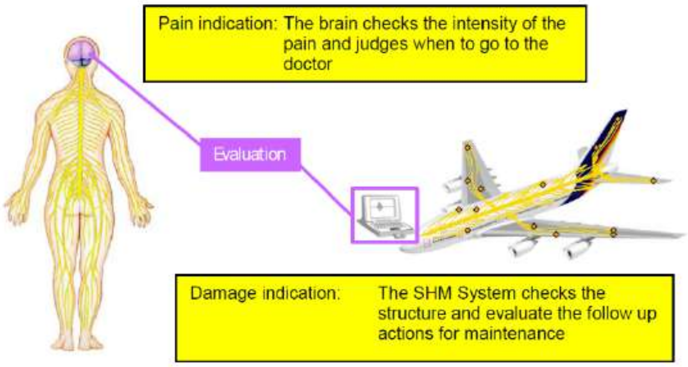

Figure 1.3: Comparison between human monitoring and a SHM system in an aircraft (Source: H. Speckmann et al. [27])

1.3.2 Fiber Optics and guided waves in SHM

In the context of SHM applications, Fiber Bragg Grating Sensors (FBGs) seem to have a high potential and applicability. Their principle of operation is shown in Figure 1.4 (a). They are based on the change of the grating period, Λ_B, inside an optical fiber when subjected to mechanical strain, inducing to a change in the reflected wavelength λ_B, accordingly to the following formula:

$$\lambda_B = n_{eff}\Lambda_B \tag{1.1}$$

Where n_{eff} is the refraction index of the optical fibre.

There are several studies using FBGs in composite structures. A. Bernasconi et al. [28] exploited the SHM capabilities of FBGs to monitoring the crack growh under fatigue load of adhesive joints. They achieved a similar resolution than ultrasonic testing. J. Frieden et al. [29,30] proposed a method to localize an impact and identify a damage using dynamic strain signals from

FBG sensors. For this purpose, several low velocity impacts were carried out in a CFRP plate as well as four sensors were placed in several parts of the plate proving a good potential for damage identification under this type of impacts. A. Riccio et al. [31] deeply investigated the proper positioning of embedded FBGs in a CFRP stiffened panel based on numerical analysis of buckling behavior. In this way, FBGs provided a reliable signal that was in good agreement with that measured by strain gauges.

The main limitation of FBGs is that they are only able to detect damages taking place near the sensor, that is, they do not offer a global overview about the health of the structure. For these reasons, there are several efforts in developing optical distributed sensors (ODS). They are comprised by a single cable which is sensitive to mechanical and thermal strain at every point, requiring a single connection to data processor instead of different grating sensors.

In this context, S. Minakuchi et al. [32] used a single optical fiber to monitor the Vacuum Assisted Resin Transfer Moldering (VARTM) process of a CFRP panel. It was found that ODS system was properly able to detect variations of strain due to heating and cooling during curing process and monitor the subsequent impact tests. J. Sierra-Pérez et al. [33] compared the damage and nonlinearities detection in wind turbines blades by FBGs, ODS and strain gauges. In this study, they observed that distributed sensing presented some limitations due to a smaller resolution when increasing the number of sensors, needing also more computational resources. In addition, they are limited, again, to monitor regions near the optical fiber.

Another common technique is Acousto-Ultrasonic (AU) guided waves. They are based on the interaction of elastic waves inside the material and the way they propagate when reaching a discontinuity or when there are changes in the state of the structure (Figure 1.4 (b)). In this context, there are many studies by using this approach to evaluate the health of the structure.

M.H. Sherafat et al. [34] used guided wave propagation for SHM of a composite skin-stringer assembly. They used a within-the-bond strategy and found that at certain pulse frequencies, it is possible to achieve a satisfactory sensitivity for detecting debonding. V. Giurgiutiu et al. [35] investigated Lamb Wave, a particular case of AU guided wave, for SHM purposes by using piezoelectric wafer active sensors (PWAS). They found several advantages over conventional ultrasonic probes as they are better coupled with the structure dynamics. Z. Su et al. [36] did an extensive review on guided waves for identification of damage in composite structures highlighting the need of a proper selection of Lamb modes as well as more sophisticated signal processing to achieve reliable results. In fact, as stated by J.L. Rose et al. [37], signal interpretation, sensor robustness and the need of long computational times are still challenging aspects of AU inspection. More specifically, their reliability to detect defects in adhesive joints, especially when there are kissing bonds (poor interface contacts) has not been totally proven.

Other techniques such as Acoustic Emission (AE) have been also object of study in bonded structures. A. Crawford et al. [38] deeply investigated this technique in metal to metal adhesive joints and observed that there is a change in the reflected waveform of the acoustic emission when finding a bonded joint. However, this technique also involves the use of complex mathematical and statistical tools and not are properly indicated for detecting defects in this type of joints.

Therefore, it is necessary to explore novel SHM techniques in order to ensure the reliability of adhesive joining. For this reason, in the last decades, there is an increasing interest on polymers reinforced with carbon nanoparticles which allow to give a overall perspective of the health of the structure.

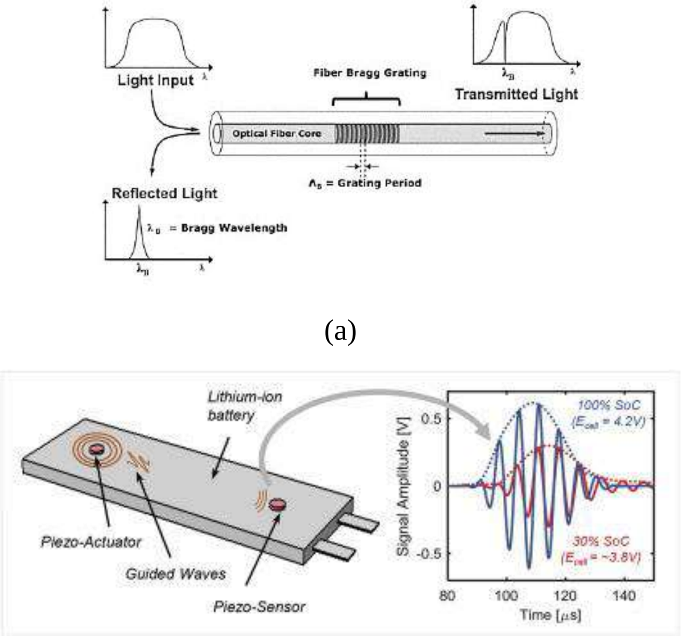

(a)

(b)

Figure 1.4: Principles of operation of (a) FBGs [39] and (b) guided wave-based systems (Source: P. Ladpli et al. [40]).

1.4 Carbon nanoparticles in SHM

1.4.1 Definition

These carbon nanoparticles can be divided in several types depending on their characteristic dimensions:

- 0D nanoparticles are those with every dimension in the range of nanometers. For example: fullerenes, Figure 1.5 (a) or carbon black (CB).
- 1D nanoparticles are those with two dimensions in the range of nanometers. For example: carbon nanotubes (CNTs), as shown in Figure 1.5 (b).
- 2D nanoparticles are those with two dimensions in the range of micrometers and the other one in the nanoscale range. For example: graphene and graphene nanoplatelets (GNPs), as shown in Figure 1.5 (c).

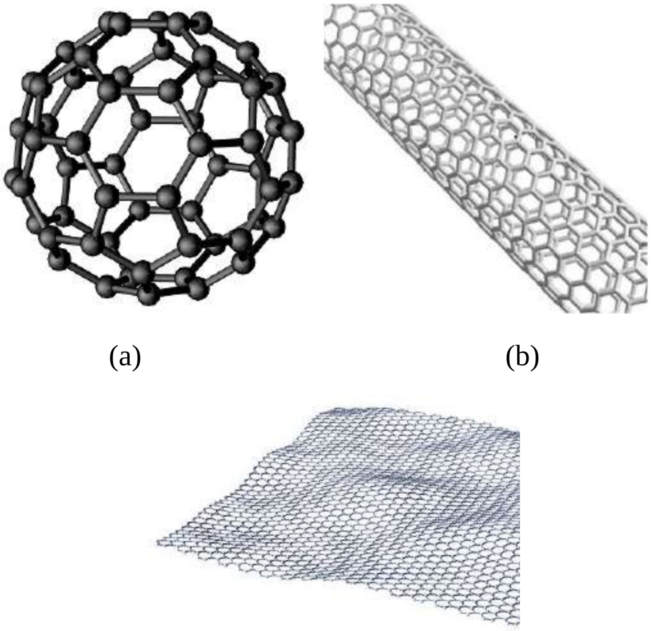

(a) (b)

(c)

Figure 1.5: Schematics of (a) fullerene, (b) carbon nanotube and (c) graphene.

CNTs, that were discovered by S. Iijima [41] show exceptional properties. In fact, the Young Modulus of isolated CNTs is about 1.8 TPa [42], much higher than conventional carbon fibers [43]. E.W. Wong et al. [44] compared the elastic capabilities of CNTs with another typical reinforcement, SiC, and found a higher Young modulus in despite of a lower bending strength of about 14.2 GPa in comparison to 53 GPa of SiC nanoparticles. M.F. Yu et al. [45] also determined the CNT tensile strength, ranging from 11 to 63 GPa, much higher also than conventional fiber reinforcements.

In addition to that, CNTs also exhibit exceptional electrical and thermal conductivities. P. Kim et al. [46] estimated the thermal conductivity of CNTs in 3000 W/mK by using an microfabricated suspended device. A summary of some interesting physical properties of carbon nanoparticles (CNPs) is shown in Table 1.1.

Table 1.1: A summary of some interesting physical properties of carbon related materials.

Property	**Graphene**	**CNTs**	**Fullerene**	**Diamond**
Specific weight (g/cm^3)	1.9-2.3	0.8-1.8	1.7	3.5
Electrical conductivity (S/m)	4000[1], 3.3[2]	10^2-10^6	10^{-5}	10^{-2}-10^{-15}
Thermal conductivity (W/mK)	2.9×10^5	3000	6.2×10^{-5}	~10^{-6}
Thermal stability in air (°C)	450-650	>600	~600	<600

---

[1] In plane

[2] Out of plane

1.4.2 Carbon nanoparticle composites

In this regard, the addition of carbon nanoparticles into a polymer matrix has a significant effect on its mechanical properties. FH. Gonjy et al. [47,48] analyzed in their studies the influence of CNT addition on elastic properties of nanocomposites. A significant enhancement of the Young Modulus is observed for Single-Wall (SWCNT) and Double-Wall (DWCNT) carbon nanotubes. An increase of around 15 % in Young Modulus and 5 % is observed at a 0.3 wt. % content. The improvement in case of multi-wall carbon nanotubes (MWCNTs) is not so prevalent, leading to a slight reduction on the tensile strength at very high contents. In addition, the CNT influence on fiber-reinforced composites has been also studied. In this regard, M.H.G. Wichmann et al. [49] showed a significant enhancement of the fracture toughness, especially in Mode-I loading conditions, by using DWCNT doped epoxy resin. D.C. Daniel et al. [50] also showed an improvement of the tensile strength, Young Modulus and failure strength under cyclic loads (tensile-tensile and tensile-compression) in a CNT doped CFRP laminate. R.J. Young et al. [51] explored the effect of graphene addition on mechanical properties, showing a significant increase on the tensile strength and Young Modulus at lower nanoreinforcement contents.

In this regard, CNP dispersion into the insulator matrix is a challenging effect because a poor CNP distribution lead to a detriment on mechanical and other physical properties, acting the CNP agglomerates as stress concentrators and weak points. There are several dispersion techniques:

- Three roll milling (3RM) technique, also called calendaring process: It consists on the nanoparticle dispersion due to shear forces involved when two consecutive rolls rotate at different speeds (Figure 1.6 (a)). There are many studies investigating the effect of 3RM technique on CNT dispersion. A. Jiménez-Suárez et al. [52,53] deeply explored the dispersion effectiveness of a batch method versus a time-controlled one in 3RM process of CNT doped nanocomposites. The first one consisted on a progressive reduction in the gap between rolls while the second one consisted on a continuous 3RM process during 180 min at a constant gap. They found that batch method had a positive effect at higher CNT contents due to a higher CNT disaggregation effect. In addition, they also observed that functionalization also plays a dominant role in CNT dispersion and, thus, on mechanical properties. Amino-functionalized CNTs showed a poorer behavior, especially at higher contents, due to a more prevalent tendency to agglomerate. M.

Chapartegui et al. [54] studied the effect of nanoparticle dispersion in the creation of CNT networks during curing. They observed that, at CNT contents above 0.3 wt. %, a physical network is formed, accelerating the curing process.

- Toroidal stirring: It consists on a mechanical stirring at a controlled rotating speed of the blades. It induces a toroidal 3D flow of the CNP/epoxy mixture (Figure 1.6 (b)). In this regard, M. Aravand et al. [55] studied the evolution of the CNT dispersion during manufacturing at different stages: as received, after dispersion process, during curing and in the final nanocomposite. They observed that there are stronger interactions between CNT clusters with storage time, redounding in significant variations of their physical and mechanical properties. This process is usually combined with 3RM to achieve the optimum nanoparticle dispersion. An example of this, is the research of B. Ahmadi-Moghadam et al. [56] who studied the effect of a combined mechanical stirring-3RM process in the mechanical and physical properties of GNP/epoxy nanocomposites, observing variations in the lateral size of the GNPs due to dispersion procedure.
- Sonication: It consists on the emission of ultrasonic pulses in a nanoparticle mixture which trends to aggressively disaggregate the largest agglomerates (Figure 1.6 (c)). Several studies [57-59] deeply investigated the effect of the media and sonication power on the CNT dispersion. It was found that a higher viscous media induces a higher CNT breakage due to the higher strain rates involved at cavitation process. R. Moriche et al. [60], however, found that sonication could have a positive effect on GNPs, inducing an exfoliation of graphene layers. When combining with 3RM, which trends to stretching GNPs, optimum mechanical and physical properties could be achieved. Nevertheless, most of research on sonication procedure were done in a low-viscous media.

CNP addition into an insulator media also induces a very significant enhancement of the electrical conductivity. A. Moisala et al. [61] achieved an electrical conductivity ranging from 10^{-3} to 1 S/m for MWCNT and SWCNT nanocomposites fabricated by means of chemical treatments and ball-milling at 0.6 wt. % CNT content. A. Allaoui et al. [62] reached conductivities of around 5 S/m at 4 wt. % content in nanocomposites manufactured by manual dispersion of CNT into an epoxy matrix. C.A. Martin et al. [63] investigated the effect of CNT alignment in the enhancement of electrical conductivity for CNT contents ranging 0.0025 to 0.01 wt. %. J.R. Potts et al. [64] studied the effect of the reduced graphene on the electrical properties of nanocomposites. They achieved conductivities of around 10^{-1} S/m at 2.5 vol. % graphene content. Z.A. Ghaleb et al. [65] also investigated the enhancement of electrical properties due to the GNP addition into an epoxy matrix. They reached electrical conductivities of 10^{-2} S/m at 1 vol. % GNP content. S.G. Prolongo et al. [66] also explored the effects of GNP addition to epoxy matrices and reached conductivities of $5x10^{-3}$ S/m at 8 wt. % GNP content.

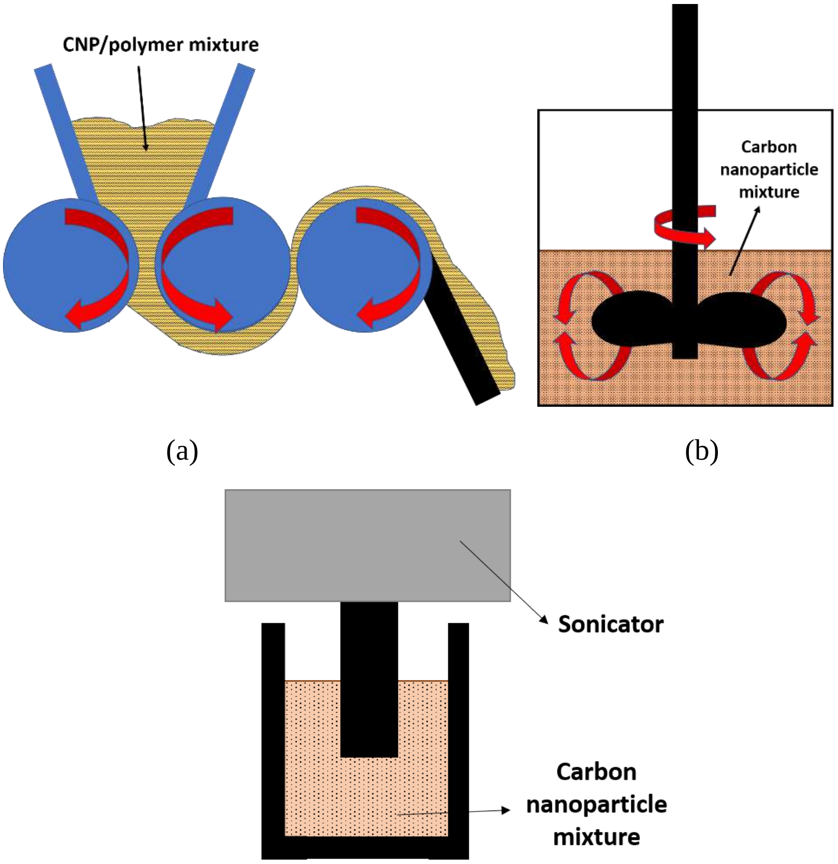

(a) (b)

(c)

Figure 1.6: Schematics of (a) three roll milling, (b) toroidal stirring and (c) sonication dispersion procedure.

The enhancement of the electrical conductivity is explained by the creation of electrical pathways inside the material when a critical volume fraction of the nanoreinforcement is achieved, called percolation threshold (Figure 1.7). At this point, the material becomes electrically conductive.

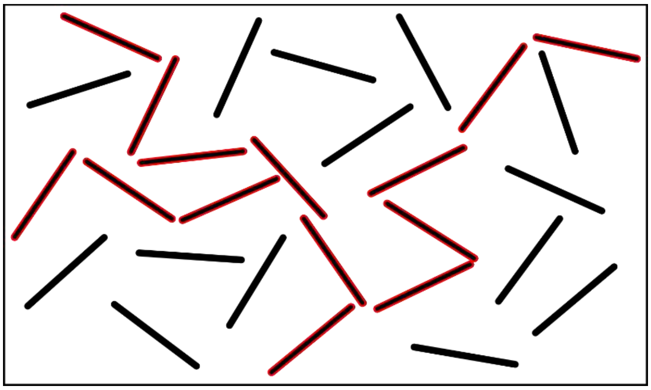

Figure 1.7: Schematics of the creation of percolating networks (in red) inside the material.

The determination of percolation threshold is not trivial and there are a lot of research in determining this volume fraction for nanoreinforced polymers, also called nanocomposites, by using CNTs and GNPs as well as other conductive nanoparticles.

W. Bauhofer et al. [67] did an extensive review about the percolation threshold in CNT doped composites. It has been observed that percolation threshold highly depends on the type of CNT, MWCNT and SWCNT, as well as on the dispersion procedure. In fact, J.K.W. Sandler et al. [68] found a percolation threshold of around 0.0025 wt. % content by using aligned MWCNTs dispersed by a shear-intensive mechanical stirring using a dissolver disk. N. Hu et al. [69], however, achieved a percolation threshold of 0.1 wt. % using MWCNTs dispersed by toroidal stirring. Other studies, such as A. Yu et al. [70] reach the percolation threshold at a weight fraction higher than 1 % by using sonication as dispersion procedure due to a higher entanglement of SWCNTs.

On the other hand, percolation threshold in GNP nanocomposites is achieved at much higher nanoparticle contents. R. Moriche et al. [71,72] achieved percolation thresholds of 2 and 8 wt. % for non-functionalized and amine-functionalized GNP nanocomposites, respectively, by using a mixed calendaring-sonication procedure. F. He et al. [73] found a PT of around 1 vol. % by using exfoliated graphene and a tip sonication process. S. Stanckovich et al. [74], however, reached PT at 0.1 vol. % GNP content by using graphene sheets of a thickness equivalent to a single graphene layer.

It has been observed that it is mainly ruled by the nanoparticle geometry and dispersion inside the material. J. Li et al. [75,76] proposed a novel analytical method to estimate the percolation threshold on CNT and GNP doped nanocomposites. Aspect ratio, that is, the ratio between the length and the thickness (in case of GNPs) and diameter (in case of CNTs), is a critical factor as well as the ratio of dispersed and agglomerated particles. In addition to that, the 1D or 2D nature of nanoparticles plays an important role when creating the percolating networks.

Therefore, it explains the higher percolation threshold when using GNPs when comparing to CNTs, due to its 2D geometry.

1.4.3 Carbon based nanocomposites as strain and damage sensors

In this context, there are three different mechanisms for electrical conductivity in nanocomposites, as shown in Figure 1.8 (a). The first one is due to the intrinsic electrical conductivity of the carbon nanoparticles, the second one is due to the electrical contacts between nanoparticles and the third one is called tunneling effect and takes place when there are two adjacent conductive nanoparticles inside an insulator media. At nanoscale, and when the distance is lower than 2 nm approximately there is a migration of electrons between the nanoparticles. In fact, the last mechanism is the most dominant due to the exponential behavior of the tunneling resistance as a function of the tunneling distance, as expressed by J.G. Simons et al. [77]:

$$R_{tunnel} = \frac{h^2 t}{Ae^2\sqrt{2m\varphi}} exp\left(\frac{4\pi t}{h}\sqrt{2m\varphi}\right) \tag{1.2}$$

Where A and t are the tunneling area and distance, respectively; m and e the electron mass and charge, h the Planck constant and φ the height barrier of the insulating resin.

Accordingly, the tunneling resistance depends on the distance between nanoparticles. This tunneling distance will change with macroscopic strain inducing, thus, a variation of the tunneling resistance.

Therefore, it will be possible to monitoring the strain of the material by means of electrical resistance measurements, being the basis for their use in strain and damage sensing applications.

Moreover, the electrical conductivity of the material will be also affected by the presence of discontinuities such as cracks, inducing a breakage of electrical pathways as observed in the schematics of Figure 1.8 (b). Therefore, the whole material will act as a sensor itself.

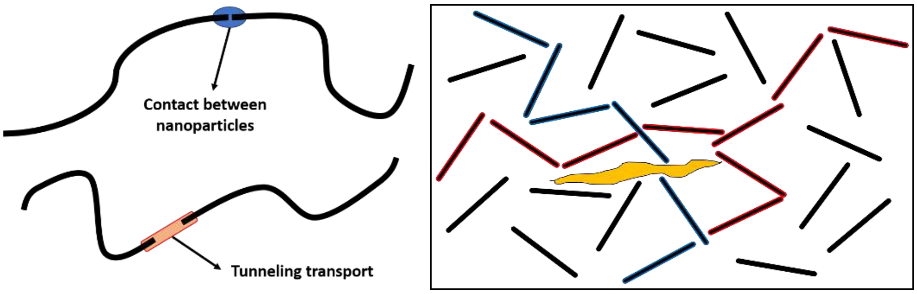

(a) (b)

Figure 1.8: Schematics of (a) electrical transport in carbon nanoparticles and (b) effect of the crack on the breakage (in blue) of electrical pathways in a percolating network.

To date, there are many studies proving the SHM capabilities of CNP doped composites. E. Thostenson et al. [78] demonstrated the high potential of CNT doped composites to strain monitoring purposes and defect detection. They remarked, in latter studies, the dominant role of tunneling resistance on their electrical properties [79]. N. Hu et al. [80] investigated the strain sensitivity of CNT based composites showing that higher CNT contents generally lead to lower gauge factors (GFs), defined as the change of the normalized resistance with applied strain. This is explained due to the exponential behavior of the tunneling resistance with distance between adjacent CNTs. B. De Vivo et al. [81] found similar results and also studied the influence of the chirality of CNTs on strain sensing purposes. In addition to that, there have been a lot of research in the last years proving the SHM potential of CNT nanocomposites [82-85].

More specifically, they show a great potential as strain sensors. C. Robert et al. [86] manufactured sensing skins made of conductive nanocomposites sprayed layer by layer on a PET woven textile. They were able to demonstrate their high sensitivity under static and cyclic deformation. B.R. Loyola et al. [87] analyzed the effect of mechanical and environmental effects on the electrical response of CNT based nanocomposites. They found that the electrical resistance has a high dependence on temperature and the sensors are highly sensitivity to humidity in the range of 35-80 % RH. S.K. Reddy et al. [88] proved the strain sensing capabilities of biocompatible CNT/UHMWPE nanocomposites processed by solution mixing technique. GF was found to be 2 in the elastic regime while in the inelastic regime was ranging from 4 to 96, showing also an improved mechanical performance. Moreover, there are also many studies using Electrical Impedance Tomography (EIT) methods for damage detection using this type of materials. In fact, B.R. Loyola et al. [87] already explored this aspect in their study. T.N. Tallman et al. [89] proposed strain sensing CNF/polyurethane composites showing their high sensitivity to strain and damage detection. Based on the variation of electrical conductivity along the specimen, it is possible to build a mapping of defect and strain distribution. J.L. Kenneth et al. [90] also developed CNT sensing skins for spatial strain and damage identification distribution. To achieve this purpose, several types of defects were induced and a complete mapping of them was carried out by using mathematical and statistical tools.

In addition to that, GNPs have been also explored as an alternative to SHM applications. R. Moriche et al. [72,91] have proved a high sensitivity to strain and a reversible electrical behavior of GNP sensing skins and bulk nanocomposites (Figure 1.9). They exhibit a much higher GF than most of CNT based nanocomposites which is explained attending to the 2D morphology of GNPs. L.M. Chiacchiarelli et al. [92] also explored the irreversible and reversible phenomena applied to GNP strain gauges. They showed a good agreement between the electrical response and the mechanical behavior as well as a high electrical sensitivity, with changes of more than 100 % in the normalized resistance at low strain levels (around 0.01). V. Eswaraiah et al. investigated the electrical response by using thermoplastic and thermosetting resins [93,94] showing also a high sensitivity with GF of around 12 and a strong linear response.

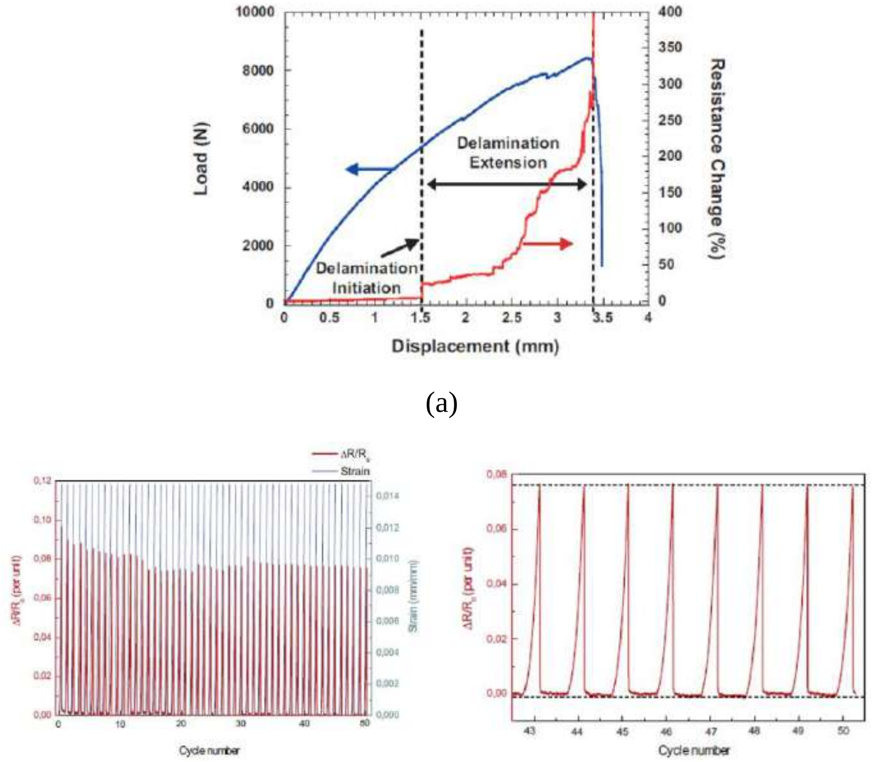

(a)

(b)

Figure 1.9: (a) Electrical monitoring of a GFRP CNT/epoxy multiscale composite showing the damage initiation and extension and (b) strain sensing reversibility of GNP/epoxy nanocomposites [91].

This high sensitivity is explained, not only because of the tunneling effect between adjacent particles but also due to the piezoresisitive properties of CNPs. It means that their electrical resistivity changes with applied strain, making them more sensitive to strain than conventional metallic foils, which have a GF in the range of 2-4. In fact, J. Cao et al. [95] determined the electromechanical properties of quasi-metallic and semiconducting CNTs under tension. They observed that semiconducting CNTs showed the highest GF, being in the range 600-1000. This GF was much lower in metallic CNTs. M.A. Culliman et al. [96] proposed a theoretical framework to analyze the dependence of the CNT sensitivity with chirality, that is, orientation of hexagonal carbon network, founding GFs of around 80.

1.4.4 Modelling of electrical properties

Although the transport mechanisms in CNP nanocomposites is well known, there are a lot of factors affecting the electrical response of these materials due to the complexity of CNP distribution. For these reasons, it is necessary to develop analytical and numerical techniques in order to properly characterize this type of sensors.

W.S. Bao et al. [97,98] studied the effect of CNT agglomeration and orientation on the electrical conductivity of nanocomposites. It was found that electrical conductivity increases with CNT alignment due to the creation of more percolating networks (Figure 1.10). However, the effect of CNT agglomeration was more complex: at low CNT contents, it seems to have a positive effect while at higher contents, the electrical conductivity decreases with increasing CNT agglomeration. S. Gong et al. [99] proposed a novel theoretical model considering the deformation of CNT at nanotube junctions. For this purpose, hey simulated a 3D random CNT distribution. Their main conclusion was that the intrinsic resistance decreases with CNT interparticle distance as there are not distortion effects while the tunneling resistance obviously increases. In addition to that, they found a good agreement between experimental results and theoretical predictions. Y Wang et al. [100] explored the tunneling-assisted interfacial conductivity of CNT/polymer nanocomposites by including interface defects. They found that the estimation of electrical conductivity is too high when not considering interface defects. However, when considered and taking the interfacial conductivity into account, theoretical predictions fit the experimental measurements.

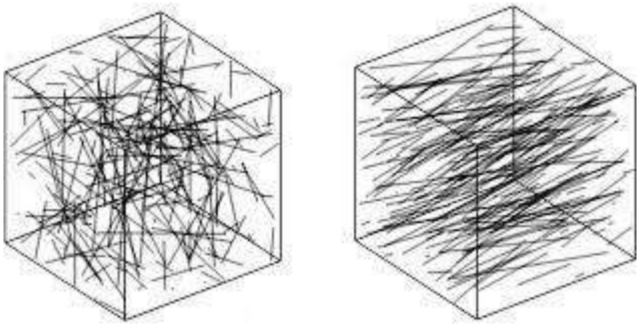

(a)

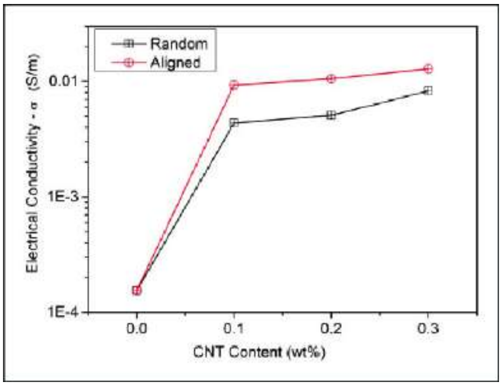

(b)

Figure 1.10: (a) Modelling of a 3D random CNT (left) and CNT aligned distribution from W.S. Bao et al. [97] and (b) influence of CNT alignment on electrical conductivity of nanocomposites (Source: S. Jangam et al. [101]).

Regarding to strain sensing capabilities, N. Hu et al. [102] explored the tunneling effect in a polymer/CNT nanocomposite strain sensor. They used a 3D random CNT distribution to simulate the electrical network and applied the Simmons formula to predict the piezoresistive behavior of the nanocomposites. What they observed is that the closer to the percolation threshold the higher the sensitivity due to the previously commented exponential effect of the tunneling resistance.

However, this assumption did not take the geometry of the CNTs and the interactions between nanoparticles into account. R. Rahman et al. [103] studied the effect of CNT alignment on electrical conductivity and sensitivity of strain sensors by proposing a novel theoretical model taking these parameters into account. They found that the higher the CNT alignment the higher the electrical conductivity and sensitivity at low strain levels. In addition, Y. Kuronuma et al. [104] proposed a novel analytical model by taking two types of CNT contacts into account: one called, in-plane contacts, in a similar way than N. Hu et al. and other called, out-of-plane contacts, dominated by Poisson effects (Figure 1.11). By this way, they observed that the sensitivity of the strain sensor is not only dominated by the CNT content but also by the interactions between nanoparticles.

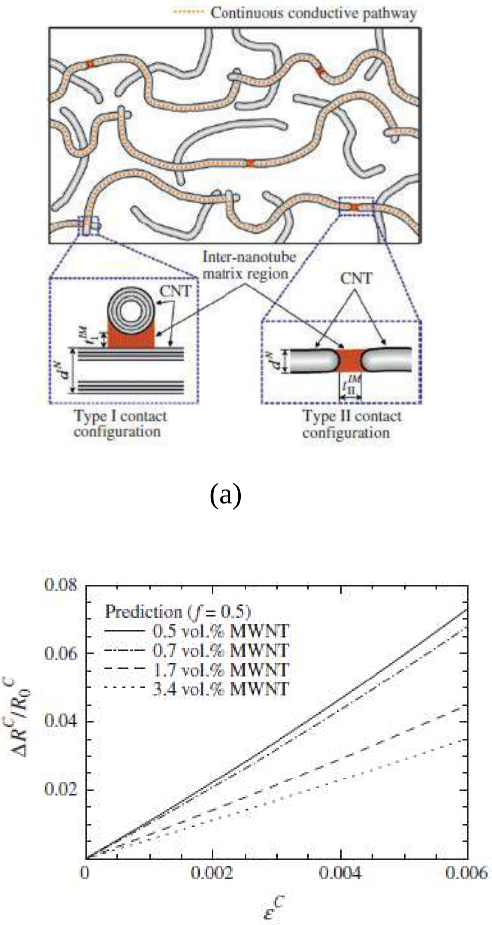

(a)

(b)

Figure 1.11: (a) Schematics of type I and II contacts defined by Y. Kuronuma et al. [104] and (b) their influence on strain sensing capabilities of CNT nanocomposites.

In a latter study, F. Panozzo et al. [105] investigated the effect of CNT waviness on the electrical sensitivity. They observed that a higher CNT entanglement generally led to an increase of sensitivity due to a higher inter-particle distance. By adjusting the parameters of the model, they found a good agreement between their theoretical predictions and experimental results.

Electrical properties of GNP/polymer nanocomposites have been also object of an extensive study. J. Hicks et al. [106] did a computational study of tunneling-percolation electrical transport. They found that the tunneling area, that is, the contact area where tunneling transport takes places, plays a very dominant role, being much more difficult to estimate than in CNT nanocomposites. In addition, they also found that a higher aspect ratio of GNP lead to much lower resistivities. W. Wang et al. [107] did a computation study of electrical conductivity of GNP/polymethacrylate nanocomposite by using Monte Carlo simulations and percolation theory. The contact area between GNPs and their geometry were discussed. It was found that the smaller the GNP size the higher the overall resistivity due to a higher prevalence of the tunneling mechanisms. The theoretical results were compared to experimental showing a good agreement. Y. Wang et al. [108] investigated the effect of filler agglomeration in a similar way than they previously did for CNTs [100]. They found that electrical conductivity of GNP nanocomposites is very dependent on the interface defects. In addition, they analyzed the contribution of the graphene rich and poor regions to the overall conductivity.

However, there is a lack, to date, of analytical models that properly correlate the electrical and mechanical properties, as most of the theoretical studies involve the use of numerical and statistical tools that do not usually offer a global overview of the overall behavior of the nanocomposite. For this reason, it is particularly important to develop novel analytical tools that properly capture all the electrical and sensing mechanisms of nanocomposites.

Therefore, this type of nanoparticles has demonstrated a huge potential for strain and damage sensing detection. For these reasons, its applicability to bonded joints, where the difficulty for inspection has been widely explained before, is nowadays of interest. To date, there are a lot of research in paste adhesive showing their ability to strain monitoring and crack detection and propagation.

1.4.5 Carbon nanostructures in adhesive joints: mechanical and sensing behavior

T. Takeda et al. [109] studied the fracture behavior and crack sensing capability under Mode-I loading in CFRP-CFRP bonded joints with CNTs. They observed a good agreement between electrical response and crack propagation with sharp increases of the electrical resistance corresponding to sudden drops in the mechanical response, as shown in Figure 1.12 (a). In addition to that, crack propagation on fatigue loading in lap joints has been widely studied. M-H. Kang et al. [110] analyzed the fatigue life evaluation and crack detection of this type of adhesives by means of electrical measurements through thickness. It has been observed that crack initiation and propagation can be effectively monitored by observing sudden changes on the electrical response. R. Mactabi et al. [111] observed a similar electromechanical behavior with a general increase of the electrical resistance baseline with number of cycles (Figure 1.12 (b)) showing the CNT pullout and bridging effect during crack propagation. A. S. Lim et al. [112] also studied the sensing response of CNT doped adhesives when joining dissimilar materials, showing also a good agreement between crack propagation and electrical monitoring.

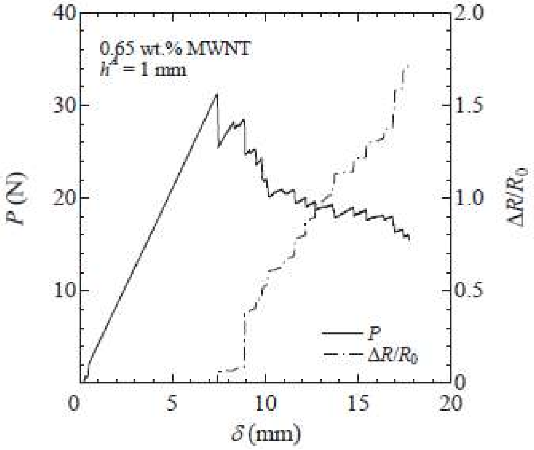

(a)

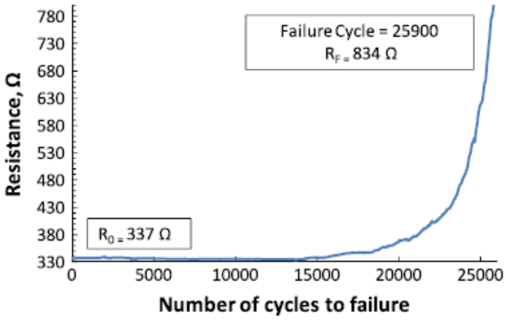

(b)

Figure 1.12: Electrical response of a (a) mode-I CFRP-CFRP specimen from T. Takeda et al. [109] and a (b) SLS joint subjected to fatigue loading as a function of the number of cycles from R. Mactabi et al. [111]

The effect of CNT addition on mechanical properties of adhesive joints has been also widely investigated. In fact, M. R. Gude [113,114] showed in several studies that Mode-I fracture energy of CFRP-CFRP bonded joints is significantly improved (from values around 220 to 275 J/m^2) due to the toughening and crack bridging effect of CNTs. U. Vietri et al. [115] observed an increase in the bond strength leading to a change in the failure mode when adding carbon nanofibers (CNFs). In addition to that, some adverse effects can be also observed when CNF content is very high, due to some dispersion problems in the epoxy mixture. I. A. Akpinar et al. [116] used functionalized graphene, CNTs and fullerene in Single Lap Shear (SLS) joints, observing an increase in the tensile load and shear strength of 15-50 % depending on the nanofiller. Other studies also reveal an enhancement on the strength and crack propagation capabilities of adhesives when adding carbon nanofillers [117-120].

It is particularly interesting the research within the field of adhesive films. They are defined as semicured adhesives having a carrier or reinforcement, which act as a support to provide a tape or film. Because of this, they have excellent strength and bonding properties and are widely used in aircraft industry [121]. One of the main advantages is that they provide a higher thickness control due to the presence of the mentioned carrier.

To date, however, the research of CNT addition into adhesive films and its sensing and crack detection properties remains to be investigated. C. García et al. [122] first proposed a novel CNT doped adhesive film by spraying an aqueous solution of CNT dispersed by means of ultrasonication onto the adhesive film surface. They proved its capability to detect debonding in composite structural repairs by correlating electrical resistance measurements with other inspection techniques such as acoustic emission and strain gauges [123]. The results were promising but a deeper approach on sensing and crack propagation monitoring capabilities of these novel adhesive films in various types of bonded joints is still needed and, thus, it constitutes one of the crucial points of the present work.

In addition to the previously commented facts, it is important to point that the increasing use of FRP structures in combination with conventional alloys, such as in the aircraft industry, makes necessary the research in adhesive joints of dissimilar materials, that is, FRP to metal interfaces. In fact, there is an increasing interest in this subject in the last years.

A. Rudwaska et al. [124] explored the Lap Shear Strength (LSS) of composite to aluminum and composite to titanium bonded joints. It was observed that, LSS of dissimilar joints differs from that obtained for composite-composite or metal-metal joints which is very dependent on the load transferring between substrates and the strength and stiffness of the adherends. For example, an increase of 15 % was observed in composite-titanium joints in comparison to composite-composite while a decrease of 15 % was achieved when comparing to titanium-titanium joints. They concluded that a hybrid solution could enhance the strength of the weaker joint if a proper load transferring takes place. M.D. Banea et al. [125] investigated the influence of adherend thickness in multi-material joints of composite-steel and composite-aluminum, showing that thicker adherends could enhance the LSS. T.E.A. Ribeiro et al. [126], on the other hand, did a damage analysis of composite-aluminum bonded joints by varying the overlap length. They observed that the higher the overlap length the higher the LSS, being this effect more prevalent depending on the adhesive. N.G. Tsouvalis et al. [127] also observed an enhancement on the tensile strength of a joint made of Glass Fiber polymer composite (GFRP) and steel. In addition to that, several studies further explored the capabilities of dissimilar joints [128,129] even using a digital image correlation technique to better characterize the crack propagation and failure modes in this type of joints [130].

The effect of nanoparticle addition into the adhesive has been also widely investigated in this type of joints. Accordingly, A.H. Korayem et al. [131] studied the effect of a CNT doped adhesive on CFRP-steel interface. It was observed that CNT trend to strengthen the joint in a similar way than previously commented for CFRP-CFRP joints. A more prevalent CFRP delamination and steel failure is observed when adding the nanoparticles. This effect is more pronounce at shorter bonding lengths where an increase of 15 % in LSS is achieved. M. Konstantakopoulu et al. [132] also investigated the effect of CNT addition at different nanofiller contents in GFRP-Aluminum joints. They observed that the optimum CNT content was around 0.1 wt. % where an increase of nearly 20 % in LSS was achieved. For contents above the mentioned, a slight decrease was observed due to a higher tendency of CNT to form agglomerates inside the matrix.

For all the aforementioned reasons, CNTs seem to be a promising technique for SHM applications without a significant detriment on mechanical properties. That is the main motivation of the present work, which will be focused on studying and analyzing the electromechanical properties of CNT nanocomposites as well as its applicability in bonded joints from coupon to skin-stringer sub-element by using adhesive films.

1.5 Framework of the present study

Based on the previously commented facts, the framework of the present study will be focused on proving SHM capabilities of CNT reinforced composites from theoretical to experimental point of view.

On the one side, a deep theoretical analysis of electromechanical properties of CNT nanocomposites is done to better understanding the role of CNT dispersion and distribution on electrical properties of this type of materials. The main aim is to evaluate the effect of CNT geometry and waviness as well as the aggregation degree of nanoparticles on tunneling mechanisms of CNT composites. To achieve this purpose, the proposed theoretical study will be focused in two different objectives:

- Understanding the role of CNT dispersion and entanglement on electrical conductivity of nanocomposites by exploring the definition of percolation threshold. In this context, a detailed study about dispersion procedures and their influence on CNT waviness will be conducted. Moreover, CNT orientation and breakage of CNTs will be also explored by understanding their role on electrical properties.
- Identifying critical parameters affecting the SHM capabilities of nanoreinforced composites by defining dispersion parameters and their role on tunneling mechanisms inside the material by simple theoretical estimations. In addition, a theoretical estimation of inter-particle distance will be also carried out based on previous literature.

In both cases, a complete study on dispersion procedures will be carried out, in order to identify the optimum manufacturing parameters to achieve the desired behavior.

On the other hand, SHM applicability of CNT reinforced composites will be also investigated.

Here, the idea is to develop a multifunctional composite structure with self-sensing properties. Due to the critical importance of joining in this type of structures, this work will be focused on crack propagation and strain sensing monitoring of bonded joints by using a novel CNT doped adhesive film. For this reason, the study will go from coupon to sub-element level in a similar way than for a building block test for an aircraft structure (Figure 1.13).

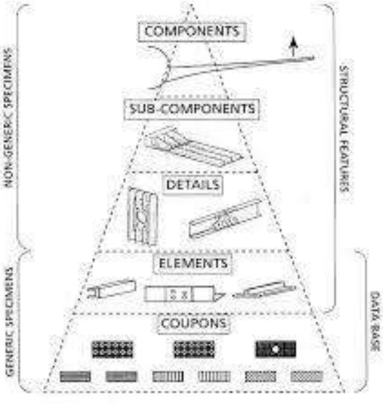

Figure 1.13: Diagram of building lock test for a fixed wing (taken from FAA Advisory Circular No. 20-107B).

In this regard, several objectives must be satisfied:

- A complete and detailed analysis of mechanical behavior at a coupon level. To achieve this purpose several SLS, Mode-I and Mode-II tests will be carried out by varying different conditions of dispersion procedure. A particularly detailed analysis of crack propagation and fracture mechanisms will be also carried out to better understanding their mechanical response
- A simultaneous monitoring of electrical response of these joints. The idea is to correlate their electrical properties to mechanical behavior to identify the main conductive mechanisms and evaluate their sensing capabilities. In this regard, some simple theoretical estimations will be conducted within the framework of those proposed for CNT nanocomposites.
- A study of ageing conditions to evaluate the durability of the proposed adhesive films. Moreover, electrical monitoring will be also evaluated as a sensing technique to better understanding ageing mechanisms in this type of materials.
- Fatigue capabilities will be also explored, in a more realistic load scenario. Here, a great effort on correlating electrical to mechanical

properties will be done and crack propagation monitoring capabilities will be determined.

- A study of electromechanical properties of joints with dissimilar materials will be carried out to demonstrate the applicability of the proposed technology for SHM applications in CFRP-metal bonded joints.
- An electromechanical characterization of skin-stringer sub-element will be finally conducted to evaluate the crack monitoring capabilities of the proposed adhesive film in more complex CFRP structures. In this regard, skin-stringer elements will be subjected to peeling and bending conditions to evaluate the sensitive response of CNTs to different load states. Moreover, a shallow comparison to other SHM techniques such as guided waves or electromechanical impedance will be conducted to highlight the main advantages of the proposed technique.

The complete study of electromechanical properties of adhesive joints together with the proposed technology will give a detailed knowledge about crack propagation mechanisms and applicability of CNTs for SHM purposes.

For these reasons, the present document will be divided in two parts: one treating the sensing and electrical properties of CNT based nanocomposites, corresponding to Chapters 3 to 5 and the other analyzing the crack propagation monitoring capabilities of CNT doped adhesive films in bonded joints at coupon and sub-element level, corresponding to Chapters 6 to 12.

CHAPTER 2: MATERIALS AND METHODS

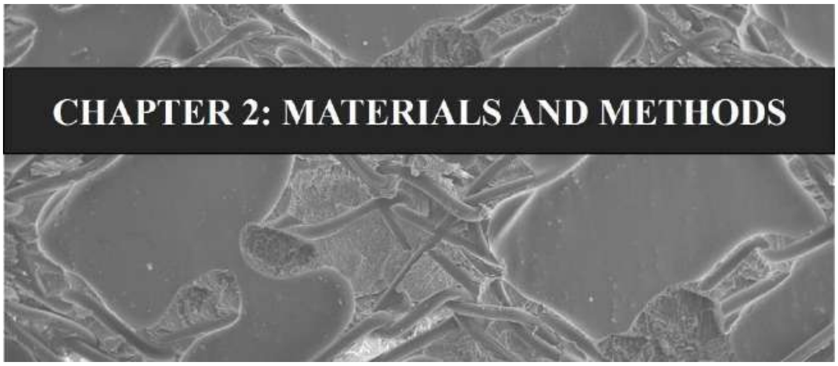

Chapter 2: Materials and methods

In this chapter, a detailed description of materials and methodology is shown. As previously commented, the present work is focused on two different objectives: CNT electromechanical modeling of nanocomposites and SHM applications in adhesive joints. Therefore, this chapter is divided in CNT nanocomposite manufacturing and adhesive joining.

2.1 CNT nanocomposite for electromechanical modeling

2.1.1 Materials

Three types of CNTs were used for the present study, supplied by Nanocyl: NC3100, with an average diameter of 9.5 nm and a length up to 1.5 µm (Figure 2.1 (a)). NC3150, with an average diameter of 9.5 nm and a length up to 1 µm (Figure 2.1 (b)) and NC3152, amino-functionalized, with an average diameter of 9.5 nm and a length up to 1 µm (Figure 2.1 (c)). They are produced by Catalytic Chemical Vapor Deposition (CCVD) and have a purity of more than 95 % in carbon content.

Resin is a bi-component epoxy, Araldite LY 556, supplied by Huntsman. Hardener, with a commercial name, XB 3473 is added in a proportion 100:23 (monomer:hardener).

The main physical properties of the resin are shown in Table 2.1, based on the Technical sheets provided by the suppliers.

Table 2.1: Properties of LY556/XB 3473 system.

Araldite LY556/XB 3473	
Viscosity (25 ºC)	5200-600 mPa s
Viscosity (45 ºC)	700-900 mPa s
Flexural strength	110-120 MPa
Young's modulus	2.7 -2.9 GPa
Strain at failure	5.5-6.5 %
Fracture Toughness (G_{IIC})	190-220 J/m^2

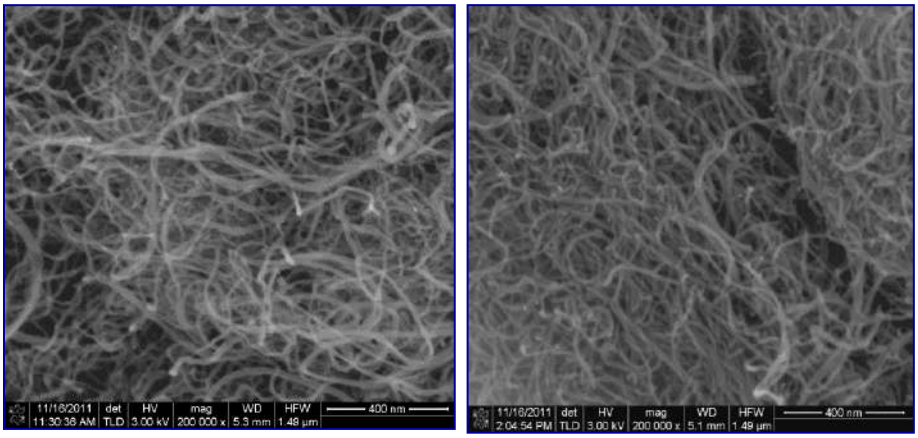

(a) (b)

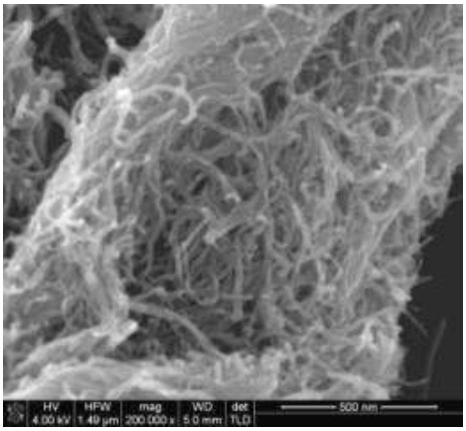

(c)

Figure 2.1: FEG-SEM images of (a) NC3100. (b) NC3150 and (c) NC3152 MWCNTs showing the aggregation degree.

2.1.2 Manufacturing of nanocomposites

CNT reinforced composites are manufactured to analyze and modeling their electrical properties. The fabrication is carried out in several steps: (1) CNT dispersion into epoxy, (2) degasification of CNT/epoxy mixture and (3) hardener mixing and curing.

CNT dispersion into the epoxy matrix is carried out by means of two different techniques in order to identify the main electrical mechanisms of nanocomposites and the role of CNT dispersion on electrical properties of nanocomposites.

On the one side, several materials were fabricated by three roll milling technique, using an EXAKT 80E apparatus. It consists, as explained before, in the presence of shear forces inducing a disaggregation of main agglomerates into the mixture by a progressive gap reduction between consecutive rolls, as observed in the schematics of Figure 2.2 (a). The parameters of roll speed and gap distance were set accordingly to previous studies [53], as shown in Table 2.2. For the theoretical model, several configurations of three roll milling steps were tested to deeper analyze the influence of the mentioned technique over electrical and SHM capabilities of nanocomposites.

On the other hand, some materials were manufactured by toroidal stirring, using a Dispermat dissolver, consisting on a blade rotation disc which induces a 3D flow into the mixture, leading to a more homogeneous CNT distribution inside the material (Figure 2.2 (b)). Rotating speed and dispersion time were set at 6000 rpm and 20 min for every tested condition.

Table 2.2: Process conditions for three roll milling dispersion.

Cycle	First roll gap (μm)	Last roll gap (μm)
1	120	40
2	75	25
3	45	15
4-7	15	5

Moreover, the combination of both techniques was also analyzed to see the prevalent effects of each process over the final dispersion of CNTs.

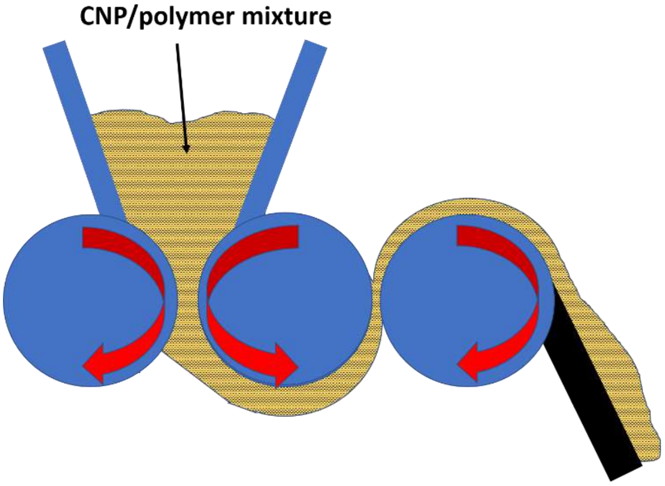

(a)

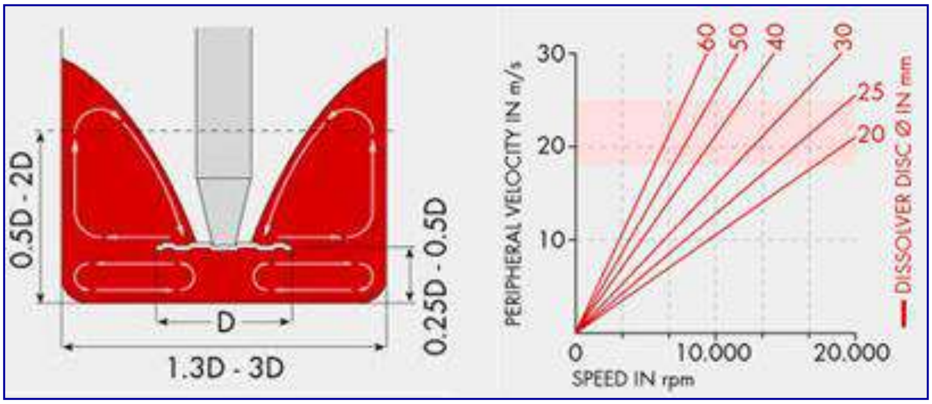

(b)

Figure 2.2: Schematics of (a) three roll milling process and (b) toroidal stirring showing the flow direction and the influence of disc rotation on periferial velocity.

The degasification step was carried out under vacuum conditions at 80 ºC for 15 min. The aim is to remove the entrapped air during dispersion procedure. It is particularly critical when the mixture viscosity is very high, usually correlated to high CNT aggregation were the reinforcement wettability is lower and thus, there is a prevalence of voids in the mixture.

After degasification step, hardener was added into the CNT/epoxy mixture in a proportion 100.23 (monomer:hardener). Curing of nanocomposites was conducted in an oven at 140 ºC for 8 hours, already optimized in other studies accordingly to mechanical and physical properties [52].

2.1.3 Electrical conductivity tests

DC volume electrical conductivity of CNT nanocomposites was evaluated at several tested conditions. It was determined, accordingly to ASTM D257 using a Source Measurement Unit (SMU, Keithley Instrument Inc. mod. 2410) as the slope of I-V curve of 10x10x1 mm specimens. Accordingly to Ohm's Law, it gives the value of electrical resistance, R, which is used to calculate the electrical conductivity, σ, from the specimen dimensions:

$$\frac{1}{R} = \frac{I}{V} \tag{2.1}$$

$$\sigma = \frac{1}{R} \cdot \frac{L}{A} \tag{2.2}$$

Where L and A are the length and transversal section of the samples.

In this case, voltage was varied in a range of 0-25 V with 10 intermediate measurement points on four specimens for each condition. Silver ink was applied in the lateral sides to ensure a good electrical contact between the material and the electrodes used to determine the electrical conductivity. An example of a I-V curve is shown in the graph of Figure 2.3.

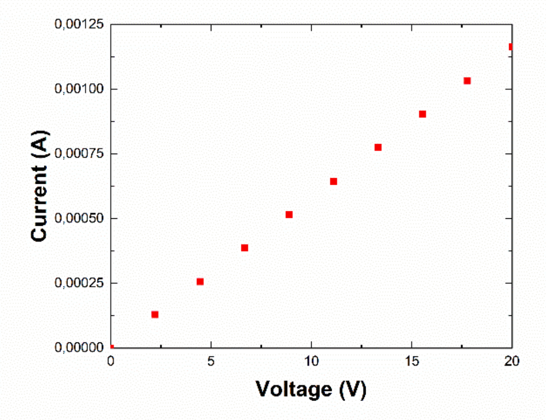

Figure 2.3: Example of a I-V curve used to determine the electrical conductivity.

2.1.4 Electromechanical testing

Electrical monitored tests were carried out to evaluate the sensitivity of the CNT nanocomposites. Therefore, electrical resistance was measured simultaneously to mechanical testing. To achieve this purpose, a hardware Agilent 34410A was used at an acquisition frequency of 10 Hz, enough for a proper monitoring in quasi-static testing.

Electrodes were made of copper wire, attached to the nanocomposite substrate with silver ink and then sealed with an adhesive layer in order to protect them from environmental issues and avoiding dettaching. This is a similar configuration than other studies, proving a good efficiency and accuracy to properly capture the electrical properties variation during mechanical tests [91,133].

Two types of mechanical tests were carried out in CNT nanocomposites to evaluate their sensing behavior: tensile and flexure testing. In the first case, the test rate was set at 5 mm/min, accordingly to standard ASTM D638 and the electrodes were placed in the central region forming two rings to ensure a volume conductivity in the specimen, as shown in Figure 2.4. Bending load was applied at a test rate of 1 mm/min, accordingly to standard ASTM D790. In this case, two electrodes were placed in each side of the specimen, to capture the tensile and compressive loads during the test and correlate them with the electrical response, also shown in Figure 2.4.

Electrical sensitivity, also called, gauge factor (GF), was calculated as the change of the normalized resistance $\Delta R/R_0$, divided by the applied strain, ε, estimated, accordingly to standard as the displacement divided by the length of the central region $\varepsilon = \Delta L/L_0$.

$$GF = \frac{\Delta R/R_0}{\varepsilon} \tag{2.3}$$

Figure 2.4: Schematics of electrode disposition in tensile (left) and flexure (right) coupons.

2.1.5 Microstructural characterization

2.1.5.1 Characterization of CNT dispersions

CNT/epoxy mixtures were characterized in order to analyze the effect of dispersion procedure in the CNT distribution and geometry. Several samples were characterized by Transmitted Optical Microscopy (TOM) using a Leica microscope equipped with a Nikon Coolpix 990 camera. In this case, a thin uncured CNT/epoxy mixture layer was characterized to better identify the quality of CNT dispersion inside the material.

On the other hand, to better characterize CNT waviness CNT/epoxy mixtures were characterized by Transmitted Electron Microscopy (TEM), due to the need of a detailed analysis of each individual CNT. A Philips Tecnai 20 – 200KV apparatus was used for this purpose. Then, an image analysis was carried out by using a SemAfore software. The aim was to empirically measure CNT waviness. To achieve this purpose, the effective length and waviness amplitude were measured for each individual CNT.

2.1.5.2 Characterization of CNT nanocomposites

CNT distribution in the cured nanocomposites was characterized by means of Field Emission-Scanning Electron Microscopy (FEG-SEM) using a Nova NanoSEM FEI 230 apparatus from Philips. To achieve that, a pre-crack was done under cryogenic conditions by immersing the samples in N_2 during 5 min. Then the specimens were coated by sputtering with a platinum layer of about 6 nm to improve their conductivity for an adequate characterization.

2.2 CNT doped adhesive films for SHM applications

2.2.1 Materials

An epoxy-based FM 300K adhesive film, supplied by Cytec, has been used for the present study to join the substrates. It has a wide knit tricot carrier to ensure a good thickness control during curing. Table 2.3 summarizes the mechanical performance of the adhesive accordingly to the data provided by the supplier.

Table 2.3: Properties of FM 300 adhesive film series.

Adhesive film serie	**Weight (g/m^2)**	**Tensile shear at 24 ºC (MPa)**	**Color**	**Carrier**
FM 300	390	35.5	Blue	Tight knit
FM 300K	390	40.3	Green	Wide open knit
FM 300M	150	29.8	Green	Random mat
FM 300U	390	36.4	Green	Unsupported film

Carbon nanoparticles used for this study were MWCNTs, with a commercial name NC7000, supplied by Nanocyl. They are produced by CCVD and have an average diameter of 9.5 nm, a length up to 1.5 µm and a carbon purity of around 90 % (Figure 2.5).

Substrates were made of UD CFRP laminates with different geometries depending on the mechanical test. In addition to that, aluminum alloy 7075 substrates were also used for joining dissimilar materials.

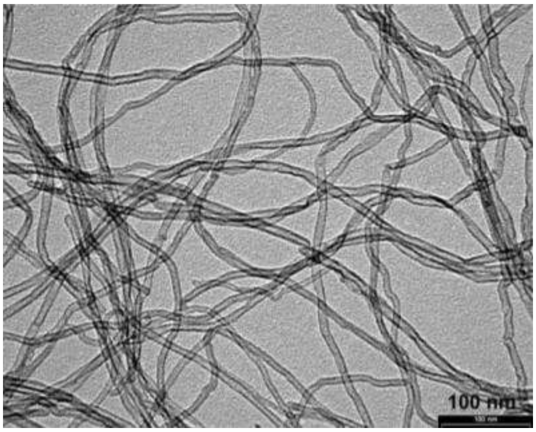

Figure 2.5: TEM images of NC7000 MWCNTs provided by Nanocyl.

2.2.2 CNT dispersion and adhesive joining manufacturing

MWCNTs addition to adhesive film is done by spraying an aqueous CNT solution over the adhesive surface. 0.1 wt. % CNT dispersion is achieved by means of ultrasonication in an aqueous media, as shown in Figure 2.6. For this purpose a horn sonicator Hielscher Ultrasonics GmbH/UP4000S is used giving a power of 20 kW. Time sonication is varied within 0-120 min to deeply analyze its effect on CNT dispersion. In addition to that, a surfactant called Sodium Dodecyl Sulphate, SDS, is used to improve the CNT dispersion by disaggregating the larger agglomerates as well as stabilizing the CNT dispersion over time. This kind of CNT dispersion procedure has been widely explored in other studies, showing a good performance [122,134,135].

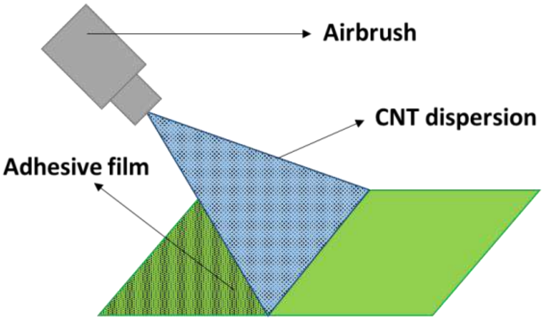

(a)

(b)

Figure 2.6: Schematics of (a) CNT addition by means of spraying over the adhesive film surface and (b) image of the CNT dispersion by ultrasonication.

CNT dispersion is then sprayed over the adhesive surface by using an airbrush at a pressure of 1 bar and a distance in the range of 20-40 cm from the adhesive surface.

After CNT dispersion and spraying, water is removed by a drying process at 70 ºC for 30 min prior to curing. Then, the adhesive film is positioned onto the substrate surface, as shown in Figure 2.7. Joining is done by secondary bonding in every case while the curing cycle depends on the samples manufactured.

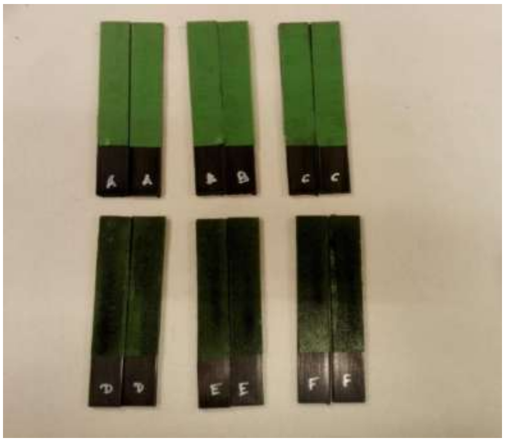

Figure 2.7: Image of adhesive joints prior to curing showing (above) neat and (below) CNT doped adhesive films prior to curing.

In case of standard coupon specimens, curing pressure and time conditions are shown in Table 2.4. Pressure is applied by an uniaxial hot press Fontijne Labecon 300.

In case of stiffened elements, due to the impossibility of using a hot press, the same curing cycle is applied under vacuum conditions in an oven. For this purpose, a vacuum bag is used, as shown in Figure 2.8. Here, it is necessary to make some folds around the stringer for a better positioning of the vacuum bag.

Table 2.4: Curing cycle parameters of secondary bonding.

Parameter	**First Stage**	**Second stage**
pressure	Ramp from 0 to 0.6 MPa for 15 min	0.6 MPa for 90 min
temperature	Ramp from 25 to 175 ºC for 45 min	175 ºC for 60 min

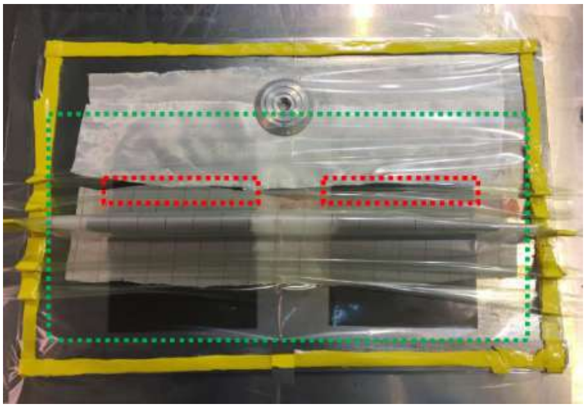

Figure 2.8: Image of vacuum bag used for manufacturing the stiffened elements where red and green areas indicate the location of stringer and skin elements, respectively.

2.2.3 Surface treatment of substrates

2.2.3.1 CFRP adherents

Peel-ply was selected as surface treatment for CFRP UD standard coupon substrates. It consists on the removal of a porous fabric after curing. It has proved an excellent interfacial adhesion due to the creation of an optimum surface roughness [13].

In case of stiffened elements, however, stringer surface treatment was peel-ply while the skin treatment was brushing with a 120 SiC sand paper.

2.2.3.2 Al 7075 adherents

In case of metal substrates, on the other hand, a study of surface treatment effect on electromechanical properties has been carried out. For this reason, several types of surface treatments were applied on the substrates: brushing with a 120 SiC sand paper and grit-blasting using a 1 mm average diameter corundum particles. The first one has a similar effect than on CFRP substrates while grit-blasting promotes the creation of an active surface, leading to high adhesion values.

2.2.4 Electromechanical testing

Electrical properties of adhesive joints were evaluated simultaneously to mechanical testing. When using CFRP substrates, electrodes were made of copper wire, silver ink and sealed with an adhesive layer in a similar way than for CNT nanocomposites. For Al 7075 substrates, the adherents themselves was used as an electrode due to their excellent electrical conductivity. The positioning and acquisition frequency depend on the mechanical test carried out.

2.2.4.1 Quasi-static testing in standard coupons

Three types of quasi-static tests were carried out in standard coupons: Single Lap Shear (SLS), Mode-I and Mode-II energy fracture tests. In every case, the electrical response was recorded with an Agilent 34410A hardware at an acquisition frequency of 10 Hz.

SLS tests were conducted accordingly to standard ASTM D5868-01 at a test rate of 1.23 mm/min to have enough acquisition points during the test. Substrate dimensions were 104x25x2.5 mm^3 with an overlap area of 25x25 mm^2. Electrodes were placed as shown in Figure 2.9 (a) and (b) for CFRP-CFRP and CFRP-Al joints respectively. The value of Lap Shear Strength, *LSS*, was estimated by using the following formula, correlating the peak force, P, divided by the lap area, A:

$$LSS = \frac{P}{A} \tag{2.4}$$

Mode-I tests were done accordingly to ISO 25217:2009 at a test rate of 1 mm/min. Substrate dimensions were 150x25x3.5 mm^3 with a pre-crack of 65 mm. The test was recorded with a video camera to properly determine crack propagation, as shown in Figure 2.10 (a). Edges were painted for a better observation of crack length and the value of fracture energy, GIC, was calculated by using the following formula:

$$G_{IC} = \frac{3P\delta}{2B(a + |\Delta|)} \cdot \frac{1}{N} \qquad (2.5)$$

Where P is the applied load, δ the piano hinge displacement, B the specimen width, a the crack length and $|\Delta|$ and N two correction factors depending on the ratio of displacement divided by the applied load.

Here, the electrodes were placed as shown in Figure 2.9 (c) in a similar way than for SLS testing.

Mode-II tests were done using 150×25×3.5 mm^3 with a pre-crack of 40 mm under bending conditions. Test rate was fixed at 1 mm/min and recorded with a camera to capture crack propagation in a similar way than for Mode-I testing, as shown in Figure 2.10 (b). Edges were also painted and the value of fracture energy, GIIC, was calculated by using the following formula:

$$G_{IIC} = \frac{9P^2 {a_e}^2}{16B^2 h^3 E_1} \qquad (2.6)$$

Being, h the adherent thickness and E_1 the Young modulus of the substrate.

Electrodes were placed similarly to Mode-I testing, as shown in Figure 2.9 (d).

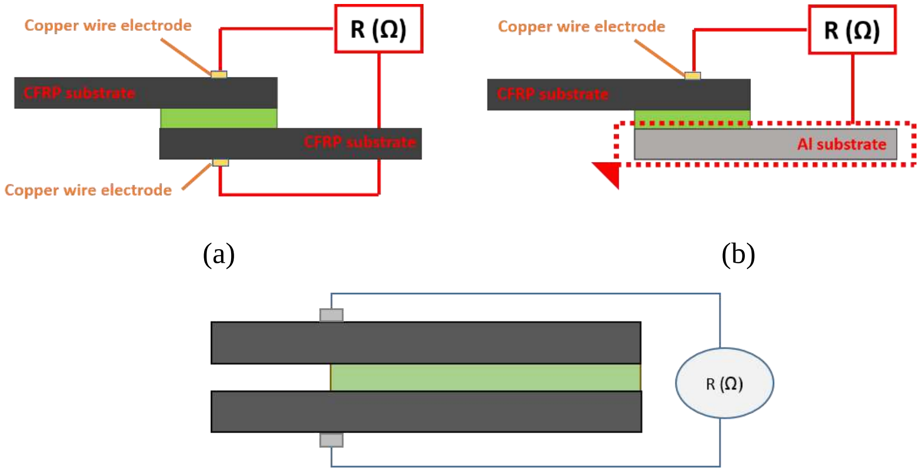

(a) (b)

(c)

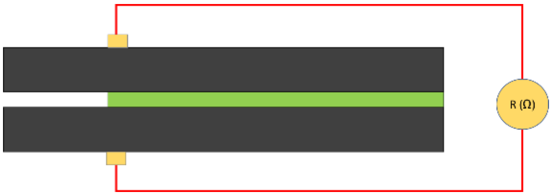

(d)

Figure 2.9: Schematics of electrode disposition in (a), (b) SLS, (c) Mode-I and (d) Mode-II electromechanical tests.

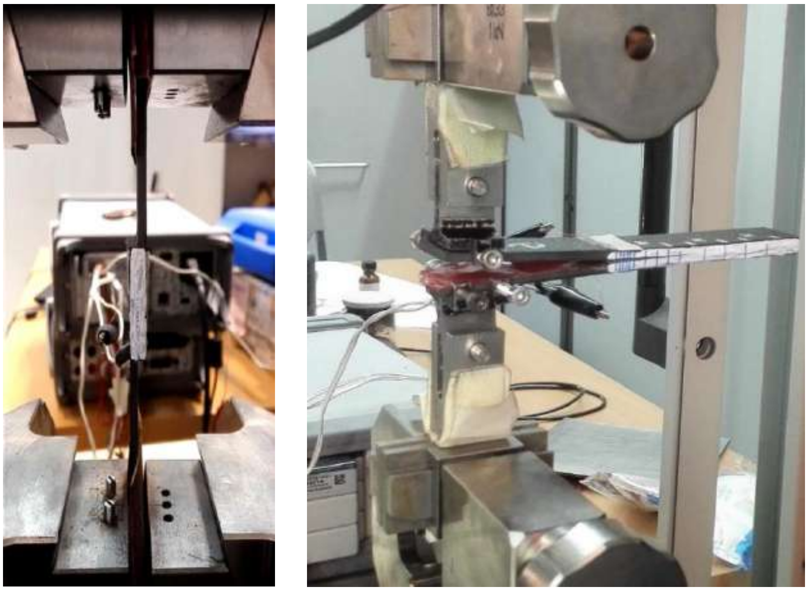

(a) (b)

(c)

Figure 2.10: Images of the actual configuration in (a) SLS, (b) Mode-I and (c) Mode-II electromechanical testing.

2.2.4.2 Fatigue testing in SLS standard coupons

Some fatigue tests were carried out SLS joints to evaluate crack propagation and mechanical properties under more realistic load conditions. Here, the experimental set-up was quite different from the one used in quasi-static conditions.

Tests were done in a MTS 810 test machine under force control with a peak load of 7 kN, a load ratio of R=0.1 and a test frequency of 10 Hz. These parameters were selected to approximately have a fatigue life of around 100000 cycles accordingly to other studies for similar substrates and adhesives [136].

In this case, electrical properties were determined by means of voltage measurements using a NI9234 module from National Instruments at a 5 KHz acquisition frequency. Current was generated by a power supply STAB AR60 with an integrated circuit kept to maintaining the current constant at 1 mA. Insulator tabs were used to properly isolate CFRP substrates from the machine. This different set-up was selected due to the impossibility of properly record electrical changes with Agilent hardware during the fatigue testing because of the low acquisition frequency. Figure 2.11 summarizes the described experimental set-up.

In addition to that, crack propagation was recorded with a portable microscope Dino-Lite AM413ZTA camera in the edges of the joint. It was recorded at several load cycles at maximum load conditions for a better crack observation.

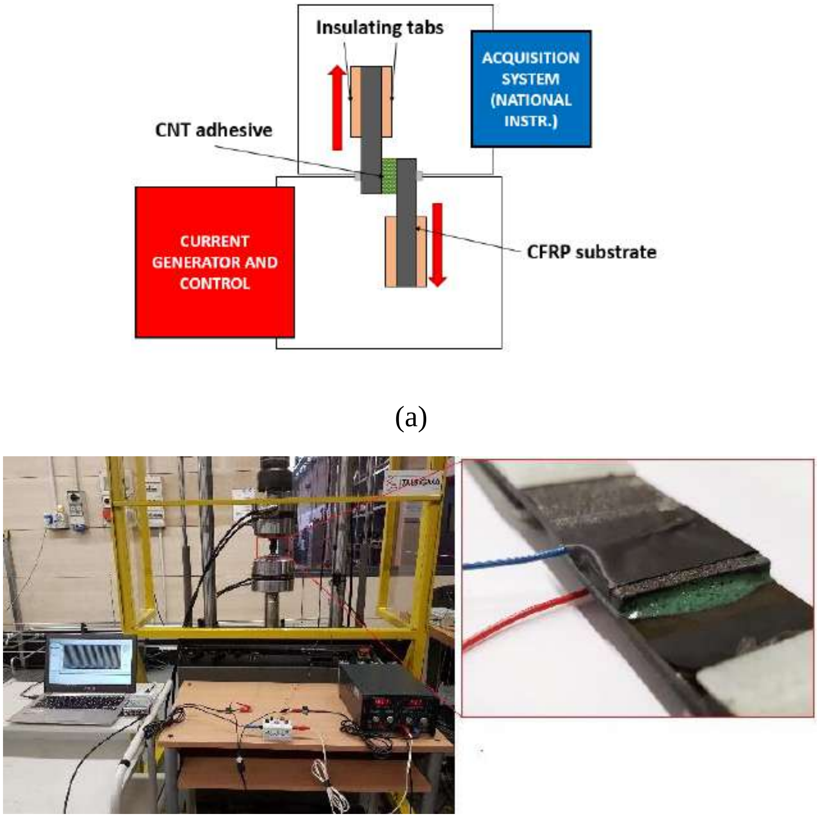

(a)

(b)

Figure 2.11: (a) Schematics of experimental set-up and (b) image of the actual configuration showing the precise location of electrodes.

2.2.4.3 Skin-stringer tests

Apart from standard coupons, some electromechanical tests were carried out in skin-stringer CFRP sub-elements. More specifically, they were subjected to Mode-I and Mode-II testing conditions while their electrical response to crack propagation was measured using an Agilent 34410A hardware at an acquisition frequency of 10 Hz.

In case of Mode-I skin-stringer elements, test rate was varied from 3 to 10 mm/min aiming to deeply analyze the mechanical response depending on peeling conditions. Electrodes were placed onto the skin and stringer surfaces as shown in the schematics of Figure 2.12 (a). Geometry of skin-stringer elements, summarized in Figure 2.12 (b) was set according to the load and geometry carrying capacities of Zwick test machine. A proper insulation layer was placed between the skin and stringer and the test machine to avoid electrical interferences during monitoring test, as shown in Figure 2.13.

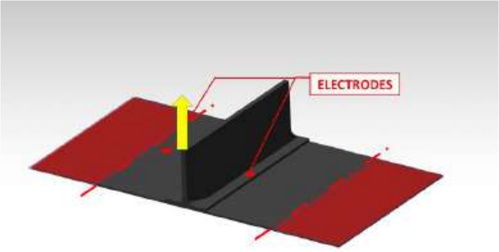

(a)

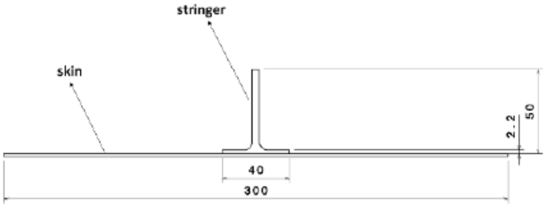

(b)

Figure 2.12: Schematics of (a) electrode disposition and (b) skin-stringer geometry.

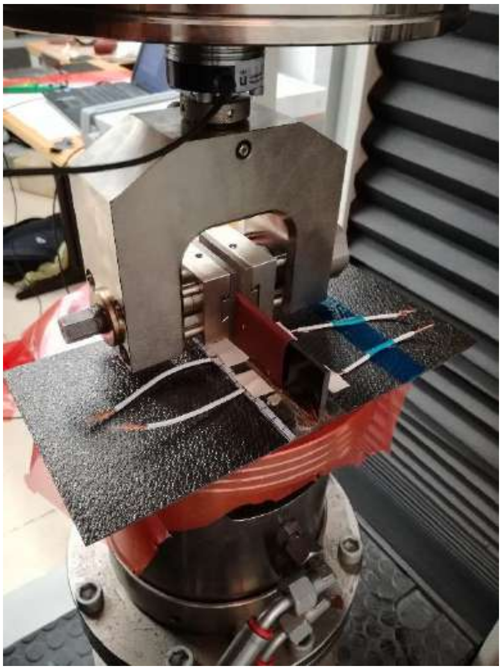

Figure 2.13: Image of the actual configuration for skin-stringer peeling tests.

In addition to that, several monitoring tests were carried out by comparing the proposed technique using CNT doped adhesive films with other available SHM methods such as acoustic-ultrasonic (AU) guided waves and electromechanical impedance in order to get a deeper knowledge about the possible benefits of the proposed adhesive. In this case, electrode disposition was set accordingly to schematics of Figure 2.14 by placing two AU sensors in the skin and other in the stringer to interrogate the skin-skin and skin-stringer response. These tests were carried out during a research stay at Universität Siegen in Germany.

In case of Mode-II sub-elements, test rate was set at 1 mm/min in a similar way than for Mode-II standard coupons. Here, a pre-crack of 15 mm was induced through the stringer edge to force the crack propagation inside the joint and the force was applied in the skin side as shown in the schematics of Figure 2.15.

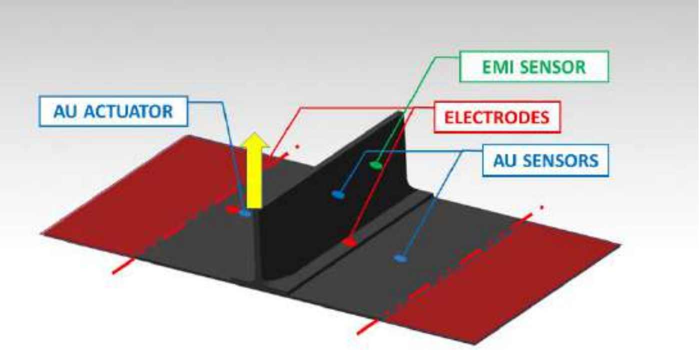

Figure 2.14: Schematics of the applied load (in yellow) and clamping system (shown as the red surface) and the positioning of CNT electrodes, AU and EMI sensors.

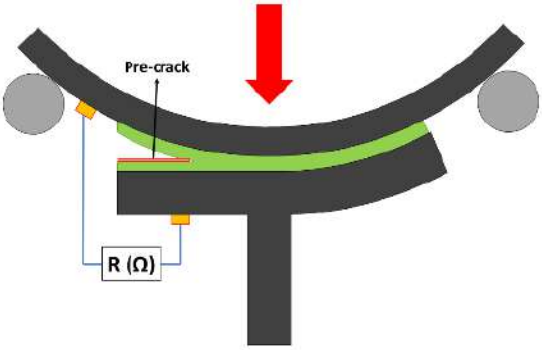

Figure 2.15: Schematics of bending test indicating the precise location of the electrodes.

In both cases, crack length was recorded by using a video camera in a similar way than for standard coupon tests.

2.2.5 Water uptake tests

Ageing behavior of CNT doped adhesive films under SLS testing conditions was studied. For this reason, some water uptake measurements on CNT doped adhesive film in-bulk samples. The amount of SDS was varied from 0 to 1 wt. % to evaluate the amphiphilic effect of the surfactant on ageing properties.

The samples were immersed in distilled water at 60 ºC to simulate aggressive humidity conditions. Prior to immersion, each sample was dried in an oven at 50 ºC for 3 days until weight loss was not observed between one measurement and the next one. Immersion time was varied from 0 to 15 days until water uptake saturation. Water uptake was calculated by comparing the weight before and after being immersed.

Apart from water uptake measurements, SLS joints were tested to evaluate their mechanical performance. Here, the ageing time was increase to 2 months, instead of 15 days due to a lower adhesive surface exposure to water absorption. The samples were mechanically tested at 0, 1 and 2 months ageing time following the ASTM D5868-01 standard at a test rate of 1.23 mm/min.

In addition to that fact, some Differential Scanning Calorimetry (DSC) measurements were carried out in a Metter Toledo mod 821 apparatus for in-bulk samples. Two scans were conducted accordingly to ISO 11357-2:13 at 10 ºC/min from ambient temperature to 250 ºC

The aim was to evaluate the effect of water uptake in the glass transition temperature, Tg, of the CNT adhesive film and then correlate it to their electromechanical performance. Tg was determined as the turning point of the heat capacity change.

2.2.6 Microstructural characterization

2.2.6.1 Characterization of CNT dispersion

CNT aqueous dispersions and in-bulk doped adhesive films were characterized to see the influence of dispersion procedure on CNT distribution. For this reason, a FEG-SEM analysis by using a Nova NanoSEM FEI 230 apparatus from Philips was carried out.

In both aqueous dispersion and in-bulk adhesives, samples were coated by a platinum layer of 5.6 nm thickness.

2.2.6.2 Characterization of fracture surfaces

Fracture surfaces were characterized to properly identify the main failure modes and breakage mechanisms.

In this context, two types of characterizations were carried out. On the one side, a macroscopic characterization of failure modes to identify a cohesive, adhesive or adherent failure. On the other hand, a more detailed characterization of fracture surface was conducted by SEM analysis using a S-3400 N apparatus from Hitachi. Here, fracture surfaces were coated by a thin layer of gold for a better observation in a similar way than for CNT nanocomposites.

In addition to that, fracture surfaces were also characterized by means of profilometry measurements using an optical profilometer ZETA Z-20. Here, the aim was to in detail observe the adhesive distribution to properly understand the electromechanical behavior of the joint.

2.2.6.3 Characterization of transversal sections

A microstructural characterization of transversal sections of adhesive joints was carried out to know the quality of adhesive joint manufacturing by identifying the presence of possible manufacturing defects such as voids, porosity of an irregular adhesive distribution. To achieve this purpose, transversal sections were properly polished and then characterized by SEM analysis. In this case, both tested and non-tested joints were analyzed. In the first case, to properly characterize the quality of manufacturing process and in the second case, to characterize the crack propagation behavior at a microscopic level.

CHAPTER 3-12: JOURNAL PAPER COMPENDIUM

Chapter 3: Novel approach to percolation threshold on electrical conductivity of carbon nanotube reinforced nanocomposites

Xoan F. Sánchez-Romate[a,b,3], *Alberto Jiménez-Suárez*[b], *María Sánchez*[b], *Alfredo Güemes*[a] *and Alejandro Ureña*[b]

Published in RSC Advances 6 (2016); 43418-43428

[a] Department of Aerospace Materials and Processes, Escuela Técnica Superior de Ingenieros Aeronáuticos, Universidad Politécnica de Madrid, Plaza del Cardenal Cisneros 3, 28040 Madrid, Spain

[b] Materials Science and Engineering Area, Escuela Superior de Ciencias Experimentales y Tecnología, Universidad Rey Juan Carlos, Calle Tulipán s/n, 28933 Móstoles (Madrid), Spain

To date, most analytical models used to calculate electrical conductivity in carbon nanotube (CNT) reinforced nanocomposites are not able to predict electrical properties for contents much higher than the percolation threshold. This is because these models do not take into account many critical factors, such as nanotube waviness, dispersion state and process parameters. In the present paper, a novel analytical model based on an equivalent percolation threshold concept, valid for all CNT contents, is developed for this approach. To achieve this, the influence of all these factors has been investigated and several experimental tests have been conducted in order to validate the model. The electrical conductivity varies by several orders of magnitude depending on the value of these parameters, increasing with carbon nanotube content and

---

[3] Corresponding author. Tel: +34 91 488 82 52. E-mail: xoan.fernandez.sanchezromate@urjc.es

aspect ratio and decreasing with its waviness. From experimental data, it is found that the waviness increases with carbon nanotube content. Besides, functionalization also causes a local distortion of CNTs, producing more entanglement. When comparing two different dispersion procedures, calendering and toroidal milling, it is noticed that the first method has a greater stretching effect because the shear forces induced are much higher, causing the breakage of carbon nanotubes.

3.1 Introduction

Since S. Iijima [1] discovered the first helical microtubules of graphitic carbon, the use of carbon nanotubes has increased due to their exceptional properties [2-6]. In fact, the addition of CNTs into an insulator resin enhances its electrical performance, providing conducting pathways, making it electrically conductive [7-9]. This has attracted the interest of many researchers, as their use in some applications like a lightning strike, or structural health monitoring due to self-sensing properties, can be made possible [10-13].

The determination of a percolation threshold, that is, the critical volume fraction at which a sharp increase in the electrical conductivity is observed when CNTs (or conductive fillers in general) form a network or an interconnected structure (conducting pathways), has attracted the interest of many researchers [14-20] as it is a key point for characterization of the electrical behavior of nanocomposites. It has been found that it depends essentially on the filler geometry [16] but also there are any other factors influencing this value, such as the orientation [17,18], waviness or distribution of carbon nanotubes [19,20].

To date, there is a lot of research focused on modelling the percolation threshold taking into account many of the parameters previously described [21-24] Calculation of the percolation onset is essential in order to predict the electrical conductivity of the material, since many analytical models are based on a scaling rule which refers to the percolation threshold [25,26]

However, it has been demonstrated that this model is not able to predict conductivities properly when the content is much higher than the percolation threshold, as it does not take into account most of the parameters influencing the electrical behavior of the nanocomposite [27,28] For this reason, there is a lot of research focused on developing numerical models including all of these parameters [29-31] but they are often very complicated, not time-effective and do not permit a general overview about the dispersion state of the material.

For all of these reasons, the aim of this study is to develop an analytical model for calculating electrical conductivity as simply as possible, but being able to include the effect of most of the parameters previously mentioned. This model would allow us to know the dispersion state which is essential not only for electrical applications, but also for mechanical ones. To achieve this purpose, a combined model between that proposed by J. Li et al. [21], which is able to estimate a percolation threshold according to the volume of agglomerates, and the classical scaling rule that allows the determination of electrical conductivity based on the percolation onset, will be used.

To validate the analytical model, several experimental measurements carried out on CNT–epoxy nanocomposites manufactured using different dispersion techniques and nanotube types have been conducted. The objective is to associate the electrical properties measured experimentally with those predicted by the analytical model depending on the dispersion state, waviness and filler geometry.

On the other hand, the correlation between experimental measurements and the analytical model will allow the estimation of the influence of each dispersion parameter on the electrical performance of the material, making it possible to optimize the dispersion processes.

3.2 Experimental procedure

3.2.1 Materials

Nanocomposites were manufactured with different multiwall carbon nanotubes (MWCNT) embedded in an epoxy resin. The epoxy resin was a low viscosity DGBEA resin recommended for Resin Transfer Moulding (RTM), with a commercial formula called HexFlow RTM 6 supplied by Hexcel. This is a single-component system developed for service temperatures from -60 ºC to 180 ºC. Three types of MWCNTs (NC3100, NC3150, NC3152) supplied by Nanocyl were used, all with a purity of 95% and an average diameter of 9.5 nm. NC3100 and NC3150 are non-functionalized and have lengths up to 1.5 mm and 1 mm, respectively. The last one, NC3152, functionalized with amine groups, also has a length up to 1 mm.

3.2.2 Manufacturing

The manufacturing of nanocomposites was carried out in three different stages: (1) addition of the nanoreinforcement into the epoxy matrix and mechanical dispersion, (2) degasification of the mixture and (3) curing.

First of all, a masterbatch at the maximum content which allows a toroidal flow (that is, 1 wt. % for NC3100, 0.8 wt. % for NC3150 and 4 wt. % for NC3152) was manufactured by toroidal stirring for 15 min using a Dispermat® dissolver at 6000 rpm with a rotating disc of 50 mm diameter. Then, the mixture was diluted with more epoxy resin in order to achieve the desired concentration. This new mixture was stirred mechanically and then dispersed into a EXAKT 80E three roll mill machine from EXAKT Technologies Inc. The calendering dispersion was optimized in previous studies [32,33] and consisted of a progressive reduction of the gaps between rolls (the minimum distance being 5 mm) at a constant rotating speed of 250 rpm for the first roll.

After the dispersion process, it was necessary to use a degasification step to evacuate the air entrapped in the epoxy mixture. Before that, the mixture was heated up to 80 ºC in order to facilitate this process. Then, degasification was done under vacuum for 15 minutes. For the manufacturing of nanocomposites, the doped resins were cured with an isothermal cycle at 180 ºC for 120 min.

3.2.3 Characterization of nanocomposites

A microstructural study of the cured nanocomposites has been carried out in order to determine the influence of the different stages of dispersion. To analyze the microstructure, materials were fractured at cryogenic conditions. First, a pre-crack was caused with the material being immersed in N2 for 3 minutes. Then, the sample was fractured and coated with a thin layer of platinum (5–6 nm). This microstructural study was carried out by TEM, using a Philips Tecnai 20–200 kV apparatus, and FEGSEM, using a Nova NanoSEM FEI 230 apparatus from Philips.

DC volume conductivity was evaluated according to ASTM D257 using a Source Measurement Unit (SUM) of Keithley Instrument Inc. (mod. 2410) connected through an interface GPIB to a PC. The electrical resistance was determined by the slope of the current–voltage curve, from which the electrical conductivity can be obtained, taking into account the specimen geometry. Three specimens (10 × 10 × 1 mm) were measured for each sample. Silver paint was used to ensure good contact with a 10 × 1 mm section of the electrodes. The applied voltage was within the range of 0–20 V and 0–250 V for nanocomposites with a high or low level of conductivity, respectively.

3.3 Theoretical analysis

3.3.1 Calculation of electrical conductivity based on an interparticle distance (IPD) and classic scaling rule

Electrical conductivity is calculated by using the classical model based on the scaling rule:

$$\sigma = \sigma_0(\phi - \phi_c)^t \tag{3.1}$$

in which ϕ is the content of the carbon nanotubes, ϕ_c is the percolation threshold, *t* is a critical exponent determined experimentally, fixed at a value of around 1.6–2 for 3D systems [27,31,34] (1.7 in this study), and σ_0 is a parameter which depends on the intrinsic conductivity of CNTs (σ_{CNT}) and the aspect ratio (Λ) [35]:

$$\sigma_0 = \sigma_{CNT} \times 10^{0.85\{\log(\Lambda)-1\}} \tag{3.2}$$

To date, most of the research focused on the analysis of the electrical conductivity of nanocomposites defines the percolation threshold as an invariable parameter. However, theoretical results obtained using these models do not fit the experimental ones very accurately because they do not consider most of the parameters that could affect the formation of an electric percolation network in the material. The aim of this study is to create a novel method for modelling electrical conductivity which allows the evaluation of the most relevant characteristics of the material, such as the dispersion state or filler geometry.

As some researchers have shown [21], the percolation threshold depends on the dispersion state and the aspect ratio:

$$\phi_c = \frac{\xi \varepsilon \pi}{6} + \frac{(1-\xi)\pi d^2 l}{4[L^{eq}]^3} \tag{3.3}$$

in which $L^{eq} = lcos\beta$ is the length of the equivalent element (β being the angle between the carbon nanotube and the preferential direction, and l being the length of the carbon nanotube), d is the diameter of the CNT, ε is the localized volume content of carbon nanotubes in an agglomerate and ξ is the volume fraction of agglomerated CNTs in the nanocomposite, defined by these expressions:

$$\varepsilon = \frac{NV_{CNT}}{\frac{\pi D^3}{6}} \qquad \xi = \frac{\sum_{i=1}^{\frac{V_{total}}{L^3}} N_i V_{CNT}}{V_{filler}} \tag{3.4}$$

with V_{CNT} being the volume of an individual nanotube, *N* being the number of CNTs presented in an agglomerate and *D* being the diameter of the equivalent element.

It is noticed that the dispersion state of the nanofiller is not constant, as it depends on the filler content, so a new parameter, named the equivalent percolation threshold, ϕ_c^*, must be defined. This new percolation onset will take into account the dispersion state, so it will be different depending on the nanotube content. By computing these parameters, the classical model is redefined by this method:

$$\sigma = \sigma_0(\phi - \phi_c^*)^t \tag{3.5}$$

Thus, it is necessary to know the value of ϕ_c^* as a function of nanotube content. In order to achieve that, a correlation between the dispersion state, average orientation and nanofiller content must be defined.

A correlation between average orientation and dispersion state can be easily found. Some research shows that the more agglomerated the dispersion state, the more random the orientation is [36]. Then, it can be supposed that in the absence of agglomerates, all the nanotubes are aligned in the flow direction (that is, with a random orientation in the x–y plane, with x being the direction of preferential orientation). On the other hand, when nanotubes are agglomerated, there is no preferential orientation, that is, they are randomly distributed. Therefore, the length of the equivalent cubic element L_{eq} would be defined as:

$$L_{eq} = (1-\xi)L_{dis} + \xi L_{agl} = (1-\xi)lcos(\beta_{dis}) + \xi lcos(\beta_{agl}) \tag{3.6}$$

with $cos(\beta_{agl}) = \frac{1}{\sqrt{3}}$ and $cos(\beta_{dis}) = \frac{1}{\sqrt{2}}$ being the average projection of agglomerated and dispersed CNTs with the x axis, respectively, supposing that all nanotubes are distributed in a random way. Therefore, combining eqn (3.3) and (3.6), the expression for the percolation threshold can be rewritten as follows:

$$\phi_c = \frac{\xi\varepsilon\pi}{6} + \frac{(1-\xi)\pi}{4\left(\frac{1}{\sqrt{2}} - \frac{\sqrt{3}-\sqrt{2}}{\sqrt{6}}\xi\right)^3} \cdot \frac{1}{\Lambda^2} \tag{3.7}$$

In order to make the calculations easier, it is going to be supposed $\varepsilon = \xi$. Once the dispersion parameters are defined, the statistical percolation threshold, that is, the lowest value of percolation obtained when all the nanotubes are well dispersed in the absence of agglomerates, (ϕ_{c0}), can be calculated:

$$\phi_{c0} = \frac{\xi_{c0}\varepsilon_{c0}\pi}{6} + \frac{(1-\xi_{c0})\pi}{4\left(\frac{1}{\sqrt{2}} - \frac{\sqrt{3}-\sqrt{2}}{\sqrt{6}}\xi_{c0}\right)^3} \cdot \frac{1}{\Lambda^2} \tag{3.8}$$

in which ξ_{c0} and ε_{c0} are the dispersion parameters at the statistical percolation threshold. In the absence of agglomerates, $\xi_{c0} = 0$, so eqn (3.8) can be rewritten as follows:

$$\phi_{c0} = \frac{\pi}{\sqrt{2}} \cdot \frac{1}{\Lambda^2} \tag{3.9}$$

Knowing ϕ_{c0}, it is possible to estimate the average number of particles in an equivalent cubic element at ϕ_c (N_c^{eq}):

$$N_c^{eq} = (1-\xi_c) + \xi_c N_{agl} = (1-\xi_c) + \xi_c \frac{\varepsilon_c}{\phi_{c0}} = (1-\xi_c) + \frac{{\xi_c}^2}{\phi_{c0}} \tag{3.10}$$

with N_{agl} being the number of nanoparticles in an agglomerate, which is $N_{agl} = \frac{\varepsilon_{c0}}{\phi_{c0}}$. For a content different from the percolation threshold, eqn (3.10) can be rewritten as follows:

$$N^{eq} = nN_{c0}^{eq} = (1 - \xi^*) + \frac{\xi^{*2}}{\phi_{c0}} \tag{3.11}$$

in which N^{eq} is the total number (volume fraction) of nanoparticles for a given content in an equivalent element and ξ^* is the dispersion parameter at this content. *n* is calculated using this formula:

$$n = \frac{\phi}{\phi_{c0}} \tag{3.12}$$

where all the contents are expressed as a volume fraction of the total nanocomposite:

$$\phi = \frac{w^N/\rho^N}{w^N/\rho^N + (1 - w^N)/\rho^M} \tag{3.13}$$

with ρ^N and ρ^M being the densities of carbon nanotube and matrix, respectively, and w^N being the weight fraction of CNTs. The density of carbon nanotubes is estimated by using the expressions given by Ch. Laurent et al. [37] depending on the average diameter and number of walls, which were measured by TEM (Figure 3.1), and is similar for the three types of CNTs tested. From these expressions, it is possible to calculate the value of the equivalent percolation threshold, given any content:

$$\phi_c^* = \frac{\xi^{*2}\pi}{6} + \frac{(1 - \xi^*)\pi}{4\left(\frac{1}{\sqrt{2}} - \frac{\sqrt{3} - \sqrt{2}}{\sqrt{6}}\xi^*\right)^3} \cdot \frac{1}{\Lambda^2} \tag{3.14}$$

At the statistical percolation threshold (ϕ_{c0}), the carbon nanotubes are going to be considered straight in order to make the calculations easier. However, at other contents, the carbon nanotubes may not be actually straight, with waviness being a key factor in the filler geometry and also in the elastic properties [38,39]. Considering each wavy carbon nanotube englobed within a perfect cylinder of an aspect ratio Λ_{cyl}, it is found that:

$$\frac{L_{eff}}{2a + d} = \Lambda_{cyl} \tag{3.15}$$

in which $L_{eff} = 4\sqrt{\left(\frac{L}{4}\right)^2 - a^2}$ is the effective length of the wavy nanotube and a is the amplitude of waviness, as can be seen in Figure 3.2 (a). Rewriting eqn (3.15), it is possible to obtain the value of the wave amplitude as follows:

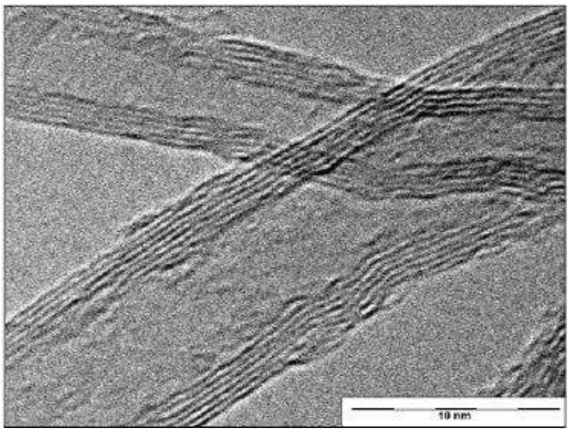

Figure 3.1: TEM image of the nanotubes.

$$a = \frac{-4d + \sqrt{16d^2{\Lambda_{cyl}}^2 - 4(4{\Lambda_{cyl}}^2 + 16)(d^2{\Lambda_{cyl}}^2 - L^2)}}{2(4{\Lambda_{cyl}}^2 + 16)} \tag{3.16}$$

Therefore, defining the waviness ratio $\lambda = a/L_{eff}$ and combining this with eqn (3.16), it is possible to calculate the waviness of CNTs:

$$\lambda = \frac{a}{L_{eff}} = \frac{a}{4\sqrt{\left(\frac{L}{4}\right)^2 - a^2}} \tag{3.17}$$

To calculate the percolation threshold and electrical conductivity, an equivalent carbon nanotube will be defined (Figure 3.2 (b)) with the same volume and a length equal to L_{eff}, so the effective diameter d_{eff} and aspect ratio Λ_{eff} will be:

$$d_{eff} = \sqrt{\frac{L}{L_{eff}}d^2} \quad \Lambda_{eff} = \frac{L_{eff}}{d_{eff}} \tag{3.18}$$

Therefore, eqn (3.2), (3.5) and (3.14) will be rewritten as follows, in which $\Lambda = \Lambda_{eff}$:

$$\sigma = \sigma_0(\phi - {\phi_c}^*)^t \qquad \sigma_0 = \sigma_{CNT} \times 10^{0.85\{\log(\Lambda_{eff}) - 1\}} \tag{3.19}$$

$$\phi_c^* = \frac{\xi^{*2}\pi}{6} + \frac{(1-\xi^*)\pi}{4\left(\frac{1}{\sqrt{2}} - \frac{\sqrt{3}-\sqrt{2}}{\sqrt{6}}\xi^*\right)^3} \cdot \frac{1}{{\Lambda_{eff}}^2}$$

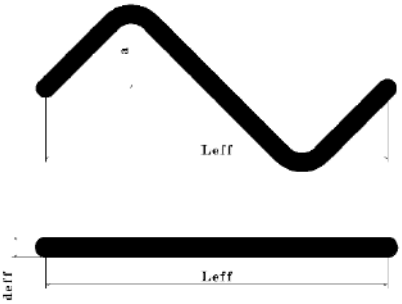

Figure 3.2: Geometry of the (a) wavy and (b) equivalent carbon nanotube.

In order to validate the theoretical calculations, this study is also going to be focused on estimating the influence of two different dispersion methods, toroidal stirring and calendering, on the dispersion and geometry parameters defined previously. The aim is to set up a correlation between the electrical conductivity and dispersion state.

The two dispersion methods are based on shear forces in order to disaggregate the agglomerates. However, sometimes these shear forces can lead to the breaking of carbon nanotubes depending on their characteristics [40], reducing their aspect ratio. Shear forces are estimated as a result of the bending stress induced by the fluid over the carbon nanotubes; leading to this formula in the case of straight CNTs:

$$\frac{\eta\dot{\gamma}}{E} \approx 100\frac{\ln(2\Lambda^*) - 1.75}{2\Lambda^{*4}} \tag{3.20}$$

in which η is the resin viscosity, $\dot{\gamma} = v/h$ is the shear rate (v being the linear velocity and h the gap), E is the Young's Modulus of the CNT and Λ^* is the resulting aspect ratio. This new effective aspect ratio Λ^* will be used as the nominal aspect ratio of carbon nanotubes, in order to calculate their waviness ratio.

Therefore, using all of these expressions, it is possible to know the dispersion state given by the dispersion parameters (correlated to the content ϕ), the actual aspect ratio Λ^* and waviness factor λ for the two dispersion methods described above. Reciprocally, it will be possible to calculate the electrical conductivity accurately by knowing an estimation of these parameters.

3.3.2 Parametric study

Parametric studies have been conducted in order to evaluate the effect of the different parameters defined previously on the electrical conductivity of nanocomposites. In that particular case, this study has been focused on the influence of the aspect ratio, given by the geometry of carbon nanotubes and the shear rate of the dispersion process, waviness and content. To achieve this purpose, both the aspect ratio and content have been graphically represented versus waviness.

Figure 3.3 describes the influence of waviness and content on the electrical conductivity at three different aspect ratios (50, 200 and 500). It is observed that conductivity decreases with waviness while it increases with content, which is obvious. For CNTs with an aspect ratio of 50, the nanocomposite is not electrically conductive for waviness values higher than 0.4 and contents lower than 0.2 wt. %. In the case of CNTs with an aspect ratio of 200, the nanocomposite is not electrically conductive for waviness values higher than 0.8 and contents lower than 0.3 wt. % and finally, in the last particular case (aspect ratio of 500), the nanocomposite is electrically conductive for all waviness and contents values given.

In addition, it is possible to know the equivalent percolation threshold as a function of waviness and filler content, given by the points at which the nanocomposite becomes electrically conductive. Figure 3.4 shows the correlation between ϕ_c^* and thementioned parameters for three aspect ratio values. It is noticed that the equivalent percolation onset increases with waviness due to the negative effect that it has on the electrical conductivity. On the other hand, the aspect ratio has a positive effect on ϕ_c^* . It is also observed that ϕ_c^* is very sensitive to CNT waviness, especially for lower values of aspect ratio.

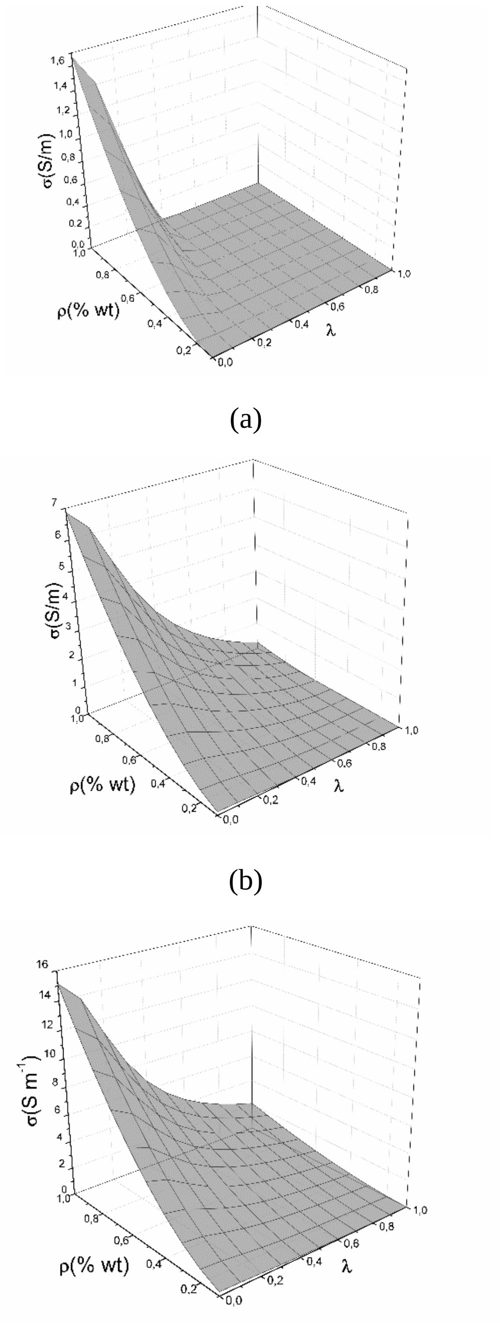

(a)

(b)

(b)

Figure 3.3: Effect of the content and waviness on electrical conductivity for aspect ratios of (a) 50, (b) 200 and (c) 500.

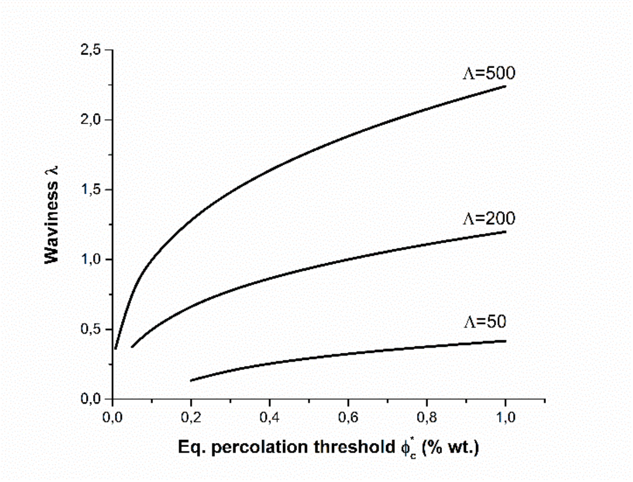

Figure 3.4: Effect of the nanotube waviness on filler content at percolation threshold for three different values of aspect ratio.

On the other hand, Figure 3.5 describes the influence of the aspect ratio and waviness on electrical conductivity at three different contents (0.1, 0.3 and 1 wt. %). It is observed that the correlation between waviness and aspect ratio is similar to that between waviness and content, as could be expected. It is particularly interesting to observe the importance of waviness in electrical conductivity, as a slight variation in this parameter has a similar effect to an appreciable reduction in aspect ratio. This could be expected because the effective aspect ratio used to calculate the electrical conductivity depends on the waviness factor. This sensitivity is larger for lower contents as the difference between the content and percolation threshold is very small, so the electrical conductivity is very sensitive to small variations in aspect ratio.

By observing these graphs it is possible to obtain a complete mapping of electrical conductivity as a function of the main characteristics of carbon nanotube dispersion; that is, content, waviness and aspect ratio. This also makes it possible to develop an efficient dispersion method in order to achieve higher values of electrical conductivity.

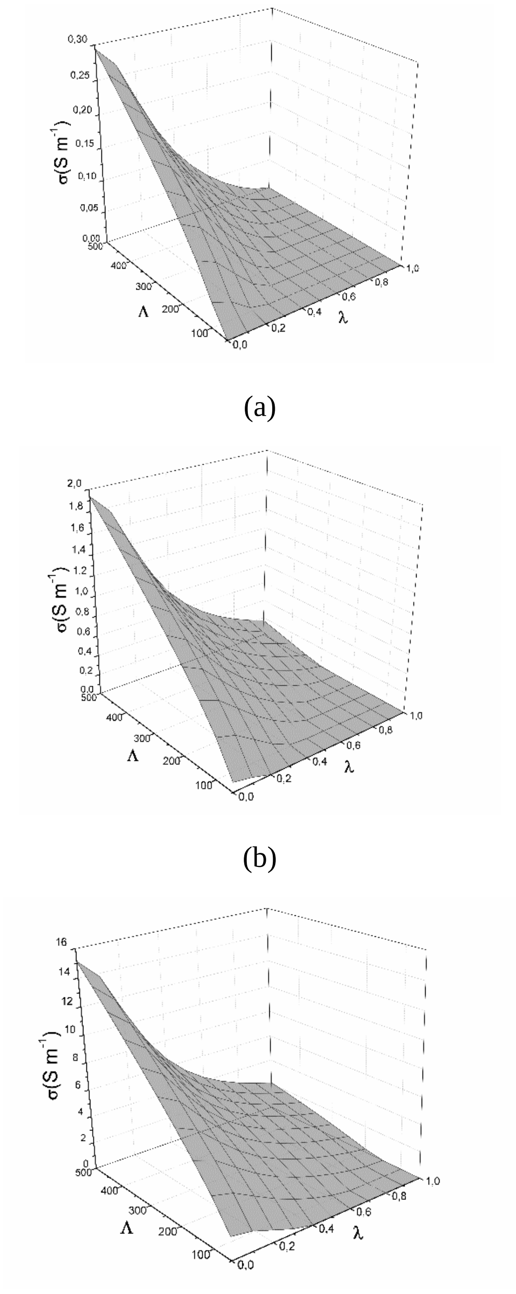

(a)

(b)

(c)

Figure 3.5: Effect of the aspect ratio and waviness on electrical conductivity for contents of (a) 0.1 % (b) 0.3 % and (c) 1 %.

3.4 Experimental analysis

As has been described previously, two dispersion methods have been conducted in order to validate the analytical model: toroidal stirring and a combination of toroidal stirring plus three roll mill calendering. The experimental results for electrical conductivity are given in Figure 3.6. Using this experimental data it is possible to calculate the value of dispersion parameters and waviness with the analytical model developed. In order to achieve this, it has been supposed that at statistical percolation, fixed at ϕ_{c0}, the waviness ratio λ is 0 (all the nanotubes are straight). The Young's modulus is estimated as 1 TPa for non-functionalized nanotubes and 0.9 TPa for functionalized ones, due to the effect of covalent bonds [6,41,42]. With these values of Young's Modulus and the shear rate, which was calculated from the processing conditions (2250 rpm of the fastest roll and a h value of 5 µm) as approximately 3×10^{6} s^{-1} in the case of the three roll mill process, and using eqn (3.20), the shear forces in calendering lead to a nominal aspect ratio $\Lambda^{*}$of 67.5 for NC3100 and NC3150 and 63.5 for NC3152. Therefore, this indicates that there is a breakage of carbon nanotubes, as it has been stated in previous studies [40,43]

Figure 3.6 also shows the calculated electrical conductivity as a function of CNT content and waviness for the actual aspect ratio after the three roll mill process, that is, 67.5 for NC3100 and NC3150 (Figure 3.6 (c)) and 63.5 for NC3152 (Figure 3.6 (d)), similar to the images in Figure 3.5. It is observed that the electrical conductivity from experimental results is much lower than the maximum that can be achieved when the nanotubes are totally straight. So, this indicates that the CNTs are curved.

By applying the model it can be concluded that CNT waviness increases with carbon nanotube content. This could be explained by nanotubes tending to be more entangled when they are part of an agglomerate, due to the greater interactions between carbon nanotubes, causing a reduction in their effective aspect ratio [44]. On the other hand, when they are well dispersed, they tend to be aligned in the flow direction. Figure 3.7 (a) shows the dependence between waviness and the content of carbon nanotubes.

This greater entanglement with content can be appreciated in the TEM images of Figure 3.8 (a)–(c) for 0.2, 0.3 and 0.5 wt. % CNT contents. However, a quantitative study of waviness ratio has been conducted for comparison to the theoretical values calculated. Figure 3.8 (d) shows that experimental values obtained by image analysis are in good agreement with those predicted by the analytical model. On the other hand, a higher entanglement and waviness ratio is observed when the CNTs are part of an agglomerate, which increases with CNT content, as is shown in these images.

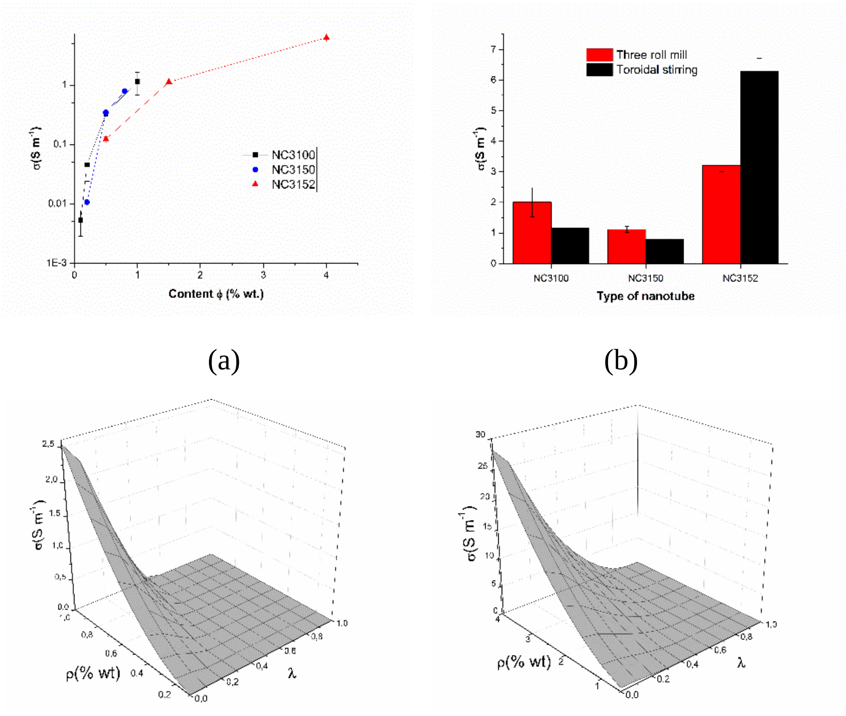

(a)

(b)

(c)

(d)

Figure 3.6: Experimental values of electrical conductivity (a) as a function of nanofiller content after calendering process and (b) at maximum content for both toroidal and three roll mill processes, and comparison to theoretical values as a function of content and waviness for aspect ratios of (c) 67.5 (NC3100 and NC3150) and (d) 63.5 (NC3152).

Nevertheless, it is important to highlight again the difficulty in obtaining an accurate value of waviness ratio from image analysis, and the values obtained only allow validation of the tendency predicted by the analytical model.

Going back to the theoretical calculations in Figure 3.7 (a), in the particular case of NC3100, it is noticed that at 0.1% content, the waviness ratio is nearly 0 and it suddenly increases when the content is 0.2%. This could happen because the theoretical model is very sensitive to small variations in contents near the percolation threshold, and a slight variation in carbon nanotube content may result in a noticeable variation of electrical conductivity and therefore a remarkable variation of waviness ratio. It is important to notice the consequence that process parameters have on the final electrical properties of the material.

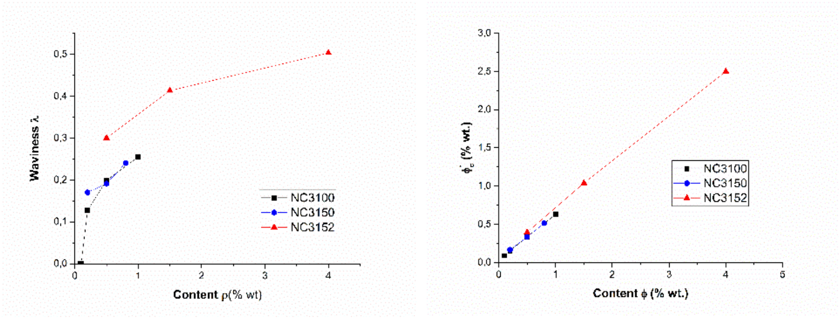

(a) (b)

Figure 3.7: Correlation between content and (a) waviness and (b) ϕ_c^* for CNTs after three roll mill process.

In addition, it is observed that NC3152 is more entangled than NC3150 and NC3100, which show similar values. This is probably due to the effect of amino-functionalization, which is not very favorable for achieving good dispersion. Moreover, the presence of amino groups induces local distortions along the radial direction of carbon nanotube sidewalls [42,45] which could also explain the increase in the waviness ratio in this case.

On the other hand, Figure 3.7 (b) shows the correlation between the equivalent percolation threshold and the content of carbon nanotubes for the three types of CNTs. It is noticed that ϕ_c^* increases approximately proportionally to the CNT content. In addition, it is observed that values of ϕ_c^* are similar for the three cases, being slightly higher for NC3152 because they are more entangled than NC3100 and NC3150.

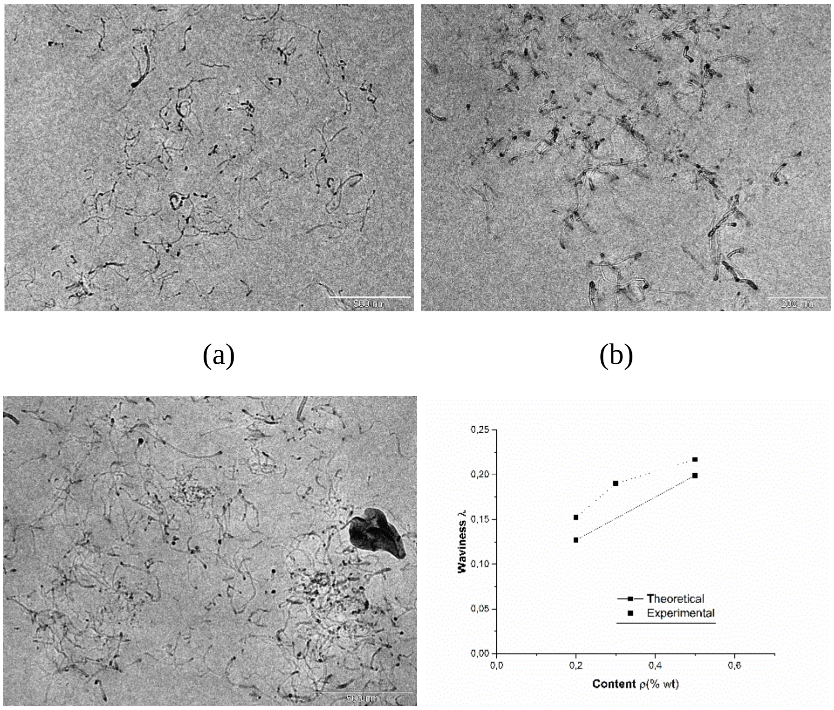

(a) (b)

(c) (d)

Figure 3.8: TEM images of carbon nanotubes at (a) 0.2 (b) 0.3 and (c) 0.5 wt. % and (d) comparison between experimental results from image analysis and theoretical predictions.

For toroidal stirring, the process parameters (6000 rpm and a *h* value of 7.5 mm) lead to a shear rate of approximately 3000 s^{-1}. Therefore, shear forces induced by toroidal stirring are much lower than for the calendering process and using eqn (3.20), it is noticed that there is no carbon nanotube breakage in these particular cases.

Figure 3.9 shows that the values of waviness ratio for toroidal stirring are much higher than for the calendering process. This could be explained because the three roll mill tends to stretch the carbon nanotubes due to the higher shear forces induced. In addition, it is observed that the reduction in waviness due to calendering process is higher in the case of NC3100 than NC3150, because the stretching effect induced by the three roll mill is more prevalent for longer nanotubes. On the other hand, the reduction in waviness for NC3152 is the highest, which is probably due to a larger stretching effect by the three roll mill on the covalent bonds.

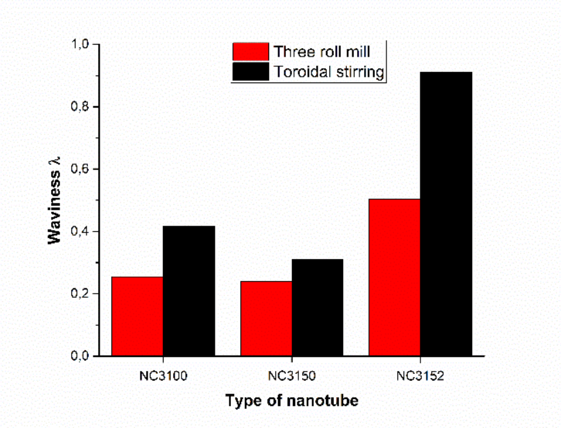

Figure 3.9: Values of waviness ratio for toroidal stirring and toroidal stirring + three roll mill calendaring processes.

In order to analyze the effect of the dispersion process on agglomeration, it is necessary to focus not only on the dispersion parameters, but also on the average number of particles per unit volume. That is because dispersion parameters only allow a general overview of dispersion quality. Due to the varying effective aspect ratio for different contents, the average number of particles per cubic element, *N*, supposing that $\varepsilon = 1$, will also change. The following expression allows us to calculate *N*:

$$N = \frac{1}{\phi_{c0}} \left(\frac{L_{eq}}{L^*_{eff}} \right)^3 \tag{3.21}$$

in which L_{eq} is the length of the equivalent cubic element for straight carbon nanotubes, and L^*_{eff} is the effective length for wavy CNTs.

As can be observed in the FEG-SEM images of Figure 3.10, the average size of larger agglomerates is drastically reduced after the three roll mill method compared to toroidal stirring (Figure 3.10 (a)–(c)), as can be expected due to calendering improving the dispersion quality (Figure 3.10 (d)–(f)). The calculated average number of particles per cubic element (which can be considered as the average size of agglomerates) listed in Table 3.1 shows that the experimental qualitative results (Figure 3.10) and the theoretical predictions are in good agreement, with a drastic reduction of larger agglomerates after the calendering process. Therefore, this model allows us to have a quantitative knowledge of the dispersion state.

Table 3.1: Average size of agglomerates for the two dispersion procedures at maximum carbon nanotube contents.

Type of nanotube	N_T	N_{T+C}
NC3100	31950	3610
NC3150	10275	3400
NC3152	37240	6335

From the theoretical results, it is possible to determine that this reduction in agglomerate size after the calendering process is probably more drastic in the case of long CNTs, because of their greater degree of entanglement by toroidal stirring.

From these results, a very appreciable reduction on the aspect ratio of carbon nanotubes after the three roll mill process is noticed, especially for NC3100. This is probably due to the separation effect induced by the three roll mill, which is more pronounced for the CNTs with a larger aspect ratio. On the other hand, there is a huge reduction in agglomerate size, especially for longer nanotubes. The waviness is also reduced due to the stretching effect induced by the three roll mill. This reduction is more prevalent in the case of NC3152 due to the effect that shear forces have on the covalent bonds.

Therefore, this model is able to predict some average dispersion and waviness parameters which could also be correlated to mechanical properties, giving a more detailed mapping of the nanocomposite, especially for contents much higher than the percolation threshold, in which the classic model is not able to predict electrical conductivity properly. By applying this model, it is noticed that calendering has a stretching effect on the nanotubes, causing the disaggregation of larger agglomerates. On the other hand, toroidal stirring induces lower shear forces but the resulted carbon nanotube are wavier, reducing the potential of this process for achieving the best electrical properties.

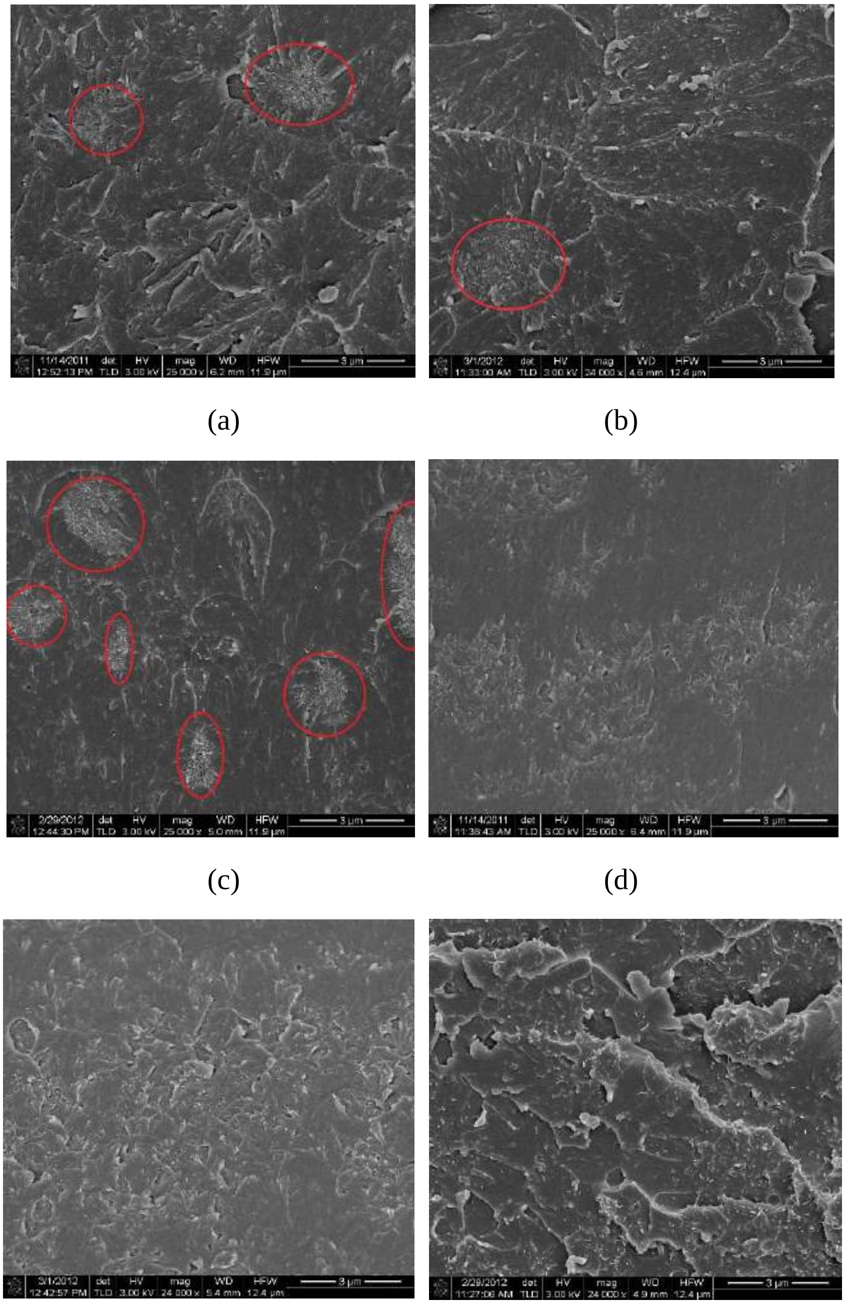

(a) (b)

(c) (d)

(e) (f)

Figure 3.10: Images of the dispersion obtained by toroidal stirring for (a) NC3100, (b) NC3150, and (c) NC3152 and by toroidal stirring + three roll

calendering for (d) NC3100, (e) NC3150, and (f) NC3152. The highlighted areas indicate the presence of larger agglomerates.

3.5 Conclusions

A novel analytical model has been developed in order to calculate the electrical conductivity in CNT reinforced nanocomposites. For this purpose, a redefinition of the classical scaling rule has been made by using an equivalent percolation threshold concept based on the dispersion state of the nanofiller.

Three parameters have been identified as the most influential on the electrical properties: content, waviness and aspect ratio, so their influence on the electrical conductivity has been studied. It has been observed that electrical conductivity increases with the aspect ratio and content and decreases with waviness. Knowing the relationship between these three parameters has made it possible to estimate the equivalent percolation threshold more accurately than using other methods previously developed.

This analytical model has been validated by experimental measurements. It has been observed that the waviness ratio increases with nanofiller content, as would be expected. In addition, the dispersion parameters increase with content, which implies a higher equivalent percolation threshold with content, which is also expected due to more entanglement.

On the other hand, the influence of dispersion procedures has also been investigated. The main effects of the three roll mill process have been identified as the stretching of CNTs due to shear forces induced by the three roll mill and a breakage of carbon nanotubes, leading to a drastic reduction of the maximum agglomerate size in comparison to toroidal stirring, which is not able to stretch the carbon nanotubes, causing more entanglement. In contrast, the shear forces induced by this method are much lower than in the calendering process.

Filler geometry and functionalization also have a strong influence on the electrical properties. By using three types of carbon nanotubes, it can be concluded that functionalization causes more entanglement with an increase in the waviness ratio, due to the effect of amino groups. In addition, it has been noticed that the stretching effect of the three roll mill method is more prevalent in the case of longer CNTs. On the other hand, after the calendering process, the waviness ratio is similar for longer and shorter nanotubes. Therefore, from the experimental results, it can be concluded that waviness has a role in governing the electrical conductivity, since the effective aspect ratio depends on it. This effect is particularly pronounced in contents near the percolation threshold because the redefined ϕ_c^* depends, essentially, on waviness.

In conclusion, this novel analytical model is able to correlate three critical factors, namely the waviness, aspect ratio and content of carbon nanotubes, to the electrical conductivity of nanocomposites. This allows the estimation of the electrical properties for contents much higher than the percolation threshold more accurately than the classical model and, in addition, it makes it possible to know the dispersion state of nanofillers more accurately.

Acknowledgements

This work was supported by the Ministerio de Economía y Competitividad of Spanish Government [Project MAT2013-46695-C3-1-R] and Comunidad de Madrid Government [Project P2013/MIT-2862].

3.6 References

[1] Iijima S. Helical Microtubules of Graphitic Carbon. Nature 1991;354(6348):56-58.

[2] Dai H. Carbon nanotubes: synthesis, integration, and properties. Acc Chem Res 2002;35(12):1035-1044.

[3] Yu MF, Lourie O, Dyer MJ, Moloni K, Kelly TF, Ruoff RS. Strength and breaking mechanism of multiwalled carbon nanotubes under tensile load. Science 2000;287(5453):637-640.

[4] Shokrieh M, Rafiee R. A review of the mechanical properties of isolated carbon nanotubes and carbon nanotube composites. Mechanics of composite materials 2010;46(2):155-172.

[5] Jorio A, Dresselhaus G, Dresselhaus MS. Carbon nanotubes: advanced topics in the synthesis, structure, properties and applications. 2007;111.

[6] Ruoff RS, Lorents DC. Mechanical and thermal properties of carbon nanotubes. carbon 1995;33(7):925-930.

[7] Ma P, Siddiqui NA, Marom G, Kim J. Dispersion and functionalization of carbon nanotubes for polymer-based nanocomposites: a review. Composites Part A: Applied Science and Manufacturing 2010;41(10):1345-1367.

[8] Khan SU, Pothnis JR, Kim J. Effects of carbon nanotube alignment on electrical and mechanical properties of epoxy nanocomposites. Composites Part A-Applied Science and Manufacturing 2013;49:26-34.

[9] Bal S, Samal S. Carbon nanotube reinforced polymer composites—a state of the art. Bull Mater Sci 2007;30(4):379.

[10] Thostenson ET, Chou T. Carbon nanotube networks: Sensing of distributed strain and damage for life prediction and self healing. Adv Mater 2006;18(21):2837-+.

[11] Hu N, Karube Y, Arai M, Watanabe T, Yan C, Li Y, Liu Y, Fukunaga H. Investigation on sensitivity of a polymer/carbon nanotube composite strain sensor. Carbon 2010;48(3):680-687.

[12] Obitayo W, Liu T. A Review: Carbon Nanotube-Based Piezoresistive Strain Sensors. Journal of Sensors 2012:652438.

[13] Li X, Levy C, Elaadil L. Multiwalled carbon nanotube film for strain sensing. Nanotechnology 2008;19(4):045501.

[14] Bauhofer W, Kovacs JZ. A review and analysis of electrical percolation in carbon nanotube polymer composites. Composites Sci Technol 2009;69(10):1486-1498.

[15] Allaoui A, Bai S, Cheng H, Bai J. Mechanical and electrical properties of a MWNT/epoxy composite. Composites Sci Technol 2002;62(15):1993-1998.

[16] Prolongo S, Melitón B, Jiménez-Suárez A, Ureña A. Study of efficiency of different commercial carbon nanotubes on manufacturing of epoxy matrix composites. J Composite Mater 2014;48(25):3169-3177.

[17] Sandler J, Kirk J, Kinloch I, Shaffer M, Windle A. Ultra-low electrical percolation threshold in carbon-nanotube-epoxy composites. Polymer 2003;44(19):5893-5899.

[18] Martin C, Sandler J, Windle A, Schwarz M, Bauhofer W, Schulte K, Shaffer M. Electric field-induced aligned multi-wall carbon nanotube networks in epoxy composites. Polymer 2005;46(3):877-886.

[19] Kovacs JZ, Velagala BS, Schulte K, Bauhofer W. Two percolation thresholds in carbon nanotube epoxy composites. Composites Sci Technol 2007;67(5):922-928.

[20] Prolongo S, Jiménez-Suárez A, Melitón B, Campo M, Ureña A. Optimum Dispersion Technique of Carbon Nanotubes in Epoxy Resin as a Function of the Desired Behaviour. 2014;26:177-186.

[21] Li J, Ma PC, Chow WS, To CK, Tang BZ, Kim J. Correlations between percolation threshold, dispersion state, and aspect ratio of carbon nanotubes. Advanced Functional Materials 2007;17(16):3207-3215.

[22] Berhan L, Sastry A. Modeling percolation in high-aspect-ratio fiber systems. I. Soft-core versus hard-core models. Physical Review E 2007;75(4):041120.

[23] Yu Y, Song S, Bu Z, Gu X, Song G, Sun L. Influence of filler waviness and aspect ratio on the percolation threshold of carbon nanomaterials reinforced polymer nanocomposites. J Mater Sci 2013;48(17):5727-5732.

[24] Berhan L, Sastry A. Modeling percolation in high-aspect-ratio fiber systems. II. The effect of waviness on the percolation onset. Physical Review E 2007;75(4):041121.

[25] Li J, Östling M. Conductivity scaling in supercritical percolation of nanoparticles–not a power law. Nanoscale 2015;7(8):3424-3428.

[26] Cunningham G, Lotya M, McEvoy N, Duesberg GS, van der Schoot P, Coleman JN. Percolation scaling in composites of exfoliated MoS 2 filled with nanotubes and graphene. Nanoscale 2012;4(20):6260-6264.

[27] Kilbride Be, Coleman J, Fraysse J, Fournet P, Cadek M, Drury A, Hutzler S, Roth S, Blau W. Experimental observation of scaling laws for alternating current and direct current conductivity in polymer-carbon nanotube composite thin films. J Appl Phys 2002;92(7):4024-4030.

[28] Kymakis E, Amaratunga GA. Electrical properties of single-wall carbon nanotube-polymer composite films. J Appl Phys 2006;99(8):084302.

[29] Bao W, Meguid S, Zhu Z, Meguid M. Modeling electrical conductivities of nanocomposites with aligned carbon nanotubes. Nanotechnology 2011;22(48):485704.

[30] Gong S, Zhu Z, Li J, Meguid S. Modeling and characterization of carbon nanotube agglomeration effect on electrical conductivity of carbon nanotube polymer composites. J Appl Phys 2014;116(19):194306.

[31] De Vivo B, Lamberti P, Spinelli G, Tucci V. Numerical investigation on the influence factors of the electrical properties of carbon nanotubes-filled composites. J Appl Phys 2013;113(24):244301.

[32] Sanchez M, Rams J, Campo M, Jimenez-Suarez A, Urena A. Characterization of carbon nanofiber/epoxy nanocomposites by the nanoindentation technique. Composites Part B-Engineering 2011;42(4):638-644.

[33] Jimenez-Suarez A, Campo M, Sanchez M, Romon C, Urena A. Influence of the functionalization of carbon nanotubes on calendering dispersion effectiveness in a low viscosity resin for VARIM processes. Composites Part B-Engineering 2012;43(8):3482-3490.

[34] Nan C, Shen Y, Ma J. Physical properties of composites near percolation. Annual Review of Materials Research 2010;40:131-151.

[35] Hu N, Masuda Z, Fukunaga H. Prediction of electrical conductivity of polymer filled by carbon nanotubes. 2007.

[36] Cueto E, Monge R, Chinesta F, Poitou A, Alfaro I, Mackley MR. Rheological modeling and forming process simulation of CNT nanocomposites. International journal of material forming 2010;3(2):1327-1338.

[37] Laurent C, Flahaut E, Peigney A. The weight and density of carbon nanotubes versus the number of walls and diameter. Carbon 2010;48(10):2994-2996.

[38] Brcic M, Canadija M, Brnic J. Influence of waviness and vacancy defects on carbon nanotubes properties. Procedia Engineering 2015;100:213-219.

[39] Fisher F, Bradshaw R, Brinson L. Fiber waviness in nanotube-reinforced polymer composites—I: Modulus predictions using effective nanotube properties. Composites Sci Technol 2003;63(11):1689-1703.

[40] Kovacs J, Bauhofer W. THE INFLUENCE OF THE DISPERSION QUALITY OF CARBON NANOTUBES IN AN EPOXY MATRIX ON THE ELECTRICAL CONDUCTIVITY OF THE COMPOSITE.

[41] Kuang Y, He X. Young’s moduli of functionalized single-wall carbon nanotubes under tensile loading. Composites Sci Technol 2009;69(2):169-175.

[42] Veloso MV, Souza Filho A, Mendes Filho J, Fagan SB, Mota R. Ab initio study of covalently functionalized carbon nanotubes. Chemical physics letters 2006;430(1-3):71-74.

[43] Fu S, Chen Z, Hong S, Han CC. The reduction of carbon nanotube (CNT) length during the manufacture of CNT/polymer composites and a method to simultaneously determine the resulting CNT and interfacial strengths. Carbon 2009;47(14):3192-3200.

[44] Jam J, Pourasghar A, Kamarian S. Effect of the aspect ratio and waviness of carbon nanotubes on the vibrational behavior of functionally graded nanocomposite cylindrical panels. Polymer Composites 2012;33(11):2036-2044.

[45] Milowska K, Birowska M, Majewski JA. Mechanical and electrical properties of carbon nanotubes and graphene layers functionalized with amines. Diamond and Related Materials 2012;23:167-171.

[46] Takeda T, Shindo Y, Kuronuma Y, Narita F. Modeling and characterization of the electrical conductivity of carbon nanotube-based polymer composites. Polymer 2011;52(17):3852-3856.

[47] Li C, Thostenson ET, Chou T. Dominant role of tunneling resistance in the electrical conductivity of carbon nanotube-based composites. Appl Phys Lett 2007;91(22):223114.

[48] YAMAMOTO S, MATSUOKA T. Dynamic Simulation of Flow-Induced Fiber Fracture. Polym Eng Sci 1995;35(12):1022-1030.

[49] Chapartegui M, Markaide N, Florez S, Elizetxea C, Fernandez M, Santamaria A. Curing of epoxy/carbon nanotubes physical networks. Polym Eng Sci 2012;52(3):663-670.

[50] Aravand M, Lomov SV, Verpoest I, Gorbatikh L. Evolution of carbon nanotube dispersion in preparation of epoxy-based composites: From a masterbatch to a nanocomposite. Express Polymer Letters 2014;8(8):596-608.

[51] Bakshi SR, Batista RG, Agarwal A. Quantification of carbon nanotube distribution and property correlation in nanocomposites. Composites Part A: Applied Science and Manufacturing 2009;40(8):1311-1318.

[52] Sul IH, Youn JR, Song YS. Quantitative dispersion evaluation of carbon nanotubes using a new analysis protocol. Carbon 2011;49(4):1473-1478.

[53] Tyson BM, Al-Rub RKA, Yazdanbakhsh A, Grasley Z. A quantitative method for analyzing the dispersion and agglomeration of nano-particles in composite materials. Composites Part B: Engineering 2011;42(6):1395-1403.

Chapter 4: Critical parameters of carbon nanotube reinforced composites for structural health monitoring applications: Empirical results versus theoretical predictions

Xoan F. Sánchez-Romate[a,b],[4], Joaquín Artigas[b] , Alberto Jiménez-Suárez[b], María Sánchez[b], Alfredo Güemes[a] and Alejandro Ureña[b]

Published in Compos Sci Technol 171 (2019) 44-53

[a] Department of Aerospace Materials and Processes, Escuela Técnica Superior de Ingenieros Aeronáuticos, Universidad Politécnica de Madrid, Plaza del Cardenal Cisneros 3, 28040 Madrid, Spain

[b] Materials Science and Engineering Area, Escuela Superior de Ciencias Experimentales y Tecnología, Universidad Rey Juan Carlos, Calle Tulipán s/n, 28933 Móstoles (Madrid), Spain

This paper reports on an investigation of the critical parameters which determine the electrical and electromechanical properties of carbon nanotube (CNT) nanocomposites. For this purpose, a novel analytical model, based on the tunnelling mechanisms of CNTs, is proposed. Three dispersion parameters are introduced in the model to reflect the CNT aggregation state. Microscopy analysis and electrical and strain monitoring tests were carried out on CNT nanocomposites manufactured by toroidal stirring and three roll milling. It is observed that electrical conductivity is greatly affected by dispersion procedure as well as strain sensitivity, measured by the gauge factor (GF). Generally, well dispersed materials have higher conductivities and GF. In this regard, the

---

[4] Corresponding author. Tel: +34 91 488 82 52. E-mail: xoan.fernandez.sanchezromate@urjc.es

aggregate ratio has a prevalent effect. Experimental data and theoretical predictions allow the correlation of dispersion parameters given by manufacturing procedures with electrical properties to develop highly sensitive nanocomposites. This demonstrates the potential and applicability of the proposed model.

Keywords: (A) carbon nanotubes; (B) electrical properties; (C) modelling; dispersion; SHM

4.1 Introduction

The use of carbon nanotubes (CNTs) has increased significantly since the studies of Iijima et al. [1] as they exhibit excellent mechanical and electrical properties [2–6]. Indeed, tensile strengths of $\sim 11-100$ GPa,Young's Modulus of $\sim 0.27-1$ TPa [5,6], and electrical conductivities of $10^3-10^6\ \mathrm{S/m}$ have been achieved [7,8]. Of particular interest is the effect of their addition as fillers in a polymer matrix on electrical properties. Their high aspect ratio, with values of more than 1000, makes it possible that very small amounts of CNTs (below 1 wt %) cause an increase in electrical conductivity of several orders of magnitude [9–13]. This is because CNTs create a conductive network inside the matrix, providing electrical pathways. That, in combination with CNT piezoresistive behaviour, makes possible their use in strain-sensing applications, which are now attracting the interest of many researchers [14–17].

In this context, the determination of the percolation threshold, i.e. the critical volume fraction of nanofiller at which the material becomes electrically conductive, is a crucial point in investigations of CNT nanocomposite electrical behaviour [18–20]. Percolation threshold has been found to be correlated with CNT geometry and orientation [21], as well as dispersion procedure, for CNT content ranging from values of 0.01 wt % [18] to above 0.5 wt % [9,22]. For this reason, the influence of these parameters has been widely studied and theoretical models for predicting the percolation threshold and electrical conductivity of CNT nanocomposites have been proposed [8,23–26].

The strain monitoring capabilities of CNT-based composites are greatly influenced by percolation threshold and electrical conductivity and correlations between these parameters have also been determined by theoretical modelling [27–29]. Tunnelling resistance has been found to be the dominant mechanism that rules the electromechanical behaviour of CNT nanocomposites [30] and is given by the distance between two adjacent CNTs. Experimental and numerical investigations have correlated tunnelling distance with CNT content [31,32], showing that the highest sensitivities are generally achieved at CNT contents near the percolation threshold. However, the influence of dispersion techniques – and thus the CNT dispersion state – on the electromechanical capabilities of CNT nanocomposites remains to be investigated.

In a previous study, an improved analytical model based on aggregation parameters was proposed [33], analysing different dispersion techniques and CNT fillers. This approach gives a precise idea of how exactly the dispersion state and CNT geometry affect electrical conductivity, but it does not allow prediction of the electromechanical properties of CNT-based nanocomposites as it does not take into account tunnelling mechanisms. For this reason, the aim of this study is to examine the influence of dispersion state on the electromechanical behaviour of CNT nanocomposites.

To achieve this, electrical conductivity measurements, strain monitoring tests, and dispersion state characterization by optical microscopy were carried out using different dispersion conditions and CNT content. A novel approach based on CNT dispersion state is proposed and critical parameters that influence the electromechanical properties are identified and correlated. The validity and applicability of this model are demonstrated by comparing theoretical predictions to experimental data.

4.2 Materials and methods

4.2.1 Materials

Nanocomposites were manufactured with multiwall carbon nanotubes (MWCNTs) embedded in an epoxy resin. Commercially available Nanocyl NC3150 MWCNTs, with an average diameter of 9.5 nm and a length up to 1 μm, were sourced. The resin was a low-viscosity DGBEA Huntsman Araldite LY556 cured with aromatic amine Araldite XB3473.

4.2.2 Manufacturing of CNT nanocomposites

MWCNT nanocomposites were manufactured in three steps: addition of the nanoparticles into the matrix and mechanical dispersion, degasification of the mixture, and curing.

Two dispersion procedures were used to prepare the MWCNT-epoxy mixtures: three roll milling and a combination of toroidal stirring and three roll milling. Toroidal stirring was carried out using a Dispermat dissolver at 6000 rpm for 15 min. The three roll milling dispersion process was optimized in previous studies [34,35]. It consists of a progressive reduction in the gap between the rolls, keeping the velocity of the third (last) roll constant at 250 rpm. The parameters of the three roll milling dispersion procedure are shown in Table 4.1. To provide a more detailed analysis of the effect of dispersion procedure on electrical properties, different CNT content mixtures (0.05, 0.1 and 0.3 wt %) were manufactured in different numbers of three roll milling cycles: 1, 3 and 7 for 0.05 and 0.1 wt %, with and without toroidal stirring; 1, 3 and 7 for 0.3 wt % mixtures without toroidal stirring, as it is not possible to achieve a 3D toroidal flow when adding such a high content). Table 4.2 summarizes the different conditions tested.

Table 4.1: Process conditions for three roll milling dispersion.

Cycle	First roll gap (μm)	Last roll gap (μm)
1	120	40
2	75	25
3	45	15
4-7	15	5

Table 4.2: Processing methods and conditions for CNT-epoxy mixture manufacturing.

Content (% wt.)	Designation	Procedure
0.05 / 0.1 / 0.3	C1	Three roll milling process. cycle 1.
0.05 / 0.1 / 0.3	C3	Three roll milling process. cycles 1–3.

0.05 / 0.1 / 0.3	C7	Three roll milling process. cycles 1–7.
0.05 / 0.1	Disp	Toroidal stirring at 6000 rpm for 15 min
0.05 / 0.1	DC1	Toroidal stirring + C1
0.05 / 0.1	DC3	Toroidal stirring + C3
0.05 / 0.1	DC7	Toroidal stirring + C7

After the dispersion process, a degasification step was carried out to evacuate the air entrapped in the epoxy mixture. For this purpose, the mixture was heated to 80 ºC and then degasification was done under vacuum for 15 min. After that, hardener was added to the mixture in a proportion 100:23 monomer:hardener. Finally, doped resins were cured in an oven at 140 ºC for 8 h in a 270x120x4 mm3 mould.

4.2.3 Characterization of nanocomposites

CNT dispersion in the CNT-epoxy mixtures was analysed using a Leica high transmission optical microscope (TOM), equipped with a Nikon Coolpix 990 camera. In addition, to analyse CNT distribution and agglomerate morphology in the nanocomposite, materials were fractured under cryogenic conditions. First, a pre-crack treatment was done with the nanocomposite immersed in liquid N2 for 5 min. Then, the sample was fractured and coated with platinum (5.6 nm). The microstructural study was carried out by Field Emission Gun Scanning Electron Microscopy FEG-SEM using a Nova NanoSEM FEI 230 apparatus from Philips.

DC volume conductivity was evaluated according to ASTM D257 using a Source Measurement Unit (SMU, Keithley Instrument Inc. mod. 2410). Three specimens (10 × 10 × 1 mm) were tested for each condition. Silver paint was used to ensure good contact between the electrode and the specimen, the surface of which was treated by brushing. The voltage applied was within the range of 0–20 V and electrical resistance was determined by the slope of the I-V curve.

4.2.4 Strain monitoring tests

Tensile tests were carried out according to ASTM D638 at a test rate of 5 mm/min and electrical resistance was measured using a multimeter (Agilent 34410A). The electrodes were made of copper wire with silver paint to ensure good contact with the nanocomposite surface. Adhesive tape was used to protect the electrodes from environmental issues. The electrodes were placed 30 mm apart on the central region of the tensile specimen, subjected to a uniform strain. Tensile specimens were isolated from the machine by using and adhesive layer at the grips. Figure 4.1 shows an image of the electrode placement.

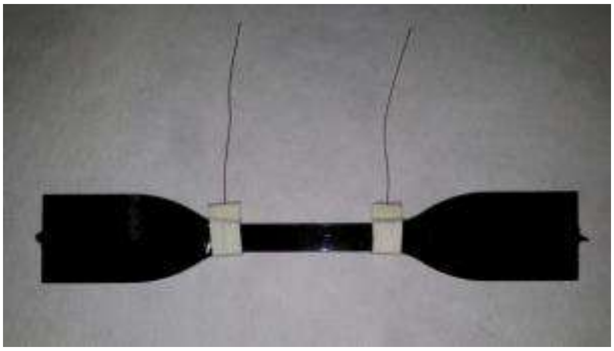

Figure 4.1: Electrode placement on tensile specimen.

4.3 Results and discussion

Electrical conductivity and strain monitoring tests were carried out for the specimens manufactured by three roll milling and a combination of three roll milling and toroidal stirring. An analytical model has been proposed to identify the main parameters affecting the electrical properties of CNT nanocomposites and a comparison between theoretical predictions and experimental measurements has been established.

4.3.1 Experimental results

Figure 4.2 and Figure 4.3 summarize the electrical properties of CNT/epoxy nanocomposites under tested conditions. At the lower counts of three roll mill processing, electrical conductivity increases drastically. At the lower counts of three roll mill processing, i.e. for C1 to C3 for all CNTs, electrical conductivity increases drastically as shown in Figure 4.2 (solid lines). This is due to the effective breakage of larger agglomerates, caused by induced shear forces, which leads to a better homogenization of the CNT, as observed by comparing TOM images after one to three cycles of the three roll milling process (Figure 4.4 (a) and (b)). In addition, as stated in a previous study, these shear forces also induce a stretching effect on CNTs [33], which causes an increase in the effective aspect ratio and thus a higher conductivity as it induces a decrease of the percolation threshold [23]. On the other hand, the increase in electrical conductivity is less significant because of the greater CNT breakage effect [36,37] for C3 to C7. Moreover, the three roll milling effect on electrical conductivity at high cycles is less significant with an increasing CNT content, even leading to a slight reduction on electrical conductivity from the 3-step to 7-step three roll milling process. This effect can be explained by increased interactions between carbon nanotubes, which lead to a higher CNT breakage effect due to a decrease in their effective elastic modulus [38,39].

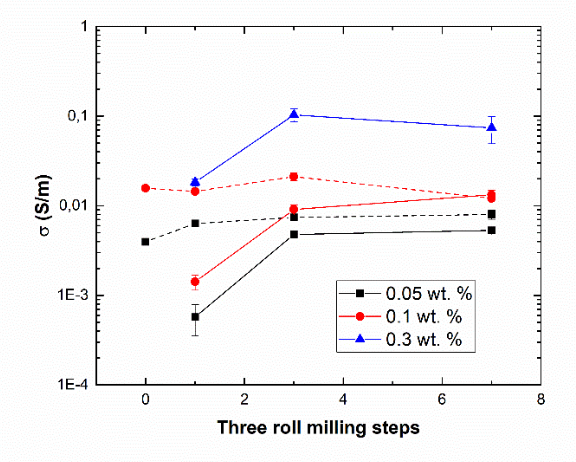

Figure 4.2: Electrical conductivity measurements for the different CNT nanocomposites prepared by three roll milling (solid lines) and the combination of toroidal stirring and three roll milling (dashed lines).

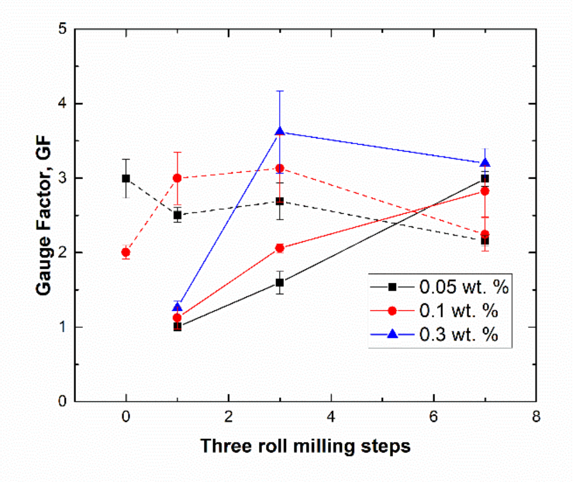

Figure 4.3: Measured GF for the different CNT nanocomposites prepared by three roll milling (solid lines) and a combination of toroidal stirring and three roll milling (dashed lines).

On the other hand, an enhancement in electrical conductivity is observed with a previous toroidal stirring step when comparing to three roll milling process, specially at lower three roll milling steps (i.e. C1 to DC1 and C3 to DC3 of Figure 4.2). This could be explained by the 3D flow induced by toroidal stirring leading to a higher homogenization effect [40] (Figure 4.4 (c)) without a CNT breakage as the shear forces involved are much lower. This causes the mean aggregate size to be reduced and thus CNT interactions are also lower when passing through the three roll mill, resulting in a well dispersed mixture (Figure 4.4 (d)). However, no significant differences between lower and higher cycles of three roll milling are observed with a prior toroidal stirring process i.e. comparing C3 with DC3, and C7 and DC7. This could be because the main homogenization effect takes place during the toroidal stirring step. Thus, in this case, three roll milling does not have a relevant effect on CNT dispersion, resulting in very similar dispersion states when comparing DC1 to DC7 (Figure 4.4 (d) and (e)). In addition, the effect of toroidal stirring is less evident at lower CNT content.

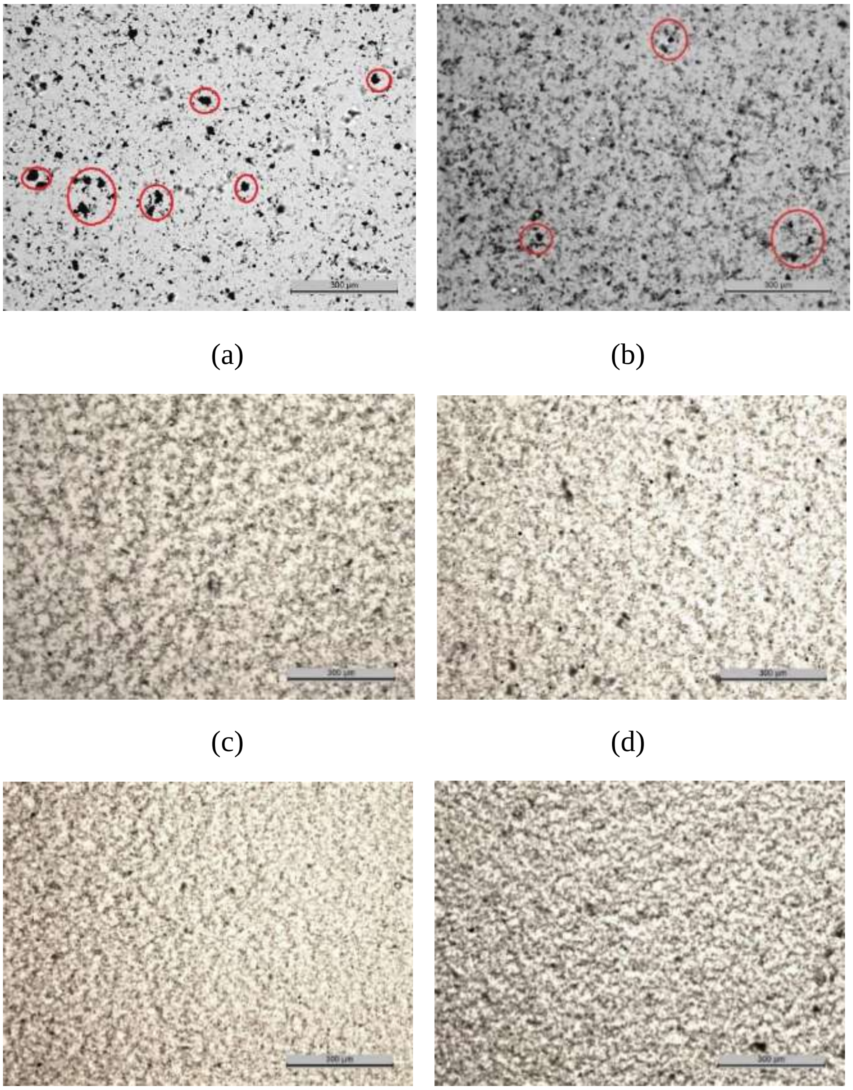

(a) (b)

(c) (d)

(e) (f)

Figure 4.4: TOM images of CNT dispersion for (a) C1, (b) C3, (c) Disp, (d) DC1, (e) DC3 at 0.05 wt % and (f) DC7 at 0.1 wt % (red circles indicate the presence of larger aggregates).

Figure 4.3 summarizes the gauge factor (GF), defined as the variation of normalized resistance between applied strain achieved, that is $\frac{\Delta R/R_0}{\varepsilon}$, for the different specimens manufactured at low strain levels ($\varepsilon = 0.005$). A significant increase in sensitivity is observed with three roll mill steps due to the high disaggregation effect induced by shear forces. On the other hand, toroidal stirring improves sensitivity when combined with a few cycles of the three roll mill process, but at higher cycles it does not seem to have a significant effect and could even give rise to lower GF. The main reason can lie in the fact that at higher three roll milling steps, there is a more prevalent CNT breakage effect due to the shear forces involved leading, thus, to a lower electrical conductivity and GF. In addition, GF values at different CNT contents were similar, although a slightly higher sensitivity is achieved with lower CNT contents, especially in the three roll milling process. This could be due to a similar dispersion state observed at different CNT contents (Figure 4.4 (e) and (f)).

Therefore, from the experimental measurements, it is clear that there is a correlation between the dispersion procedure and electromechanical properties. Thus, to attain a deeper understanding of electromechanical properties, an analytical model correlating the crucial parameters is proposed.

4.3.2 Theoretical analysis

In the model, CNT agglomerates are considered to be perfect spheres, as shown in Figure 4.5, supposing that adjacent carbon nanotubes in an agglomerate are in contact. Electrical resistance is thus composed of three terms, CNT intrinsic, contact and tunnelling resistance, as follows:

$$R_T = R_{CNT} + R_{contact} + R_{tunnel} \tag{4.1}$$

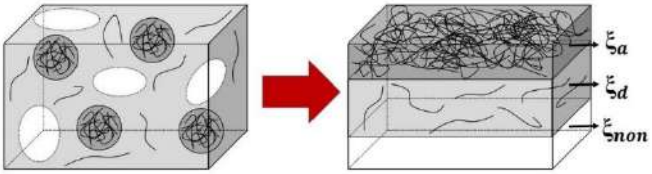

Figure 4.5: Schematic of the proposed model showing (left) the real dispersion state and (right) the equivalent block disposition.

The electrical intrinsic resistance of CNTs can be obtained using the following expression:

$$R_{CNT} = \frac{1}{\sigma_{CNT}} \cdot \frac{l}{A} \tag{4.2}$$

where l is the length between two contact points, A the cross-sectional area and σ_{CNT} the intrinsic conductivity of the CNT.

For contact resistance, an expression such as that stated by Gong et al. [41] can be used, assuming there is no deformation at CNT junctions:

$$R_{contact} = \frac{h}{e^2} \cdot \frac{1}{MT} \tag{4.3}$$

where M is the number of conducting channels, estimated between 400 and 500 for MWCNTs as stated previously by Li et al. [42]; $\frac{h}{e^2}$ is the Planck resistance and T the transmission probability for electrons tunnelling through the polymer, which is estimated as:

$$T = exp\left(\frac{-d_w}{h/\sqrt{8m\varphi_{CNT}}}\right) \tag{4.4}$$

where d_w is the van der Waals distance, 0.34 nm, m the mass of an electron and φ_{CNT} the work function of CNTs (set at 4.5 eV) [43].

Thus for a CNT cluster, total resistance can be calculated by the sum of intrinsic and contact resistance at CNT junctions, leading to the following expression:

$$R_{cluster} = R_{CNT} + R_{contact} = \frac{1}{\sigma_{CNT}} \cdot \frac{l}{A} + \frac{h}{e^2} \cdot \frac{1}{MT} \tag{4.5}$$

The expression presented in Eq. () denotes the electrical resistance term, which is assumed to be invariable with strain and is called intrinsic resistance. It is considered invariable as it refers to the intrinsic resistance of the cluster. CNTs can be deformed due to strain and it induces a change on the electrical conductivity. However, due to the 3D disposition of CNTs in a cluster, Poison effects can mitigate the electrical change due to CNT deformation. In addition, the poor CNT-matrix interaction in an agglomerate also mitigates the overall nanocomposite strain effect over the CNTs and therefore, for simplicity, intrinsic resistance will be considered invariable.

However, the other term, the tunnelling resistance, changes with applied strain and gives the electromechanical properties of the nanocomposite.

The tunnelling resistance is calculated using the following expression, as stated by Hu et al. [27]:

$$R_{tunnel} = \frac{h^2 t}{Ae^2\sqrt{2m\varphi}} exp\left(\frac{4\pi t}{h}\sqrt{2m\Phi}\right) \tag{4.6}$$

in which A is the tunnelling area, estimated as the cross-sectional area of the CNTs (that is $A = \pi \cdot {d_{CNT}}^2/4$); t the tunnelling distance, given by the distance between two neighbouring CNTs in which the tunnelling effect occurs; and Φ the height of the barrier of epoxy (set at 0.75 eV) [27,29].

4.1.1.1 Modelling of the dispersion state

To date, most studies have assumed that CNTs are perfectly dispersed in the matrix and thus electromechanical behaviour is directly given by the expression in Eq. (). However, the dispersion state is a key factor for electrical conductivity and electromechanical behaviour, as shown in the experimental measurements, so it is necessary to take it into account when modelling the strain monitoring capabilities of CNT nanocomposites.

For this reason, and to attain a better understanding of CNT dispersion state, three parameters are defined: ξ_a is the volume fraction of material that is occupied by CNT agglomerates, i.e. the agglomerate volume fraction dominated by intrinsic resistance; ξ_d is the volume fraction occupied by well dispersed CNTs in which tunnelling resistance is prevalent and over the percolation threshold; ξ_{non} is the volume fraction of the material in which the CNT concentration is much lower than the average content, called the non-percolated region.

$$\xi_a = \frac{V_a}{V} \qquad \xi_d = \frac{V_d}{V} \qquad \xi_n = \frac{V_n}{V} \tag{4.1}$$

where V_a, V_d and V_n are the volumes of the agglomerated, dispersed and non-percolated regions respectively.

In a previous study [23], ε has been defined as the localized volume of CNT in an agglomerate using the following expression:

$$\varepsilon = \frac{nV_{CNT}}{\frac{\pi D^3}{6}} \quad (1 > \varepsilon > \varepsilon_0) \tag{4.2}$$

where ε_0 is defined as the minimum localized volume of CNTs needed to consider them as agglomerates, n is the number of nanoparticles in a cluster and D the diameter of the equivalent sphere.

Once the volume fraction of agglomerated and well dispersed CNTs is defined, it is necessary to correlate them to the electrical properties of the materials. As previously stated, the electrical resistance of aggregates, R_a, is given by the intrinsic resistance, $R_{intrinsic}$, using Eq. (). In the case of well dispersed CNTs, the electrical resistance of the dispersed regions, R_d, is given by R_{tunnel}, defined in Eq. (), while the resistance of the non-percolated region can be considered infinite. Therefore, the material can be divided into three different blocks (ξ_a, ξ_d and ξ_{non}), i.e. the volume fraction of agglomerated, well dispersed and non-percolated nanoparticles as shown in Figure 4.5. This configuration overestimates the total electrical resistance of the nanocomposite but gives an idea of how dispersion state affects the electrical properties of the material. Thus, it is possible to calculate the equivalent electrical resistance along the material, R.

$$\frac{1}{R} = \xi_a \cdot \frac{1}{R_a} + \xi_d \cdot \frac{1}{R_d} + \underbrace{\xi_{non} \cdot \frac{1}{R_\infty}}_{\sim 0} \rightarrow \quad R = \frac{R_a R_d}{(\xi_d R_a + \xi_a R_d)} \tag{4.3}$$

Using this expression, it is possible to see the change in electrical resistance due to applied strain as a function of the dispersion state:

$$\frac{\Delta R}{R_0} = \frac{\frac{R_a R_d}{(\xi_d R_a + \xi_a R_d)}}{\frac{R_{a0} R_{d0}}{(\xi_d R_{a0} + \xi_a R_{d0})}} - 1 = \frac{R_a R_d}{R_{a0} R_{d0}} \cdot \left(\frac{\xi_d R_{a0} + \xi_a R_{d0}}{\xi_d R_a + \xi_a R_d}\right) - 1 \tag{4.4}$$

in which the subscript 0 denotes the initial stage with no applied strain. This expression can be simplified by defining several non-dimensional parameters, such as: the ratio of agglomerated (χ_a) and dispersed (χ_d) CNTs; the coefficients of electrical resistance before and after applied strain ($\chi_a = \frac{R_a}{R_{a0}}$

and $\chi_d = \frac{R_d}{R_{d0}}$ respectively); the ratio between agglomerated and dispersed CNTs ($\varphi = \xi_a/\xi_d$, also defined as the aggregate ratio); the correlation between R_{d0} and R_{a0} (Ψ). This leads to the following expression:

$$\frac{\Delta R}{R_0} = \chi_a \chi_d \cdot \left(\frac{1 + \varphi\Psi}{\chi_a + \varphi \chi_d \Psi} \right) - 1 \tag{4.5}$$

In the case of well dispersed material, that is $\varphi = 0$, Eq. (4.5) leads to $\frac{\Delta R}{R_0} = \chi_d - 1$, and if the CNTs are all in the form of aggregates, that is $\varphi \to \infty$, it leads to $\frac{\Delta R}{R_0} = \chi_a - 1$.

In addition, the electrical conductivity of CNT nanocomposites can be calculated from R using the following expression:

$$\sigma = \frac{L}{R \cdot A} = \frac{L_{eq}}{R \cdot {L_{eq}}^2} = \frac{1}{R \cdot L_{eq}} = \frac{1}{L_{eq}} \cdot \frac{(\xi_d R_a + \xi_a R_d)}{R_a R_d} \tag{4.6}$$

where L_{eq} is the length of the equivalent cubic element, defined in a previous study [33].

Therefore, it is possible to correlate electrical properties with the CNT dispersion state in a very simple way. However, it is important to point out that this proposed model is only valid at lower strain levels, in which the effect of the breakage of electrical pathways due to matrix fracture and damage [44] is not so prevalent. For higher applied strain, it is necessary to take these effects into account in the model to obtain more accurate results.

4.1.1.2 Modelling approach to inter-particle distance

To calculate the tunnelling resistance, it is necessary to determine the mean tunnelling distance, also called the inter-particle distance (IPD). This is defined as the mean distance of two adjacent particles. IPD depends fundamentally on CNT volume content, as it implies a higher number of nanoparticles in the material. The main issue is to determine this value for any given content.

IPD depends on the number of particles per unit volume, n, following a power law of exponent α [31]:

$$IPD \sim \left(\frac{1}{n}\right)^{\alpha} \tag{4.7}$$

Therefore, supposing that the value of the tunnelling distance at the percolation threshold, t_0, is known and set at 1.4 nm, as proposed by Li et al. [30], it is possible to obtain the mean tunnelling distance, t, for any CNT concentration using the following expression:

$$t = t_0 \left(\frac{\rho_0}{\rho}\right)^{\alpha} \tag{4.8}$$

where ρ and ρ_0 are the volume fraction at a general concentration and the percolation threshold, respectively. The percolation threshold is determined using the following expression, assuming CNTs are straight and with no alignment:

$$\rho_0 = \frac{3\sqrt{3}}{4} \cdot \frac{1}{\Lambda^2} \tag{4.9}$$

in which Λ is the aspect ratio of CNTs. As stated previously, three roll milling has a breakage effect on CNTs, so it affects the value of ρ_0 due to reduction of the effective aspect ratio of CNTs. The resulting aspect ratio after a three roll milling process can be calculated based on the formula proposed by Yamamoto et al. [45]:

$$\frac{\eta\dot{\gamma}}{E} \sim 100 \frac{\ln(2\Lambda) - 1.75}{2\Lambda^4} \tag{4.10}$$

where E is the Young’s Modulus of CNTs, (1 TPa); η the viscosity of the epoxy resin, (4 Pa·s) and $\dot{\gamma}$ the shear rate of the three roll milling process.

The exponent α can be calculated assuming that, at the maximum CNT content (ρ_m), IPD is equal to the minimum distance between two particles, i.e. the van der Waals distance (d_w), resulting in the following expression:

$$t_0 \left(\frac{\rho_0}{\rho_m}\right)^{\alpha} = d_w \quad \rightarrow \quad \alpha = \frac{ln\left(\frac{d_{wd}}{t_0}\right)}{ln\left(\frac{\rho_0}{\rho_m}\right)} \tag{4.11}$$

$$\rho_m = \frac{\pi}{6} \quad (max. package\ factor\ of\ a\ sphere)$$

As previously stated, the effect of tunnelling resistance is relevant when CNTs are well dispersed, so to calculate the mean tunnelling distance, only the volume fraction of well dispersed CNTs is taken into account. Assuming the localized volume content of well dispersed CNTs is equal to the overall CNT volume fraction in the material, Eq. (4.8) can be rewritten as follows:

$$t_d = t_0 \left(\frac{\rho_0}{\rho}\right)^{\alpha} \tag{4.12}$$

4.3.3 Parametric study

A parametric study was carried out to evaluate the effect that dispersion state has on the electromechanical sensitivity of the material. To achieve this purpose, the change in contact resistance due to the variation of tunnelling distance on the junctions was considered negligible. Thus, R_a was constant with applied strain, which implies that $\chi_a = 1$. In addition, χ_d can be calculated at a known tunnelling distance and thus so can the ratio between the electrical resistance of agglomerates and well dispersed CNTs, Ψ.

Figure 4.6 (a) shows the calculated GF from Eq. (4.5) with varying IPD and aggregation rate, (φ) at a value of $\varepsilon = 0.005$. It can be seen that the better the dispersion state, that is the lower the aggregate ratio, the higher the sensitivity of the material. This is because there are fewer preferential electrical pathways the lower the agglomerates size, so the whole material acts as a sensor. Therefore, the highest values of aggregation rate lead to the lowest sensitivities as those agglomerates act as preferential areas since the intrinsic resistance is usually much lower than tunnelling resistance.

In addition, IPD is observed to have a combined effect on the sensitivity of the material. At lower values of IPD, the sensitivity increases with tunnelling distance because of a relevant effect of tunnelling resistance which varies exponentially with applied strain. However, at a certain IPD, sensitivity begins to decrease again. This is because the value of tunnelling resistance is so high that electricity trends to go through agglomerates, even when the CNTs are well dispersed.

In this regard, Figure 4.6 (b) shows the correlation between IPD and CNT geometries at different contents based on Eq. (11). It can be seen that lower aspect ratios lead to higher IPDs as the percolation threshold is increased. In addition, IPD decreases with CNT content due to the presence of a higher number of particles per unit volume.

The correlation between electrical conductivity and aggregation parameters is shown in Figure 4.7 at different CNT concentrations. At lower CNT content, the electrical conductivity is given mainly by the value of ξ_a due to the presence of preferential pathways along the CNT agglomerates. For a value of ξ_a, it is observed that the presence of more well dispersed material leads to higher conductivities. At higher CNT content, variation of electrical conductivity with ξ_d is more significant, as the IPD of well dispersed CNTs is lower, and thus tunnelling resistance is also lower, so its contribution to electrical conductivity is more prevalent.

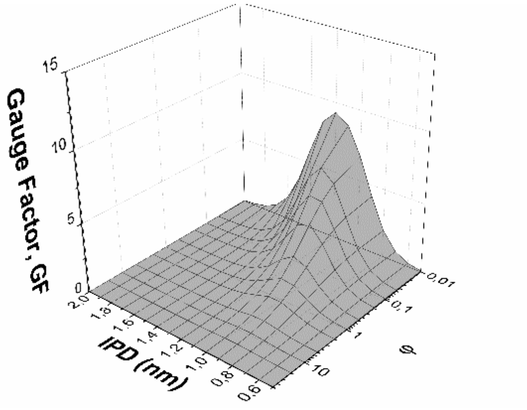

(a)

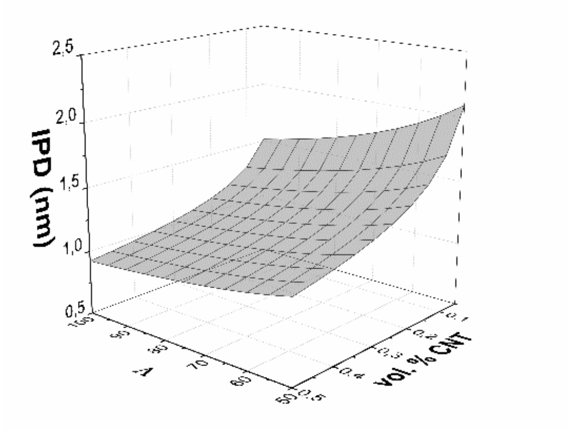

(b)

Figure 4.6: (a) Effect of the aggregate ratio and IPD on GF and (b) effect of the aspect ratio and CNT content on the mean IPD.

Therefore, the above parametric study gives an accurate idea of how dispersion state can affect electromechanical properties. It has been shown that the highest conductivities are achieved for well dispersed materials, i.e. those with a lower aggregate ratio. In this context, electrical conductivity is significantly dependent on ξ_a at low CNT content, and the effect of the well dispersed region, ξ_d, is controlling at high CNT content, while the IPD distance is greatly affected by CNT aspect ratio and content. Thus, it is necessary to compare theoretical predictions to the experimental data to provide a detailed analysis of the influence of dispersion technique on the electromechanical properties of CNT/epoxy nanocomposites.

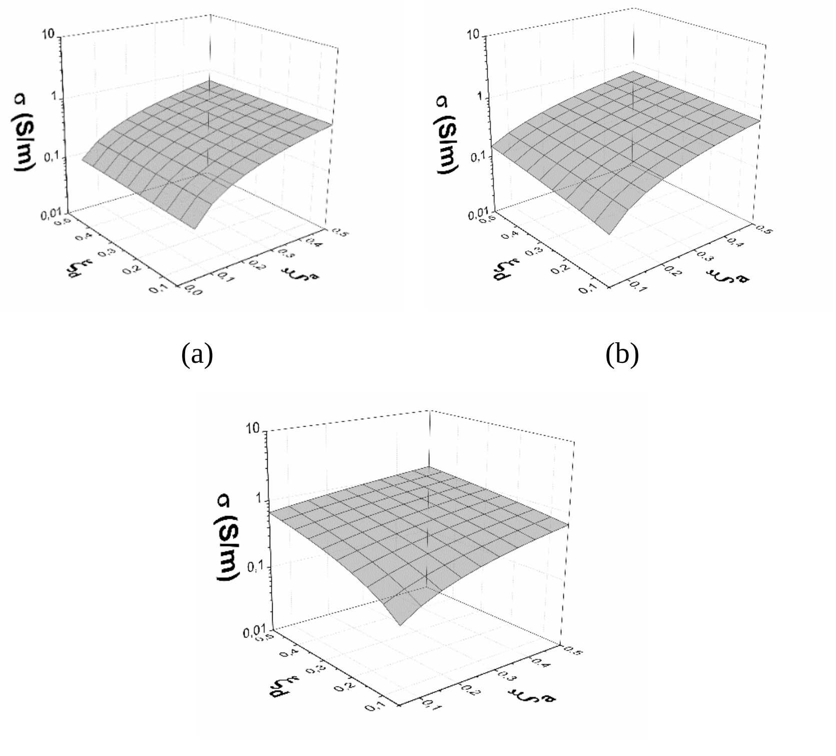

(a) (b)

(c)

Figure 4.7: Effect of aggregation parameters on electrical conductivity at (a) 0.1 (b) 0.2 and (c) 0.5 vol. % CNT.

4.3.4 Comparison between theoretical approach and experimental measurements

Figure 4.8 presents the effect of the dispersion procedure at different mean IPD on the GF predicted by Eq. (4.5), with varying aggregation parameters, compared to experimental data obtained from the strain monitoring tests. The values of GF used for the calculation are those at lower strain levels, i.e. $\varepsilon = 0.005$. In addition, the effective aspect ratio was calculated using Eq. (16). To account for the higher interactions between CNTs at higher contents, the resulting aspect ratio was multiplied by a factor of 1.2, 1 and 0.7 for 0.05, 0.1 and 0.3 wt % respectively. These factors were set to take into account the interaction forces between adjacent nanoparticles. As previously stated [37], the expression used in Eq. (16) overestimates the real aspect ratio at high CNT contents, while at low contents the shear forces presented are much lower.

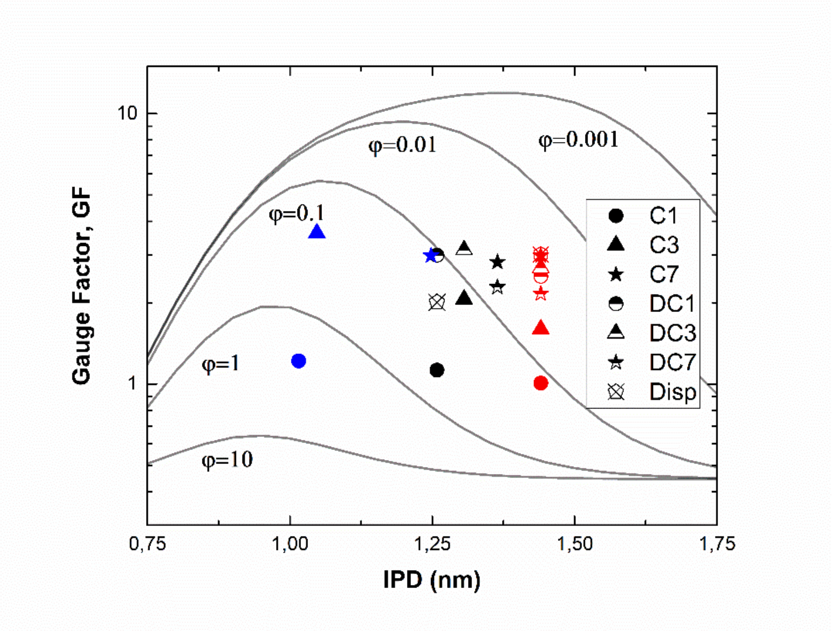

Figure 4.8: Effect of different process conditions on the aggregation ratio and IPD. Red, black and blue symbols refer 0.05, 0.1 and 0.3 wt %, respectively.

The aggregate ratio was observed to change dramatically depending on CNT content and dispersion procedure. A general increase is observed with CNT content from values from 0.024–0.13 at 0.05 wt % to 0.14–4 at 0.3 wt %.

This is due to a higher number of nanoparticles forming larger agglomerates and increasing the volume fraction of CNT aggregates. In addition, the three roll milling process was observed to reduce drastically the aggregate ratio by approximately an order of magnitude. However, the addition of a toroidal stirring step does not seem significantly to improve the aggregate ratio of CNT nanocomposites over a three roll milling process, as previously stated, because toroidal stirring does not significantly improve homogeneity as an additional step to a three roll milling process. However, a slight enhancement is observed at 0.1 wt % due to a better homogenization effect of toroidal stirring at higher CNT content. IPD is also greatly affected by process conditions. IPD generally decreases with CNT content from 1.02–1.24 nm at 0.3 wt % to 1.44 nm at 0.05 wt %. Nevertheless, it increases with three roll milling cycles, due to reduction in the effective aspect ratio, which induces an increase in the percolation threshold. This effect is more pronounced at higher contents because breakage – and thus the reduction of the effective aspect ratio – of CNTs is much higher.

Figure 4.9 summarizes the main dispersion parameters obtained for each process condition. ξ_a generally increases with CNT content (from 0.0005–0.004 at 0.05 wt % to 0.04–0.055 at 0.3 wt %) and the three roll milling and toroidal stirring process (varying by an order of magnitude in some cases). This seems contradictory to expected behaviour. However, higher values of ξ_a do not mean higher entanglement. It is correlated with the fraction of total volume occupied by agglomerates. The degree of entanglement is given by the aggregate ratio. Therefore, higher values of ξ_a in combination with lower values of φ indicate higher agglomerated areas with lower localized volume content, i.e. better homogenization of CNT dispersion, as shown in Figure 4.10. In this regard, it is observed that the non-percolated area decreases significantly with three roll milling cycles, from values of 0.98–0.99 to 0.7–0.87 from one to seven cycles of three roll milling, respectively; and with the addition of a toroidal stirring step, reaching values below 0.1, indicating the homogenization effect that these processes have on CNT dispersion by inducing the creation of more electrical pathways, which leads to an increase in well dispersed regions. Toroidal stirring also induces a decrease in the non-percolated region to values around 0.75–0.85 due to the homogenization effect on CNT dispersion. In addition, a general decrease is also observed with CNT content, especially at C7, from 0.87 at 0.05 wt % to 0.7 at 0.3 wt %, due to a higher breakage effect from three roll milling.

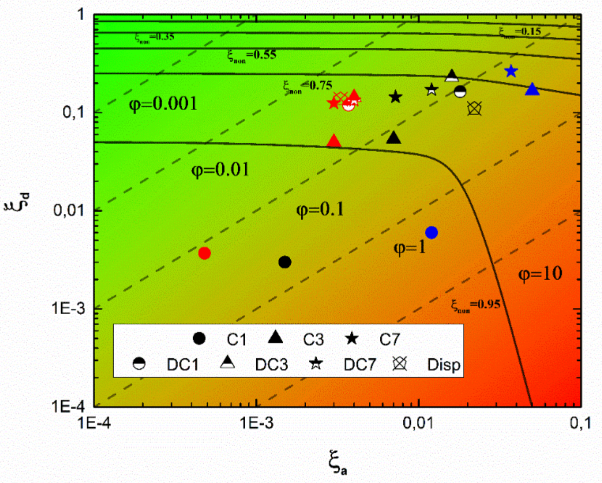

Figure 4.9: Calculated dispersion parameters for each condition. Solid lines indicate the non-percolated area and dashed lines the aggregate ratio. The green-coloured areas correspond to well dispersed materials and the red regions to poorly dispersed ones. Red, black and blue symbols denote 0.05, 0.1 and 0.3 wt %, respectively.

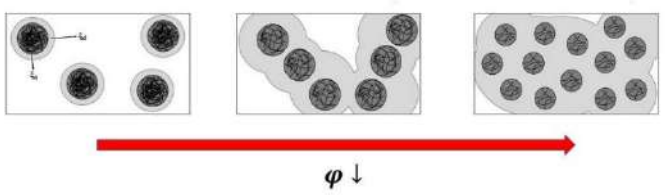

Figure 4.10: Schematics of dispersion state for (left) low ξ_a and high φ, (center) medium ξ_a and φ and (right) high ξ_a and low φ.

In addition, by observing the fractured surface in the FEG-SEM images Figure 4.11, the agglomerated areas, occupying a small volume fraction of the material, show a higher concentrated distribution of CNTs at low steps of the three roll milling process (Figure 4.11 (a)) in comparison to high-step three roll milling, in which well dispersed regions are more common (Figure 4.11 (b) and (c)). This means that CNTs are more entangled in the case of low steps and there is a significant decrease in the non-percolated area with the number of three roll milling steps, as stated in the theoretical analysis. A similar CNT distribution for high-step three roll milling is observed compared with toroidal stirring (Figure 4.11 (d)), as expected.

Therefore, a good agreement between theoretical predictions and experimental measurements is found. It is important to point out that the determination of dispersion parameters, such as the agglomerate volume fraction or non-percolated area, is not trivial using microscopy analysis. In addition, the dispersion state could change during curing due to a re-aggregation of agglomerates [46,47]. However, the results found in the literature for a more detailed microscopy analysis [48–50] also show good agreement with predictions based on this novel analytical model, indicating an increase in well dispersed areas with the addition of proper dispersion procedures.

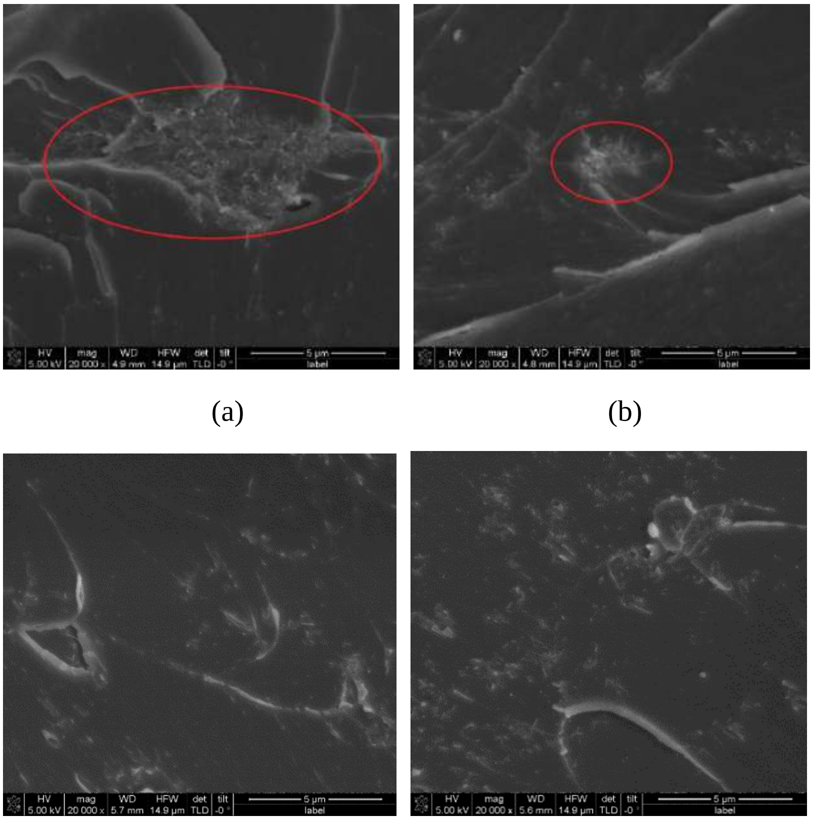

(a) (b)

(c) (d)

Figure 4.11: FEG-SEM images of fractured surface at (a) C1, (b) C3, (c) C7 and (d) DC7 0.05 wt % CNT. Red areas indicate the presence of aggregates.

4.4 Conclusions

Experimental measurements and theoretical studies were carried out to determine the crucial parameters that define electrical conductivity and – especially – the strain monitoring properties of CNT/epoxy nanocomposites. To achieve this, CNT nanocomposites were produced by two dispersion techniques under varying process conditions and their electrical conductivity and strain monitoring capabilities were determined while the CNT dispersion state was observed using transmitted optical microscopy. In addition, a novel analytical model has been proposed to calculate electrical conductivity and electromechanical properties. This model uses three descriptive parameters of the aggregation state: the aggregate and dispersed volume fractions and the non-percolated areas.

From the experimental measurements, it was found that electrical conductivity increases drastically from one to three cycles of three roll milling. The addition of a toroidal stirring step does not cause significant changes at seven cycles of three roll milling. The highest sensitivities were achieved with seven cycle three roll milling at lower contents due to a significant enhancement of CNT dispersion. However, at higher contents, the effect of three roll milling process can be negative due to a more prevalent CNT breakage effect induced by higher CNT interactions. In this case. It is also observed that toroidal stirring does not drastically improve the sensitivity obtained with three roll milling. From the proposed model, it was found that electrical conductivity increases with agglomerate volume fraction and, given the same aggregate fraction, is improved with higher fractions of well dispersed CNTs, which explains the positive effect of three roll milling on electrical conductivity. Furthermore, the aggregate ratio was found to be the main parameter determining the sensitivity capabilities of CNT nanocomposites. Highest sensitivities were achieved for well dispersed materials in which there were no preferential electrical pathways. Moreover, inter-particle distance was also found to be a relevant parameter for electrical properties and a simple, but effective, correlation with CNT content was proposed. It was pointed out that there is an optimal value of inter-particle distance at which sensitivity is the highest, depending on the aggregate ratio. Thus, from these results, it is possible to select the optimum process conditions to achieve the highest sensitivities.

To conclude, experimental measurements and theoretical predictions were compared and showed good agreement. Thus, the potential and applicability of the analytical model proposed was demonstrated.

Acknowledgements

This work was supported by the Ministerio de Economía y Competitividad of Spanish Government [Project MAT2013-46695-C3-1-R] and Comunidad de Madrid Government [Project P2013/MIT-2862]. The authors wish to thank Proof-Reading-Service.com for editing a version of this manuscript.

4.5 References

[1] Iijima S. Helical Microtubules of Graphitic Carbon. Nature 1991;354(6348):56-58.

[2] Ruoff RS, Lorents DC. Mechanical and thermal properties of carbon nanotubes. carbon 1995;33(7):925-930.

[3] Wong EW, Sheehan PE, Lieber CM. Nanobeam mechanics: Elasticity, strength, and toughness of nanorods and nanotubes. Science 1997;277(5334):1971-1975.

[4] Xie S, Li W, Pan Z, Chang B, Sun L. Mechanical and physical properties on carbon nanotube. Journal of Physics and Chemistry of solids 2000;61(7):1153-1158.

[5] Yu MF, Lourie O, Dyer MJ, Moloni K, Kelly TF, Ruoff RS. Strength and breaking mechanism of multiwalled carbon nanotubes under tensile load. Science 2000;287(5453):637-640.

[6] Peng B, Locascio M, Zapol P, Li S, Mielke SL, Schatz GC, Espinosa HD. Measurements of near-ultimate strength for multiwalled carbon nanotubes and irradiation-induced crosslinking improvements. Nature nanotechnology 2008;3(10):626-631.

[7] Deheer W, Bacsa W, Chatelain A, Gerfin T, Humphreybaker R, Forro L, Ugarte D. Aligned Carbon Nanotube Films - Production and Optical and Electronic-Properties. Science 1995;268(5212):845-847.

[8] Bao W, Meguid S, Zhu Z, Meguid M. Modeling electrical conductivities of nanocomposites with aligned carbon nanotubes. Nanotechnology 2011;22(48):485704.

[9] Allaoui A, Bai S, Cheng H, Bai J. Mechanical and electrical properties of a MWNT/epoxy composite. Composites Sci Technol 2002;62(15):1993-1998.

[10] Martin C, Sandler J, Shaffer M, Schwarz M, Bauhofer W, Schulte K, Windle A. Formation of percolating networks in multi-wall carbon-nanotube–epoxy composites. Composites Sci Technol 2004;64(15):2309-2316.

[11] Kim YJ, Shin TS, Do Choi H, Kwon JH, Chung Y, Yoon HG. Electrical conductivity of chemically modified multiwalled carbon nanotube/epoxy composites. Carbon 2005;43(1):23-30.

[12] Bryning MB, Islam MF, Kikkawa JM, Yodh AG. Very Low Conductivity Threshold in Bulk Isotropic Single-Walled Carbon Nanotube–Epoxy Composites. Adv Mater 2005;17(9):1186-1191.

[13] Hu N, Masuda Z, Yan C, Yamamoto G, Fukunaga H, Hashida T. The electrical properties of polymer nanocomposites with carbon nanotube fillers. Nanotechnology 2008;19(21):215701.

[14] Thostenson ET, Chou T. Carbon nanotube networks: Sensing of distributed strain and damage for life prediction and self healing. Adv Mater 2006;18(21):2837-+.

[15] Li C, Thostenson ET, Chou T. Sensors and actuators based on carbon nanotubes and their composites: A review. Composites Sci Technol 2008;68(6):1227-1249.

[16] Hu N, Karube Y, Arai M, Watanabe T, Yan C, Li Y, Liu Y, Fukunaga H. Investigation on sensitivity of a polymer/carbon nanotube composite strain sensor. Carbon 2010;48(3):680-687.

[17] Heeder NJ, Shukla A, Chalivendra V, Yang S, Park K. Electrical Response of Carbon Nanotube Reinforced Nanocomposites Under Static and Dynamic Loading. Exp Mech 2012;52(3):315-322.

[18] Sandler J, Kirk J, Kinloch I, Shaffer M, Windle A. Ultra-low electrical percolation threshold in carbon-nanotube-epoxy composites. Polymer 2003;44(19):5893-5899.

[19] Kovacs JZ, Velagala BS, Schulte K, Bauhofer W. Two percolation thresholds in carbon nanotube epoxy composites. Composites Sci Technol 2007;67(5):922-928.

[20] Bauhofer W, Kovacs JZ. A review and analysis of electrical percolation in carbon nanotube polymer composites. Composites Sci Technol 2009;69(10):1486-1498.

[21] Kale S, Sabet FA, Jasiuk I, Ostoja-Starzewski M. Effect of filler alignment on percolation in polymer nanocomposites using tunneling-percolation model. J Appl Phys 2016;120(4):045105.

[22] Cui S, Canet R, Derre A, Couzi M, Delhaes P. Characterization of multiwall carbon nanotubes and influence of surfactant in the nanocomposite processing. Carbon 2003;41(4):797-809.

[23] Li J, Ma PC, Chow WS, To CK, Tang BZ, Kim J. Correlations between percolation threshold, dispersion state, and aspect ratio of carbon nanotubes. Advanced Functional Materials 2007;17(16):3207-3215.

[24] Bao W, Meguid S, Zhu Z, Pan Y, Weng G. A novel approach to predict the electrical conductivity of multifunctional nanocomposites. Mech Mater 2012;46:129-138.

[25] Wang Y, Weng GJ, Meguid SA, Hamouda AM. A continuum model with a percolation threshold and tunneling-assisted interfacial conductivity for carbon nanotube-based nanocomposites. J Appl Phys 2014;115(19):193706.

[26] Li J, Östling M. Conductivity scaling in supercritical percolation of nanoparticles–not a power law. Nanoscale 2015;7(8):3424-3428.

[27] Hu N, Karube Y, Yan C, Masuda Z, Fukunaga H. Tunneling effect in a polymer/carbon nanotube nanocomposite strain sensor. Acta Materialia 2008;56(13):2929-2936.

[28] Kuronuma Y, Takeda T, Shindo Y, Narita F, Wei Z. Electrical resistance-based strain sensing in carbon nanotube/polymer composites under tension: Analytical modeling and experiments. Composites Sci Technol 2012;72(14):1678-1682.

[29] De Vivo B, Lamberti P, Spinelli G, Tucci V, Vertuccio L, Vittoria V. Simulation and experimental characterization of polymer/carbon nanotubes composites for strain sensor applications. J Appl Phys 2014;116(5):054307.

[30] Li C, Thostenson ET, Chou T. Dominant role of tunneling resistance in the electrical conductivity of carbon nanotube-based composites. Appl Phys Lett 2007;91(22):223114.

[31] Takeda T, Shindo Y, Kuronuma Y, Narita F. Modeling and characterization of the electrical conductivity of carbon nanotube-based polymer composites. Polymer 2011;52(17):3852-3856.

[32] Rahman R, Servati P. Effects of inter-tube distance and alignment on tunnelling resistance and strain sensitivity of nanotube/polymer composite films. Nanotechnology 2012;23(5):055703.

[33] Sanchez-Romate XF, Jimenez-Suarez A, Sanchez M, Guemes A, Urena A. Novel approach to percolation threshold on electrical conductivity of carbon nanotube reinforced nanocomposites. RSC Advances 2016;6(49):43418-43428.

[34] Sanchez M, Rams J, Campo M, Jimenez-Suarez A, Urena A. Characterization of carbon nanofiber/epoxy nanocomposites by the nanoindentation technique. Composites Part B-Engineering 2011;42(4):638-644.

[35] Jimenez-Suarez A, Campo M, Sanchez M, Romon C, Urena A. Influence of the functionalization of carbon nanotubes on calendering dispersion effectiveness in a low viscosity resin for VARIM processes. Composites Part B-Engineering 2012;43(8):3482-3490.

[36] Fu S, Chen Z, Hong S, Han CC. The reduction of carbon nanotube (CNT) length during the manufacture of CNT/polymer composites and a method to simultaneously determine the resulting CNT and interfacial strengths. Carbon 2009;47(14):3192-3200.

[37] Kovacs J, Bauhofer W. The influence of the dispersion quality of carbon nanotubes in an epoxy matrix on the electrical conductivity of the composite. Proceeding of the 17th International Conference on Composite Materials, 2009.

[38] Shi D, Feng X, Huang YY, Hwang K, Gao H. The effect of nanotube waviness and agglomeration on the elastic property of carbon nanotube-reinforced composites. Journal of Engineering Materials and Technology 2004;126(3):250-257.

[39] Jarali CS, Basavaraddi SR, Kiefer B, Pilli SC, Lu YC. Modeling of the effective elastic properties of multifunctional carbon nanocomposites due to agglomeration of straight circular carbon nanotubes in a polymer matrix. Journal of Applied Mechanics 2014;81(2):021010.

[40] Chakraborty AK, Plyhm T, Barbezat M, Necola A, Terrasi GP. Carbon nanotube (CNT)–epoxy nanocomposites: a systematic investigation of CNT dispersion. Journal of Nanoparticle Research 2011;13(12):6493-6506.

[41] Gong S, Zhu Z, Haddad E. Modeling electrical conductivity of nanocomposites by considering carbon nanotube deformation at nanotube junctions. J Appl Phys 2013;114(7):074303.

[42] Li H, Lu W, Li J, Bai X, Gu C. Multichannel ballistic transport in multiwall carbon nanotubes. Phys Rev Lett 2005;95(8):086601.

[43] Gao R, Pan Z, Wang Z. Work function at the tips of multiwalled carbon nanotubes. Appl Phys Lett 2001;78(12):1757-1759.

[44] Shindo Y, Kuronuma Y, Takeda T, Narita F, Fu S. Electrical resistance change and crack behavior in carbon nanotube/polymer composites under tensile loading. Composites Part B-Engineering 2012;43(1):39-43.

[45] Yamamoto S, Matsuoka T. Dynamic Simulation of Flow-Induced Fiber Fracture. Polym Eng Sci 1995;35(12):1022-1030.

[46] Chapartegui M, Markaide N, Florez S, Elizetxea C, Fernandez M, Santamaria A. Curing of epoxy/carbon nanotubes physical networks. Polym Eng Sci 2012;52(3):663-670.

[47] Aravand M, Lomov SV, Verpoest I, Gorbatikh L. Evolution of carbon nanotube dispersion in preparation of epoxy-based composites: From a masterbatch to a nanocomposite. Express Polymer Letters 2014;8(8):596-608.

[48] Bakshi SR, Batista RG, Agarwal A. Quantification of carbon nanotube distribution and property correlation in nanocomposites. Composites Part A: Applied Science and Manufacturing 2009;40(8):1311-1318.

[49] Sul IH, Youn JR, Song YS. Quantitative dispersion evaluation of carbon nanotubes using a new analysis protocol. Carbon 2011;49(4):1473-1478.

[50] Tyson BM, Al-Rub RKA, Yazdanbakhsh A, Grasley Z. A quantitative method for analyzing the dispersion and agglomeration of nano-particles in composite materials. Composites Part B: Engineering 2011;42(6):1395-1403.

Chapter 5: Highly Sensitive Strain Gauges with Carbon Nanotubes: From Bulk Nanocomposites to Multifunctional Coatings for Damage Sensing

Xoan F. Sánchez-Romate[a,b,*], *Rocío Moriche*[b] , *Alberto Jiménez-Suárez*[b], *María Sánchez*[b], *Silvia G. Prolongo*[b], *Alfredo Güemes*[a] *and Alejandro Ureña*[b]

Published in Appl Surf Sci 424 (2017) 213-221

[a] Department of Aerospace Materials and Processes, Escuela Técnica Superior de Ingenieros Aeronáuticos, Universidad Politécnica de Madrid, Plaza del Cardenal Cisneros 3, 28040 Madrid, Spain

[b] Materials Science and Engineering Area, Escuela Superior de Ciencias Experimentales y Tecnología, Universidad Rey Juan Carlos, Calle Tulipán s/n, 28933 Móstoles (Madrid), Spain

* Corresponding author: xoan.fernandez.sanchezromate@urjc.es Tel: +34 91 488 82 52

Sensing capabilities of carbon nanotube (CNT) epoxy materials have been studied in order to develop multifunctional coatings for damage detection. For that purposes CNT epoxy mixtures have been manufacturing using toroidal stirring. The microstructural characterization of CNT dispersion has been carried out by optical microscopy, showing the good homogenization effect induced by toroidal stirring. Then, electromechanical tests have been carried out on bulk nanocomposites and strain gauges. From tensile tests, it has been noticed that the Gauge Factor (GF) of strain gauges is much higher than those of bulk nanocomposites and conventional metallic gauges. Bending tests, which gauges made over tensile or compressive faces of the samples show that strain gauges have different behaviors while bulk materials show similar ones due to electrical volume interactions, proving the potential of strain gauges for monitoring complex load states. Damage sensing of CNT/epoxy materials has been also proved by inducing artificial defects on a monitored coating as changes in electrical resistance related to damage size. Thus damage detection, location and quantification have been achieved.

Keywords: carbon nanotube, multifunctional coating, SHM, damage sensing, electrical properties

5.1 Introduction

During the last years, the increasing use of polymer reinforced composite materials due to their better specific mechanical properties and corrosion behavior in comparison to many traditional alloys has led to the development of new technologies to overcome some of their main limitations such as their poor damage tolerance, transversal electrical and thermal conductivity or fire resistance.

Therefore, carbon nanoparticles are attracting the interest of many researchers due to their exceptional properties [1-5]. In fact, some studies have shown that their addition to fiber reinforced polymers (FRPs) enhances their mechanical, electrical and interfacial properties [6-10].

The enhancement of electrical conductivity is based on the addition of carbon nanoparticles, which induces the creation of an electrical network inside an insulator matrix making it electrically conductive [11-14]. This is a key point for their use in applications such as lightning strike protection or Structural Health Monitoring (SHM) systems [15-18].

In this regard, this work aims to develop carbon nanotube reinforced epoxy films as a coating in order to create multifunctional coatings. The main objective is the creation of an electrically conductive coating with the capability of strain monitoring and damage sensing.

To date, sensing capabilities of CNTs have been demonstrated as they exhibit a much higher Gauge Factor (GF) than other conventional strain gauges due to their piezoresistive behavior [19-22]. Thus, the use of CNT reinforced polymers as strain monitoring systems is being widely investigated [23-25].

This work presents a detailed study on sensing capabilities of CNT strain gauges. The main novelty of this study is the analysis of sensitivities at different load states, from tensile to bending tests (in both tensile and compression faces) and the comparison between CNT reinforced bulk nanocomposites and multifunctional coatings, proving the potential of the last ones.

Dispersion state of nanoparticles has a dominant role on electrical properties of nanocomposites [26,27]. This is due to the influence that aggregation state of CNTs has on the creation of electrical networks. Higher aggregates and entanglement leads to a higher percolation threshold [28,29], defined as the point in which insulator material becomes electrically conductive. The percolation threshold determination is a key point for sensing capabilities. It is known that the highest sensitivities are achieved for contents near percolation onset [30-32], due to the dominant effect that tunneling distance between adjacent CNTs has on electromechanical behavior of nanocomposites [33]. For these reasons, it is important to properly characterize the dispersion state of the material in order to achieve the best sensing results.

This microstructural characterization is carried out by means of transmission optical microscopy (TOM) analysis of manufactured CNT-epoxy dispersions prior to curing. In addition, a profilometry analysis of strain gauges is also carried out in order to characterize thickness and roughness of multifunctional coatings.

Finally, damage sensing capabilities are then proved on a CNT-epoxy film applied over a GFRP substrate. Firstly, an electrical conductivity mapping of the coating is carried out in order to know the homogenization degree of the CNT dispersion which is a key point on sensing capabilities as commented before. Then, many artificial defects are induced over the coating while their electrical response is measured by different channels. This allows to build a new 2D mapping of the electrical resistance of the damaged specimen. The aim is to detect possible changes on the electrical response and correlate them to the induced damage. It is important to notice that the use of 2D mapping is currently attracting the interest of many researches as it gives a more detailed information about the health of a structure [34,35].

5.2 Materials and Methods

5.2.1 Materials

Nanocomposites were manufactured using multiwall carbon nanotubes (MWCNTs) embedded in an epoxy resin. MWCNTs are supplied by Nanocyl with a commercial name NC7000, an average diameter of 11 nm and a length up to 2 μm.

The epoxy resin was a low viscosity DGBEA with a commercial formula called Araldite LY 556, cured with an aromatic amine Araldite XB3473; supplied by Hunstman.

5.2.2 Manufacturing

The epoxy mixture with 0.1 wt. % CNT was prepared by toroidal stirring for 15 min, using a Dispermat dissolver at 6000 rpm with a rotating disc of 15 mm diameter. To evacuate the air entrapped in the epoxy mixture, a degasification step was necessary at 80 ºC to reduce mixture viscosity. Degasification was carried out under vacuum during 15 min. After that, XB3473 hardener was added in a weight ratio of 100:23 (monomer:hardener). Then, to manufacture strain gauges and multifunctional coatings, CNT/epoxy mixture was applied manually, using an applicator, over a GFRP substrate in order to create a thin film, while having a good control of the thickness. Finally, cure cycle was carried out in an oven at 140 ºC during 8 h. In addition, bulk nanocomposites were also manufactured at the same conditions in order to compare them to strain gauges.

5.2.3 Microstructural analysis

Analysis of uncured CNT/epoxy dispersions has been performed by an optical microscope Leica equipped with a camera Nikon Coolpiz 990 as received and after toroidal stirring.

Surface roughness and thickness of strain gauges has been measured by using an optical profilometer ZETA Z-20 in three representative specimens.

5.2.4 Monitoring Tests

The strain monitoring capabilities of the CNT/epoxy materials have been analyzed in tensile and bending tests. Electrical resistance was simultaneously registered by using a hardware called Agilent 34410A. For that purpose, electrodes were made of copper wires attached with silver ink and sealed to the surface with an adhesive. This arrangement has proved its reliability to give accurate measurements of electromechanical properties [36,37].

Tensile and bending tests were carried out using 6 samples for bulk materials and 4 in the case of strain gauges following the ASTM D638 and ASTM D790 standards respectively. In tensile tests, electrodes were placed at 30 mm distance, while on bending tests, they were placed at 15 mm on both tensile and compressive faces for bulks (Figure 5.1 (a)) and CNT/epoxy strain gauges (Figure 5.1 (b)).

Damage sensing capabilities of multifunctional CNT/epoxy coatings were tested by electrical resistance measurements before and after damage was induced on a CNT/epoxy coated GFRP substrate of 100×180 mm^2.

(a)

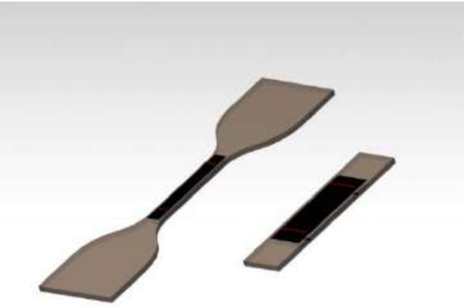

(b)

Figure 5.1: Schematic of electrode disposition on monitoring tests for (a) bulk nanocomposites and (b) CNT/epoxy strain gauges.

5.3 Results and discussion

5.3.1 Microstructural characterization of CNT epoxy system

As commented before, the analysis of the dispersion state is a crucial point in order to properly characterize the electrical properties and, thus, the sensing capabilities of CNT/epoxy materials. It is important to notice that heterogeneities are correlated to variability on tunneling distance between CNTs. Thus, it is necessary to achieve a good dispersion state in order to achieve strain sensors with repetitive sensing characteristics. In this regard, toroidal stirring is selected as the dispersion procedure as it is less time consumption than other techniques such as three roll milling and leads to a good dispersion state [38-40].

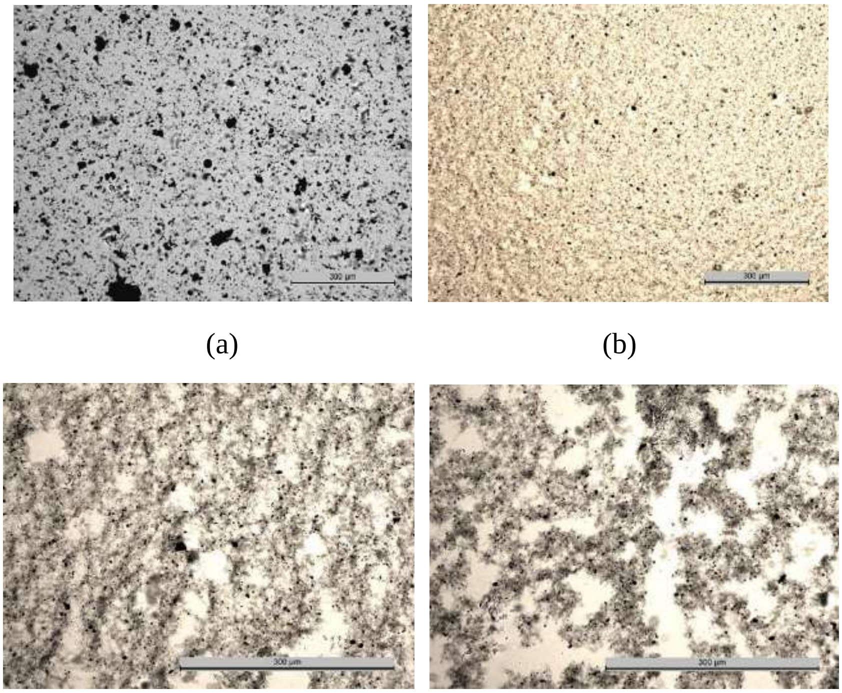

(a) (b)

(c) (d)

Figure 5.2: TOM images of 0.1 wt. % CNT reinforced epoxy resin (a) as received and after toroidal sittirng at (b) lower and, (c) and (d), higher mangnifications.

Figure 5.2 shows TOM images of the CNT mixture before and after toroidal stirring. It is observed that toroidal stirring improves the CNT dispersion state, due to the effect that the rotating disc has on CNTs, leading to a breakage of larger agglomerates and inducing an homogenization effect (Figure 5.2 (b)), as stated in previous studies [29]. These studies also show that CNTs present higher waviness degree when using toroidal stirring in comparison to other dispersion procedures. However, many heterogeneities are also observed at in the CNT dispersion after toroidal stirring at higher magnifications (Figure 5.2 (c)), which induce the creation of percolating networks in preferential directions (Figure 5.2 (d)). These heterogeneities could lead, thus, to different sensing behaviors.

In addition, Figure 5.3 shows an image of the strain gauge profile carried out by optical profilometry. It is shown that the mean thickness of the film is ~300 μm as shown in Figure 5.3 (a) with a mean surface roughness of 0.46 μm, resulting in a highly smooth surface as observed in Figure 5.3 (b).

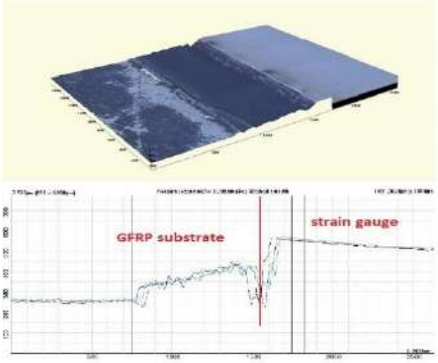

(a)

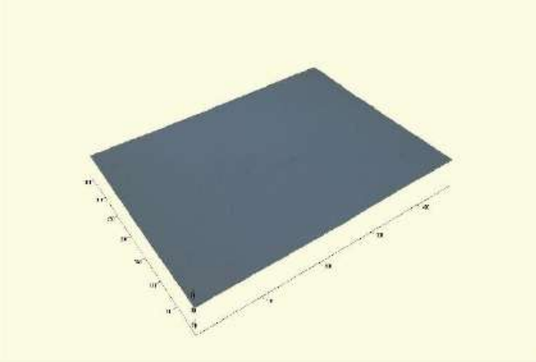

(b)

Figure 5.3: Optical profilometer images of the (a) thickness profile and (b) strain gauge surface.

5.3.2 Electromechanical tests of CNT-epoxy strain gauges

In order to characterize the electromechanical behavior of CNT-epoxy strain gauges, monitoring tensile tests have been carried out on strain gauges and CNT-epoxy bulk nanocomposites to compare sensitivities of both systems. In this regard, GF can be defined as normalized resistance change, $\Delta R/R_0$, divided by the applied strain, ε, as shown in the following expression:

$$GF = \frac{\Delta R/R_0}{\varepsilon} \tag{5.1}$$

Electromechanical curves of bulk and CNT films are shown in Figure 5.4 (a) It is observed that GF is much higher in the case of the strain gauges with a more accused exponential effect as Figure 5.4 (b) indicates. This is probably due to a higher effect that breakage of electrical pathways has on thin films in comparison to bulk nanocomposites which leads to a more prevalent increase on tunneling distance and, therefore, electrical resistance [16,42]. In both cases, it is observed a general increase on the GF with applied strain, due to the exponential behavior that electrical resistance follows. It is important to point out that GF of CNT strain gauges, especially at high applied strain levels, are significantly higher than those achieved on conventional metallic strain gauges [43].

However, it is particularly interesting to compare electromechanical behavior of both systems (bulk and strain gauges) on flexure tests in which local tensile and compressive loads are involved. Therefore, bending tests have been carried out while the electrical response of the specimens has been measured. The main goal is to show the potential of CNT-epoxy films in comparison to conventional bulk nanocomposites for complex load states in which two or more phenomena are present.

For these purposes, both tensile and compressive faces have been monitored during the flexure test for bulk nanocomposites and multifunctional strain gauges.

Figure 5.5 shows the electromechanical behavior at bending tests for bulk CNT reinforced epoxy. Firstly, a significant decrease on the GF is observed in comparison to tensile tests. This is due to the effect of both tensile and compression faces which induces a combined effect between the breakage and creation of new electrical pathways, in agreement with other sensing studies for GNP nanocomposites [36].

In addition, it is important to notice that there is not a distinguishable difference between electromechanical behavior on tensile and compressive face in the case of bulk materials as could be expected. This is due to the similar interaction volumes, as shown in Figure 5.6, in both faces. Thus, tensile subjected face has an influence over compression subjected face electromechanical behavior and vice versa. Therefore, GF for both tensile and compressive faces are very similar, as shown in Figure 5.5 (b).

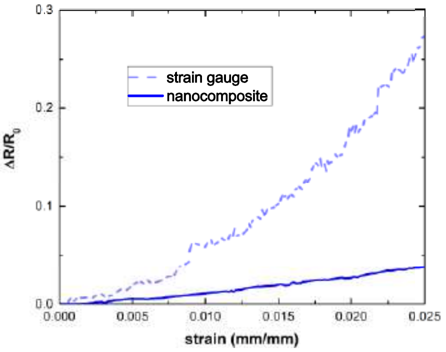

(a)

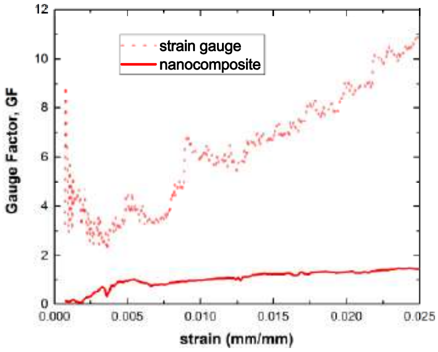

(b)

Figure 5.4: Electromechanical curves at tensile tests for both bulk material and strain gauges representing (a) the normalized resistance and (b) GF as a function of strain.

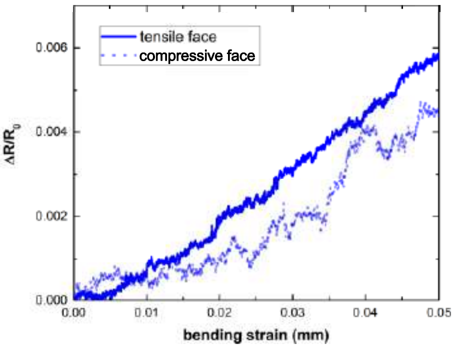

(a)

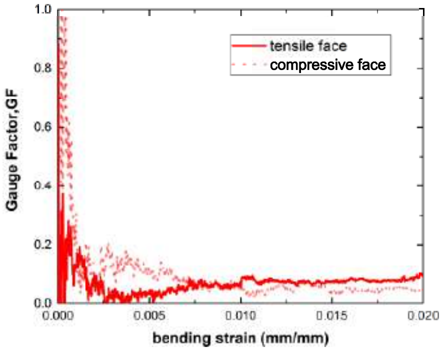

(b)

Figure 5.5: Electromechanical curves at bending tests of bulk material representing (a) the normalized resistance and (b) GF as a function of strain.

On the other hand, Figure 5.7 shows the electromechanical behavior of CNT/epoxy strain gauges for both compression and tensile faces. At tensile subjected face, there is an increase on electrical resistance as the tunneling distance increases following approximately an exponential law such as in tensile tests. However, at compression, there is a decrease on tunneling distance at the beginning which induces also a decrease on electrical resistance due a rearrangement of electrical network [44,45]. For higher strain levels, buckling effects could lead to a breakage of electrical pathways, which would induce a stabilization or even an increase on electrical resistance [36,46]. In this case, it is also observed that GF increases with applied strain at tensile face while at compression there is a decreasing on GF because of the above mentioned effect of breakage of electrical pathways due to local buckling. Therefore, it is possible to clearly distinguish two different electromechanical behaviors as a function of applied load, unlike bulk CNT/epoxy which shows a similar behavior in both cases. These different behaviors are due to the fact that there is not an interaction volume between tensile and compressive faces. In addition, it is important to point out that electrical response on tensile face tests is more stable than in compression due to the fact that there is not breakage and creation of electrical pathways. This is also reflected on the variation of GF with applied strain (Figure 5.7 (b)).

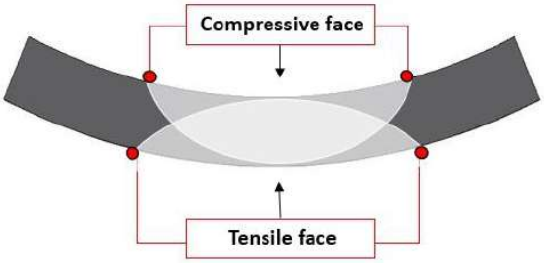

Figure 5.6: Schematic of the influence volumes of tensile and compressive faces during bending on bulk nanocomposites.

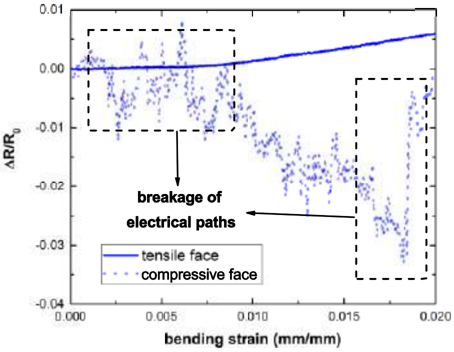

(a)

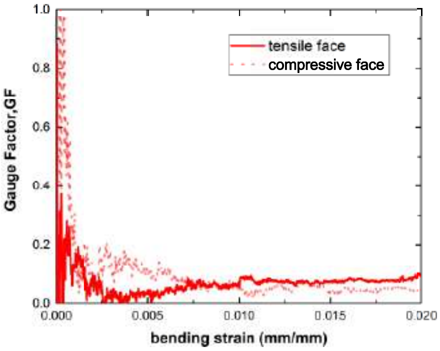

(b)

Figure 5.7: Electromechanical curves at bending tests of strian gauges representing (a) the normalized resistance and (b) GF as a function of strain.

Therefore, sensitivity of films shows their potential as strain gauges in comparison to bulk nanocomposites, especially in the case of bending tests, showing two different electromechanical behaviors depending upon the load state.

5.3.3 Surface mapping and damage detection

Once electromechanical capabilities of strain gauge sensors based on CNT reinforced epoxy films have been demonstrated, it is necessary to prove damage sensing capabilities of these materials.

The aim is to study the electrical properties of these developed strain gauges based on CNTs and correlate them to the level of damage. Thus, in order to achieve that, a gridded specimen has been manufactured by manually application of CNT-epoxy films over a GFRP substrate. Electrode disposition is shown in Figure 5.8 (a), indicated by red points.

In order to properly calculate electrical conductivity through the specimen, electrical measurements have been carried out between the electrodes and conductivity has been calculated at the center of each grid by interpolating the experimental values obtained in each adjacent point of the grid as follows:

$$c_{mn} = \frac{1}{N} \cdot \left(\sum_{i=m}^{m+1} a_{in} + \sum_{l=n}^{n+1} b_{ml} \right) \tag{5.2}$$

Being a and b the values of the electrical resistance in horizontal and vertical channels respectively, N the number of surrounding channels, and c the resulting resistance at the center of the grid, as shown in Figure 5.8 (b). Thus, electrical conductivity will be:

$$\sigma_{mn} = \frac{l}{c_{mn} \cdot A} \tag{5.3}$$

In which l is the channel length, set as 20 mm and A the section area calculated has $A = b \cdot t$, being b the channel influence width, also set as 20 mm and t the thickness of the CNT/epoxy film, that is 300 µm.

This is a first estimation of electrical conductivity which gives a very accurate idea of the electrical properties of the specimen. Figure 5.9 shows the mapping of the electrical conductivity. It is observed that it ranges between

0.01-0.02 S/m. This is in good agreement with other studies carried out for similar epoxy-CNT systems using the same dispersion procedure and indicates that it is near percolation threshold [29].

The differences on electrical conductivity along the specimen are correlated to the CNT dispersion state. Although, as commented before, toroidal stirring provides a good homogenization of CNT dispersions, as shown before in Figure 5.2 there are still heterogeneities which could induce a CNT re-aggregation during curing process [28,47,48] which leads to a less homogeneous CNT dispersion along the coating and thus, to a more significant differences on electrical conductivity.

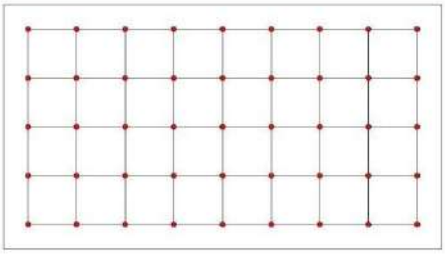

(a)

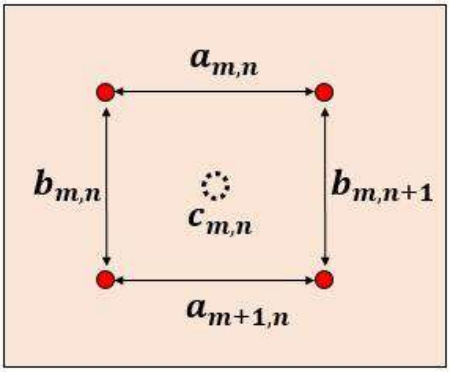

(b)

Figure 5.8: Schematic of (a) electrode disposition on the CNT/epoxy coating and (b) channel configuration used for calculations.

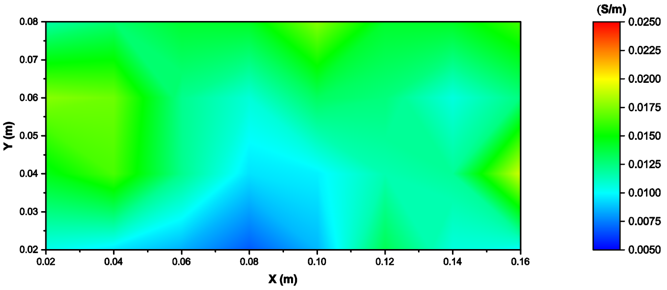

Figure 5.9: 2D electrical conductivity mapping of the CNT/epoxy coating.

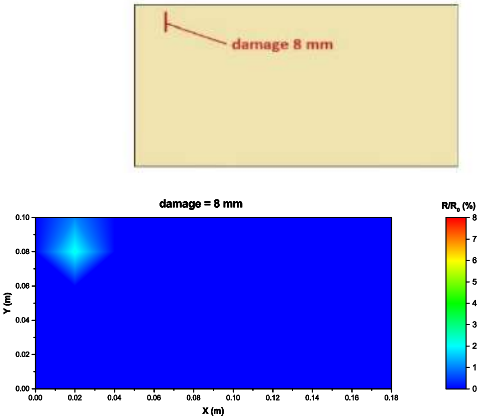

(a)

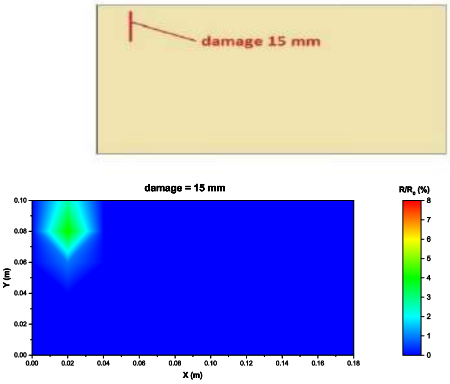

(b)

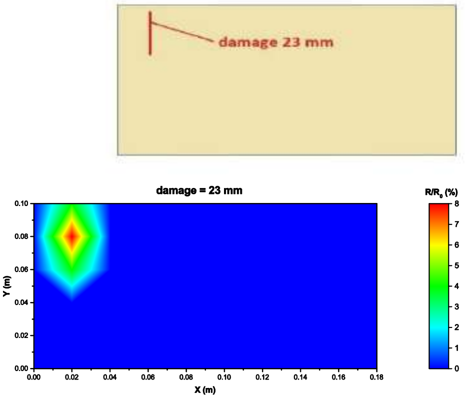

(c)

Figure 5.10: Schematic of defect induced (above) and their corresponding 2D electrical resistance mapping (below) for (a) 8 mm, (b) 15 mm and (c) 23 mm damage length.

Damage sensing capabilities of CNT/epoxy coatings have been characterized by the inclusion of artificial defects along the specimen. Figure 5.10 shows the artificial defects induced and the corresponding electrical response. Changes in electrical resistance have been observed by the inclusion of the different artificial defects. For the damage of 8 mm length (Figure 5.10 (a)), it is observed a 2 % increasing on electrical resistance. This is due to the breakage of electrical pathways in the region near the defects. It is noticed, that an increasing on damage length induces a higher increase on resistance (nearly an 8 % for the 23 mm damage, as shown in Figure 5.10 (c)) because the area affected by the damage is also higher and thus, there is a higher breakage of electrical paths. Thus, it is possible to establish a first quantification of damage depending on electrical resistance changes.

Figure 5.11 shows the electrical resistance changes in the two neighboring channels. It is observed that changes in resistance at Channel A are proportional to damage length as the its location is just between the channel electrodes. On the other hand, at Channel B, no changes on electrical resistance are observed when defect length is 8 mm because the location of damage does not affect electrical properties of the neighboring area. However, when defect length is higher, an increase on electrical resistance is noticed also in Channel B even if it is not exactly located between the electrodes because it affects the channel interaction area as shown in Figure 5.12.

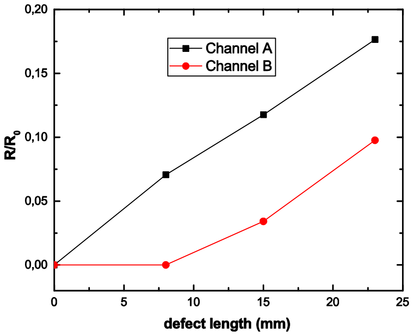

Figure 5.11: Normalized electrical resistance of the two channels surrounding the defect.

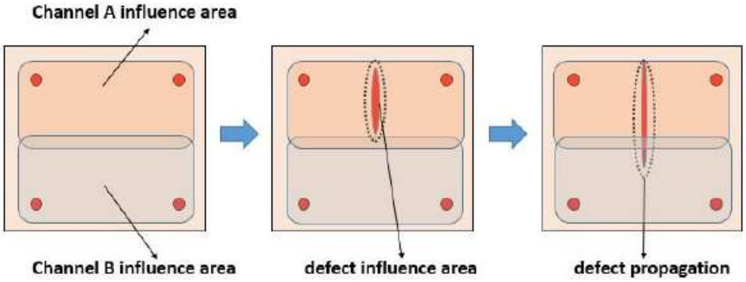

Figure 5.12: Influence of defect length on the electrical measurements of surrounding channels.

These results are in good agreement with other studies [49,50] and prove the sensing capabilities of these materials for damage sensing as their detection, location and a first quantification has been achieved.

5.4 Conclusions

Strain and damage sensing capabilities of multifunctional CNT/epoxy coatings have been studied and a comparison to bulk nanocomposites monitoring capacities has been carried out in order to prove their potential as sensors.

From electromechanical tests, it has been observed that strain gauges have much higher values of Gauge Factor than bulk materials. This is due to the more prevalent effect of breakage of electrical pathways on thin films in comparison to bulk CNT reinforced epoxy which leads to higher sensitivity. From bending tests, it has been shown that bulk nanocomposites present a very similar electromechanical behavior in both tensile and compressive faces due to the interaction volume involved on the electrical measurement at both faces. However, strain gauges show two clearly distinguishable behaviors, with an increase on electrical resistance at tensile face and an initial decrease and later increase under compression, avoiding the interaction effects in bulk nanocomposites.

In addition, damage sensing capabilities of a CNT/epoxy coating have been demonstrated. Artificial defects have been induced and an electrical 2D mapping of the pristine and damaged surface has been carried out. Damage detection has been correlated to changes on electrical resistance, being the variation of normalized resistance higher with the damage size. Thus, detection, location and a first quantification of damage has been achieved.

Acknowledgements

The authors would like to acknowledge the Ministerio de Economía y Competitividad of Spanish Government [Project MAT2013-46695-C3-1-R] and Comunidad de Madrid Government [Project P2013/MIT-2862] for their financial support.

5.5 References

[1] R.S. Ruoff, D.C. Lorents, Mechanical and thermal properties of carbon nanotubes, Carbon. 33 (1995) 925-930.

[2] M.F. Yu, O. Lourie, M.J. Dyer, K. Moloni, T.F. Kelly, R.S. Ruoff, Strength and breaking mechanism of multiwalled carbon nanotubes under tensile load, Science. 287 (2000) 637-640. doi:10.1126/science.287.5453.637.

[3] S. Stankovich, D.A. Dikin, G.H.B. Dommett, K.M. Kohlhaas, E.J. Zimney, E.A. Stach, R.D. Piner, S.T. Nguyen, R.S. Ruoff, Graphene-based composite materials, Nature. 442 (2006) 282-286. doi:10.1038/nature04969.

[4] C. Gomez-Navarro, M. Burghard, K. Kern, Elastic properties of chemically derived single graphene sheets, Nano Lett. 8 (2008) 2045-2049. doi:10.1021/nl801384y.

[5] M.F.L. De Volder, S.H. Tawfick, R.H. Baughman, A.J. Hart, Carbon Nanotubes: Present and Future Commercial Applications, Science. 339 (2013) 535-539. doi:10.1126/science.1222453.

[6] P. Karapappas, A. Vavouliotis, P. Tsotra, V. Kostopoulos, A. Palpetis, Enhanced fracture properties of carbon reinforced composites by the addition of multi-wall carbon nanotubes, J. Compos. Mater. (2009).

[7] V. Kostopoulos, A. Baltopoulos, P. Karapappas, A. Vavouliotis, A. Paipetis, Impact and after-impact properties of carbon fibre reinforced composites enhanced with multi-wall carbon nanotubes, Compos. Sci. Technol. 70 (2010) 553-563.

[8] B. Ashrafi, J. Guan, V. Mirjalili, Y. Zhang, L. Chun, P. Hubert, B. Simard, C.T. Kingston, O. Bourne, A. Johnston, Enhancement of mechanical performance of epoxy/carbon fiber laminate composites using single-walled carbon nanotubes, Compos. Sci. Technol. 71 (2011) 1569-1578. doi:10.1016/j.compscitech.2011.06.015.

[9] M. Palmeri, K. Putz, T. Ramanathan, L. Brinson, Multi-scale reinforcement of CFRPs using carbon nanofibers, Compos. Sci. Technol. 71 (2011) 79-86.

[10] C. Deng, J. Jiang, F. Liu, L. Fang, J. Wang, D. Li, J. Wu, Influence of carbon nanotubes coatings onto carbon fiber by oxidative treatments combined with electrophoretic deposition on interfacial properties of carbon fiber composite, Appl. Surf. Sci. 357, Part A (2015) 1274-1280. doi:http://dx.doi.org/10.1016/j.apsusc.2015.09.178.

[11] N. Hu, Z. Masuda, C. Yan, G. Yamamoto, H. Fukunaga, T. Hashida, The electrical properties of polymer nanocomposites with carbon nanotube fillers, Nanotechnology. 19 (2008) 215701. doi:10.1088/0957-4484/19/21/215701.

[12] J.R. Potts, D.R. Dreyer, C.W. Bielawski, R.S. Ruoff, Graphene-based polymer nanocomposites, Polymer. 52 (2011) 5-25. doi:10.1016/j.polymer.2010.11.042.

[13] R. Sengupta, M. Bhattacharya, S. Bandyopadhyay, A.K. Bhowmick, A review on the mechanical and electrical properties of graphite and modified graphite reinforced polymer composites, Prog. Polym. Sci. 36 (2011) 638-670. doi:10.1016/j.progpolymsci.2010.11.003.

[14] S.U. Khan, J.R. Pothnis, J. Kim, Effects of carbon nanotube alignment on electrical and mechanical properties of epoxy nanocomposites, Composites Part A. 49 (2013) 26-34. doi:10.1016/j.compositesa.2013.01.015.

[15] E.T. Thostenson, T. Chou, Carbon nanotube networks: Sensing of distributed strain and damage for life prediction and self healing, Adv. Mater. 18 (2006) 2837-+. doi:10.1002/adma.200600977.

[16] N. Hu, Y. Karube, M. Arai, T. Watanabe, C. Yan, Y. Li, Y. Liu, H. Fukunaga, Investigation on sensitivity of a polymer/carbon nanotube composite strain sensor, Carbon. 48 (2010) 680-687. doi:10.1016/j.carbon.2009.10.012.

[17] M. Gagne, D. Therriault, Lightning strike protection of composites, Prog. Aerospace Sci. 64 (2014) 1-16. doi:10.1016/j.paerosci.2013.07.002.

[18] L. Guadagno, M. Raimondo, V. Vittoria, L. Vertuccio, C. Naddeo, S. Russo, B. De Vivo, P. Lamberti, G. Spinelli, V. Tucci, Development of epoxy mixtures for application in aeronautics and aerospace, Rsc Advances. 4 (2014) 15474-15488. doi:10.1039/c3ra48031c.

[19] J. Cao, Q. Wang, H. Dai, Electromechanical properties of metallic, quasimetallic, and semiconducting carbon nanotubes under stretching, Phys. Rev. Lett. 90 (2003) 157601. doi:10.1103/PhysRevLett.90.157601.

[20] C. Stampfer, A. Jungen, R. Linderman, D. Obergfell, S. Roth, C. Hierold, Nano-electromechanical displacement sensing based on single-walled carbon nanotubes, Nano Lett. 6 (2006) 1449-1453. doi:10.1021/nl0606527.

[21] M.A. Cullinan, M.L. Culpepper, Carbon nanotubes as piezoresistive microelectromechanical sensors: Theory and experiment, Phys. Rev. B. 82 (2010) 115428. doi:10.1103/PhysRevB.82.115428.

[22] W. Obitayo, T. Liu, A Review: Carbon Nanotube-Based Piezoresistive Strain Sensors, Journal of Sensors. (2012) 652438. doi:10.1155/2012/652438.

[23] C. Li, E.T. Thostenson, T. Chou, Sensors and actuators based on carbon nanotubes and their composites: A review, Compos. Sci. Technol. 68 (2008) 1227-1249. doi:10.1016/j.compscitech.2008.01.006.

[24] Y. Kuronuma, T. Takeda, Y. Shindo, F. Narita, Z. Wei, Electrical resistance-based strain sensing in carbon nanotube/polymer composites under tension: Analytical modeling and experiments, Compos. Sci. Technol. 72 (2012) 1678-1682. doi:10.1016/j.compscitech.2012.07.001.

[25] B. De Vivo, P. Lamberti, G. Spinelli, V. Tucci, L. Vertuccio, V. Vittoria, Simulation and experimental characterization of polymer/carbon nanotubes composites for strain sensor applications, J. Appl. Phys. 116 (2014) 054307. doi:10.1063/1.4892098.

[26] P. Ma, N.A. Siddiqui, G. Marom, J. Kim, Dispersion and functionalization of carbon nanotubes for polymer-based nanocomposites: A review, Composites Part A. 41 (2010) 1345-1367. doi:10.1016/j.compositesa.2010.07.003.

[27] Y.S. Song, J.R. Youn, Influence of dispersion states of carbon nanotubes on physical properties of epoxy nanocomposites, Carbon. 43 (2005) 1378-1385. doi:10.1016/j.carbon.2005.01.007.

[28] J. Sandler, J. Kirk, I. Kinloch, M. Shaffer, A. Windle, Ultra-low electrical percolation threshold in carbon-nanotube-epoxy composites, Polymer. 44 (2003) 5893-5899. doi:10.1016/S0032-3861(03)00539-1.

[29] X.F. Sanchez-Romate, A. Jimenez-Suarez, M. Sanchez, A. Guemes, A. Ureña, Novel approach to percolation threshold on electrical conductivity of carbon nanotube reinforced nanocomposites, Rsc Advances. 6 (2016) 43418-43428. doi:10.1039/c6ra03619h.

[30] N. Hu, Y. Karube, C. Yan, Z. Masuda, H. Fukunaga, Tunneling effect in a polymer/carbon nanotube nanocomposite strain sensor, Acta Mater. 56 (2008) 2929-2936. doi:10.1016/j.actamat.2008.02.030.

[31] Y. Kuronuma, T. Takeda, Y. Shindo, F. Narita, Z. Wei, Electrical resistance-based strain sensing in carbon nanotube/polymer composites under tension: Analytical modeling and experiments, Compos. Sci. Technol. 72 (2012) 1678-1682. doi:10.1016/j.compscitech.2012.07.001.

[32] B. De Vivo, P. Lamberti, G. Spinelli, V. Tucci, L. Vertuccio, V. Vittoria, Simulation and experimental characterization of polymer/carbon

nanotubes composites for strain sensor applications, J. Appl. Phys. 116 (2014) 054307. doi:10.1063/1.4892098.

[33] C. Li, E.T. Thostenson, T. Chou, Dominant role of tunneling resistance in the electrical conductivity of carbon nanotube-based composites, Appl. Phys. Lett. 91 (2007) 223114. doi:10.1063/1.2819690.

[34] B.R. Loyola, V. La Saponara, K.J. Loh, T.M. Briggs, G. O'Bryan, J.L. Skinner, Spatial Sensing Using Electrical Impedance Tomography, Ieee Sensors Journal. 13 (2013) 2357-2367. doi:10.1109/JSEN.2013.2253456.

[35] T.N. Tallman, S. Gungor, K.W. Wang, C.E. Bakis, Tactile imaging and distributed strain sensing in highly flexible carbon nanofiber/polyurethane nanocomposites, Carbon. 95 (2015) 485-493. doi:10.1016/j.carbon.2015.08.029.

[36] R. Moriche, M. Sanchez, A. Jimenez-Suarez, S.G. Prolongo, A. Ureña, Strain monitoring mechanisms of sensors based on the addition of graphene nanoplatelets into an epoxy matrix, Compos. Sci. Technol. 123 (2016) 65-70. doi:10.1016/j.compscitech.2015.12.002.

[37] R. Moriche, M. Sanchez, S.G. Prolongo, A. Jimenez-Suarez, A. Ureña, Reversible phenomena and failure localization in self-monitoring GNP/epoxy nanocomposites, Compos. Struct. 136 (2016) 101-105. doi:10.1016/j.compstruct.2015.10.006.

[38] J. Sandler, M. Shaffer, T. Prasse, W. Bauhofer, K. Schulte, A. Windle, Development of a dispersion process for carbon nanotubes in an epoxy matrix and the resulting electrical properties, Polymer. 40 (1999) 5967-5971. doi:10.1016/S0032-3861(99)00166-4.

[39] M. Moniruzzaman, F. Du, N. Romero, K.I. Winey, Increased flexural modulus and strength in SWNT/epoxy composites by a new fabrication method, Polymer. 47 (2006) 293-298.

[40] S.G. Prolongo, M. Buron, M.R. Gude, R. Chaos-Moran, M. Campo, A. Ureña, Effects of dispersion techniques of carbon nanofibers on the thermo-physical properties of epoxy nanocomposites, Compos. Sci. Technol. 68 (2008) 2722-2730. doi:10.1016/j.compscitech.2008.05.015.

[41] S. Fernberg, R. Joffe, G. Nilsson, S.S. AB, Strain and damage sensing during loading of carbon nanotube doped composites, (2009).

[42] A.L.W. G.S. Holister, Strain Gauge Technology, Elsevier Applied Science, London, 1982.

[43] S.T. Buschhorn, M.H.G. Wichmann, J. Gehrmann, L. Boeger, K. Schulte, Direction sensitive deformation sensing with CNT/epoxy nanocomposites, Polymer-Based Smart Materials - Processes, Properties and Application. 1134 (2009) 187-192.

[44] N.J. Heeder, A. Shukla, V. Chalivendra, S. Yang, K. Park, Electrical Response of Carbon Nanotube Reinforced Nanocomposites Under Static and Dynamic Loading, Exp. Mech. 52 (2012) 315-322. doi:10.1007/s11340-011-9488-x.

[45] L. Wang, X. Wang, Y. Li, Relation between repeated uniaxial compressive pressure and electrical resistance of carbon nanotube filled silicone rubber composite, Composites Part A. 43 (2012) 268-274. doi:10.1016/j.compositesa.2011.10.017.

[46] M. Chapartegui, N. Markaide, S. Florez, C. Elizetxea, M. Fernandez, A. Santamaria, Curing of epoxy/carbon nanotubes physical networks, Polym. Eng. Sci. 52 (2012) 663-670. doi:10.1002/pen.22131.

[47] M. Aravand, S.V. Lomov, I. Verpoest, L. Gorbatikh, Evolution of carbon nanotube dispersion in preparation of epoxy-based composites: From a masterbatch to a nanocomposite, Express Polym. Lett. 8 (2014) 596-608. doi:10.3144/expresspolymlett.2014.63.

[48] A. Raghavan, S.S. Kessler, C.T. Dunn, D. Barber, S. Wicks, B.L. Wardle, Structural health monitoring using carbon nanotube (CNT) enhanced composites, International Workshop on Structural Health Monitoring (2009).

[49] C. Viets, S. Kaysser, K. Schulte, Damage mapping of GFRP via electrical resistance measurements using nanocomposite epoxy matrix systems, Composites Part B. 65 (2014) 80-88. doi:10.1016/j.compositesb.2013.09.049.

Chapter 6: Development of Bonded Joints Using Novel CNT Doped Adhesive Films: Mechanical and Electrical Properties

Xoan F. Sánchez-Romate[a,b,], Alberto Jiménez-Suárez[b], Javier Molinero[b], María Sánchez[b], Alfredo Güemes[a] and Alejandro Ureña[b]*

Published in Int J Adh Adh 86 (2018) 98-104

[a] Department of Aerospace Materials and Processes, Escuela Técnica Superior de Ingenieros Aeronáuticos, Universidad Politécnica de Madrid, Plaza del Cardenal Cisneros 3, 28040 Madrid, Spain

[b] Materials Science and Engineering Area, Escuela Superior de Ciencias Experimentales y Tecnología, Universidad Rey Juan Carlos, Calle Tulipán s/n, 28933 Móstoles (Madrid), Spain

* Corresponding author: xoan.fernandez.sanchezromate@urjc.es Tel: +34 91 488 82 52

The effect of the addition of carbon nanotubes (CNTs) to adhesive films in composite joints has been studied due to their potential on Structural Health Monitoring (SHM) applications. Carbon nanotube dispersion has been prepared by sonication in an aqueous media using sodium dodecyl sulfate (SDS) as surfactant. Conditions of dispersion procedure have been set up in order to achieve an homogeneous dispersion over the adhesive. Therefore, a study of aqueous dispersions has been carried out by FEG-SEM analysis, proving the disaggregation effect that SDS has on the CNT dispersion and the breakage induced by sonication. By mechanical testing of adhesive joints, it has been observed that the addition of CNTs does not have a significant effect on Lap Shear Strength (LSS), being achieved the best results in the case of dispersions made with 0.25 wt. %. A microstructural study of fracture surfaces shows that the main failure mode is cohesive although in some areas adhesive failure has been observed. In this regard, there is no significant difference between doped and non-doped joints. In addition, electrical conductivity through the bonding line is highly improved, making the adhesive joint electrically conductive, which proves its potential for SHM applications.

Keywords: carbon nanotubes; lap-shear; composites; electrically conductive adhesives; adhesive films

6.1 Introduction

At present, there is an incipient increase in the using of carbon fiber reinforced polymers (CFRPs) composite structures, especially in aircraft components. Their better specific properties lead to a weight reduction, supposing cost saving and energy efficiency.

Thus, as CFRP structures are more often used, it is necessary to design adequate assembly techniques. In this context, adhesive bonding is a very suitable joining technique for this type of structures as it presents many advantages in comparison to bolted joints such as a good distribution of joint stresses and good fatigue and impact characteristics [1]. However, their inspection is often quite difficult and requires the assessment of novel non-destructive and Structural Health Monitoring (SHM) techniques [2,3].

In this regard, the use of carbon nanotubes has increased [4] since they were discovered [5] two decades ago, not only because their exceptional properties [6-8] but also due to the fact that their addition to an insulator material enhances its electrical conductivity by creating an electrical network [9-11]. This makes it possible their use as lightning strike protection materials [12,13] or as strain sensors for SHM applications [14-16].

The aim of this research is to study the effect that the addition of CNTs has on bonded joints made with adhesive films, which is often used on structural applications. To date, there are many researches on paste adhesives doped with CNTs [17-19] showing their potential to improve mechanical properties of adhesive joints. However, their influence on adhesive films remains to be investigated.

CNT dispersions are prepared by means of sonication on an aqueous media and they are placed over the adhesive surface. The disaggregation of larger agglomerates is achieved by the combined effect of the ultrasounds and the addition of a surfactant as it has been proved as an effective way to disaggregate the larger agglomerates [20-22]. In a previous study [23] this method was proved to be an adequate technique to dope the adhesive films in order to ensure electrical conductivity along the bonding line. However, many dispersion parameters such as surfactant content or sonication time, which have a significant effect on material properties as stated in other studies, remain to be studied. For these reasons, this study is focused on the analysis of these parameters in order to develop a method, which leads to get the better mechanical and electrical performance of the joints.

To achieve that, several specimens were manufactured with different surfactant contents and sonication times. A microstructural analysis of the CNT dispersions has been carried out by FEG-SEM techniques at different sonication times. In addition, lap shear strength tests have been conducted in CFRP joints with different surfactant contents in order to see the effect that CNTs and the addition of surfactant have on the mechanical performance of bonded joints. Failure modes have been identified and a microstructural study of the fracture areas has been carried out. Finally, electrical measurements have been carried out on the adhesive joints in order to characterize the electrical behavior because it is a crucial aspect of their potential use in SHM applications.

6.2 Materials and methods

6.2.1 Manufacturing and characterization of CNT dispersions

Adhesive film was an FM 300K epoxy supplied by Cytec and indicated for CFRP-CFRP and CFRP-metal bonds. It has a wide open knit tricot carrier which allows a good thickness control. Carbon nanotubes used in this study are supplied by Nanocyl with the commercial name NC7000. They have an average diameter of 11 nm and a length up to 2 μm. CNTs are dispersed in water in a weight fraction of 0.1 % with the action of a surfactant called sodium dodecyl sulfate (SDS) at different contents (without SDS, at 0.1, 0.25 and 1 wt. %) The CNT content has been selected according to previous experience in order to get a high electrical conductivity through the joint [23]. Then, dispersions were sonicated at different times (0, 20 and 120 min) at 80 % Amplitude and 1 Hz of frequency.

CNT dispersion was then sprayed over the adhesive film surface with an airbrush at a pressure of 1 bar and at distance of 40 cm, during 0.5 s. These parameters were set up in order to achieve a better homogenization of CNT dispersion over the film.

CNT dispersions and doped adhesive films have been analyzed by FEG-SEM, using a Nova NanoSEM FEI 230 apparatus from Philips. Three different sonication times have been analyzed for CNT dispersions (0, 20 and 120 min) and, once sonication time has been selected, surfactant content has been varied in order to see its disaggregation effect (0, 0.1, 0.25 and 1 wt. % SDS).

6.2.2 Mechanical Tests

Adhesive joints were manufactured by secondary bonding of unidirectional CFRP substrates supplied by Fundación para la Investigación, Desarrollo y Aplicación de Materiales Compuestos (FIDAMC). Cure cycle was set as shown in Table 6.1.

Single lap shear tests were carried out in four specimens at each condition in order to analyze the effect that the addition of CNTs on the adhesive surface has on mechanical properties of adhesive joints. The data analysis has been made according to the standard deviation procedure. These tests were conducted according to standard ASTM D 5868-95 issue 01 using substrates of 100 x 25.4 x 2.5 mm with an overlapping area of 25.4 x 25.4 mm at a test rate of 13 mm/min. Mechanical tests were performed in a Zwick test machine. A microstructural analysis of both fracture surfaces of CFRP joints and the doped adhesive film and CNT dispersions has been carried out in order to determine main failure modes and homogeneity of CNT dispersions. Fracture surfaces have been analyzed by Scanning electron microscopy (SEM) using a S-3400N apparatus from Hitachi.

Table 6.1: Cure cycle parameters of secondary bonding.

Parameter	First Stage	Second stage
pressure	Ramp from 0 to 0.6 MPa during 15 min	0.6 MPa during 90 min
temperature	Ramp from 25 to 175 ºC during 45 min	175 ºC during 60 min

6.2.3 Electrical measurements

Electrical properties of CFRP joints were determined by means of electrical resistance measurements in two points through thickness, which disposition is shown in Figure 6.1. Electrodes were made of copper wire and silver paint was applied on the substrate surface in order to ensure a good contact between them. To protect the electrodes from environmental issues, an adhesive tape was used. Three measurements were carried out for each different SDS conditions in order to see the effect that surfactant has on electrical properties.

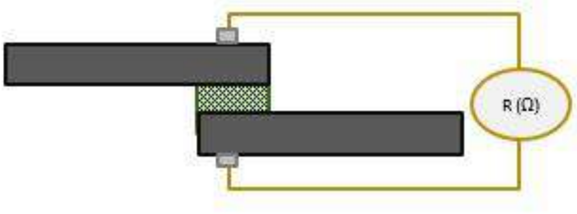

Figure 6.1: Schematic of electrode disposition and resistance measurement in SLS tests.

6.3 Results and discussion

6.3.1 Analysis of CNT dispersions

An analysis of CNT aqueous dispersions has been carried out in order to see the effect that sonication conditions have on the dispersions. The aim is to select the appropriate conditions in order to achieve a good homogeneous dispersion onto the adhesive surface without affecting mechanical and electrical performance of CNTs.

Figure 6.2 shows the CNT dispersion at three sonication times. It is observed that without sonication, there is a very high entanglement of CNTs which are mainly as agglomerates (Figure 6.2 (a)). The sample at 20 min sonication shows a much better CNT dispersion with a drastic reduction of the entanglement (Figure 6.2 (b)). However, no significant differences are observed when increasing the sonication time to 120 min (Figure 6.2 (c)) as the breakage of higher aggregates takes place at the beginning of sonication process. In addition, it is important to notice that the higher the sonication time, the higher the breakage of CNTs, as stated in several studies [24,25]. That implies a detriment on mechanical properties of CNTs and especially on their electrical performance, as their aspect ratio is drastically reduced, inducing an increase on the percolation threshold [26] which gives rise to a decrease on electrical conductivity. In addition, it has been studied that much higher sonication times leads to lower mechanical properties of CNT doped epoxy systems [27,28]. For these reasons, it is necessary to reach a compromise solution. Sonication time has been selected as 20 min because CNT dispersion achieved is good and very similar to those achieved at 120 min sonication and, as stated before, higher sonication times could induce a more prevalent CNT breakage.

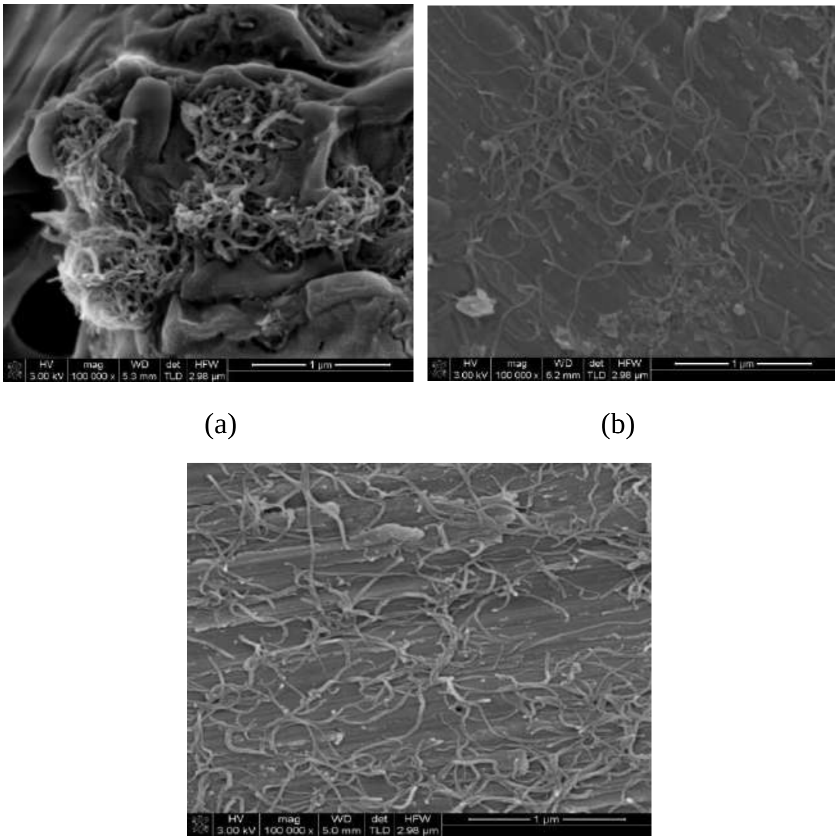

(a) (b)

(c)

Figure 6.2: FEG-SEM images of the CNT dispersion (a) without sonication, (b) at 20 min and (c) at 120 min sonication.

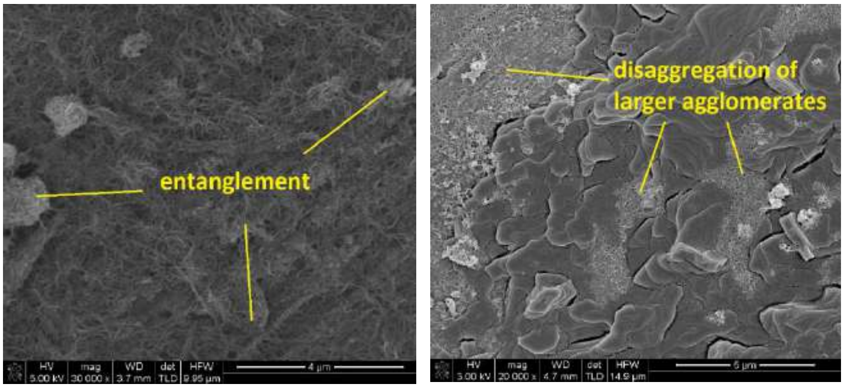

(a) (b)

Figure 6.3: FEG-SEM images of the CNT dispersion (a) without the addition of SDS and with (b) 0.25 wt. % of SDS

On the other hand, Figure 6.3 shows a comparison of two different CNT dispersions (with and without surfactant) at the same sonication conditions (20 min) so that effect of SDS can be analyzed. It is observed that SDS tends to disaggregate the CNTs (Figure 6.3 (b)) inducing the creation of separated CNT regions. This could have a positive effect on adhesive properties by reducing CNT entanglement and by creating more dispersed areas. But on the other hand, a huge SDS addition could induce an excessive separation of CNT regions leading to a poor dispersion and, thus, a detriment on adhesive properties. For that reason, it is necessary to investigate its effect on the mechanical performance of the adhesive joints.

6.3.2 Single Lap Shear Tests

Single Lap Shear (SLS) specimens have been manufactured with different SDS contents (0, 0.1, 0.25 and 1 wt. %) at the same sonication time, fixed at 20 min. LSS is calculated by dividing the maximum force applied F_{max} by the overlapping area A of the specimens.

$$LSS = \frac{F_{max}}{A} \tag{6.1}$$

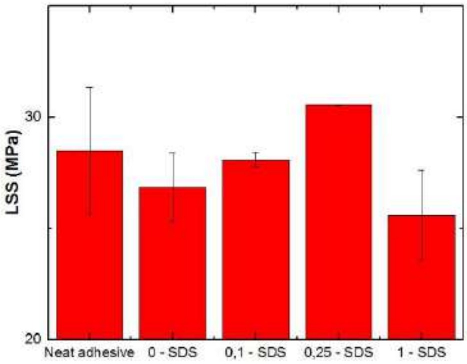

Figure 6.4: Lap shear strength (LSS) values for the different SDS content specimens.

The graph presented in Figure 6.4 summarizes the values of LSS for the different specimens. It is observed that as the content of surfactant increases up to 0.25 wt. % the shear strength value of the joint also does, although the differences with the neat adhesive are not really significant. However, for higher surfactant contents LSS suddenly drops. This is due to a combined effect between the dispersion state and the addition of surfactant. At lower contents of SDS, CNT agglomeration effect induces stress concentration points, which lead to a detriment on mechanical performance in comparison to the neat adhesive. On the other hand, for higher SDS contents, there is a significant improvement on CNT dispersion, which induces therefore an enhancement on mechanical performance. However, SDS addition could have a negative effect on mechanical properties due to the presence of the surfactant itself. That explains LSS value detriment at the highest SDS content because in this case, the effect of the presence of SDS is more prevalent than the disaggregation effect that induces on the CNT dispersion.

In this regard, Figure 6.5 shows the force-displacement curves for the different specimens. It is observed that the addition of SDS enhances the failure strain at lower contents while a slight decrease is observed for the highest SDS contents due to the combined effect previously commented. In doped specimens, strain failure is lower than for the neat adhesive because aggregation effect of CNTs leads to an earlier failure of doped adhesive, already reported in several studies [29,30]. This explains the increase of failure strain with SDS due to a better CNT dispersion on the adhesive.

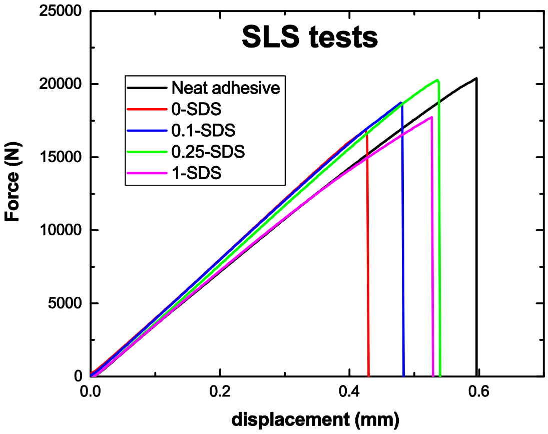

Figure 6.5: Force-displacement curve of Single Lap Shear specimens for the different conditions of SDS content.

The results in the mechanical performance on adhesive films shown a similar trend than for paste adhesives, where a slight increase of LSS is observed in the case of a good CNT dispersion inside the epoxy matrix in comparison to neat joints [31].

6.3.3 Microstructural analysis of fracture surfaces

In order to properly determine the failure mode and the effect of SDS content on the CFRP joints, a microstructural analysis has been carried out.

Figure 6.6 shows SEM images of fracture surfaces of adhesive joints. It is observed that in all the cases the failure mode is mainly cohesive. However, it is important to notice that in many specimens, a laminate failure is observed near the edges (Figure 6.6 (b)). This is explained because of the shear stress distribution along the bonding line, which is higher at the edges [32,33].

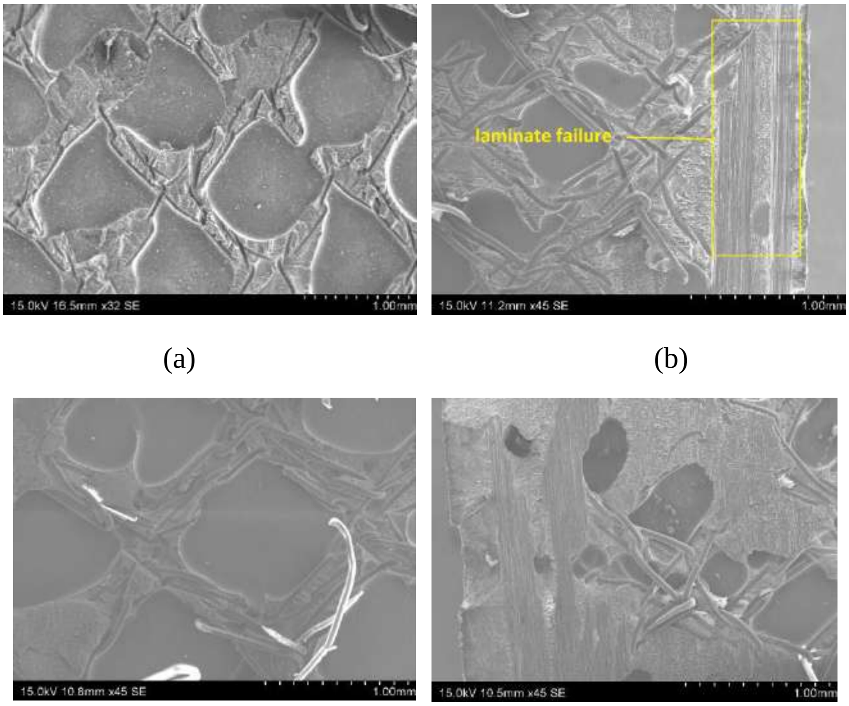

(a) (b)

(c) (d)

Figure 6.6: SEM images of fracture surface of (a) neat adhesive and (b) (c) and (d) doped adhesive.

On the other hand, lack of adhesive is observed in many internal areas inside the carrier. It is also noticed that this lack of adhesive is higher in the central part of the bonded joint while adhesive is more present near the edges (Figure 6.6 (c) and (d), respectively) This could be explained due to an overflow effect that can take place during curing probably because of the curing pressure applied. Therefore, although mechanical performance of adhesive joints seems to be satisfactory, it is necessary a deeper study on the effect of curing pressure on mechanical and microstructural properties of the bonded joints. It is important to notice that, in this case, SDS content and CNT presence do not seem to have a significant effect as these laminate failure areas are observed in all the specimens.

Figure 6.7 shows more detailed images of the fracture surface. It is observed that, in the case of CNT doped adhesive without surfactant, the agglomeration is very high through the carrier junctions while SDS has a disaggregation effect (as observed in the reduction of the size of red areas in

Figure 6.7 (b)). Figure 6.8 shows a more detailed image of the adhesive carrier without surfactant, confirming the presence of those larger aggregates through the junctions. Therefore, this presence of large aggregates can explain the detriment on mechanical properties for those joints with lower SDS content.

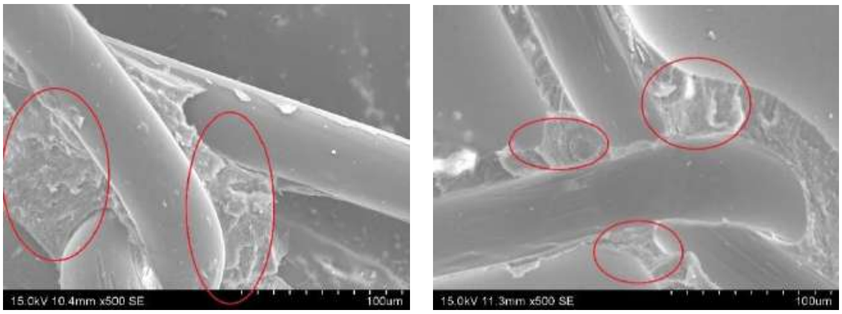

(a) (b)

Figure 6.7: SEM images of carrier junctions for (a) 0 and (b) 0.1 wt. % SDS. Red areas indicate the presence of aggregates.

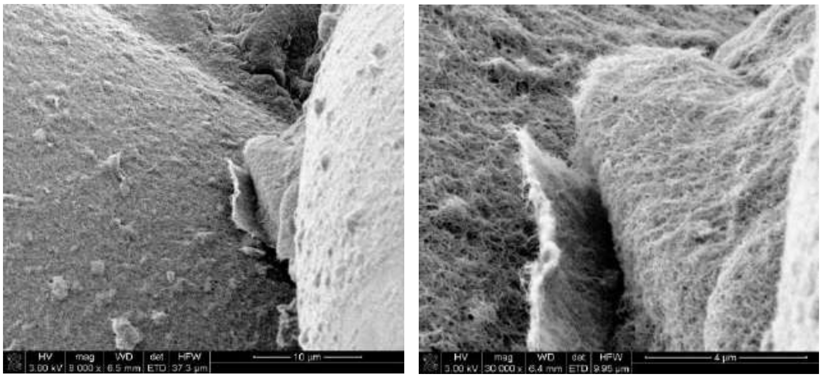

(b)

Figure 6.8: FEG-SEM images of carrier junctions at (a) lower and (b) higher magnifications for 0 wt. % SDS.

6.3.4 Electrical properties of adhesive joints

Figure 6.9 summarizes the values of the electrical resistivity for the specimens at different SDS content. Doped adhesive joints are electrically conductive and SDS content has a significant impact on electrical properties of adhesive joints. The highest electrical resistivity takes place in the specimen without SDS due to the poor quality of CNT dispersions over the adhesive surface. Then, electrical resistance decreases with SDS content until achieving a minimum value at 0.25 wt. % SDS. This is due to a better homogenization of the CNT dispersion along the adhesive and the steric stabilization induced by SDS. However, at 1 wt. % SDS content, an increase on electrical resistivity is observed, probably, due to a larger steric stabilization and larger distances between CNTs [34].

Figure 6.10 shows FEG-SEM images of the uncured adhesive after spraying of CNT dispersions over the surface. CNTs are homogeneously distributed especially along the carriers, which makes it possible the creation of electrical pathways giving rise to an adhesive electrically conductive.

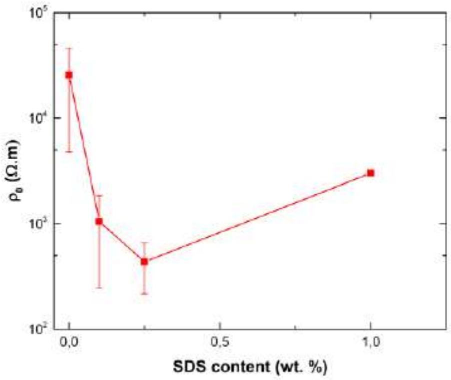

Figure 6.9: Electrical resistivity measurements for SLS bonded joints as a function of SDS content.

(b)

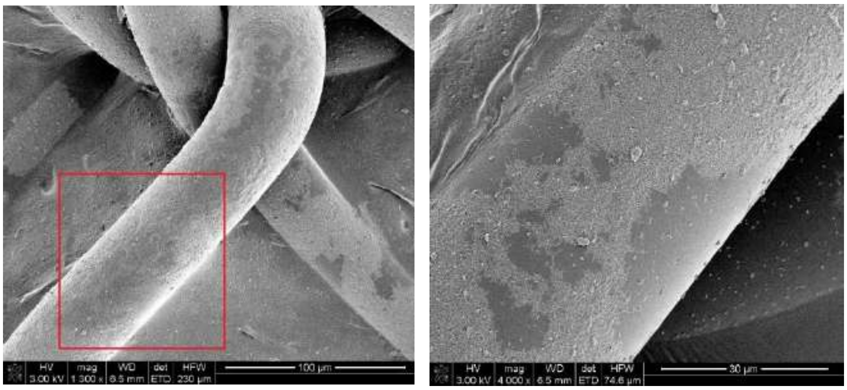

(a) (b)

Figure 6.10: FEG-SEM images of uncured adhesive at (a) lower and (b) higher magnifications for 0.25 wt. % SDS.

6.4 Conclusions

A novel CNT doped adhesive film has been developed and studied. CNT deposition over the adhesive surface has been carried out by spraying an aqueous dispersion of CNTs. It has been observed that sonication during 20 min gives rise to an effective CNT dispersion and the disaggregation effect of surfactant has been confirmed.

On the other hand, it has been noticed that at low SDS contents lap shear strength (LSS) is not significantly affected by the addition of surfactant, while for the highest SDS content (1 wt. %) a decrease in LSS is observed, due to the action of the surfactant itself. The highest value of LSS has been achieved for CNT dispersion with 0.25 wt. % of SDS. The analysis of fracture areas reveals that failure mode is mainly cohesive showing areas of laminate failure near the edges.

In addition, electrical resistance measurements indicate that electrical conductivity is achieved through the thickness in all the CNT doped adhesive joints. This could be used for detecting possible debondings by means of electrical measurements along the thickness. This potential application would require a deeper investigation but, at a first sight, this work constitutes a first step to achieve that by optimizing the manufacturing conditions in order to achieve the best mechanical performances.

Acknowledgements

The authors would like to acknowledge the Ministerio de Economía y Competitividad of Spanish Government [Project MAT2013-46695-C3-1-R] and Comunidad de Madrid Government [Project P2013/MIT-2862] for their financial support, and Fundación para la Investigación, Desarrollo y Aplicación de Materiales Compuestos [FIDAMC – AIRBUS] for providing the CFRP substrates.

6.5 References

[1] Peters ST. Handbook of composites. 2013.

[2] Bernasconi A, Carboni M, Comolli L, Galeazzi R, Gianneo A, Kharshiduzzaman M. Fatigue Crack Growth Monitoring in Composite Bonded Lap Joints by a Distributed Fibre Optic Sensing System and Comparison with Ultrasonic Testing. J Adhesion 2016;92(7-9):739-757.

[3] Tamborrino R, Palumbo D, Galietti U, Aversa P, Chiozzi S, Luprano VAM. Assessment of the effect of defects on mechanical properties of adhesive bonded joints by using non destructive methods. Composites Part B-Engineering 2016;91:337-345.

[4] De Volder MFL, Tawfick SH, Baughman RH, Hart AJ. Carbon Nanotubes: Present and Future Commercial Applications. Science 2013;339(6119):535-539.

[5] Iijima S. Helical Microtubules of Graphitic Carbon. Nature 1991;354(6348):56-58.

[6] Ruoff RS, Lorents DC. Mechanical and thermal properties of carbon nanotubes. carbon 1995;33(7):925-930.

[7] Yu MF, Lourie O, Dyer MJ, Moloni K, Kelly TF, Ruoff RS. Strength and breaking mechanism of multiwalled carbon nanotubes under tensile load. Science 2000;287(5453):637-640.

[8] Popov VN. Carbon nanotubes: properties and application. Materials Science and Engineering: R: Reports 2004;43(3):61-102.

[9] Song YS, Youn JR. Influence of dispersion states of carbon nanotubes on physical properties of epoxy nanocomposites. Carbon 2005;43(7):1378-1385.

[10] Hu N, Masuda Z, Yan C, Yamamoto G, Fukunaga H, Hashida T. The electrical properties of polymer nanocomposites with carbon nanotube fillers. Nanotechnology 2008;19(21):215701.

[11] Ma P, Siddiqui NA, Marom G, Kim J. Dispersion and functionalization of carbon nanotubes for polymer-based nanocomposites: A review. Composites Part A-Applied Science and Manufacturing 2010;41(10):1345-1367.

[12] Gagne M, Therriault D. Lightning strike protection of composites. Prog Aerospace Sci 2014;64:1-16.

[13] Guadagno L, Raimondo M, Vittoria V, Vertuccio L, Naddeo C, Russo S, De Vivo B, Lamberti P, Spinelli G, Tucci V. Development of epoxy mixtures for application in aeronautics and aerospace. Rsc Advances 2014;4(30):15474-15488.

[14] Li X, Levy C, Elaadil L. Multiwalled carbon nanotube film for strain sensing. Nanotechnology 2008;19(4):045501.

[15] Park M, Kim H, Youngblood JP. Strain-dependent electrical resistance of multi-walled carbon nanotube/polymer composite films. Nanotechnology 2008;19(5):055705.

[16] Vemuru SM, Wahi R, Nagarajaiah S, Ajayan PM. Strain sensing using a multiwalled carbon nanotube film. J Strain Anal Eng Des 2009;44(7):555-562.

[17] Meguid S, Sun Y. On the tensile and shear strength of nano-reinforced composite interfaces. Mater Des 2004;25(4):289-296.

[18] Burkholder GL, Kwon YW, Pollak RD. Effect of carbon nanotube reinforcement on fracture strength of composite adhesive joints. J Mater Sci 2011;46(10):3370-3377.

[19] Gude MR, Prolongo SG, Gomez-del Rio T, Urena A. Mode-I adhesive fracture energy of carbon fibre composite joints with nanoreinforced epoxy adhesives. Int J Adhes Adhes 2011;31(7):695-703.

[20] Islam MF, Rojas E, Bergey DM, Johnson AT, Yodh AG. High weight fraction surfactant solubilization of single-wall carbon nanotubes in water. Nano Letters 2003;3(2):269-273.

[21] Yu J, Grossiord N, Koning CE, Loos J. Controlling the dispersion of multi-wall carbon nanotubes in aqueous surfactant solution. Carbon 2007;45(3):618-623.

[22] Rastogi R, Kaushal R, Tripathi SK, Sharma AL, Kaur I, Bharadwaj LM. Comparative study of carbon nanotube dispersion using surfactants. J Colloid Interface Sci 2008;328(2):421-428.

[23] Garcia C, Sanchez M, Urena A, Rams J. Carbon Nanotubes for Assessing the Structural Integrity of Composite Bonded Joints with Film Adhesives. Structural Health Monitoring 2015: System Reliability for Verification and Implementation, Vols.1 and 2 2015:2169-2176.

[24] Hennrich F, Krupke R, Arnold K, Stuetz JAR, Lebedkin S, Koch T, Schimmel T, Kappes MM. The mechanism of cavitation-induced scission of single-walled carbon nanotubes. J Phys Chem B 2007;111(8):1932-1937.

[25] Huang YY, Terentjev EM. Dispersion of Carbon Nanotubes: Mixing, Sonication, Stabilization, and Composite Properties. Polymers 2012;4(1):275-295.

[26] Sanchez-Romate XF, Jimenez-Suarez A, Sanchez M, Guemes A, Urena A. Novel approach to percolation threshold on electrical conductivity of carbon nanotube reinforced nanocomposites. Rsc Advances 2016;6(49):43418-43428.

[27] Montazeri A, Khavandi A, Javadpour J, Tcharkhtchi A. An investigation on the effect of sonication time and dispersing medium on the Mechanical properties of MWCNT/epoxy nanocomposites. Advances in Materials and Processing Technologies Ii, Pts 1 and 2 2011;264-265:1954-1959.

[28] Montazeri A, Montazeri N, Pourshamsian K, Tcharkhtchi A. The Effect of Sonication Time and Dispersing Medium on the Mechanical Properties of Multiwalled Carbon Nanotube (Mwcnt)/epoxy Composite. International Journal of Polymer Analysis and Characterization 2011;16(7):465-476.

[29] Bai J, Allaoui A. Effect of the length and the aggregate size of MWNTs on the improvement efficiency of the mechanical and electrical

properties of nanocomposites - experimental investigation. Composites Part A-Applied Science and Manufacturing 2003;34(8):689-694.

[30] Gojny F, Wichmann M, Kopke U, Fiedler B, Schulte K. Carbon nanotube-reinforced epoxy-compo sites: enhanced stiffness and fracture toughness at low nanotube content. Composites Sci Technol 2004;64(15):2363-2371.

[31] Jojibabu P, Jagannatham M, Haridoss P, Ram GDJ, Deshpande AP, Bakshi SR. Effect of different carbon nano-fillers on rheological properties and lap shear strength of epoxy adhesive joints. Composites Part A-Applied Science and Manufacturing 2016;82:53-64.

[32] Li G, Lee-Sullivan P, Thring R. Nonlinear finite element analysis of stress and strain distributions across the adhesive thickness in composite single-lap joints. Composite Structures 1999;46(4):395-403.

[33] Kim H, Kedward K. Stress analysis of adhesively-bonded joints under in-plane shear loading. J Adhesion 2001;76(1):1-36.

[34] Chiang TH, Liu C, Lin Y. The effect of an anhydride curing agent, an accelerant, and non-ionic surfactants on the electrical resistivity of graphene/epoxy composites. J Appl Polym Sci 2015;132(20):41975.

Chapter 7: Electrical Monitoring as a Novel Route to Understanding the Ageing Mechanisms of Carbon Nanotube-Doped Adhesive Film Joints

Xoan F. Sánchez-Romate[a,b,*]*, Alberto Jiménez-Suárez*[b]*, María Sánchez*[b]*, Silvia González-Prolongo*[b]*, Alfredo Güemes*[a] *and Alejandro Ureña*[b]

Submitted to Compos Part B (2019)

[a] Department of Aerospace Materials and Processes, Escuela Técnica Superior de Ingenieros Aeronáuticos, Universidad Politécnica de Madrid, Plaza del Cardenal Cisneros 3, 28040 Madrid, Spain

[b] Materials Science and Engineering Area, Escuela Superior de Ciencias Experimentales y Tecnología, Universidad Rey Juan Carlos, Calle Tulipán s/n, 28933 Móstoles (Madrid), Spain

*Corresponding author: xoan.fernandez.sanchezromate@urjc.es Tel: +34914888252

Carbon fibre reinforced plastic bonded joints with novel carbon nanotube (CNT) adhesive films are manufactured and tested under ageing conditions by varying the surfactant content, added to enhance the CNT dispersion. Single lap shear (SLS) tests are conducted in their initial state and after 1 and 2 months immersed in distilled water at 60 ºC. In addition, their electrical response is measured in terms of the electrical resistance change through thickness. The lap shear strength shows an initial decrease due to plasticisation of weak hydrogen bonds and then a partial recovery due to secondary crosslinking. This plasticisation effect is confirmed by differential scanning calorimetry analysis with a decrease in the glass transition temperature. The electrical response varies with ageing conditions, showing a higher plasticity region in the 1-month SLS joints and a sharper increase in the case of the non-aged and 2-month aged samples, with these changes more prevalent with increasing surfactant content. By adjusting the measured electrical data to simple theoretical calculations, it is possible to establish the first estimation of damage accumulation, which is higher in the case of non-aged and 2-month aged samples due to the presence of more prevalent brittle mechanisms for the CNT-doped joints.

Keywords: carbon nanotubes; ageing; water uptake; SHM; surfactant

7.1 Introduction

The increasing requirements of industry in terms of structural components make the development of novel materials necessary. In this context, composite structures present many advantages over conventional metallic alloys due to their exceptional specific properties that lead to energy efficiency and weight savings.

Therefore, the assembly of several composite parts is a challenging subject as the complexity of these structures is continuously increasing. For these purposes, bonded joints have some advantages over bolted ones as they are lightweight and avoid stress concentrations around the holes [1]. However, the inspection of adhesive joints sometimes is not always straightforward, since it involves many complex techniques, such as fibre Bragg grating sensors or Lamb waves, which often do not give a complete overview of the quality of the bonded joint [2-4]. Therefore, it is necessary to develop novel procedures that do not involve complex data analysis techniques and are not detrimental to the physical properties of the joint.

In this regard, carbon nanotubes (CNTs) seem to be a very promising solution. Their exceptional properties [5-7] and the enhancement of the electrical conductivity that they induce when added to an insulator resin [8-11] makes them very useful for multifunctional applications [12,13]. In fact, their use in structural health monitoring (SHM) applications is now of interest because of their piezoresistive and tunnelling properties that lead to high sensitivities [14-17].

The aim of this work is to exploit the superb physical properties of CNTs in developing novel multifunctional adhesives with an inherent self-sensing capability. To date, most research into reinforced bonded joints has been focused on paste adhesives [18-21]. They exhibit excellent sensing properties and are capable of properly monitoring strain and debonding [22-24]. These paste adhesives can be treated as nanoreinforced composites, with the CNT dispersion procedure representing a challenging subject that often involves complex and expensive techniques, such as three-roll milling [25-27]. Therefore, this work is focused on the effect that CNT addition has on adhesive films, which allows for better thickness control and is used for structural applications in the aircraft industry.

In previous studies, CNT reinforced adhesive films have demonstrated high sensing properties and a good capability to properly monitor crack evolution [28]. The dispersion procedure has also been optimised in order to achieve a degree of good homogenisation without any substantial detriment to the mechanical properties [29]. This is achieved by means of ultrasonication of a CNT dispersion in an aqueous solution, which is assisted by the addition of a surfactant, namely, sodium dodecyl sulfate (SDS). The addition of SDS improves the mechanical dispersion of the CNTs in the aqueous solution [30-33].

The effect of CNT dispersion on the mechanical and electrical properties of carbon fiber reinforced plastic (CFRP) bonded joints in their initial state has been characterised in previous works [29]. It has been concluded that these CNT adhesive films do not induce a detrimental effect on mechanical performance and they have proved to have excellent monitoring capabilities by means of electrical measurements [34]. This work takes a further step by analysing the potential and applicability of these proposed bonded joints under ageing conditions.

The amphiphilic behaviour of SDS [35,36] plays an important role in the ageing properties of adhesive joints. For this reason, immersion tests have been carried out in CNT-doped adhesive films once cured by varying the amount of SDS. In addition to this, single lap shear (SLS) tests have also been conducted in standard coupons in order to see the effect of water and temperature ageing. The main application of these reinforced joints is the SHM. The electrical response has been also monitored during these tests so that the electrical properties can be better characterised in order to obtain a deeper knowledge of the ageing mechanisms.

7.2 Experimental

7.2.1 Materials

The multi-wall CNTs used for this study were NC7000 supplied by Nanocyl with an average diameter of 10 nm and a length of up to 2 μm.

The adhesive was a FM300K adhesive film, supplied by Cytec. This is an epoxy base adhesive with a knit tricot carrier, which allows enhanced bondline thickness control. It has a high elongation and toughness together with an ultimate shear strength of 36.8 MPa. It is suitable for bonding metal to metal and CFRP to CFRP systems.

CNT dispersion takes place by means of ultrasonication by using a previously optimised dispersion procedure [29,37]. It consists of a 20-min ultrasonication of a CNT aqueous solution at 0.1 wt.%. The disaggregation of larger agglomerates is enhanced by the addition of a SDS surfactant. To study the influence of this surfactant on the ageing properties, the amount of SDS was fixed at 0.00, 0.25 and 1.00 wt.%.

After the dispersion procedure, the CNT suspension is sprayed over the adhesive surface prior to curing at a pressure of 1 bar at 40 cm for 0.5 s in order to achieve good homogenisation of the CNTs over the surface.

In order to see the effects of ageing, two types of specimens were prepared. One is the adhesive without substrate once cured, named in-bulk adhesive, in order to see the water uptake without any influence of the CFRP substrates. The second one was the SLS specimens, which were made by secondary bonding of unidirectional CFRP substrates. The curing cycle was set for both the cured adhesive and the SLS joints in a hot press, as shown in Table 7.1. To improve the interfacial adhesion, the substrate surfaces were brushed.

Table 7.1: Cure cycle parameters of secondary bonding.

Parameter	First Stage	Second stage
Pressure	Ramp from 0 to 0.6 MPa for 15 min	0.6 MPa for 90 min
Temperature	Ramp from 25 to 175 ºC for 45 min	175 ºC for 60 min

7.2.2 Ageing tests

Cured adhesive and SLS specimens were subjected to ageing conditions by immersion in distilled water at 60 ºC, similar to some found in the literature [38]. Prior to immersion, the samples were dried in an oven at 50 ºC for three days until weight loss was not observed between one and the next measurement. The ageing time was set at 2 weeks (14 days) for the in-bulk adhesive and up to 2 months (60 days) for SLS specimens. The reasons for these different immersion times are due to differences in the nature of each material and the exposed area subjected to water uptake. Adhesives tend to reach the water uptake saturation before the composite substrates [39], and in the case of the in-bulk adhesive, the exposed area of the adhesive is higher than in the CFRP joints. Therefore, the process of water uptake is accelerated [40].

Water absorption was measured in the in-bulk samples in their initial state and 1, 2, 3, 4, 7, 10 and 14 days after immersion. The water uptake was calculated by comparing the measured weight after immersion and the initial one in which is supposed that the samples are totally dry.

7.2.3 Electromechanical tests

As commented before, bonded joints were subjected to SLS tests in order to study the ageing effect on the electromechanical properties. They were conducted in three specimens for each condition (neat adhesive without CNTs and with 0.1 wt.% CNTs with 0, 0.25 and 1 wt.% SDS). The tests were made according to standard ASTM D 5868-95 issue 01 using substrates of 100 × 25.4 × 2.5 mm with an overlapping area of 25.4 × 25.4 mm at a test rate of 13 mm/min. They were performed in a universal tensile Zwick machine.

Simultaneously, the electrical response was also monitored. Electrodes were made of copper wire sealed with silver ink in order to ensure a good electrical contact with the substrate surface. To protect the electrodes from environmental influences during testing, an adhesive layer was used. The measurements were carried out by an Agilent 34401A hardware and they were correlated to the mechanical response given by the tensile machine.

7.2.4 Characterisation

Differential scanning calorimetry (DSC) measurements were conducted in a Metter Toledo mod 821 apparatus for the in-bulk adhesive. Two scans were carried out according to the standard ISO 11357-2:13, at 10 ºC/min from ambient temperature to 250 ºC. The glass transition temperature (T_g) was determined as the turning point of the heat capacity change. Two specimens of the non-aged and 14-day aged in-bulk specimens were measured in order to see the water uptake effect in the physical properties of the neat and CNT-doped adhesive.

7.3 Results and discussion

This section presents an analysis of the physical and mechanical evolution of SLS joints under ageing conditions. First of all, the water uptake measurements for the in-bulk specimens are shown. Then, the mechanical properties of the SLS joints are discussed and finally, their electromechanical behaviour is characterised.

7.3.1 Water uptake measurements

Figure 7.1 shows the water uptake in terms of percentage of the initial weight for the in-bulk cured samples at each condition. The graph is in good agreement with the typical behaviour of water uptake for this kind of samples, previously stated in other studies [38,41,42]. It is observed that water uptake is more prevalent in the initial stages and then the weight gain is going less significant until the water saturation is reached at 2 weeks of ageing.

A similar water uptake behaviour is found at every condition although some slight differences can be noticed. In this context, two opposite effects can play an important role. The first one is the hydrophobic behaviour of carbon nanofillers, which can be introduced into the free volume of the polymer improving the barrier properties and leading to a reduction in the water uptake [43,44]. The second one is the amphiphilic behaviour of the SDS that remains attached to the CNT surface [45,46], which can lead to an increase of the water absorption induced by the hydrophilic head groups [47]. In addition, CNT dispersion also plays a significant role. A poor dispersion can induce the presence of larger agglomerates, higher heterogeneity and higher distributed porosity. This irregular distribution leads, thus, to an irregular effect of the barrier properties of CNTs, which, in combination with the higher porosity, promotes a higher water uptake. However, a better dispersion of nanofillers improves the barrier properties leading, thus, to a lower water uptake.

The combination of these effects, as shown in the schematics of Figure 7.2, thus, explains the slight differences observed for each condition. In the case of the CNT reinforced adhesive without surfactant, a poor CNT dispersion is achieved, as stated in previous studies [48], so that the hydrophobic effect of CNTs is not so prevalent. Alternatively, the samples with 0.25 and 1 wt.% SDS shows a similar trend, with a slightly lower water uptake than the sample without surfactant. In this case, the effect of the better CNT dispersion achieved is slightly prevalent over the amphiphilic effect of SDS surfactant. In the case of the neat adhesive, the water uptake is given directly by the physical behaviour of the epoxy matrix.

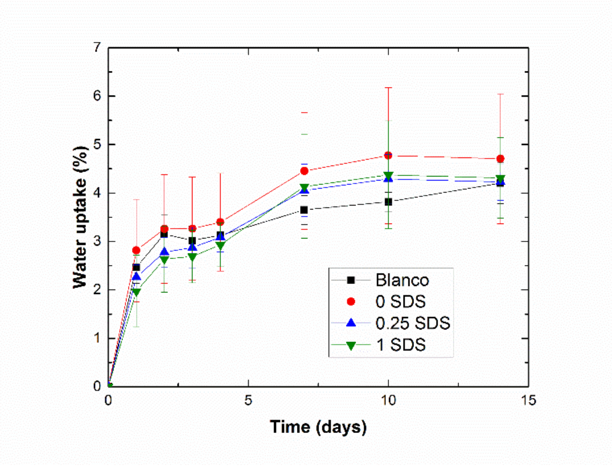

Figure 7.1: Water uptake graph for in-bulk specimens.

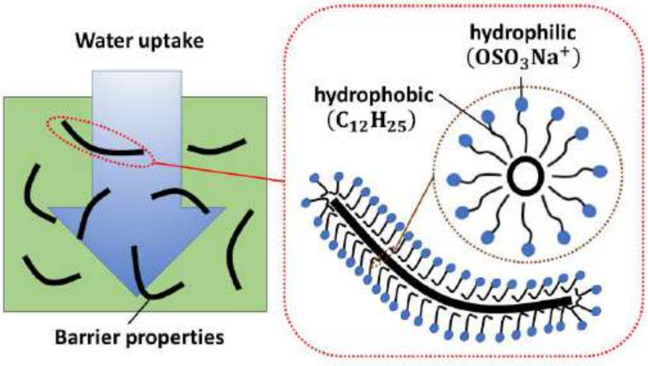

Figure 7.2: Schematics of combined effect of the water uptake (left) and amphiphilic behaviour of SDS (right).

7.3.2 DSC measurements

Table 7.2 shows the T_g values at different testing conditions for the in-bulk specimens. In the initial state, a drastic reduction of T_g is observed when comparing the non-doped with the doped adhesive. This means that CNTs accelerate the curing process, leading to the maximum conversion point of the system ($T_g \sim 150$ ºC). This affirmation is stated by the measurements of the second scanning, where the T_g of all the samples is close to 150 ºC, indicating the point of the maximum conversion of the resin. In addition, by observing the T_g of the aged samples, a significant decrease in comparison to the non-aged specimens is observed when adding CNTs, resulting in a similar glass transition temperature than for the neat adhesive. However, by observing the T_g obtained in a second scanning, it reaches the point of the maximum conversion in every case. This indicates that there is a plasticisation effect caused by the water absorption in the case of CNT-doped samples. In the case of the neat adhesive, no significant differences are found when comparing aged and non-aged samples, so the plasticisation effect is similar for the non-aged and aged samples. This affirmation is given by the fact that the network of the neat adhesive is not initially totally cured, with the plasticisation effect less prevalent due to water absorption. It is important to note that the selected curing cycle is the same as that given by the supplier.

Alternatively, when comparing the CNT-doped samples, it is observed that the addition of surfactant results in a more drastic reduction of the T_g, implying, thus, a higher plasticisation effect. In order to better explain the possible effects that can take place in the material, it is necessary to focus on the mechanical testing of the SLS joints.

Table 7.2: Glass transition temperature for different in-bulk conditions.

Condition	**Non-aged T_g (°C)**		**2-week aged T_g (°C)**	
	1st scanning	**2nd scanning**	**1st scanning**	**2nd scanning**
Neat adhesive	117.0	146.0	115.5	146.0
0.00 SDS	144.0	148.0	119.0	146.0
0.25 SDS	148.5	149.5	118.0	148.5
1.00 SDS	146.0	147.5	109.0	149.5

7.3.3 Single lap shear tests

Figure 7.3 shows the lap shear strength (LSS) of the SLS specimens for each condition. It is observed that the LSS strength is significantly affected by the ageing conditions. In every condition, a significant decrease of the LSS is observed after 1 month ageing while, for most of the cases, a slight recovery of the LSS is noticed by increasing the ageing time. This different behaviour can be explained by attending the water uptake results and also by the different chemical interactions inside the adhesive joint.

First of all, it is necessary to understand the role of ageing mechanisms due to water absorption. The water uptake generally induces the creation of weak hydrogen bonds, leading to a swelling of the polymer chains and causing, thus, a drastic reduction of the physical properties. This effect is called plasticisation and is detrimental to the mechanical properties [41]. However, after this initial stage, a slight recovery is generally observed. This has already been shown in other studies [43,49,50] and can be explained by a change in the mechanism of water absorption. After reaching the water uptake saturation, longer ageing times can induce a transformation of the weak hydrogen bonds into multiple chemical connections between the water molecules and the polymer chains, promoting an increase in secondary crosslinking, thus leading to a stiffening of the material and also an embrittlement, as observed in the examples given in Figure 7.4 (a). This cannot be confirmed by the T_g as there is only one measurement. Therefore, it is necessary to focus on the mechanical response of the adhesive joints, particularly on the displacement at failure.

In the particular case of the neat adhesive, there is only a partial conversion of the epoxy matrix at the initial state, as the T_g is significantly below the maximum value (~150 ºC). Therefore, the water uptake does not affect significantly the plastic properties of the epoxy matrix, as it presents a more prevalent plasticisation effect at the initial state. This is confirmed by a slight variation of the displacement at failure with ageing time, as shown in Figure 7.4 (b).

However, in the case of CNT-doped adhesive joints, there are some different mechanisms. Here, the CNT addition itself and the dispersion state, dominated by the surfactant addition, play an important role in the ageing mechanisms. As commented previously, a good dispersion implies a high homogeneity of CNT distribution in the matrix, improving the barrier properties. This acts in an opposite way to the amphiphilic behaviour of SDS. In addition, the SDS also induces variations in the chemical interactions between the epoxy matrix and the CNTs, leading to a more drastic reduction of the T_g, as shown in Table 7.2. This is also observed by the displacement at failure shown in Figure 7.4 (b). In this case, the higher the SDS content, the higher the displacement at failure is. Moreover, it can be noted that the displacement at failure decreases after 2 months of ageing. This is explained by the stiffening effect induced by the secondary crosslinking, which also leads to an embrittlement of the material, as previously stated. Therefore, the combination of the two effects explains the initial reduction of the LSS after 1 month and the general recovery for longer ageing times.

In the case of the CNT sample without surfactant, a slight reduction of the LSS is observed after 1 month (~2 %), while the effect on the mechanical properties is much more prevalent after 2 months, leading to a LSS reduction of more than 18%. In this case, the role of CNT dispersion is even more critical, as the absence of any surfactant leads to a much lower homogeneity of CNT distribution, inducing some areas with very high CNT content, acting as stress concentrators. Here, the embrittlement effect is more prevalent than the stiffening due to secondary crosslinking. This is confirmed by a higher relative reduction in the displacement at failure after 2 months of ageing, similar to that initially obtained.

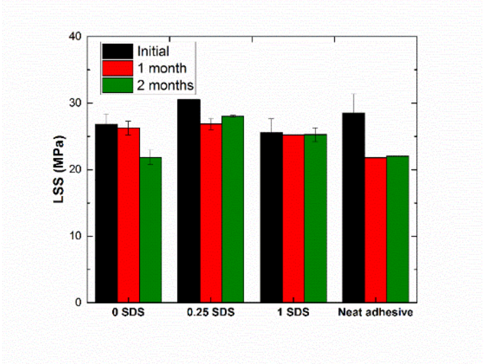

Figure 7.3: LSS of adhesive joints for each testing condition.

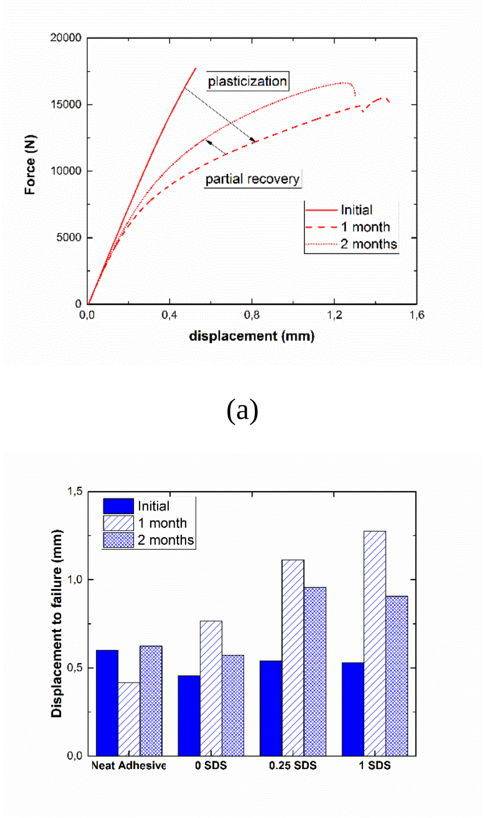

(a)

(b)

Figure 7.4: (a) Mechanical effect of water uptake showing a plasticisation stage.

7.3.4 Electrical monitoring

The aforementioned results give an initial idea of how ageing conditions can affect the mechanical properties of CNT-doped adhesive film joints. In order to have a deeper understanding of ageing effects on CNT-doped adhesive joints, it is necessary to analyse their electromechanical behaviour. Figure 7.5 shows an example of electrical monitoring of a SLS specimen for different ageing times. In every case, it is observed that the electrical resistance increases with displacement. This increase follows an approximately exponential behaviour until failure, with the changes being more prevalent in the last stages of SLS testing. As stated in a previous study proving the monitoring capabilities of these CNT reinforced joints [34], the changes in the electrical resistance are due to the combination of two effects. The first effect is the increase of the tunnelling distance between adjacent particles due to strain, leading to an increase of the tunnelling resistance [51,52]. The second is the sudden crack propagation in the last stages of the tests, causing a prevalent breakage of electrical pathways through the joint. However, some important differences between the aged and non-aged specimens can be found.

By deeply analysing the curves for the sample with 1 wt.% SDS, the electrical behaviour as a function of the applied strain changes is observed from the initial state to the 1-month aged sample. In the aged sample, softer behaviour is observed, due to the plasticisation effect. This effect causes a steadier response of the material, with no abrupt changes in the electrical monitoring, as adhesive deformation and crack propagation take place in a softer way. By increasing the ageing time, as discussed before, a secondary crosslinking is induced so the effect of plasticisation is reduced, showing a mixed behaviour between the initial state and the 1-month aged sample, as noticed in the right graph of Figure 7.5 (c), where an abrupt change of the electrical behaviour is observed.

The sample without surfactant shows similar behaviour. At the initial state, some abrupt changes in the electrical resistance are observed, while the effect of plasticisation is clearly shown after 1 month of ageing (left graph of Figure 7.5 (b)). By increasing the ageing time, the stiffening effect of the secondary crosslinking is also observed by abrupt changes in the electrical behaviour. In this case, as noticed before in the mechanical response, the behaviour of the 2-month aged sample is more similar to the non-aged one.

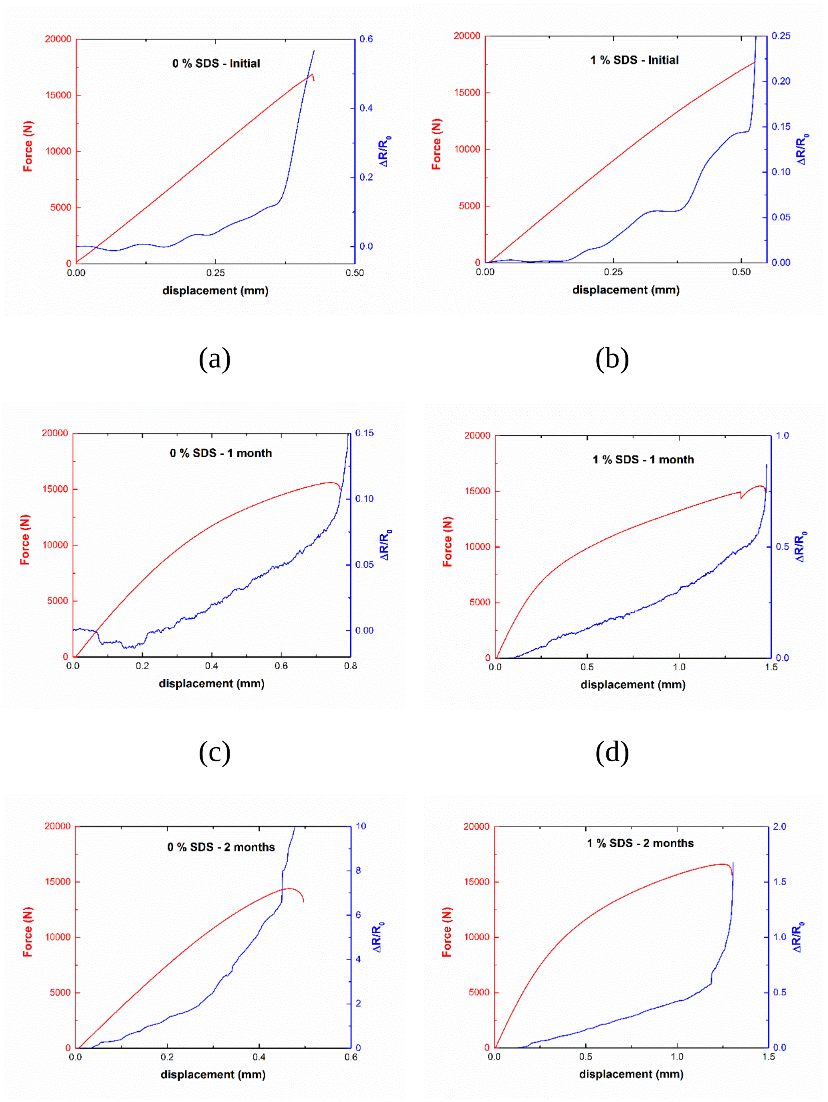

(a) (b)

(c) (d)

(e) (f)

Figure 7.5: Electromechanical curves for SLS specimens with (left) no surfactant and (right) 1 wt.% SDS at (a) initial state and (b) after 1 and (c) 2 months of water immersion.

These initial results can give a good qualitative approximation of how aged and non-aged samples behave and prove the capability of CNT reinforced joints to properly monitor their mechanical behaviour by means of electrical measurements. However, from the electrical response, it is possible to obtain estimations regarding damage evolution. To achieve this purpose, a simple analytical model, based on the tunnelling effect of CNT reinforced polymers is proposed.

7.3.5 Theoretical approach

The CNT reinforced adhesive film is modelled as a nanocomposite with an homogeneous CNT distribution. The changes in the electrical resistance can be divided into two terms, the first one depends on the changes due to the tunnelling effect between adjacent nanoparticles and the second one is correlated to the breakage of electrical pathways due to the effect of damage accumulation, as shown in the schematics of **Figure 7.6**, leading to the following expression:

$$\Delta R_{total} = \Delta R_{tunnel} + \Delta R_{damage} \tag{9.1}$$

The tunnelling effect can be calculated by using the well-known Simmons formula for the tunnelling resistance [53]:

$$R_{tunnel} = At \cdot e^{bt} \tag{9.2}$$

where A and b are two constants depending on the CNT geometry and matrix barrier characteristics and t is the tunnelling distance, which changes with the applied strain.

The changes due to damage accumulation are not easy to model. There are many studies investigating this effect by proposing different damage evolution laws [54,55], but the particularities of the tested systems make the damage calculation very difficult. Therefore, damage accumulation is estimated by comparing the measured changes in the electrical resistance and the known tunnelling effect.

$$\Delta R_{damage} = \Delta R_{measured} - \Delta R_{tunnel} \tag{9.3}$$

For this purpose, the initial tunnelling distance is calculated as the distance that best fits the initial changes of the electrical resistance, where no damage is supposed.

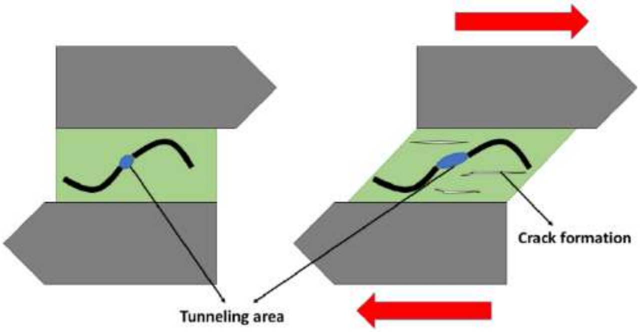

Figure 7.6: Schematics of electromechanical behaviour in a SLS test showing the increase of tunnelling distance and crack nucleation inside the adhesive.

Figure 7.7 shows the comparison between the theoretical line, taking only the tunnelling effect and the experimental measurements for aged and non-aged samples with 1 wt.% SDS into account. The pattern areas indicate the differences between the theoretical and the experimental ones being, thus, the damage accumulation during the SLS test.

The non-aged sample shows significant irregular behaviour. The threshold for damage accumulation is observed at ~0.25 mm displacement. After this point, the evolution of damage accumulation is very irregular. This can be explained due to the brittle mechanisms dominating the mechanical behaviour of the adhesive. Secondary cracks start to nucleate and then they coalesce around the main crack [56], inducing a higher breakage of electrical paths in a similar way than that observed in other studies for fatigue testing [57]. This nucleation is not uniform so the unstable damage accumulation is explained. In the case of 1-month aged samples, this damage accumulation starts to take place at 1 mm of displacement, that is, much later than in the non-aged specimen. This is in good agreement with the stated conclusions from water uptake and LSS measurements, as the induced plasticity in the first stages of water uptake avoids the early crack nucleation inside the adhesive joint. After that, damage accumulation takes places in a sudden way, that is, the cracks start to nucleate and then immediately coalesce. The 2-month aged sample has a damage threshold of 0.5 mm, lower than in the 1-month aged sample, due to the stiffening effect of the change in the water absorption mechanisms discussed above. Then, a softer evolution of damage accumulation is observed and finally, in the last stages of SLS tests a rapid coalescence takes place until final failure.

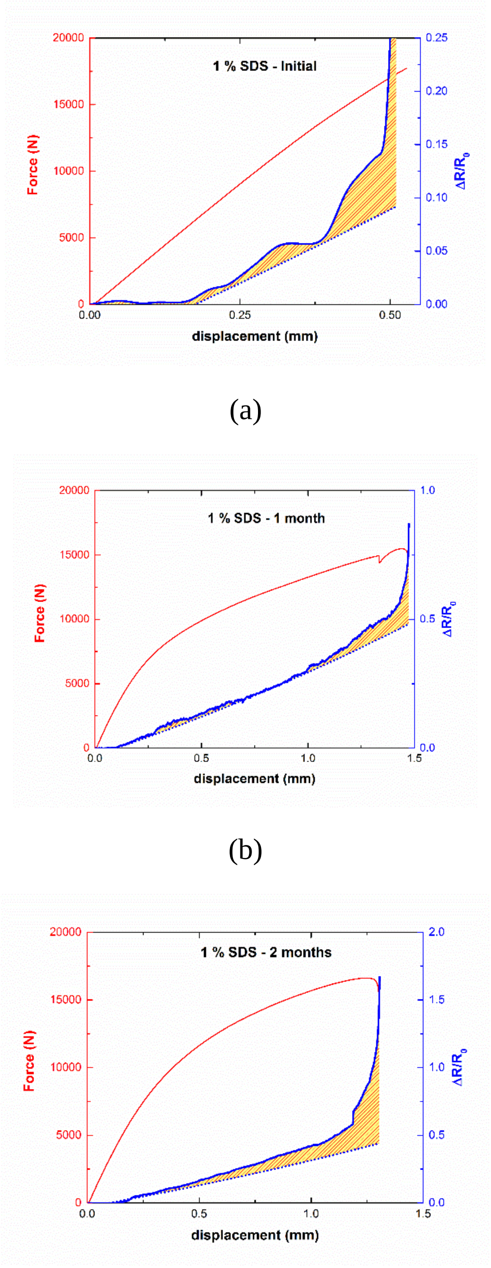

(a)

(b)

(c)

Figure 7.7: Damage accumulation evolution (red pattern area) by comparing experimental measurements (solid lines) and theoretical predictions (dashed lines) for 1 wt.% SDS samples at (a) initial state and (b) after 1 and (c) 2 months of ageing.

The previously described behaviour was similar in the case of the 0.25 wt.% SDS samples. However, in the case of the samples without surfactant, the electromechanical behaviour shows some slight differences regarding the 1 wt.% SDS samples, especially, concerning the sensitivity of the electrical response. Figure 7.8 presents the comparison between the theoretical and the experimental lines at different ageing times. At the initial state, similar behaviour for the 1 wt. % SDS samples is observed with abrupt changes in the electrical resistance, inducing a high damage accumulation rate due to the rapid nucleation and coalescence of micro-cracks inside the material. The 1-month aged specimen shows a much softer behaviour, as expected due to the plasticisation effect of the water uptake process. The threshold of damage accumulation is observed at a 0.7 mm displacement, that is, much later than for non-aged samples. However, unexpected behaviour is observed for the 2 month-aged sample. In this case, the threshold for damage accumulation is observed nearly at the beginning of the SLS tests, that is, earlier than in the case of non-aged specimens. In addition, the damage accumulation is very high also in comparison to the other specimens as they show a much higher sensitivity.

This behaviour can be explained by the interaction of two effects. One of them is due to the fact that the highly heterogeneous CNT distribution can induce high stress concentrations, leading to highly weak points in the matrix. This effect is also present in the non-aged and aged specimens, but in the case of the 2-month aged one, the stiffening effect induced by the change in the mechanism of water absorption previously described can lead also to much higher embrittlement of the adhesive. This can also be stated in the reduction of the displacement at failure, so that the nucleation and coalescence of microcavities takes place more rapidly. The second one is correlated to the different interactions between the larger agglomerates of CNTs (which are much more prevalent in the non-surfactant samples) and the water molecules. This promotes a different electromechanical behaviour than for the other samples.

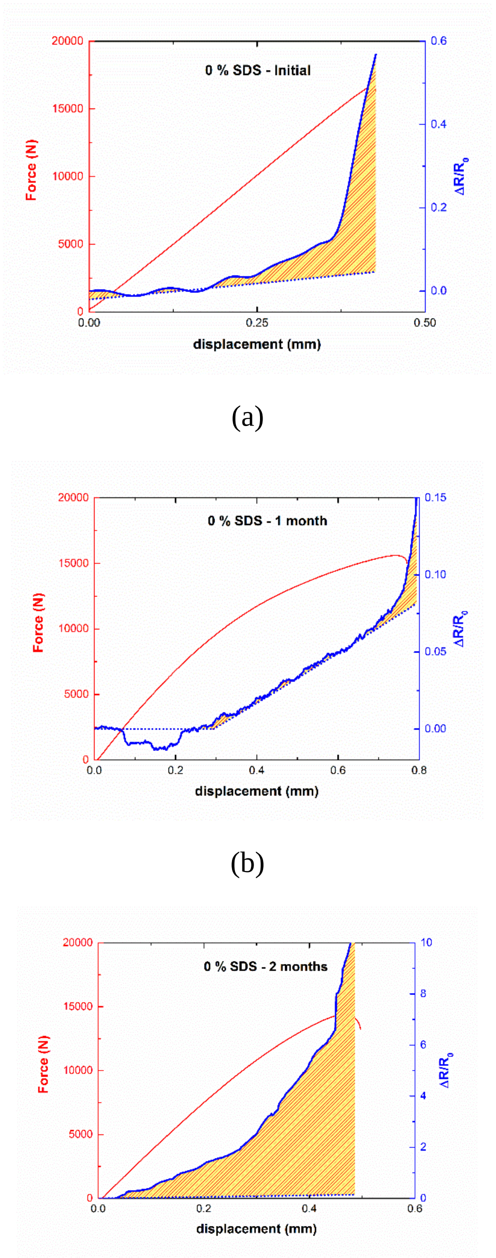

Figure 7.8: Damage accumulation evolution (red pattern area) by comparing experimental measurements (solid lines) and theoretical predictions (dashed lines) for non-surfactant samples at (a) initial state and (b) after 1 and (c) 2 months of ageing.

7.4 Conclusions

SLS joints with CNT-doped adhesive films have been tested under ageing conditions while their electromechanical properties have been monitored.

The water uptake measurements for the cured adhesive without substrate show that the behaviour does not change significantly with the addition of both CNTs and SDS surfactant. This is explained by the combined effect of the amphiphilic behaviour of the SDS and the barrier properties of CNT dispersion, acting in an opposite way.

The LSS of the bonded joints shows a general decrease after 1 month of ageing because of the plasticiser effect of the water, which promotes the creation of weak hydrogen bonds. This statement is also confirmed by an increase of the displacement at failure. After 2 months of ageing, there is a slight increase of LSS and a general reduction on the displacement at failure, which is explained by the secondary crosslinking that takes place due to water uptake saturation. In the case of the sample without surfactant, this behaviour is slightly different because of the poor CNT distribution that can induce higher embrittlement, leading to a sudden decrease of LSS even after 2 months of ageing.

Finally, the analysis of the electromechanical behaviour of SLS joints confirms the previously described statements. A higher plasticisation is observed for 1-month aged specimens, while a partial recovery of the stiffness is observed after 2 months. By comparing the measured electrical response with simple theoretical calculations, it is possible to obtain the first quantitative idea of damage accumulation and how ageing conditions affect the damage evolution. Therefore, this first estimation can be used to better understand the physical mechanisms taking place on CNT-doped adhesive joints under ageing conditions subjected to SLS tests.

As a future work, however, it would be necessary to refine the theoretical predictions by taking some effects such as CNT distribution and orientation or the barrier properties of the epoxy matrix into account. This could give more accurate knowledge of the physical behaviour of CNT-doped bonded joints under ageing conditions.

Acknowledgements

This work was supported by the Ministerio de Economía y Competitividad of Spanish Government (Project MAT2016-78825-C2-1-R) and the Comunidad de Madrid Government (Project P2013/MIT-2862).

7.5 References

[1] Hussey R, Wilson J. Structural Adhesives: Directory and Databook. : Springer Science & Business Media, 1996.

[2] Palaniappan J, Wang H, Ogin SL, Thorne AM, Reed GT, Crocombe AD et al. Changes in the reflected spectra of embedded chirped fibre Bragg gratings used to monitor disbonding in bonded composite joints. Composites Sci Technol 2007;67:2847-53.

[3] Palaniappan J, Ogin SL, Thorne AM, Reed GT, Crocombe AD, Capell TF et al. Disbond growth detection in composite-composite single-lap joints using chirped FBG sensors. Composites Sci Technol 2008;68:2410-7.

[4] Bernasconi A, Carboni M, Comolli L. Monitoring of fatigue crack growth in composite adhesively bonded joints using fiber Bragg gratings. Procedia Engineering 2011;10:207-12.

[5] Ruoff RS, Lorents DC. Mechanical and thermal properties of carbon nanotubes. carbon 1995;33:925-30.

[6] Yu MF, Lourie O, Dyer MJ, Moloni K, Kelly TF, Ruoff RS. Strength and breaking mechanism of multiwalled carbon nanotubes under tensile load. Science 2000;287:637-40.

[7] De Volder MFL, Tawfick SH, Baughman RH, Hart AJ. Carbon Nanotubes: Present and Future Commercial Applications. Science 2013;339:535-9.

[8] Allaoui A, Bai S, Cheng H, Bai J. Mechanical and electrical properties of a MWNT/epoxy composite. Composites Sci Technol 2002;62:1993-8.

[9] Bryning MB, Islam MF, Kikkawa JM, Yodh AG. Very Low Conductivity Threshold in Bulk Isotropic Single-Walled Carbon Nanotube–Epoxy Composites. Adv Mater 2005;17:1186-91.

[10] Hu N, Masuda Z, Yan C, Yamamoto G, Fukunaga H, Hashida T. The electrical properties of polymer nanocomposites with carbon nanotube fillers. Nanotechnology 2008;19:215701.

[11] Wang M, Zhang K, Dai X, Li Y, Guo J, Liu H et al. Enhanced electrical conductivity and piezoresistive sensing in multi-wall carbon nanotubes/polydimethylsiloxane nanocomposites via the construction of a self-segregated structure. Nanoscale 2017;9:11017-26.

[12] Gibson RF. A review of recent research on mechanics of multifunctional composite materials and structures. Composite Structures 2010;92:2793-810.

[13] Ferreira ADBL, Nóvoa PRO, Marques AT. Multifunctional Material Systems: A state-of-the-art review. Composite Structures 2016;151:3-35.

[14] Li C, Thostenson ET, Chou T. Sensors and actuators based on carbon nanotubes and their composites: A review. Composites Sci Technol 2008;68:1227-49.

[15] Hu N, Karube Y, Arai M, Watanabe T, Yan C, Li Y et al. Investigation on sensitivity of a polymer/carbon nanotube composite strain sensor. Carbon 2010;48:680-7.

[16] Gong S, Zhu Z. Giant piezoresistivity in aligned carbon nanotube nanocomposite: account for nanotube structural distortion at crossed tunnel junctions. Nanoscale 2015;7:1339-48.

[17] Pu J, Zha X, Zhao M, Li S, Bao R, Liu Z et al. 2D end-to-end carbon nanotube conductive networks in polymer nanocomposites: a conceptual design to dramatically enhance the sensitivities of strain sensors. Nanoscale 2018.

[18] Vietri U, Guadagno L, Raimondo M, Vertuccio L, Lafdi K. Nanofilled epoxy adhesive for structural aeronautic materials. Composites Part B-Engineering 2014;61:73-83.

[19] Gude MR, Prolongo SG, Urena A. Toughening effect of carbon nanotubes and carbon nanofibres in epoxy adhesives for joining carbon fibre laminates. Int J Adhes Adhes 2015;62:139-45.

[20] Akpinar IA, Gültekin K, Akpinar S, Akbulut H, Ozel A. Research on strength of nanocomposite adhesively bonded composite joints. Composites Part B: Engineering 2017;126:143-52.

[21] Akpinar IA, Gültekin K, Akpinar S, Akbulut H, Ozel A. Experimental analysis on the single-lap joints bonded by a nanocomposite adhesives which obtained by adding nanostructures. Composites Part B: Engineering 2017;110:420-8.

[22] Lim AS, Melrose ZR, Thostenson ET, Chou T. Damage sensing of adhesively-bonded hybrid composite/steel joints using carbon nanotubes. Composites Sci Technol 2011;71:1183-9.

[23] Mactabi R, Rosca ID, Hoa SV. Monitoring the integrity of adhesive joints during fatigue loading using carbon nanotubes. Composites Sci Technol 2013;78:1-9.

[24] Kang M, Choi J, Kweon J. Fatigue life evaluation and crack detection of the adhesive joint with carbon nanotubes. Composite Structures 2014;108:417-22.

[25] Sandler J, Shaffer M, Prasse T, Bauhofer W, Schulte K, Windle A. Development of a dispersion process for carbon nanotubes in an epoxy matrix and the resulting electrical properties. Polymer 1999;40:5967-71.

[26] Prolongo SG, Buron M, Gude MR, Chaos-Moran R, Campo M, Urena A. Effects of dispersion techniques of carbon nanofibers on the thermo-physical properties of epoxy nanocomposites. Composites Sci Technol 2008;68:2722-30.

[27] Chakraborty AK, Plyhm T, Barbezat M, Necola A, Terrasi GP. Carbon nanotube (CNT)–epoxy nanocomposites: a systematic investigation of CNT dispersion. Journal of Nanoparticle Research 2011;13:6493-506.

[28] Sánchez-Romate XF, Sánchez M, García-Nieto C, Molinero J, Jiménez-Suárez A, Güemes A et al. Structural health monitoring of bonded joints using carbon nanotube doped adhesive films. Eur Workshop Struct Health Monit , EWSHM 2016;4:2450-5.

[29] Sánchez-Romate XF, Jiménez-Suarez A, Molinero J, Sánchez M, Güemes A, Ureña A. Development of Bonded Joints Using Novel CNT Doped Adhesive Films: Mechanical and Electrical Properties. International Journal of Adhesion and Adhesives 2018.

[30] Vaisman L, Wagner HD, Marom G. The role of surfactants in dispersion of carbon nanotubes. Adv Colloid Interface Sci 2006;128:37-46.

[31] Rastogi R, Kaushal R, Tripathi SK, Sharma AL, Kaur I, Bharadwaj LM. Comparative study of carbon nanotube dispersion using surfactants. J Colloid Interface Sci 2008;328:421-8.

[32] Moshammer K, Hennrich F, Kappes MM. Selective suspension in aqueous sodium dodecyl sulfate according to electronic structure type allows simple separation of metallic from semiconducting single-walled carbon nanotubes. Nano Research 2009;2:599-606.

[33] Zhao P, Einarsson E, Lagoudas G, Shiomi J, Chiashi S, Maruyama S. Tunable separation of single-walled carbon nanotubes by dual-surfactant density gradient ultracentrifugation. Nano Research 2011;4:623-34.

[34] Fernández Sánchez-Romate XX, Molinero J, Jiménez-Suárez A, Sánchez M, Güemes A, Ureña A. Carbon Nanotube Doped Adhesive Films for Detecting Crack Propagation on Bonded Joints: A Deeper Understanding of Anomalous Behaviors. ACS applied materials & interfaces 2017.

[35] Lawrence A, Pearson J. Electrical properties of soap water amphiphile systems. Electrical conductance and sodium ion activity of aqueous 2% sodium dodecyl sulphate with added homologous n-aliphatic C 2–7 alcohols. Transactions of the Faraday Society 1967;63:495-504.

[36] Song Y, Wang F, Guo G, Luo S, Guo R. Amphiphilic-Polymer-Coated Carbon Nanotubes as Promoters for Methane Hydrate Formation. Acs Sustainable Chemistry & Engineering 2017;5:9271-8.

[37] Garcia C, Sanchez M, Urena A, Rams J. Carbon Nanotubes for Assessing the Structural Integrity of Composite Bonded Joints with Film Adhesives. Structural Health Monitoring 2015: System Reliability for Verification and Implementation, Vols.1 and 2 2015:2169-76.

[38] Weiss J, Voigt M, Kunze C, Sanchez JEH, Possart W, Grundmeier G. Ageing mechanisms of polyurethane adhesive/steel interfaces. Int J Adhes Adhes 2016;70:167-75.

[39] Mora VB, Mieloszyk M, Ostachowicz W. Model of moisture absorption by adhesive joint. Mechanical Systems and Signal Processing 2018;99:534-49.

[40] Gurtin ME, Yatomi C. On a model for two phase diffusion in composite materials. J Composite Mater 1979;13:126-30.

[41] Bal S, Saha S. Effect of sea and distilled water conditioning on the overall mechanical properties of carbon nanotube/epoxy composites. Int J Damage Mech 2017;26:758-70.

[42] Kondrashov S, Merkulova YI, Marakhovskii P, D'yachkova T, Shashkeev K, Popkov O et al. Degradation of physicomechanical properties of epoxy nanocomposites with carbon nanotubes upon heat and humidity aging. Russian Journal of Applied Chemistry 2017;90:788-96.

[43] Prolongo SG, Gude MR, Urena A. Water uptake of epoxy composites reinforced with carbon nanofillers. Composites Part A-Applied Science and Manufacturing 2012;43:2169-75.

[44] Liu L, Tan SJ, Horikawa T, Do D, Nicholson D, Liu J. Water adsorption on carbon-A review. Adv Colloid Interface Sci 2017.

[45] Bystrzejewski M, Huczko A, Lange H, Gemming T, Büchner B, Rümmeli MH. Dispersion and diameter separation of multi-wall carbon nanotubes in aqueous solutions. Journal of Colloid and Interface Science 2010;345:138-42.

[46] Kastrisianaki-Guyton ES, Chen L, Rogers SE, Cosgrove T, van Duijneveldt JS. Adsorption of sodium dodecylsulfate on single-walled carbon nanotubes characterised using small-angle neutron scattering. Journal of Colloid and Interface Science 2016;472:1-7.

[47] Tsutsumi Y, Fujigaya T, Nakashima N. Polymer synthesis inside a nanospace of a surfactant–micelle on carbon nanotubes: creation of highly-stable individual nanotubes/ultrathin cross-linked polymer hybrids. RSC Advances 2014;4:6318-23.

[48] Xoan F. Sánchez-Romate, Alberto Jiménez-Suarez, Javier Molinero, Maria Sánchez, Alfredo Güemes and Alejandro Ureña. Development of Bonded Joints Using Novel CNT Doped Adhesive Films: Mechanical and Electrical Properties. Int J Adhes Adhes.

[49] Carter HG, Kibler KG. Langmuir-Type Model for Anomalous Moisture Diffusion In Composite Resins. J Composite Mater 1978;12:118-31.

[50] Popineau S, Rondeau-Mouro C, Sulpice-Gaillet C, Shanahan ME. Free/bound water absorption in an epoxy adhesive. Polymer 2005;46:10733-40.

[51] Thostenson ET, Chou T. Carbon nanotube networks: Sensing of distributed strain and damage for life prediction and self healing. Adv Mater 2006;18:2837.

[52] Li C, Thostenson ET, Chou T. Dominant role of tunneling resistance in the electrical conductivity of carbon nanotube-based composites. Appl Phys Lett 2007;91:223114.

[53] Simmons JG. Generalized formula for the electric tunnel effect between similar electrodes separated by a thin insulating film. J Appl Phys 1963;34:1793-803.

[54] Mao H, Mahadevan S. Fatigue damage modelling of composite materials. Composite Structures 2002;58:405-10.

[55] Pham K, Amor H, Marigo J, Maurini C. Gradient Damage Models and Their Use to Approximate Brittle Fracture. Int J Damage Mech 2011;20:618-52.

[56] Fiedler B, Hojo M, Ochiai S, Schulte K, Ando M. Failure behavior of an epoxy matrix under different kinds of static loading. Composites Sci Technol 2001;61:1615-24.

[57] Sbarufatti C, Sánchez-Romate XF, Scaccabarozzi D, Cinquemani S, Libonati F, Güemes A et al. On the dynamic acquisition of electrical signals for structural health monitoring of carbon nanotube doped composites. Struct Health Monit : Real-Time Mater State Aware Data-Driven Safety Assur - Proc Int Workshop on Struct Health Monit , IWSHM 2017;2:1921-8.

Chapter 8: Carbon Nanotube Doped Adhesive Films for Detecting Crack Propagation on Bonded Joints: A Deeper Understanding of Anomalous Behaviors

Xoan Xosé Fernández Sánchez-Romate[a,b,*], Javier Molinero[b], Alberto Jiménez-Suárez[b], María Sánchez[b], Alfredo Güemes[a] and Alejandro Ureña[b]

Published in ACS Appl Mater Inter 9, (2017), 43267-43274

[a] Department of Aerospace Materials and Processes, Escuela Técnica Superior de Ingenieros Aeronáuticos, Universidad Politécnica de Madrid, Plaza del Cardenal Cisneros 3, 28040 Madrid, Spain

[b] Materials Science and Engineering Area, Escuela Superior de Ciencias Experimentales y Tecnología, Universidad Rey Juan Carlos, Calle Tulipán s/n, 28933 Móstoles (Madrid), Spain

*Corresponding author: xoan.fernandez.sanchezromate@urjc Tel: +34 91 488 8252

A novel nanoreinforced adhesive film has been developed in order to detect adhesive deformation and crack propagation along the bonding line by means of the electrical response of the material. Adhesive films were doped by spraying an aqueous dispersion of carbon nanotubes (CNTs) over the surface. In order to determine the sensitivity of bonded joints, Single Lap Shear (SLS) and Mode-I fracture energy tests have been carried out while their electrical response has been measured. It has been found that CNT-doped adhesive films are able to detect adhesive deformation and final failure for SLS specimens and crack initiation and propagation along the bonding line for Mode-I specimens with a high sensitivity. Sudden increases on electrical resistance are correlated to a rapid growing of crack length due to instability on crack propagation in a tick-slip case, while specimens with a more uniform crack propagation are linked to a steadier increase on electrical resistance and both of them are properly correlated to the mechanical response. By analyzing more in detail the

electrical response and comparing with theoretical approaches, the stick-slip behavior is associated to the presence of porosity and lack of adhesive due to possible manufacturing issues such as adhesive overflowing. These statements are also validated by microstructural analysis. Therefore, the potential and applicability of the proposed adhesive film for evaluating the structural integrity has been demonstrated.

8.1 Introduction

In the last decades, the use of polymer-based composite structures has increased, due to their exceptional specific performance and durability in comparison to traditional alloys. This has made it possible their implementation in aircraft primary structures. In this regard, due to the complexity of these structures, joining techniques are often necessary to assembly different components.

CFRP structural joints can be made using several methods as mechanical fastening or adhesive bonding. Particularly, adhesive joints present many advantages over fastened joints such as a good distribution of joint stresses and good fatigue and impact characteristics [1]. However, their inspection is not easy and requires complex non-destructive methods to ensure their reliability [2-4].

For these reasons, the development of Structural Health Monitoring (SHM) methods to predict joint quality and reliability during service life is attracting the interest of many researchers [5-8]. Most of these techniques are based on Fiber Bragg Grating sensors [5,6] and guided Lamb waves [7,8] to detect debonding along the joint but they still have many limitations as they usually give only a local information about damage or their signal interpretation is not easy. Therefore, it is necessary to develop another SHM techniques to properly detect damage growth in adhesive joints.

The use of carbon nanotubes (CNTs), since their discovery [9], has increased due to their exceptional both mechanical and physical properties [10-15]. For that reasons, there are a high variety of applications where they can be used, such as highly thermal conductivity devices[16], rechargeable batteries or automotive parts [17]. More specifically, their addition into an insulator resin enhances its electrical performance, giving conductive pathways [18-20]. Due to their piezoresistivity behavior and tunneling effect between CNTs, they are often used as strain sensors [21,22].

In this context, this study aims to use CNT-doped adhesives in order to detect crack propagation along bonded joints. To date, there are many research on SHM in bonded joints with paste adhesives [23-26] but sensing capabilities of adhesive films have not been demonstrated. For these purposes a novel CNT-doped adhesive film is going to be used. Adhesive films are widely used in structural applications due to their easier handling and placement, allowing better control of the bonding line thickness [27]. In addition, CNT-based thin films have been proved to have an exceptional sensitivity as strain sensors [28-30].

In a previous study [31], many electrical measurements were carried out in a manually CNT-doped adhesive films in order to prove the viability of the technology. In this study, the addition of CNTs to an adhesive film is carried out by spraying an aqueous dispersion of carbon nanotubes over the surface as it has been proved as an effective way of CNT deposition onto thin films [32,33]. In this regard, CNT dispersion, which is a critical factor on sensing capabilities, is controlled by the addition of a surfactant (sodium dodecyl sulfate, SDS) which improves dispersion state of CNTs [34-36]. In addition, SDS content was previously optimized [37] in order to get the highest electrical and mechanical properties of the joint.

Electromechanical properties of bonded joints with adhesive films have been evaluated by testing Single Lap Shear (SLS) and Mode-I specimens. The aim is to characterize the electrical properties as a function of mechanical loads. More specifically, Mode-I tests allow to correlate the electrical response with the mechanical one as a function of crack length, so the extent of damage can be clearly evaluated.

Furthermore, experimental results have been also correlated with theoretical predictions in order to detect possible anomalous behaviors and a microstructural analysis has been carried out. The aim is to have an idea of the extent of damage by comparing theoretical predictions, by using simple analytical modeling, with experimental measurements, similarly to CNT-doped nanocomposites [38-40] and thin films [41,42]. This would lead to a better understanding of crack propagation and monitoring of adhesive joints.

8.2 Methods

8.2.1 CNT dispersions

Carbon nanotubes are supplied by Nanocyl with the commercial name NC7000. They have an average diameter of 11 nm and a length of 2 µm. CNTs are dispersed in water in a weight fraction of 0.1 % with the help of a surfactant (in order to stabilize the CNT dispersion) called sodium dodecyl sulfate (SDS) at 0.25 wt. %. This CNT dispersion was, then, sonicated during 20 min at 80 % amplitude and 0.5 s of acoustic irradiation time using a horn sonicator UP400S supplied by Hielscher, as shown in the schematics of Figure 8.1 (a).

CNT dispersion was then sprayed over the adhesive film surface with an airbrush (Figure 8.1 (b)) at a pressure of 1 bar and at distance of 40 cm, during 0.5 s. These parameters were set in order to achieve a better homogenization of CNT dispersion over the film.

The adhesive film was a FM 300K, supplied by Cytec. It is an epoxy based adhesive with a wide open knit tricot carrier, shown in Figure 8.1 (c), which allows a better thickness control during curing.

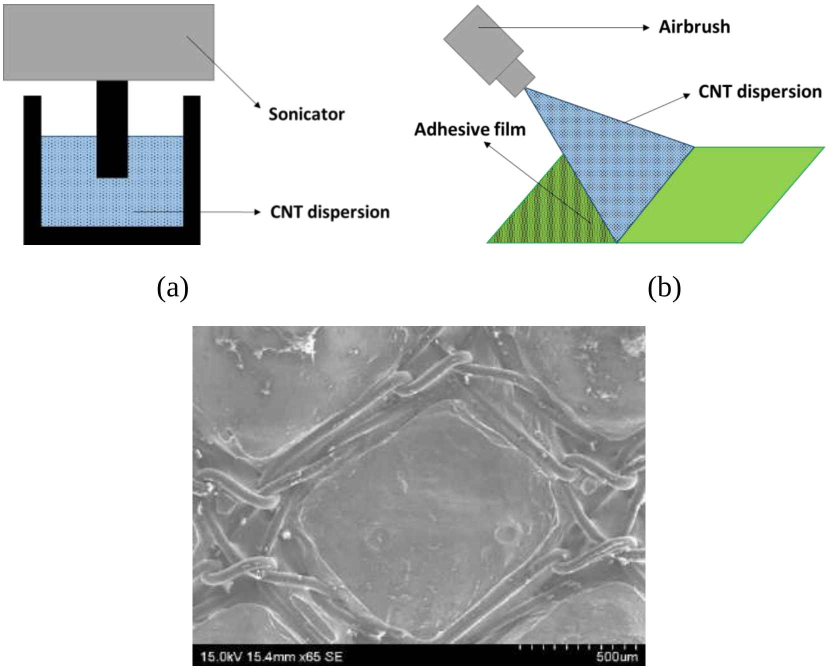

(a) (b)

(c)

Figure 8.1: Schematics of the (a) CNT dispersion by means of ultrasonication, (b) addition to adhesive layer by spraying and (c) adhesive film structure showing the carrier.

8.2.2 Joint manufacturing

Adhesive joints were manufactured in a hot press by secondary bonding of CFRP unidirectional substrates, supplied by Fundación para la Investigación, Desarrollo y Aplicación de Materiales Compuestos (FIDAMC). Curing cycle was set as shown in Table 8.1 based in the supplier requirements for this type of adhesive.

The analysis of transversal joints and fractured surfaces has been carried out by Scanning electron microscopy (SEM) using a S-3400N apparatus from Hitachi, as well as by using an optical profilometer ZETA Z-20.

Table 8.1: Cure cycle parameters of secondary bonding.

Parameter	First Stage	Second stage
pressure	Ramp from 0 to 0.6 MPa during 15 min	0.6 MPa during 90 min
temperature	Ramp from 25 to 175 ºC during 45 min	175 ºC during 60 min

8.2.3 Electromechanical tests

Single Lap Shear and Mode-I tests have been conducted according to standards ASTM D5868-01 and ISO 25217:2009, respectively. For Mode-I tests, a video-camera was used to record crack propagation during the tests. In order to see the crack length clearer, the edges were white painted and several marks were made.

The monitoring of the adhesive joints was carried out by means of electrical resistance measurements between two points through thickness as shown in the schematics of Figure 8.2. Electrodes were made of copper wire attached to the substrate surface with silver ink in order to ensure a good electrical contact. An adhesive layer was also used to protect them from environmental influences. The measurements were done using an Agilent 34410A hardware.

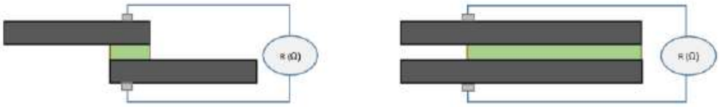

Figure 8.2: Schematics of the electrode disposition for (left) SLS and (right) Mode-I joints.

8.3 Results and discussion

8.3.1 Microstructural analysis of CNT doped adhesives

Prior to analyze the electromechanical behavior of the adhesive joints, it is necessary to get a deeper knowledge about the CNT dispersion into the adhesive film. In a previous study [37], an analysis of the influence of the dispersion procedure was carried out, by varying the sonication time and surfactant content leading to an optimized weight fraction of 0.25 and 0.1 % of SDS surfactant and CNTs respectively in the aqueous solution. FEG-SEM images of Figure 8.3 show the CNT structure in the adhesive film once cured for these conditions. Figure 8.3 (a) and (b) show the structure of the cured adhesive film and the presence of embedding CNTs during curing by observing the pull-out effect on a fractured adhesive, respectively. That embedding contributes to the creation of electrical paths through the joint which leads, thus, to a drastic electrical conductivity increase, being that the basis for SHM applications.

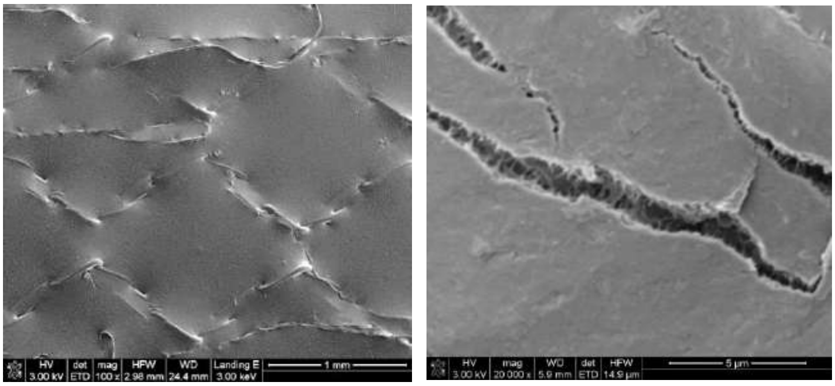

(a) (b)

Figure 8.3: FEG-SEM images showing (a) the adhesive surface after curing and a (b) fractured area with a CNT pull-out effect.

8.3.2 Single Lap Shear Tests

Single Lap shear tests on bonded joints with CNT doped adhesive films have been conducted while their electrical response has been measured.

The influence of CNT addition on Lap Shear Strength (LSS) has been studied previously [37], showing that it does not affect significantly the mechanical performance of adhesive joints, with even an increase of the LSS when adding a 0.25 wt. % surfactant. In addition, the failure mode for both neat and CNT reinforced adhesive is cohesive. Therefore, this work is going to be focused on the electromechanical behavior.

Figure 8.4 shows an example of the electrical monitoring of SLS specimens. It is observed that electrical resistance increases with displacement. This increase is more prevalent just before the final failure of the joint whereas at an initial stage the variation is not significant. It can be associated to the combination of two effects.

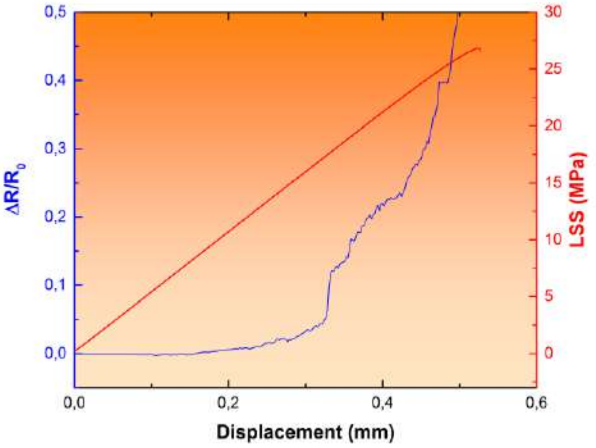

Figure 8.4: Electromechanical behavior of a SLS specimen.

On the one side, the distance between CNTs, also called tunneling distance, t, increases with displacement. This induces an increase on electrical resistance due to tunneling effect, following an exponential law as a function of the distance between adjacent particles dominating the electrical behavior in the first stages of SLS test.

On the other side, in the last stages of SLS testing, there is a breakage of electrical paths due to crack initiation and propagation along the bonding line, inducing, thus, an increase on the electrical resistance through thickness as shown in Figure 8.5. Both effects, therefore, lead to a more prevalent changes of the electrical response of the joint, which is in good agreement with other results for fatigue testing using CNT doped paste adhesives [24,25]. Thus, it implies that these CNT joints have higher sensitivities, defined as the change on the electrical normalized resistance divided by the applied strain, $\frac{\Delta R}{R_0}/\varepsilon$, than on conventional nanocomposites subjected to tensile stress [43], especially in the last stages of the test, as stated previously.

Thus, monitored single lap shear tests prove the high sensitivity of CNT doped adhesive films. However, they do not give detailed information about the correlation between mechanical and electrical behavior during crack propagation, as it takes places very rapidly so the correlation between crack length and electrical response remains to be investigated. For that reasons, Mode-I fracture energy tests on bonded joints with CNT-doped adhesive films have been conducted in order to see crack propagation along the bonding line. The aim is to correlate crack length to electrical response of bonded joint.

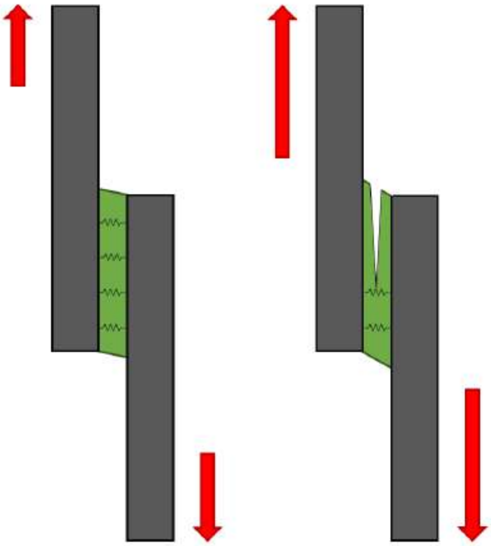

Figure 8.5: Schematics of conductive networks breakage due to crack propagation in SLS joints.

8.3.3 Mode-I mechanical tests

Mode-I adhesive fracture energy, GIC, has been calculated by using the corrected beam theory by Blackman et al. [44] with the following formula:

$$G_{IC} = \frac{3P\delta}{2B(a+|\Delta|)} \cdot \frac{1}{N} \tag{7.1}$$

Being P the applied load, δ the piano hinge displacement, B the specimen width, a the crack length and $|\Delta|$ a correction factor of crack length with is correlated to cubic root of compliance $(C/N)^{1/3}$. The compliance, C, is the ratio between displacement and load (δ/P) and N is a correction factor calculated by following this expression:

$$N = 1 - \left(\frac{l_2}{a}\right)^3 - \frac{9}{8}\left[1 - \left(\frac{l_2}{a}\right)^2\right]\frac{\delta l_1}{a^2} - \frac{9}{35}\left(\frac{\delta}{a}\right)^2 \tag{7.2}$$

Being l_1 the vertical distance between the piano hinge pin and the CFRP substrate mid plane and l_2 the horizontal from the pin to the edge of the piano hinge.

The value of GIC has been calculated for several crack lengths. Specifically, for each millimeter of the first 5 mm and at 10, 15, 20 and 25 mm from the crack initial length.

Figure 8.6 summarizes the mean value of GIC for the doped and neat adhesive joints. It is observed that the addition of carbon nanotubes do not affect significantly the fracture energy in Mode-I. The average value is slightly higher probably due the bridging effect of CNTs on the adhesive, making the crack propagation more difficult [45,46]. Moreover, the failure mode is identified as mainly cohesive for both doped and not doped adhesive in all cases which indicates a correct surface preparation and a good interaction between the adhesive layer and the CFRP substrate.

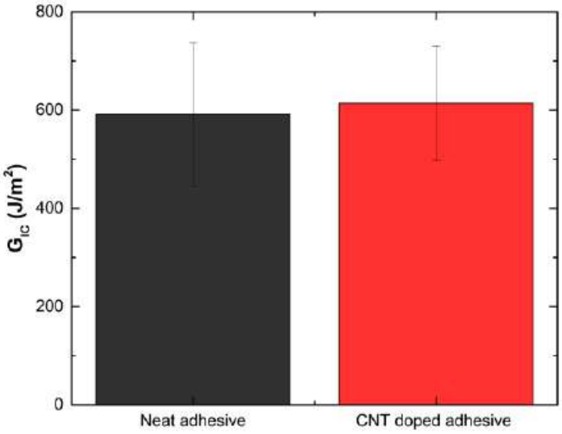

Figure 8.6: GIC values for the neat adhesive and the CNT doped Mode-I joints.

8.3.4 Electrical behavior of Mode-I joints

Figure 8.7 shows two examples of the electromechanical response of the joint as a function of piano hinge displacement.

It is observed that mechanical response can follow a uniform trend (Figure 8.7 (a)), associated to a more uniform crack propagation or sudden changes (Figure 8.7 (b)), correlated to sharp increases on the crack length followed by arrest phases. They are called stick-slip curves and their fractured surface usually follows a stick-slip pattern [47], also observed in Figure 8.7 (b). The reasons for this stick-slip behavior are usually correlated to high test rates [48,49] so in this case, where it was fixed at 1 mm/min in according to ASTM standard, it is necessary a deeper analysis.

In addition, by comparing the electrical response of the two specimens, a more stable increase on the electrical resistance is observed when mechanical behavior follows a uniform trend (Figure 8.7 (a)) whereas in stick-slip curves, the increase of the electrical resistance is more unstable, showing sudden increases and arrest phases (Figure 8.7 (b)).

By analyzing more in detail the electrical response of stick-slip curve, shown in Figure 8.7 (b), four regions can be distinguished: the first one (1) corresponds to crack initiation in which a drop on mechanical load takes places and it is correlated to a sudden increase on electrical resistance. Then there are many arrest phases (2) in which electrical resistance increases slightly and uniformly as crack propagation is slow which implies a more uniform breakage of electrical pathways; and sudden drops on mechanical performance (3) which are correlated to sudden increases on electrical resistance. They are associated to areas with fast crack propagation, inducing a sudden breakage of prevalent electrical pathways. In addition, an increase on the applied load can be observed when crack propagation is stopped (4) being the electrical resistance approximately steady as there are no breakage on electrical network and they are usually followed by sudden drops of the mechanical performance. It is also observed that the sharp increases of the electrical resistance are correlated to the darker bands of the fractured surface.

Therefore, these results show a good correlation between electrical and mechanical curves, proving the potential of this application for detecting crack growth and being an indicative of the extent of damage.

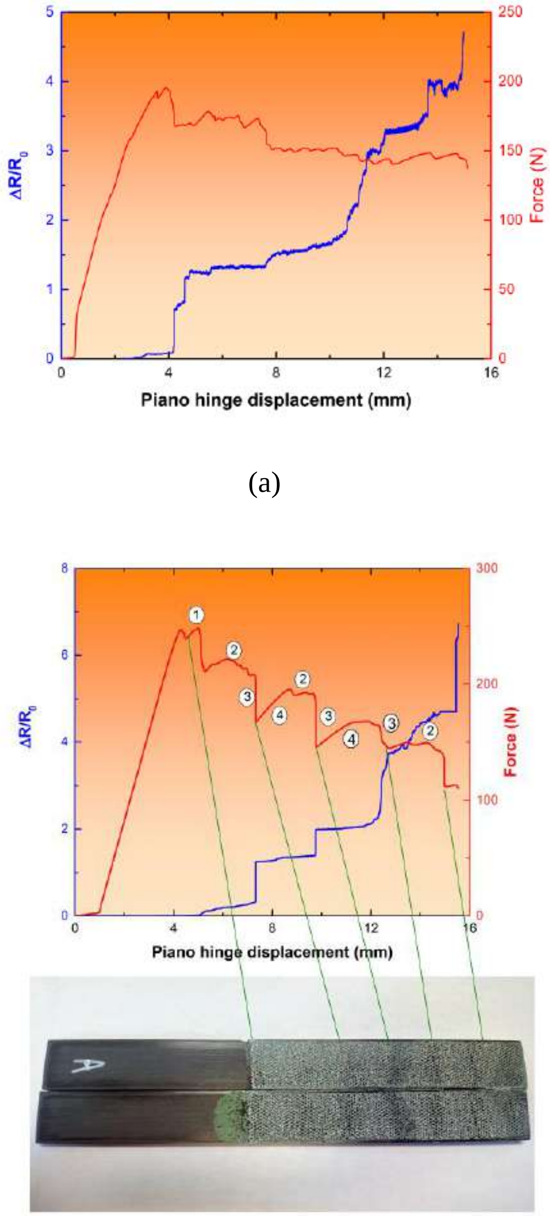

(a)

(b)

Figure 8.7: Electromechanical behavior of Mode-I joints in which (a) corresponds to a uniform crack propagation and (b) to a typical stick-slip behavior (the different areas are highlighted).

In order to properly understand the electromechanical response of the joint, it is necessary to get a deeper knowledge on how electrical response is affected by crack propagation. For that reasons, an exhaustive analysis of electrical properties as a function of crack length is carried out, by comparing the experimental measurements with the expected theoretical ones.

8.3.5 Theoretical and experimental analysis

Adhesive joint is modeled as an electrical circuit. Resistance is calculated by using the following formula, supposing that CNTs are homogeneously distributed along the bonding line and the electrical conductivity of CFRP substrate is considerably higher than the adhesive one. In addition, adhesive thickness is supposed to be perfectly controlled so that it is uniform along the joint:

$$R = \rho \cdot \frac{l}{A} \tag{7.3}$$

Being ρ is the resistivity, l the thickness of adhesive and A the cross-sectional area.

Crack propagation is modeled as a breakage of electrical pathways, so it affects the electrical resistance along the adhesive layer. Thus, at a crack length xa Equation (3) is rewritten as follows:

$$\frac{1}{R} = \frac{1}{\rho} \int_{x_a}^{x_0} \frac{b \cdot dx}{l} \tag{7.4}$$

Being b the width of the specimen and x the length of the joint.

Therefore, it is possible to find a direct correlation between electrical response and crack length. This would allow to evaluate both the extent of damage and joint quality which is the main objective of monitoring tests.

Test time and crack length are correlated by the crack propagation velocity, v, which is obtained from the test by applying the following formula:

$$\mathrm{v} = \frac{dx_a}{dt} \qquad \rightarrow \qquad \Delta x_a = v\Delta t \tag{7.5}$$

Figure 8.8 shows the comparison between experimental results and those predicted by the model as a function of crack length.

There are many differences that can be observed between theoretical predictions and experimental measurements. The first one is that the electrical resistance presents several sharp increases. Theoretically, this increase should be softer as shown in the dashed curves of Figure 8.8, being these sudden increases only observed in the time domain due to the rapid crack propagation, as commented before. This anomalous behavior can be explained by the presence of some defects such as porosity and overflowing which could affect the electrical properties by forming regions with higher CNT reinforcement or areas with lower adhesive thickness. These areas could lead to the creation of preferential conductive pathways and, thus, the breakage of these networks could induce a higher increase of the total electrical resistance. On the other hand, it is observed that theoretical predictions and experimental measurements follow a similar trend when crack propagation is more uniform, as shown in the central region of the uniform curve (Figure 8.8 (b)). Moreover, it is observed, as shown in the green curves, that sharp increases correspond to those regions in where crack propagates more rapidly, as expected by analyzing the previous time domain curves.

The presence of manufacturing defects in stick-slip behavior can be modeled as a gradient of electrical conductivity through the joint. By simplifying, adhesive joints can be modeled as a block diagram of areas with different conductivities/resistivities (Figure 8.9 (a)), so that the electrical resistance from Equation (6) can be calculated as follows:

$$\frac{1}{R} = \sum_{\mathrm{i}=0}^{\mathrm{n}} \frac{1}{\rho_0} \cdot \frac{\mathrm{b} \cdot \mathrm{x_i}}{\mathrm{l}} = \sum_{\mathrm{i}=0}^{\mathrm{n}} \frac{1}{\mathrm{R_i}} \qquad 7.6)$$

Where the i subscript denotes each one of the different blocks along the adhesive joint, being 0 the corresponding to the average resistivity through the joint and i=1,…,n the corresponding to each one of the stick-slip bands.

Supposing that when rapid crack propagation takes place many preferential electrical pathways are formed, that is, the electrical conductivity of this block is higher, it is possible to estimate the electrical behavior of the joint as a function of crack length. Figure 8.9 (b) shows the calculated normalized resistance for the stick-slip curve as a function of electrical conductivity, being d the correlation between the average resistivity (ρ_0) and the resistivity of the defected area (ρ_i), that is, $d = \frac{\rho_i}{\rho_0}$. A higher variation of electrical conductivity, thus, a higher d, implies a more prevalent presence of defects and irregularities through the joints (less homogeneous CNT distribution, high discontinuities, etc) which causes sharper increases of the electrical resistance. This explains the significant difference between the theoretical response in an ideal joint and the response in the real joint.

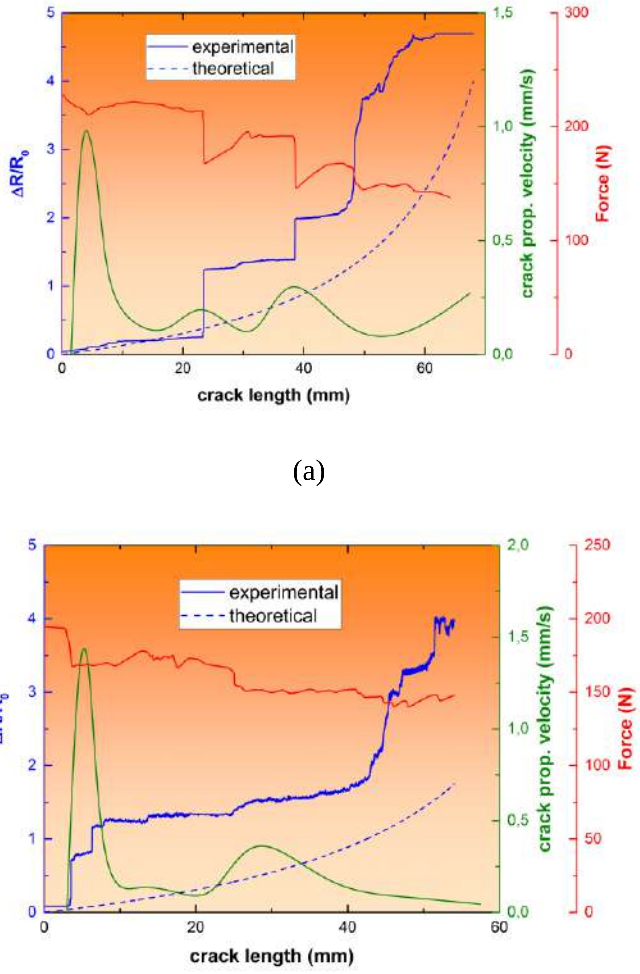

(a)

(b)

Figure 8.8: Electrical response of the Mode-I joints as a function of the crack length for (a) stick slip curve and (b) uniform crack propagation. Blue

lines correspond to measured (solid line) and theoretical (dash line) electrical resistance, green curves to crack velocity and red ones to measured force.

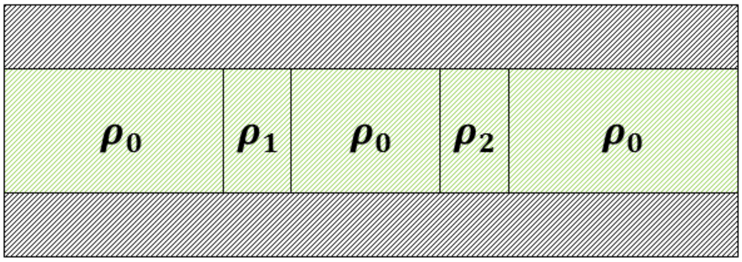

(a)

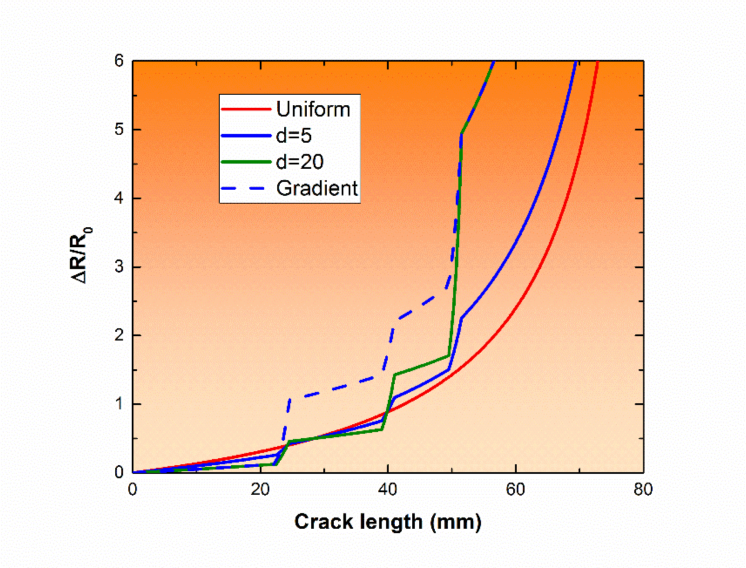

(b)

Figure 8.9: (a) Block distribution of electrical resistivity showing the stick-slip areas and (b) graph of normalized resistance comparing the uniform theoretical calculation with the stick-slip one; the dashed line indicates a case in which the resistivity of each stick-slip band is changing depending on defect magnitude.

Therefore, from electromechanical analysis, it can be concluded that unstable crack growing is correlated to the presence of defects within the joints.

8.3.6 Microstructural study of fractured surfaces

Figure 8.10 shows SEM images of adhesive joints. As commented before, the failure mode is cohesive. However, it is observed that the fractured surfaces, showing the characteristic carrier pattern, present regions with high (Figure 8.10 (a)) and lower presence of adhesive in both faces (Figure 8.10 (b)). This can be correlated to an induced porosity during curing. A SEM analysis of transversal joints proves that statement. An irregular distribution of porosity is observed along the joint, as shown in Figure 8.10 (c) and (d). This statement is also proved by profilometry analysis of fractured surfaces, as shown in Figure 8.11 with areas with high (Figure 8.11 (a)) and low (Figure 8.11 (b)) presence of adhesive. Moreover, it is observed that the areas with lower presence of adhesive are correlated to those regions in which crack propagation takes place in a sudden way (the dark bands of the fractured surface of Figure 8.7 (b)), proving the previous statements made in the theoretical analysis. In addition, no differences are observed when comparting neat adhesive joints and CNT reinforced ones.

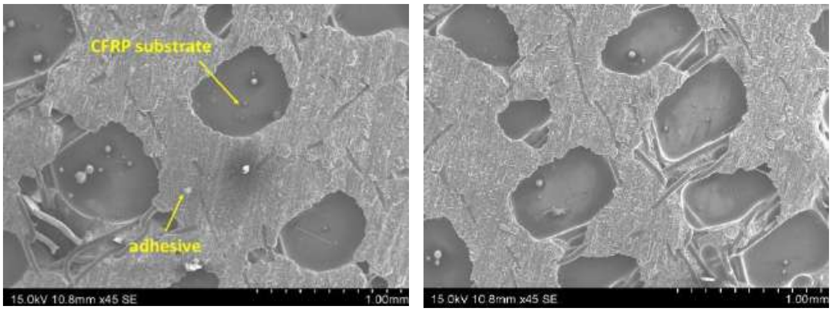

(a) (b)

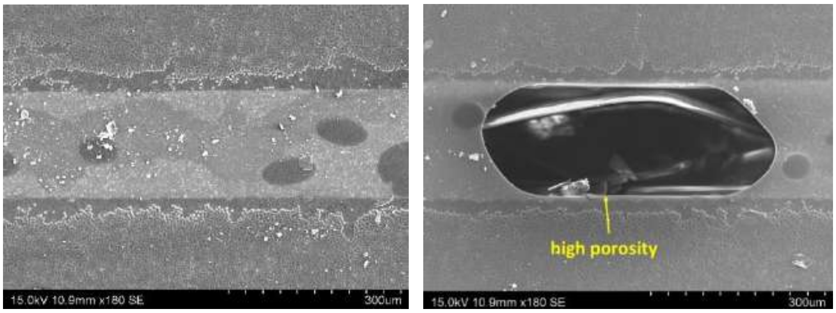

(c) (d)

Figure 8.10: SEM images of the adhesive joints showing the fractured areas with (a) higher and (b) lower presence of adhesive and the transervsal section showing regions with (c) higher presence of adhesive and (d) higher porosity.

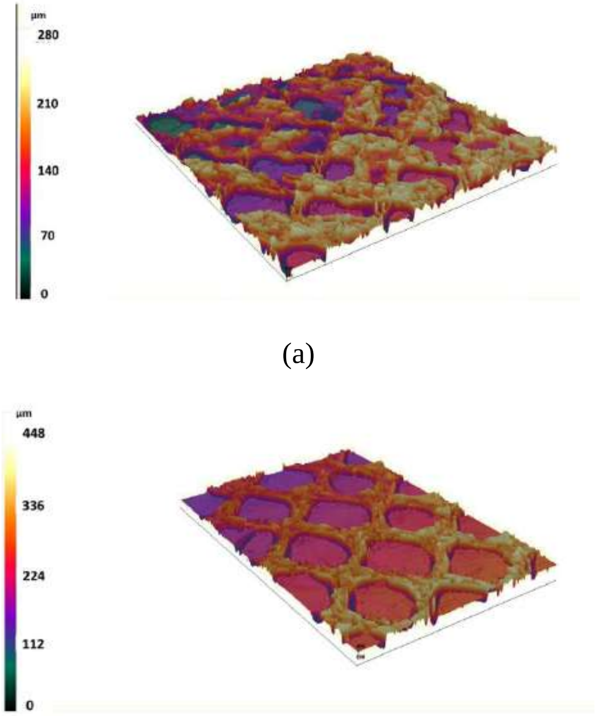

(a)

(b)

Figure 8.11: Profilometry images of fractured surfaces showing areas with (a) high and (b) low presence of adhesive.

Therefore, this porosity can be associated to manufacturing issues. The pressure distribution is uniaxial over the adhesive joint so it can induce some overflow effects, leading to an irregular distribution of the adhesive along the joint. An autoclave technology would probably improve the joint quality as it induces a uniform pressure along the three axes.

8.4 Conclusions

An innovative CNT-doped adhesive film has been developed in order to detect crack propagation along bonded joints due to electrical properties that carbon nanotubes provide to the adhesive. Electromechanical curves of SLS joints show that the electrical resistance increases with displacement due to a combinative effect of tunneling phenomenon and breakage of conductive pathways due to crack propagation.

To further investigate the electromechanical response of the adhesive joint, Mode-I joints were manufactured. They show a total correlation between electrical properties and mechanical response. It has been observed that a more unstable electrical behavior is observed in stick-slip curves while the increase of the electrical resistance is steadier when crack propagation is more uniform. In addition, by analyzing in detail the electromechanical behavior, it can be concluded that the regions in where crack propagates more rapidly are those in which the electrical resistance presents a sharp increase as a function of crack length which is not clearly explained by analytical analysis. This anomalous behavior is correlated to the presence of defects such as an irregular distribution of the adhesive, porosity or overflowing effects during curing and are closely associated to a stick-slip behavior. These statements were also proved by SEM and profilometry analysis of fractured surfaces.

In conclusion, the proposed adhesive films are able to properly monitor the integrity of bonded joints as well as explain some anomalous behaviors. In addition, some information about crack evolution velocity can be obtained. Therefore, although a deeper analysis of mechanical issues, such as test rate, fiber orientation, etc. would be valuable, as at first sight they present a huge potential and applicability for SHM applications.

Acknowledgements

This work was supported by the Ministerio de Economía y Competitividad of Spanish Government [Project MAT2016-78825-C2-1-R] and Comunidad de Madrid Government [Project P2013/MIT-2862]

8.5 References

[1] Peters ST. Handbook of composites. 2013.

[2] Johnson WS, Butkus LM. Designing for the durability of bonded structures. 1996;1:147-160.

[3] Zweschper T, Dillenz A, Busse G. NDE of adhesive joints and riveted structures with lock-in thermography methods. 2001:567-573.

[4] Tamborrino R, Palumbo D, Galietti U, Aversa P, Chiozzi S, Luprano VAM. Assessment of the effect of defects on mechanical properties of adhesive bonded joints by using non destructive methods. Composites Part B-Engineering 2016;91:337-345.

[5] Palaniappan J, Wang H, Ogin SL, Thorne AM, Reed GT, Crocombe AD, Rech Y, Tjin SC. Changes in the reflected spectra of embedded chirped fibre Bragg gratings used to monitor disbonding in bonded composite joints. Composites Sci Technol 2007;67(13):2847-2853.

[6] Palaniappan J, Ogin SL, Thorne AM, Reed GT, Crocombe AD, Capell TF, Tjin SC, Mohanty L. Disbond growth detection in composite-composite single-lap joints using chirped FBG sensors. Composites Sci Technol 2008;68(12):2410-2417.

[7] Habib F, Martinez M, Artemev A, Brothers M. Structural health monitoring of bonded composite repairs - A critical comparison between ultrasonic Lamb wave approach and surface mounted crack sensor approach. Composites Part B-Engineering 2013;47:26-34.

[8] Sherafat MH, Guitel R, Quaegebeur N, Hubert P, Lessard L, Masson P. Structural health monitoring of a composite skin-stringer assembly using

within-the-bond strategy of guided wave propagation. Mater Des 2016;90:787-794.

[9] Iijima S. Helical Microtubules of Graphitic Carbon. Nature 1991;354(6348):56-58.

[10] Ruoff RS, Lorents DC. Mechanical and thermal properties of carbon nanotubes. carbon 1995;33(7):925-930.

[11] Wong EW, Sheehan PE, Lieber CM. Nanobeam mechanics: Elasticity, strength, and toughness of nanorods and nanotubes. Science 1997;277(5334):1971-1975.

[12] Yu MF, Lourie O, Dyer MJ, Moloni K, Kelly TF, Ruoff RS. Strength and breaking mechanism of multiwalled carbon nanotubes under tensile load. Science 2000;287(5453):637-640.

[13] Smalley RE, Dresselhaus MS, Dresselhaus G, Avouris P. Carbon nanotubes: synthesis, structure, properties, and applications. 2003;80.

[14] Popov VN. Carbon nanotubes: properties and application. Materials Science and Engineering: R: Reports 2004;43(3):61-102.

[15] Wang M, Li T, Yao Y, Lu H, Li Q, Chen M, Li Q. Wafer-scale transfer of vertically aligned carbon nanotube arrays. J Am Chem Soc 2014;136(52):18156-18162.

[16] Wang M, Chen H, Lin W, Li Z, Li Q, Chen M, Meng F, Xing Y, Yao Y, Wong C. Crack-free and scalable transfer of carbon nanotube arrays into flexible and highly thermal conductive composite film. ACS applied materials & interfaces 2013;6(1):539-544.

[17] De Volder MFL, Tawfick SH, Baughman RH, Hart AJ. Carbon Nanotubes: Present and Future Commercial Applications. Science 2013;339(6119):535-539.

[18] Song YS, Youn JR. Influence of dispersion states of carbon nanotubes on physical properties of epoxy nanocomposites. Carbon 2005;43(7):1378-1385.

[19] Simien D, Fagan JA, Luo W, Douglas JF, Migler K, Obrzut J. Influence of nanotube length on the optical and conductivity properties of thin single-wall carbon nanotube networks. Acs Nano 2008;2(9):1879-1884.

[20] Khan SU, Pothnis JR, Kim J. Effects of carbon nanotube alignment on electrical and mechanical properties of epoxy nanocomposites. Composites Part A-Applied Science and Manufacturing 2013;49:26-34.

[21] Thostenson ET, Chou T. Carbon nanotube networks: Sensing of distributed strain and damage for life prediction and self healing. Adv Mater 2006;18(21):2837-+.

[22] Hu N, Karube Y, Arai M, Watanabe T, Yan C, Li Y, Liu Y, Fukunaga H. Investigation on sensitivity of a polymer/carbon nanotube composite strain sensor. Carbon 2010;48(3):680-687.

[23] Lim AS, Melrose ZR, Thostenson ET, Chou T. Damage sensing of adhesively-bonded hybrid composite/steel joints using carbon nanotubes. Composites Sci Technol 2011;71(9):1183-1189.

[24] Mactabi R, Rosca ID, Hoa SV. Monitoring the integrity of adhesive joints during fatigue loading using carbon nanotubes. Composites Sci Technol 2013;78:1-9.

[25] Kang M, Choi J, Kweon J. Fatigue life evaluation and crack detection of the adhesive joint with carbon nanotubes. Composite Structures 2014;108:417-422.

[26] Kim C, Choi J, Kweon J. Defect detection in adhesive joints using the impedance method. Composite Structures 2015;120:183-188.

[27] Hussey R, Wilson J. Structural Adhesives: Directory and Databook. 1996.

[28] Li X, Levy C, Elaadil L. Multiwalled carbon nanotube film for strain sensing. Nanotechnology 2008;19(4):045501.

[29] Park M, Kim H, Youngblood JP. Strain-dependent electrical resistance of multi-walled carbon nanotube/polymer composite films. Nanotechnology 2008;19(5):055705.

[30] Vemuru SM, Wahi R, Nagarajaiah S, Ajayan PM. Strain sensing using a multiwalled carbon nanotube film. J Strain Anal Eng Des 2009;44(7):555-562.

[31] Garcia C, Sanchez M, Urena A, Rams J. Carbon Nanotubes for Assessing the Structural Integrity of Composite Bonded Joints with Film Adhesives. Structural Health Monitoring 2015: System Reliability for Verification and Implementation, Vols.1 and 2 2015:2169-2176.

[32] Robert C, Feller JF, Castro M. Sensing Skin for Strain Monitoring Made of PC-CNT Conductive Polymer Nanocomposite Sprayed Layer by Layer. Acs Applied Materials & Interfaces 2012;4(7):3508-3516.

[33] De Pascali G, Melisi D, Valentini M, Valentini A, Nitti MA, Nasi R, Casamassima G, Ambrico PF, Cardone A. Spray deposited carbon nanotubes for organic vapor sensors. Microelectron J 2014;45(12):1691-1694.

[34] Islam MF, Rojas E, Bergey DM, Johnson AT, Yodh AG. High weight fraction surfactant solubilization of single-wall carbon nanotubes in water. Nano Letters 2003;3(2):269-273.

[35] Yu J, Grossiord N, Koning CE, Loos J. Controlling the dispersion of multi-wall carbon nanotubes in aqueous surfactant solution. Carbon 2007;45(3):618-623.

[36] Rastogi R, Kaushal R, Tripathi SK, Sharma AL, Kaur I, Bharadwaj LM. Comparative study of carbon nanotube dispersion using surfactants. J Colloid Interface Sci 2008;328(2):421-428.

[37] Sánchez-Romate XF, Sánchez M, García-Nieto C, Molinero J, Jiménez-Suárez A, Güemes A, Ureña A. Structural health monitoring of bonded joints using carbon nanotube doped adhesive films. Eur Workshop Struct Health Monit , EWSHM 2016;4:2450-2455.

[38] Hu N, Karube Y, Yan C, Masuda Z, Fukunaga H. Tunneling effect in a polymer/carbon nanotube nanocomposite strain sensor. Acta Materialia 2008;56(13):2929-2936.

[39] Kuronuma Y, Takeda T, Shindo Y, Narita F, Wei Z. Electrical resistance-based strain sensing in carbon nanotube/polymer composites under tension: Analytical modeling and experiments. Composites Sci Technol 2012;72(14):1678-1682.

[40] De Vivo B, Lamberti P, Spinelli G, Tucci V, Vertuccio L, Vittoria V. Simulation and experimental characterization of polymer/carbon nanotubes composites for strain sensor applications. J Appl Phys 2014;116(5):054307.

[41] Behnam A, Ural A. Computational study of geometry-dependent resistivity scaling in single-walled carbon nanotube films. Physical Review B 2007;75(12):125432.

[42] Lee BM, Loh KJ. A 2D percolation-based model for characterizing the piezoresistivity of carbon nanotube-based films. J Mater Sci 2015;50(7):2973-2983.

[43] Sánchez-Romate XF, Moriche R, Jiménez-Suárez A, Sánchez M, Prolongo SG, Güemes A, Ureña A. Highly sensitive strain gauges with carbon nanotubes: From bulk nanocomposites to multifunctional coatings for damage sensing. Appl Surf Sci.

[44] Blackman BRK, Kinloch AJ, Paraschi M, Teo WS. Measuring the mode I adhesive fracture energy, GIC, of structural adhesive joints: the results of an international round-robin. Int J Adhes Adhes 2003;23(4):293-305.

[45] Gude MR, Prolongo SG, Urena A. Toughening effect of carbon nanotubes and carbon nanofibres in epoxy adhesives for joining carbon fibre laminates. Int J Adhes Adhes 2015;62:139-145.

[46] Li X, Zhang W, Zhai S, Tang S, Zhou X, Yu D, Wang X. Investigation into the toughening mechanism of epoxy reinforced with multi-wall carbon nanotubes. E-Polymers 2015;15(5):335-343.

[47] Ashcroft IA, Hughes DJ, Shaw SJ. Mode I fracture of epoxy bonded composite joints: 1. Quasi-static loading. Int J Adhes Adhes 2001;21(2):87-99.

[48] Blackman BRK, Kinloch AJ, Rodriguez Sanchez FS, Teo WS, Williams JG. The fracture behaviour of structural adhesives under high rates of testing. Eng Fract Mech 2009;76(18):2868-2889.

[49] Karac A, Blackman BRK, Cooper V, Kinloch AJ, Sanchez SR, Teo WS, Ivankovic A. Modelling the fracture behaviour of adhesively-bonded joints as a function of test rate. Eng Fract Mech 2011;78(6):973-989.

Chapter 9: Fatigue Crack Growth Identification in Bonded Joints by Using Carbon Nanotube Doped Adhesive Films

Xoan F. Sánchez-Romate[a,b]*, Claudio Sbarufatti*[c,*]*, María Sánchez*[b]*,*
Andrea Bernasconi[c]*, Diego Scaccabarozzi*[c]*, Simone Cinquemani*[c]*, Alfredo*
Güemes[a] *and Alejandro Ureña*[b]

Submitted to Compos Struct (2019)

[a] Department of Aerospace Materials and Processes, Escuela Técnica Superior de Ingenieros Aeronáuticos, Universidad Politécnica de Madrid, Plaza del Cardenal Cisneros 3, 28040 Madrid, Spain

[b] Materials Science and Engineering Area, Escuela Superior de Ciencias Experimentales y Tecnología, Universidad Rey Juan Carlos, Calle Tulipán s/n, 28933 Móstoles (Madrid), Spain

[c] Politecnico di Milano, Dipartimento di Meccanica, Via La Masa 1, 20156, Milano, Italy

*Corresponding author: claudio.sbarufatti@polimi.it Tel: +39 022399 8213

An investigation on fatigue crack growth monitoring of bonded joints has been conducted employing a novel carbon nanotube (CNT) adhesive film, chosen for their proven exceptional properties for sensing purposes. Single lap shear fatigue tests have been carried out at a 7 kN load, load ratio 0.1 and 10 Hz frequency. A correlation between the electrical response of the adhesive joints and the fatigue crack growth has been established by means of voltage acquisition through the thickness in combination with crack length monitoring by microscopy analysis. Three phases can be distinguished during the fatigue tests: phase one without crack initiation with a steady electrical response; phase two in which cracks start propagating, with a slight increase of the electrical resistance, and phase three, corresponding to final propagation to failure with a drastic increase of the electrical resistance. A correlation between the electrical response, the estimated crack area and the measured edge-crack size is achieved, allowing to get a deeper understanding of crack growth phenomenon as a function of the number of cycles. Thus, the potential and the applicability of the proposed technique for monitoring crack growth in lap joint fatigue tests have been demonstrated.

Keywords: adhesive films; carbon nanotube; fatigue; composites; damage identification

9.1 Introduction

Nowadays, composite materials are attracting the interest of many researchers due to their exceptional mechanical properties and their corrosion resistance, which make them very competitive in comparison to conventional metallic alloys. Research on composite material structures is particularly active in the aerospace industry, where the light-weight design is a driving requirement, thus justifying the effort in developing new materials with increasing specific properties, sometimes applied to complex mechanical systems. However, this results in complex or unknown failure modes, which can often only be identified and predicted with difficulty, especially when stress concentrations occur, e.g. in correspondence of mechanical joints. Therefore, it is necessary to develop efficient assembly techniques with a higher reliability.

When joining composites, care must be exercised not to damage them or to induce damage by letting stresses flow smoothly across the parts to join. In the case of mechanical joints like bolts, the contact between the bolt and the inner surface of the hole can induce delamination if the contact pressure exceeds some limit values. Thus, metal inserts have to be placed into the laminate and co-cured. This allows the creation of a joint that can be easily disassembled and inspected. However, the presence of the bolt and the insert add mass to the structure. In this context, bonded joints present many advantages over bolted connections as they avoid stress concentrations at bolt holes and do not increase the overall mass, thus increasing the potential for weight savings [1,2].

However, a specific program of off-line non-destructive inspections is mandatory in order to ensure their reliability, e.g. by means of either ultrasonic or eddy current tests, just to mention a few. More recently, Structural Health Monitoring (SHM) as a technology offers the promise of reduced cost-of-ownership and increased safety of operation by a real-time inspection of critical engineering structures. SHM, in its general form, combines either local or distributed measures with damage identification algorithms in order to provide real-time anomaly detection and assessment. Local monitoring is often based on fiber optic strain sensors, leveraging on the multiplexing capabilities of the local Bragg grating sensors [3,4] and on their reduced size, which favors sensor embedding in the composite material [5] with minor effects on the mechanical performances. However, they only provide a punctual information about the damage, making the damage inference strongly dependent on the availability of a robust process for feature identification and extraction from the raw sensor data. A quasi-distributed measure is also possible based on fiber optic sensors, exploiting the Rayleigh backscatter [6]. Differently, piezoelectric transducers are widely used for distributed SHM, e.g. for guided Lamb Waves monitoring [7,8] and acoustic emission sensing [9,10] to mention a few applications, but the interpretation of the acquired signal is often very complex, especially if realistic structures are considered, due to boundary wave reflections and environmental influences.

In this framework, carbon nanoparticles such as carbon nanotubes (CNTs) are now attracting the interest of many researchers showing excellent mechanical and electrical properties [11-14]. Their addition as a reinforcement into a resin leads, thus, to an enhancement of its mechanical and, especially, electrical properties [15-19]. The improvement of the electrical properties is explained by the formation of percolating networks inside the material [20-23], which causes an increase of the electrical conductivity in several orders of magnitude. This fact, their piezoresistive behaviour and the tunneling effect between adjacent nanoparticles make them very useful for SHM applications [24-31] showing much more sensitivity than other conventional SHM techniques [32,33].

In this paper, the excellent sensing characteristics of CNTs are exploited for bonded joint monitoring, specifically concerning adhesive films. Some studies are available in the literature using CNT reinforced paste adhesives [34-37] proving the huge potential of this technology for detecting defects. In addition, it has been observed that the mechanical properties of the bonding layer are not negatively affected due to a CNT bridging effect on the adhesive [38-40]. However, if compared to paste adhesives, which require the adoption of more complex dispersion techniques such as three roll milling or toroidal stirring [41,42], the use of adhesive films, such as those adopted in the current study, implies a higher thickness control and a generally lower distributed porosity. The effect of CNT addition on the electrical and mechanical properties of adhesive films has been rarely investigated in the literature [43]. It has been observed in previous studies [44] that CNTs provide good conductive pathways without being detrimental to the mechanical properties. Crack propagation monitoring in adhesive films has been performed by comparing the mechanical and electrical response of the joints [45] at specific instants during the tests with a static and constant load application, noticing that the electrical resistance increases with the crack length and identifying a trend during fatigue crack growth. However, to date, no studies are available in the literature regarding real-time monitoring of CNT-doped adhesive films by continuous acquisition of the CNT signals for each load cycle during the fatigue tests.

This study, thus, aims to investigate the real-time SHM capabilities of the CNT-doped adhesive films during fatigue testing. To achieve this purpose, single lap shear (SLS) specimens have been subjected to fatigue loading while their electrical response is continuously measured by means of a voltage acquisition system. In addition, crack length has been also measured by using a microscope camera. The final target is to establish a correlation between some features of the real-time electrical response from the CNT circuit and the fatigue damage.

9.2 Methods

9.2.1 Manufacturing of bonded joints

Adhesive joints were manufactured by secondary bonding of unidirectional CFRP substrates, supplied by Fundación para la Investigación, Desarrollo y Aplicación de Materiales Compuestos (FIDAMC-AIRBUS) by using a CNT reinforced adhesive film. This adhesive film is an epoxy based FM300K, supplied by Cytec, with the highest mechanical performance over the FM300 series. It has a wide open knit tricot carrier which allows better thickness control during curing. CNTs are NC7000, supplied by Nanocyl, with an average diameter of 11 nm and a length up to 2 μm.

CNTs were dispersed in distilled water in a weight fraction of 0.1 %. CNT dispersion was achieved by means of ultrasonication for 20 min at 80 % of amplitude and a radiation time of 0.5 s using a horn sonicator UP400S supplied by Hielscher. In order to induce a higher CNT disaggregation, a surfactant called sodium dodecyl sulfate (SDS) was added, in a weight fraction of 0.25 %. Then, CNT dispersion was sprayed over the adhesive surface by using an airbrush at a pressure of 1 bar and at a distance of 40 cm for 0.5 s in order to achieve a high CNT homogenization into the adhesive. The curing cycle of both CNT and neat adhesive joints was set as shown in Table 9.1. After curing, the CNTs were embedded through the adhesive joint as shown in the microstructural studies of previous works [45], making the creation of electrical pathways through the joint possible.

Table 9.1: curing cycle parameters of secondary bonding.

Parameter	First Stage	Second stage
pressure	Ramp from 0 to 0.6 MPa for 15 min	0.6 MPa for 90 min
temperature	Ramp from 25 to 175 ºC for 45 min	175 ºC for 60 min

9.2.2 Electromechanical tests

Fatigue tests were carried out for the neat adhesive and CNT reinforced bonded joints in a MTS 810 test machine. The tests were carried out under force control and the mechanical response (in terms of force and displacements) was measured simultaneously with the electrical monitoring. The peak load was set at 7 kN with a load ratio R of 0.1 at a test frequency of 10 Hz. These parameters were selected in order to obtain a reasonable finite fatigue life, according to S-N curves in the literature for similar adhesives and substrates [46].

The dimensions of the bonded joints are according to the standard SLS coupons. Each substrate is 104 x 25.6 x 2.5 mm3 with an overlapping area of 25.6 x 25.6 mm2.

The monitoring of adhesive joints was carried out by means of voltage measurement between two points through the thickness as shown in the set-up schematics of Figure 9.1. The electrodes, placed in the midpoint of the overlap area, were made of copper wire attached to the CFRP substrate with silver ink and sealed with an adhesive layer to protect them from the environment. This electrode configuration is valid due to the much higher electrical conductivity of the CFRP substrates (in the range of 2 S/m) in comparison to the CNT adhesive layer (around 10-3 S/m, accordingly to a previous study [47]). Therefore, the contribution of the CFRP substrate to the total resistance of the joint can be neglected. The current was generated by using a power supply

STAB AR60 connected with an integrated circuit in order to keep the current (1 mA approximately) constant. Voltage acquisition was carried out by using a NI 9234 module from National Instruments with a sampling frequency of 5 kHz. This set up implies a great effort for noise reduction by grounding all the connections and isolating the CFRP substrates with GFRP tabs, in order to avoid electrical interference with the testing machine instrumentation. This configuration of insulating tabs and electrodes on the substrate surface is similar to that used in other studies analyzing sensing capabilities and crack propagation monitoring in SLS joints [48,49]. Although in a realistic scenario the load would be inherently present in the monitored system, due to connection with adjacent components, this could hamper the joint monitoring strategy if multiple and varying electrical paths will exist, due to modification of the baseline reference signal. A possible solution to this problem can be the adoption of an insulating layer (i.e. GFRP) to avoid the interferences with other equipment, but these aspects require a deeper analysis and dedicated research. However, this is considered outside the scopes of the present activity, this being the first attempt of monitoring lap joints under fatigue by CNT networks. Future research must be dedicated in finding electrical isolating solutions for practical implementation of the sensing technology at larger scale.

Crack edge length was measured at different load cycles during the tests, always referring to the same reference maximum load to control crack opening. A portable microscope Dino-Lite AM413ZTA was used to scan the edges of the lap joint, while the edge crack length was measured by using a calibrated image-processing software and then correlated with the electrical resistance variation. This optical configuration has been explored in other studies, being a good approach to measuring the crack length in SLS joints [50]. Figure 9.2 shows an example of edge crack length measured on a specimen after failure of the joint. A direct measure of the crack area, highlighted in the same figure in a similar way than other studies [50], was not available during the test, but an equivalent estimation is proposed later in this study, based on a correlation with the electrical resistance variation.

Four fatigue tests were carried out for the neat adhesive and for the CNT reinforced bonded joints, respectively, for a preliminary assessment of the effect of the CNT embedding on the mechanical performance of the joint, specifically concerning fatigue resistance, as reported in Section 2.3. Then, two specimens with CNT reinforced bonding were selected, named as Specimen 1 and 2, and analyzed in the Results and Discussion section. They were selected in order to show two typical types of fatigue behaviour of SLS joints under repeated fatigue load and to demonstrate how their behaviour is reflected in the

CNT monitoring signal. The other 2 specimens showed a similar electromechanical behaviour and relative results were omitted for brevity.

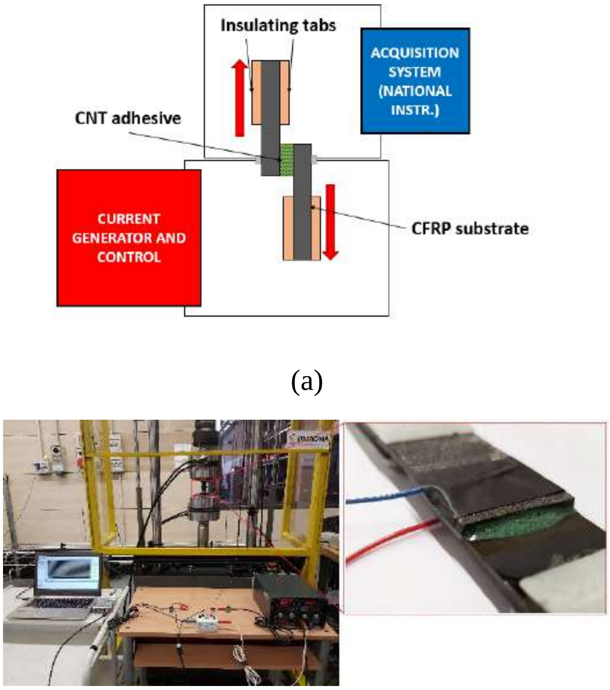

(a)

(b)

Figure 9.1: (a) Schematics of fatigue test set-up and (b) image of the actual configuration.

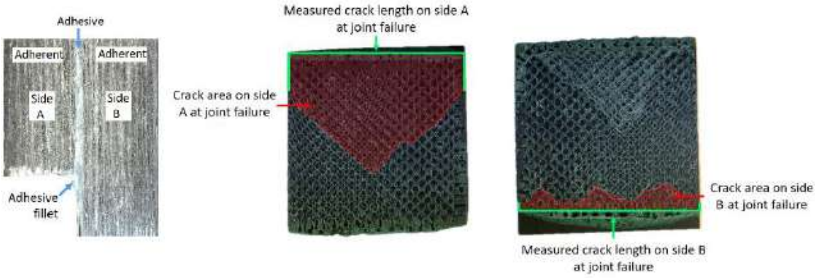

Figure 9.2: optical image of the fractured surface after joint failure with schematics of the measured edge crack length and with highlighted the crack area at joint failure.

9.2.3 Effect of CNT embedding on fatigue resistance

A preliminary investigation on the influence of CNT addition to SLS joint fatigue resistance was performed to verify any potential detrimental effect on the bonding mechanical resistance. Figure 9.3 shows the total number of cycles to failure and to crack initiation of both CNT doped and neat adhesives for the four specimens tested. Specifically, crack initiation is intended as the number cycles at which the crack is first detected during visual inspection of the joint. The average fatigue life of the CNT doped adhesive was found to be slightly higher than the neat adhesive. However, the scattering was also higher, probably due to heterogeneities in the CNT distribution along the adhesive, as reported in previous studies [44]. In fact, these heterogeneities counteract the bridging effect of the CNTs and can lead to differences in the mechanical properties of the joint. Similar results were found when analyzing the number of cycles to crack initiation. An ANOVA single factor analysis was carried out for the two adhesive conditions in order to statistically infer the influence of the CNT on the fatigue resistance. The results suggest the addition of CNTs does not significantly affect the cycles to failure of the SLS joints, while a potential benefit exists on the number of cycles to crack initiation. It is necessary to point out that this statistical analysis is only a rough estimation of how the CNT addition potentially affects the mechanical properties of SLS joints during fatigue testing. More test repetitions are required in order to provide a more quantitative analysis.

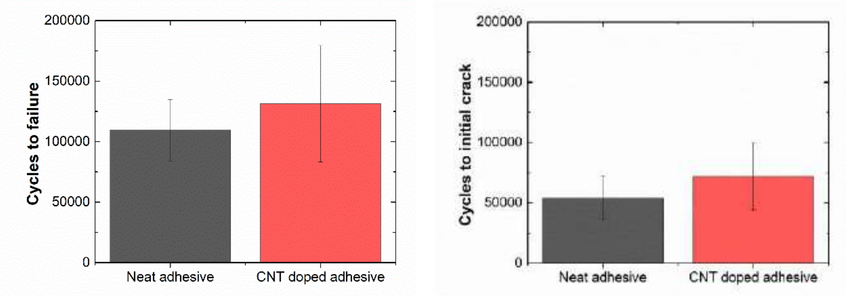

(a) (b)

Figure 9.3: Number of cycles to (a) failure and (b) crack initiation for neat and CNT doped adhesive joints.

9.2.4 Microstructural study

Fractured surfaces were characterized by means of Scanning Electron Microscopy (SEM), using a S-3400N apparatus from Hitachi in order to identify the main failure mechanisms. For that purpose, lap joint fractured surfaces were cut and gold coated with a layer of approximately 10 nm thickness.

9.3 Monitoring results and discussion

In this section, the electromechanical behaviour of two kinds of specimens is shown and analyzed. The first one, named Specimen 1, showed a more uniform crack propagation whereas in the second one, Specimen 2, a stick-slip effect was observed, which is an unstable crack growth [45]. Firstly, a detailed analysis of the Specimen 1 was carried out in order to understand and characterize the electrical behaviour of the joints subjected to fatigue testing. Then, the stick-slip phenomenon was analysed to gain a better understanding of the crack propagation mechanisms and to show the sensitivity of the proposed monitoring method.

9.3.1 Electrical measurements

Figure 9.4 shows the electrical response of the Specimen 1 during fatigue tests. Test time and number of cycles were correlated to the frequency of the load during the tests, 10 Hz. A current generator was used to keep the current constant. The changes in the normalized resistance were obtained from the voltage measurements by applying the Ohm's Law:

$$\frac{\Delta R}{R_0} = \frac{R - R_0}{R_0} = \frac{\frac{V - V_0}{I}}{\frac{V_0}{I}} = \frac{V - V_0}{V_0}$$

Being R0, V0, R and V the resistance and the voltage at the initial stage and at a generic time, respectively.

The electrical response of the specimens during SLS joint fatigue testing was affected by two factors.

First, when a sinusoidal load is applied to the substrate, the adhesive layer is experiencing a shear deformation which varies along the length and through the adhesive thickness. The local strain variations in a load cycle generate an average global cyclic modification of the electrical resistance, as observed in Figure 9.4 (b), due to tunneling resistance variation. This is due to the CNT piezoresistive behaviour and the tunneling effect between adjacent particles, which leads to an approximately exponential increase of the electrical resistance with the applied strain, as previously observed for quasi-static SLS tests [45]. The non-linearity of the strain in the joint section as a function of the applied force, coupled with the non-linearity between the strain and the tunneling resistance, cause a non-sinusoidal signal from the CNT network. The signal anomaly in the valley region of Figure 9.4 (b) can be associated to the occurrence of plastic deformation at the lap fillets (Figure 9.2), which manifests as some strain increase during unloading. Although this assumption is corroborated in Figure 9.5 (c) by the progressive disappearing of the signal anomaly when the crack evolves further outside the fillets, additional research is needed to verify this hypothesis.

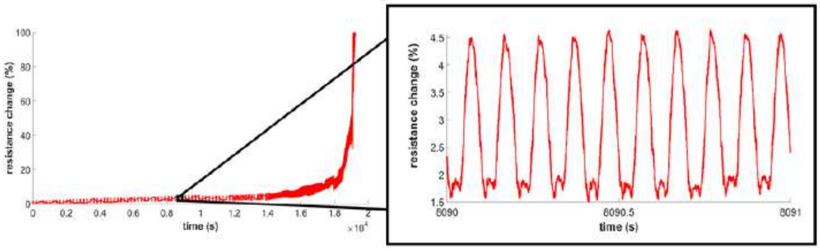

(a) (b)

Figure 9.4: Variation of the electrical resistance as a function of time (a) for the entire fatigue test and (b) detailed at 10 consecutive cycles.

Second, the crack evolution during fatigue tests induces a variation of the electrical response, as analyzed in detail below. Figure 9.5 shows a detailed analysis of the electromechanical behaviour of the joints. The electrical response was correlated with the crack edge length measured by the microscope camera through the top, bottom and lateral sides of the joint, as shown in the schematics of Figure 9.2. For that purpose, the peak and the valley trends were presented (Figure 9.5 (a)), defined as the value of the normalized resistance at maximum and minimum force on each fatigue load cycle. A sensitivity parameter was also defined as the difference between the peak and valley within a single cycle (Figure 9.5 (b)), provided a constant load cycle was applied by the test machine as a boundary condition. A more detailed graph of the acquired electrical signal can be observed for three different stages of the fatigue test (Figure 9.5 (c)). In this regard, significant changes in the shape of the signal can be noticed. For this purpose, the cross-correlation, xcorr, of a 10-cycles signal window with respect to a baseline signal window taken at the start of the test was used in Figure 9.5 (d) to highlight modifications of the signal shape within one load cycle. In this context, three regions were visible.

The first region reflects the steady behaviour of the electrical response. A small trend was observed in the normalized resistance as a function of the number of cycles and the sensitivity was almost constant, as shown in the region I of Figure 9.5 (a) and (b). At this stage, no nucleation of the fatigue damage was detectable by optical microscopy (Figure 9.5 (c)) and the sensitivity only took the tunneling effect due to adhesive deformation into account. The small variations of the normalized resistance and the sensitivity were caused by the presence of microcavities, which usually appear at the interface between the nano-reinforcement and the matrix before crack starts to propagate as stated in other studies for nanocomposites [51], and which cause crack nucleation. Figure 9.5 (d) showed a general decrease of the cross-correlation factor with the number of cycles due to the presence of the aforementioned microcavities.

The second region is associated to a significant variation of the electrical response. An increase of the normalized resistance was observed as a function of the number of cycles (region II of Figure 9.5 (a)) as well as a slight variation of the sensitivity (Figure 9.5 (b)), associated to crack initiation and propagation (Figure 9.5 (c)). In fact, the electrical resistance increased with the crack length, due to the breakage of the conductive pathways. The variation of the sensitivity can be explained by observing the schematics of Figure 9.6. At the maximum force, the crack was totally open, while closure occurred in correspondence of the minimum load due to a lower applied stress and strain. This crack opening differences induced a higher variation of the electrical resistance within a single load cycle, leading to higher sensitivities. Therefore, the higher the crack length, the higher the variations of the electrical resistance and, thus, the sensitivity. However, the analysis of the xcorr evolution was unclear at this point, as shown in Figure 9.5 (d). Crack opening effect on the electrical sensitivity of the material manifested itself as increases and decreases in the xcorr factor. Depending on the crack propagation inside the material, this effect can lead to a partial recovery of the initial shape of the electrical curve at some points.

Finally, the third region is associated to a drastic increase of both the normalized resistance and the sensitivity as a function of the number of cycles. This is correlated to the last stages of fatigue testing in which crack propagates very rapidly until final brittle failure, inducing drastic variations of the electrical response. This can be also reflected in a sudden decrease of the xcorr factor in the last stages of region III, which is associated to a significant modification of the signal shape after one load cycle.

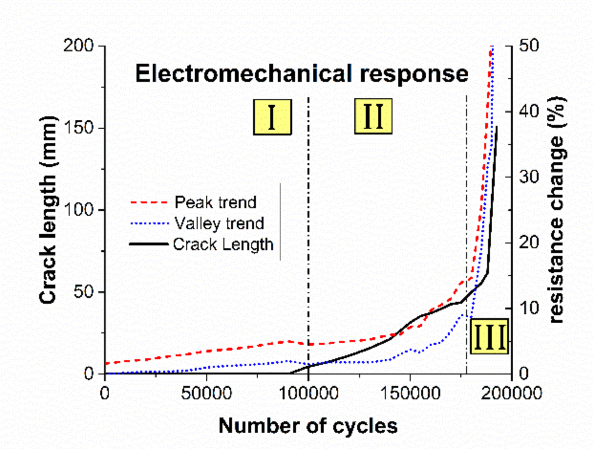

(a)

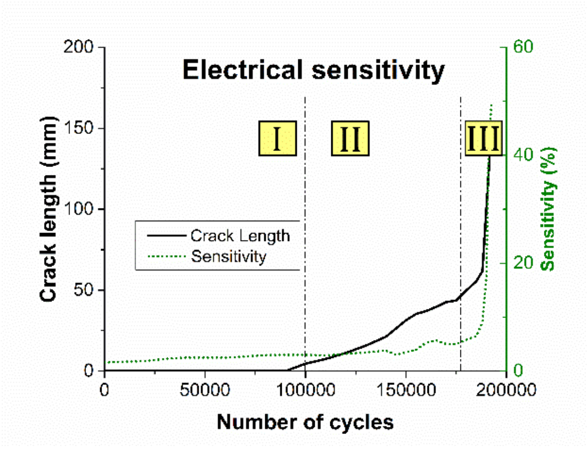
Electrical sensitivity
Crack length (mm)
Sensitivity (%)
Number of cycles
I
II
III
Crack Length
Sensitivity
0
50
100
150
200
0
20
40
60
0
50000
100000
150000
200000

(b)

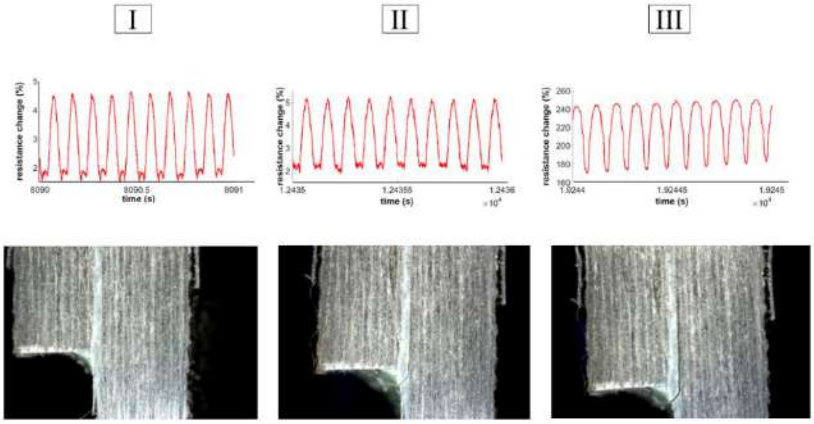
I
II
III
resistance change (%)
time (s)
resistance change (%)
time (s)
resistance change (%)
time (s)

(c)

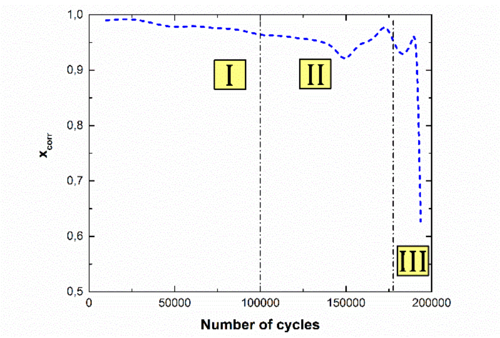
x_{corr}
Number of cycles
I
II
III
1,0
0,9
0,8
0,7
0,6
0,5
0
50000
100000
150000
200000

(d)

Figure 9.5: (a) Detailed analysis of the electromechanical response during fatigue tests in which red and blue lines correspond to the peak and the valley trends of the normalized resistance, (b) analysis of the electrical sensitivity, (c) correlation with the crack length measured by optical microscopy and (d) graph of the xcorr parameter as a function of the number of cycles.

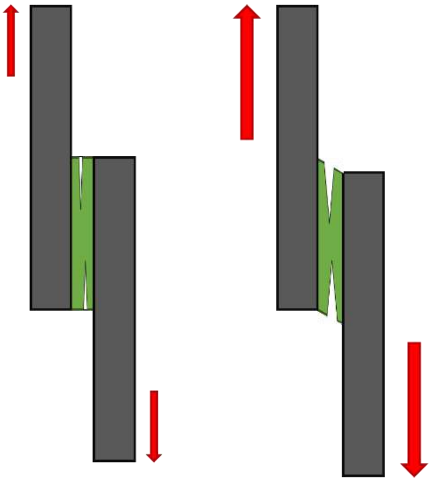

Figure 9.6: The effect of crack opening during a single cycle of a fatigue SLS test.

9.3.2 Analysis of debonding area evolution

A more detailed analysis was performed to analyze the crack propagation behavior during the fatigue test, leveraging on an equivalent estimated crack area. In practice, although not directly measured, the size of the crack area can be estimated as a function of the number of cycles, based on the measure of the normalized resistance. The bonded joint was modeled as an electrical circuit, supposing that CNTs were homogenously distributed along the adhesive and assuming that the electrical conductivity of the CFRP substrates was much higher. The electrical resistance can be expressed by the second Ohm's law:

$$R = \rho \cdot \frac{l}{A}$$

where ρ, l and A are the electrical resistivity, the thickness and the overlap area of the bonded joint, respectively. The normalized resistance at a generic time can thus be expressed in terms of the bonded area:

$$\frac{\Delta R}{R_0} = \frac{R}{R_0} - 1 = \frac{A_0}{A} - 1$$

where A_0 and A are the initial (undamaged) and actual (cracked) bonded areas, respectively. The crack area, A_d, can finally be estimated as:

$$A_d = A_0 - A$$

Figure 9.7 (a) shows the measured crack edge length and the estimated crack area as a function of the number of cycles. At the initial stage, previously identified as region I in Figure 9.5, there was a slight increase in the estimated crack area although the measured crack length remained constantly zero, as no edge crack was visible from the microscope camera. This is explained by the presence and coalescence of microcavities inside the adhesive joints. As commented on above, these microcavities usually appear at the interfaces between the matrix and the carbon nanoparticles [51], globally affecting the electrical resistance, though without inducing visible edge cracks.

Some additional information about the crack shape was obtained by analyzing the estimated crack area as a function of the crack length measured at the edges of the joint (Figure 9.7 (b)). The initial value of the estimated crack area (point 1 in the schematics of Figure 9.7 (b) and (c)) corresponded to the total size of the internal microcavities at the end of phase I. Then, a minor increase of the estimated crack area was observed, although a significant increase of the crack length was measured at the edges of the joint. This means that the evolution of the debonded area took mainly place at the lap joint edges (points 2 and 3 of schematics of Figure 9.7 (b) and (c)).

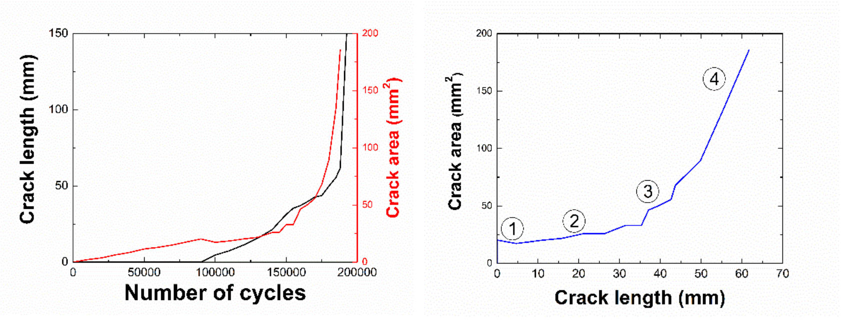

(a) (b)

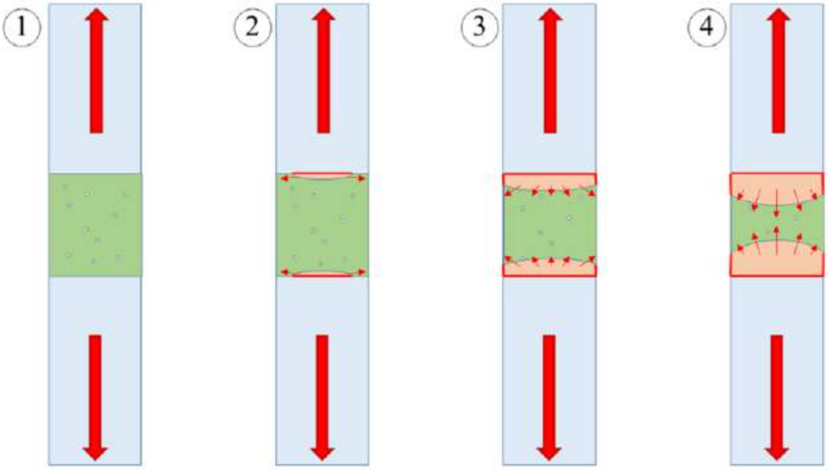

(c)

Figure 9.7: (a) Measured crack side length and calculated crack area as a function of the number of cycles, (b) correlation between them with region 1 corresponding to the initial condition, region 2 to the first stages of crack propagation through the edges, region 3 to the propagation in both edges and inside the lap joint and region 4 to the final propagation to failure, with a crack propagation mainly inside the joint, as highlighted with the schematics in (c).

At higher edge-crack length levels (4), the estimated crack area increased faster, which means that the debonding was propagating inside the lap joint, as shown in the region 4 of the schematics of Figure 9.7 (c) and also confirmed by Bernasconi et al. [52]. Finally, in the last stages of the fatigue test, the crack propagated quickly along the entire surface of the lap joint until the final failure reflected in a sudden increase of the damage area vs. the crack length. The fractured surface after the joint failure of Specimen 1 is visible in Figure 9.2, where the final crack evolution in the central region of the bonded area is clearly highlighted. These results are in good agreement with the numerical investigation shown in other studies [53], demonstrating that higher stresses are concentrated at the edges of the lap joint where crack initiates. However, though a symmetric damage growth morphology is shown in the schematics of Figure 9.7 (c), the non-perfectly homogeneous adhesive properties in the upper and lower fillets and the presence of randomly distributed porosity inevitably translate in a delay of the crack nucleation at the lower fillet, which can be considered limited if compared with the test duration.

9.3.3 Fatigue assessment based on crosshead displacement

As detailed in the Methods section, the fatigue test was executed under force control and the crosshead displacement was measured synchronously to the CNT signal. Although rigorously an extensometer is required to exactly measure the displacement of the specimen under test neglecting the test machine deformability, it was not applicable in this test due to the presence of electrical cables and the need for the specimen electrical isolation. However, though the measure of the crosshead displacement includes a bias related to the deformability of the test machine, it is possible to correlate any deviation from the initial condition to the presence of cracks and debonding in the joint area. In fact, by analyzing the mechanical response in Figure 9.8, the crosshead displacement followed a similar trend to the electrical resistance through the joint thickness, with a more rapid increase in the last stages of the fatigue test, just before failure. This is explained by the presence of fatigue damage implying a reduction of the lap joint stiffness, thus leading to higher displacement ranges for the same applied load cycle. However, by comparing the electrical response from Figure 9.4 and Figure 9.5 to the monitored displacement of Figure 9.8, the electrical resistance acquisition was evidently much more sensitive to crack growth.

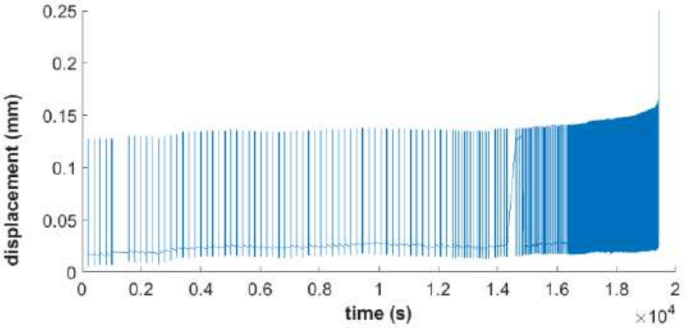

Figure 9.8: Displacement of the specimen grips as a function of the number of cycles.

9.3.4 Analysis of other crack propagation mechanisms: Stick-slip case

The electromechanical behaviour of the SLS joints can significantly change depending on the crack propagation mechanisms. Figure 9.9 shows the electromechanical response of Specimen 2. In this case, the edge crack length followed a stick slip pattern as a function of the number of cycles. This means an unstable crack growth with sudden and softer increases, usually correlated to high test rates [54,55]. The electrical response presented clearer differences among the regions previously defined, that is, region one (I) with no crack nucleation, region two (II) in which crack starts propagating and finally region three (III) with rapid crack propagation until final failure.

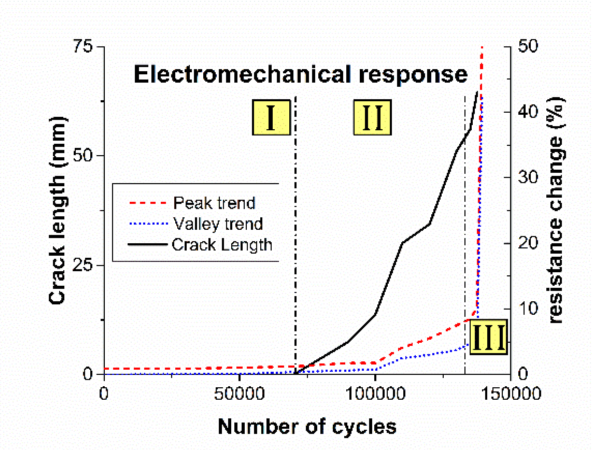

(a)

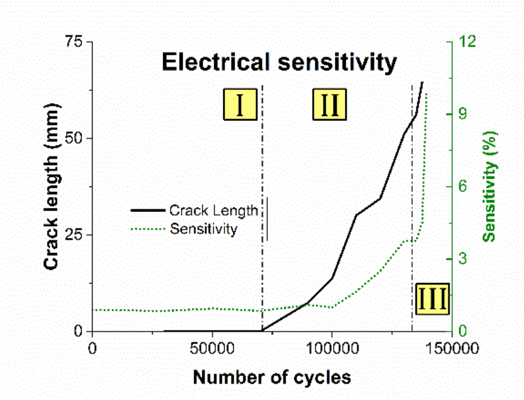

(b)

Figure 9.9: (a) Electromechanical response and (b) sensitivity of the stick-slip pattern specimen. Red and blue lines denote peak and valley trends.

By observing the estimated debonded area as a function of the measured edge crack length, the phases with reduced crack growth rate were noticeably associated to the damage evolution inside the lap joint (point 3 of Figure 9.10 (b) and (c)), as the crack area increased rapidly. On the other hand, sharp increases of measured edge crack length were correlated to faster crack propagation through the joint edges (points 2 and 4 of Figure 9.10 (b) and (c)). This anomalous behavior could be associated to some manufacturing defects such as overflowing or an irregular pressure distribution during curing, as commented on in previous studies [45]. In fact, these irregularities could lead to the presence of areas with a different adhesive distribution and, thus, a non-uniform stress distribution, as detailed in the next paragraph. Therefore a microstructural characterization of the fractured surfaces was carried out in order to have a more detailed knowledge of the fracture mechanics and the adhesive distribution. This could be correlated to the CNT signal, in order to validate the previous statements about the electrical and mechanical response of lap joints.

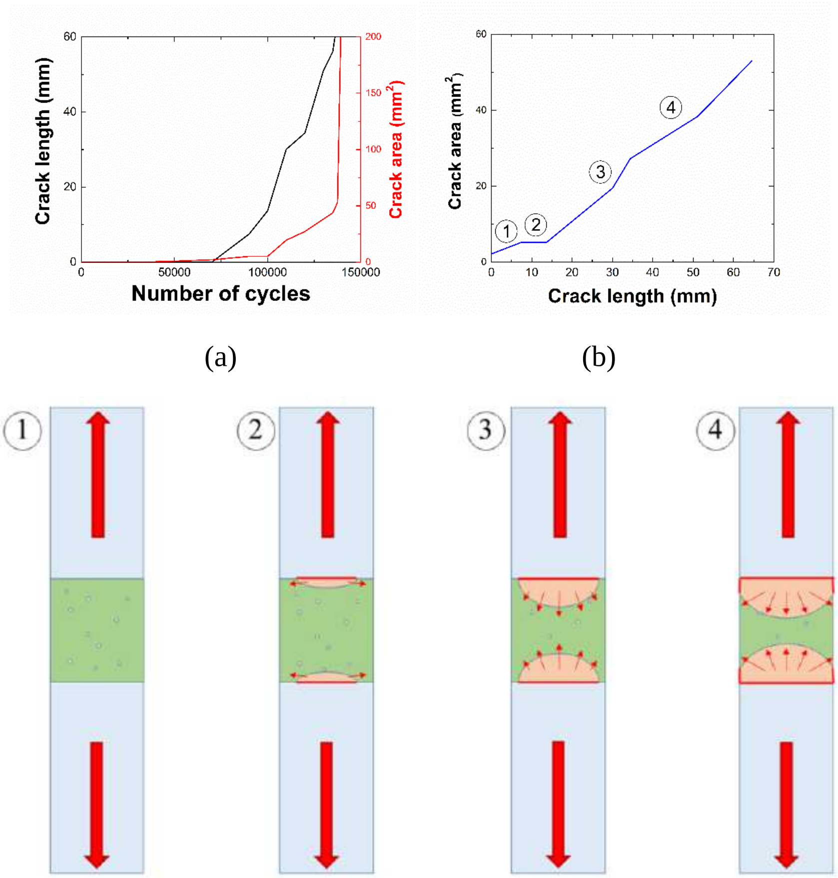

(a) (b)

(c)

Figure 9.10: (a) Crack area and crack length as a function of the number of cycles, (b) correlation between them and (c) schematics of the debonding evolution.

9.3.5 SEM analysis of specimens 1 and 2

Figure 9.11 shows SEM images of the fractured surfaces after the fatigue test. An irregular distribution of adhesive was observed in case of Specimen 1, showing areas with higher (Figure 9.11 (a)) and lower (Figure 9.11 (b)) presence of adhesive. This effect was more prevalent in the Specimen 2 due to the stick-slip effect (Figure 9.11 (c) and (d), respectively). As reported in a previous study [45], the regions with a lower adhesive content can be correlated to a faster crack propagation, due to manufacturing defects such as overflowing caused by an irregular pressure distribution during hot press compaction. In addition, a more prevalent adhesive failure was observed on the edges of the lap joint (Figure 9.11 (e) and (f)), due to a higher stress concentration in these areas, as commented on above. Moreover, these variations in the crack growth can be also associated to the variation of the strain energy release rate with the crack length. Therefore, the analysis of the fractured surfaces stood in good agreement with the measurements and theoretical analysis previously described. In this context, Figure 9.11 (g) shows a global overview of the fractured area where the irregular adhesive distribution can be observed.

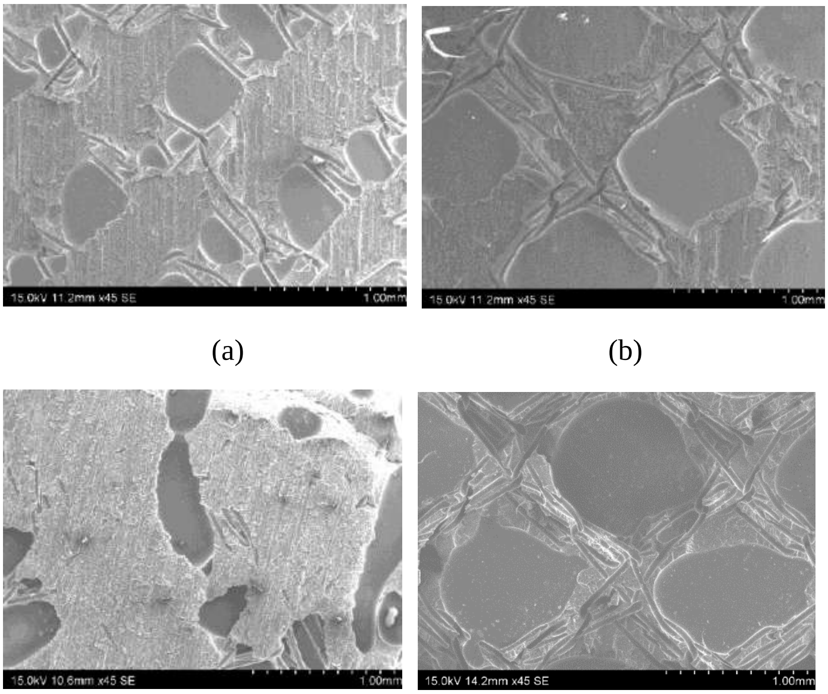

(a) (b)

(c) (d)

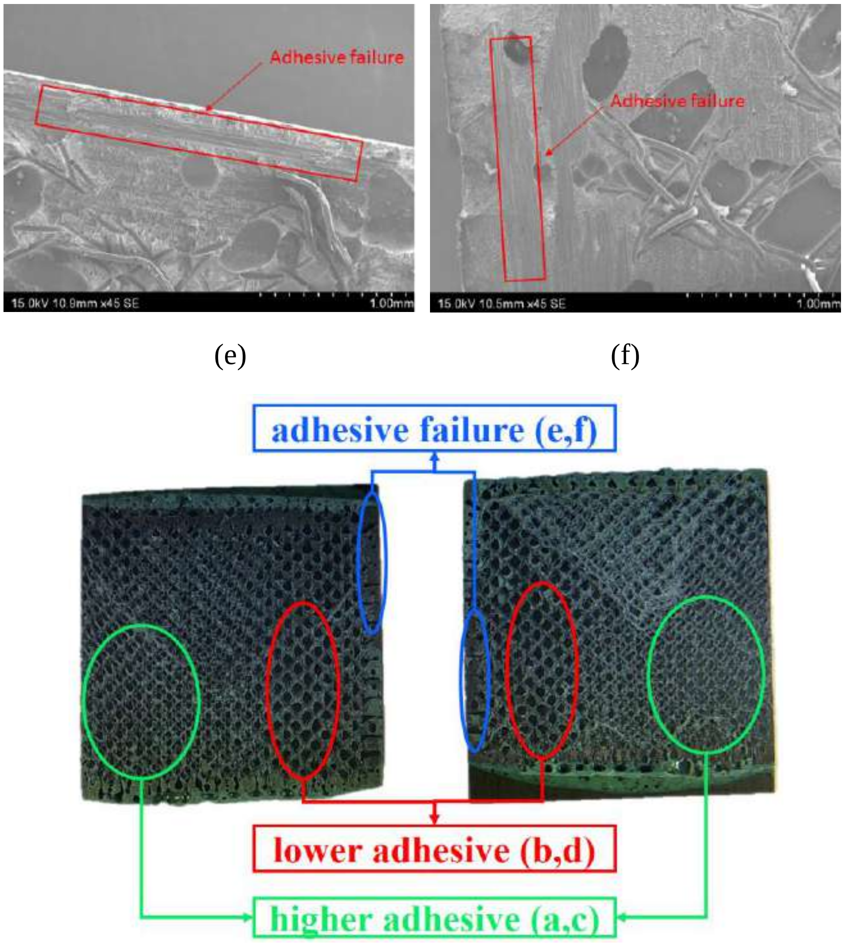

(e) (f)

(g)

Figure 9.11: SEM images of the fractured areas with a higher (left) and lower (right) presence of adhesive for (a), (b) Specimen 1 and (c), (d) Specimen 2 and (e) and (f) images of the fractured surface near the edges showing the prevalent presence of substrate, indicating an adhesive failure and (g) optical image of the fractured surface with red and green areas indicating regions with lower and higher presence of adhesive, respectively while blue areas indicate regions with adhesive failure.

9.4 Conclusions

Fatigue tests on single lap shear bonded joints using CNT reinforced adhesive films were carried out while their electrical response was measured by means of voltage acquisition.

The proposed technology was proven to be able to properly monitor crack propagation without a detriment of the mechanical properties. A clear correlation between the electrical and the mechanical response was observed. Three distinguishable regions were identified during fatigue tests: region one without crack nucleation and thus, approximately constant electrical resistance; region two, with a slight increase of the electrical resistance associated to the first stages of crack propagation; and region three exhibiting a sudden increase of the electrical resistance due to a rapid crack propagation.

In addition, by carefully analyzing the electrical response, the crack evolution inside the joint could be monitored. Cracks were shown to propagate through the edges and then inside the joint, according to other numerical studies. Stick-slip behavior was also detected by sharp increases and arrest phases and was found to be associated to an irregular adhesive distribution along the joint further supported by the analysis of SEM images of fractured areas which exhibited zones with higher and lower presence of adhesive.

Therefore, the applicability of the proposed adhesive for monitoring of fatigue crack growth in SLS joints was proven. It provides not only detailed information about crack evolution but furthermore allows to distinguish between different mechanical behaviour types without having a detrimental effect on the mechanical performance, showing, thus, a huge potential for SHM applications.

Acknowledgements

This work was supported by the Ministerio de Economía y Competitividad of Spanish Government [Project MAT2016-78825-C2-1-R], Comunidad de Madrid Government [Project P2013/MIT-2862] and by the Department of Mechanical Engineering (DMEC) of Politecnico di Milano under the Young Researcher Program.

9.5 References

[1] Hussey R, Wilson J. Structural Adhesives: Directory and Databook. 1996.

[2] Johnson WS, Butkus LM. Designing for the durability of bonded structures. 1996;1:147-160.

[3] Bernasconi A, Carboni M, Comolli L. Monitoring of fatigue crack growth in composite adhesively bonded joints using fiber Bragg gratings. Procedia Engineering 2011;10:207-212.

[4] Ruzek R, Kudrna P, Kadlec M, Karachalios V, Tserpes KI. Strain and damage monitoring in CFRP fuselage panels using fiber Bragg grating sensors. Part II: Mechanical testing and validation. Composite Structures 2014;107:737-744.

[5] Shivakumar K, Bhargava A. Failure mechanics of a composite laminate embedded with a fiber optic sensor. J Composite Mater 2005;39(9):777-798.

[6] Sierra-Pérez J, Torres-Arredondo MA, Güemes A. Damage and nonlinearities detection in wind turbine blades based on strain field pattern recognition. FBGs, OBR and strain gauges comparison. Composite Structures 2016;135:156-166.

[7] Lanza di Scalea F, Rizzo P, Marzani A. Propagation of ultrasonic guided waves in lap-shear adhesive joints: case of incident A 0 Lamb wave. J Acoust Soc Am 2004;115(1):146-156.

[8] Duflo H, Morvan B, Izbicki J. Interaction of Lamb waves on bonded composite plates with defects. Composite structures 2007;79(2):229-233.

[9] Nair A, Cai C. Acoustic emission monitoring of bridges: Review and case studies. Eng Struct 2010;32(6):1704-1714.

[10] Scholey JJ, Wilcox PD, Wisnom MR, Friswell MI. Quantitative experimental measurements of matrix cracking and delamination using acoustic emission. Composites Part A: Applied Science and Manufacturing 2010;41(5):612-623.

[11] Ruoff RS, Lorents DC. Mechanical and thermal properties of carbon nanotubes. carbon 1995;33(7):925-930.

[12] Popov VN. Carbon nanotubes: properties and application. Materials Science and Engineering: R: Reports 2004;43(3):61-102.

[13] De Volder MFL, Tawfick SH, Baughman RH, Hart AJ. Carbon Nanotubes: Present and Future Commercial Applications. Science 2013;339(6119):535-539.

[14] Wang M, Chen H, Lin W, Li Z, Li Q, Chen M, Meng F, Xing Y, Yao Y, Wong C. Crack-free and scalable transfer of carbon nanotube arrays into flexible and highly thermal conductive composite film. ACS applied materials & interfaces 2013;6(1):539-544.

[15] Allaoui A, Bai S, Cheng H, Bai J. Mechanical and electrical properties of a MWNT/epoxy composite. Composites Sci Technol 2002;62(15):1993-1998.

[16] Song YS, Youn JR. Influence of dispersion states of carbon nanotubes on physical properties of epoxy nanocomposites. Carbon 2005;43(7):1378-1385.

[17] Hu N, Masuda Z, Yan C, Yamamoto G, Fukunaga H, Hashida T. The electrical properties of polymer nanocomposites with carbon nanotube fillers. Nanotechnology 2008;19(21):215701.

[18] Gibson RF. A review of recent research on mechanics of multifunctional composite materials and structures. Composite Structures 2010;92(12):2793-2810.

[19] Khan SU, Pothnis JR, Kim J. Effects of carbon nanotube alignment on electrical and mechanical properties of epoxy nanocomposites. Composites Part A-Applied Science and Manufacturing 2013;49:26-34.

[20] Martin C, Sandler J, Shaffer M, Schwarz M, Bauhofer W, Schulte K, Windle A. Formation of percolating networks in multi-wall carbon-nanotube–epoxy composites. Composites Sci Technol 2004;64(15):2309-2316.

[21] Bryning MB, Islam MF, Kikkawa JM, Yodh AG. Very Low Conductivity Threshold in Bulk Isotropic Single-Walled Carbon Nanotube–Epoxy Composites. Adv Mater 2005;17(9):1186-1191.

[22] Pantano A, Buongiorno Nardelli M. Simulation of the electromechanical behavior of multiwall carbon nanotubes. ACS nano 2009;3(10):3266-3272.

[23] Kale S, Sabet FA, Jasiuk I, Ostoja-Starzewski M. Effect of filler alignment on percolation in polymer nanocomposites using tunneling-percolation model. J Appl Phys 2016;120(4):045105.

[24] Cullinan MA, Culpepper ML. Carbon nanotubes as piezoresistive microelectromechanical sensors: Theory and experiment. Physical Review B 2010;82(11):115428.

[25] Hu N, Karube Y, Arai M, Watanabe T, Yan C, Li Y, Liu Y, Fukunaga H. Investigation on sensitivity of a polymer/carbon nanotube composite strain sensor. Carbon 2010;48(3):680-687.

[26] Alamusi, Hu N, Fukunaga H, Atobe S, Liu Y, Li J. Piezoresistive Strain Sensors Made from Carbon Nanotubes Based Polymer Nanocomposites. Sensors 2011;11(11):10691-10723.

[27] Kuronuma Y, Takeda T, Shindo Y, Narita F, Wei Z. Electrical resistance-based strain sensing in carbon nanotube/polymer composites under tension: Analytical modeling and experiments. Composites Sci Technol 2012;72(14):1678-1682.

[28] Robert C, Feller JF, Castro M. Sensing Skin for Strain Monitoring Made of PC-CNT Conductive Polymer Nanocomposite Sprayed Layer by Layer. Acs Applied Materials & Interfaces 2012;4(7):3508-3516.

[29] Segev-Bar M, Haick H. Flexible sensors based on nanoparticles. 2013.

[30] Boland CS, Khan U, Backes C, O’Neill A, McCauley J, Duane S, Shanker R, Liu Y, Jurewicz I, Dalton AB. Sensitive, high-strain, high-rate bodily motion sensors based on graphene–rubber composites. ACS nano 2014;8(9):8819-8830.

[31] Boztepe S, Liu H, Heider D, Thostenson ET. Novel carbon nanotube interlaminar film sensors for carbon fiber composites under uniaxial fatigue loading. Composite Structures 2018;189:340-348.

[32] Cao J, Wang Q, Dai H. Electromechanical properties of metallic, quasimetallic, and semiconducting carbon nanotubes under stretching. Phys Rev Lett 2003;90(15):157601.

[33] Cullinan MA, Culpepper ML. Carbon nanotubes as piezoresistive microelectromechanical sensors: Theory and experiment. Physical Review B 2010;82(11):115428.

[34] Kang M, Choi J, Kweon J. Fatigue life evaluation and crack detection of the adhesive joint with carbon nanotubes. Composite Structures 2014;108:417-422.

[35] Kim C, Choi J, Kweon J. Defect detection in adhesive joints using the impedance method. Composite Structures 2015;120:183-188.

[36] Akpinar IA, Gültekin K, Akpinar S, Akbulut H, Ozel A. Research on strength of nanocomposite adhesively bonded composite joints. Composites Part B: Engineering 2017;126:143-152.

[37] Khashaba UA. Static and fatigue analysis of bolted/bonded joints modified with CNTs in CFRP composites under hot, cold and room temperatures. Composite Structures 2018;194:279-291.

[38] Burkholder GL, Kwon YW, Pollak RD. Effect of carbon nanotube reinforcement on fracture strength of composite adhesive joints. J Mater Sci 2011;46(10):3370-3377.

[39] Vietri U, Guadagno L, Raimondo M, Vertuccio L, Lafdi K. Nanofilled epoxy adhesive for structural aeronautic materials. Composites Part B-Engineering 2014;61:73-83.

[40] Gude MR, Prolongo SG, Urena A. Toughening effect of carbon nanotubes and carbon nanofibres in epoxy adhesives for joining carbon fibre laminates. Int J Adhes Adhes 2015;62:139-145.

[41] Sandler J, Shaffer M, Prasse T, Bauhofer W, Schulte K, Windle A. Development of a dispersion process for carbon nanotubes in an epoxy matrix and the resulting electrical properties. Polymer 1999;40(21):5967-5971.

[42] Aravand M, Lomov SV, Verpoest I, Gorbatikh L. Evolution of carbon nanotube dispersion in preparation of epoxy-based composites: From a masterbatch to a nanocomposite. Express Polymer Letters 2014;8(8):596-608.

[43] Garcia C, Sanchez M, Urena A, Rams J. Carbon Nanotubes for Assessing the Structural Integrity of Composite Bonded Joints with Film Adhesives. Structural Health Monitoring 2015: System Reliability for Verification and Implementation, Vols.1 and 2 2015:2169-2176.

[44] Sánchez-Romate XF, Sánchez M, García-Nieto C, Molinero J, Jiménez-Suárez A, Güemes A, Ureña A. Structural health monitoring of bonded joints using carbon nanotube doped adhesive films. Eur Workshop Struct Health Monit , EWSHM 2016;4:2450-2455.

[45] Fernández Sánchez-Romate XX, Molinero J, Jiménez-Suárez A, Sánchez M, Güemes A, Ureña A. Carbon Nanotube Doped Adhesive Films for Detecting Crack Propagation on Bonded Joints: A Deeper Understanding of Anomalous Behaviors. ACS applied materials & interfaces 2017.

[46] Quaresimin M, Ricotta M. Fatigue behaviour and damage evolution of single lap bonded joints in composite material. Composites Sci Technol 2006;66(2):176-187.

[47] Sánchez-Romate XF, Jiménez-Suárez A, Molinero J, Sánchez M, Güemes A, Ureña A. Development of bonded joints using novel CNT doped adhesive films: Mechanical and electrical properties. International Journal of Adhesion and Adhesives 2018;86:98-104.

[48] Lim AS, Melrose ZR, Thostenson ET, Chou T. Damage sensing of adhesively-bonded hybrid composite/steel joints using carbon nanotubes. Composites Sci Technol 2011;71(9):1183-1189.

[49] Sam-Daliri O, Faller L, Farahani M, Roshanghias A, Araee A, Baniassadi M, Oberlercher H, Zangl H. Impedance analysis for condition monitoring of single lap CNT-epoxy adhesive joint. International Journal of Adhesion and Adhesives 2019;88:59-65.

[50] Sun G, Liu X, Zheng G, Gong Z, Li Q. On fracture characteristics of adhesive joints with dissimilar materials – An experimental study using digital image correlation (DIC) technique. Composite Structures 2018;201:1056-1075.

[51] Moriche R, Jiménez-Suárez A, Sánchez M, Prolongo SG, Ureña A. Sensitivity, influence of the strain rate and reversibility of GNPs based multiscale composite materials for high sensitive strain sensors. Composites Science and Technology 2018;155:100-107.

[52] Bernasconi A, Carboni M, Comolli L, Galeazzi R, Gianneo A, Kharshiduzzaman M. Fatigue crack growth monitoring in composite bonded lap joints by a distributed fibre optic sensing system and comparison with ultrasonic testing. The Journal of Adhesion 2016;92(7-9):739-757.

[53] Anyfantis KN, Tsouvalis NG. Loading and fracture response of CFRP-to-steel adhesively bonded joints with thick adherents - Part II: Numerical simulation. Composite Structures 2013;96:858-868.

[54] Blackman BRK, Kinloch AJ, Rodriguez Sanchez FS, Teo WS, Williams JG. The fracture behaviour of structural adhesives under high rates of testing. Eng Fract Mech 2009;76(18):2868-2889.

[55] Karac A, Blackman BRK, Cooper V, Kinloch AJ, Sanchez SR, Teo WS, Ivankovic A. Modelling the fracture behaviour of adhesively-bonded joints as a function of test rate. Eng Fract Mech 2011;78(6):973-989.

Chapter 10: Exploring the Mechanical and Sensing Capabilities of Multi-Material Bonded Joints with Carbon Nanotube-Doped Adhesive Films

Xoan F. Sánchez-Romate[a,b,*], *Lucía Baena*[b], *Alberto Jiménez-Suárez*[b], *María Sánchez*[b], *Alfredo Güemes*[a] *and Alejandro Ureña*[b]

Submitted to Compos Part A (2019)

[a] Department of Aerospace Materials and Processes, Escuela Técnica Superior de Ingenieros Aeronáuticos, Universidad Politécnica de Madrid, Plaza del Cardenal Cisneros 3, 28040 Madrid, Spain

[b] Materials Science and Engineering Area, Escuela Superior de Ciencias Experimentales y Tecnología, Universidad Rey Juan Carlos, Calle Tulipán s/n, 28933 Móstoles (Madrid), Spain

*Corresponding author: xoan.fernandez.sanchezromate@urjc.es; Tel: +34914888252

Single lap shear tests are carried out at the joints of similar and dissimilar materials, and their electrical resistance through thickness is monitored to evaluate their sensing capabilities. Al-Al and carbon fibre reinforced polymer (CFRP)-Al joints are manufactured with two types of surface treatments of the Al substrates: brushing (B) and grit blasting (GB). The lap shear strength (LSS) is higher with grit blasting due to the optimum surface roughness and the creation of an active surface. Carbon nanotube (CNT)-doped samples are detrimental to the LSS in Al-Al joints compared to the neat adhesive, while a slight increase in LSS for CFRP-Al and CFRP-CFRP is observed due to a better CNT-CFRP interaction and good load transfer between the substrates. Electrical monitoring tests are strongly influenced by the surface treatment. It is observed that better adhesive-substrate interfaces lead to a more stable response and higher sensitivity, proving the high applicability of the proposed technique.

Keywords: A. Carbon nanotubes and nanofibers; A. Smart materials; B. Mechanical properties; D. Microstructural analysis

10.1 Introduction

The increasing requirements of the automotive and aircraft industries make the development of lightweight materials, such as aluminium alloys or carbon fibre reinforced polymers (CFRPs), essential. On this basis, joining techniques represent a crucial topic to be investigated.

Adhesive joints present multiple advantages over bolted connections, such as weight saving or the fact that they avoid stress concentrations around the holes [1,2]. In particular, the investigation of adhesive joints involving dissimilar materials has received significant attention in recent years [3-5]. It has been observed that several factors, such as the substrate stiffness [6,7] and the geometry of the overlapping area [3,4], play an important role in the final strength of the joint.

However, one of the main disadvantages of adhesive joints is correlated to their difficulty to inspect, an especially critical factor in this case, where the interface between the substrate and adhesive, and the presence of possible debondings, are very prevalent factors that affect their strength.

To date, there have been several studies dealing with adhesive joint inspection by conventional non-destructive testing (NDT) techniques, such as fibre Bragg grating sensors and acoustic ultrasonic waves [8-10]. However, these techniques are not often easy to understand as their analysis requires the use of complex mathematical and statistical tools [11-13]. For these reasons, there have been substantial efforts to develop novel NDT methods [14].

In this regard, the use of carbon nanoparticles, and more specifically, carbon nanotubes (CNTs), seems to be a powerful alternative due to their good physical properties [15-17]. In fact, their addition into an insulating medium enhances its electrical conductivity [18-20] allowing, by means of electrical measurements, its use in structural health monitoring (SHM) and other sensing applications [21-23].

In the context of SHM in bonded joints, there have been several reports of the use of CNT-doped paste adhesives with CFRP, metal and CFRP-metal joints [24-26]. However, the addition of CNTs to adhesive films, which are widely used in the aircraft industry, has been rarely investigated [27].

This particular need to develop other SHM techniques lies in the fact that the applicability of other available techniques such as Acoustic Ultrasonic waves or FBGs, when detecting defects, especially kissing bonds, has not been proven [28]. Thus, it remains as a challenging aspect of SHM of adhesive joints.

Therefore, this work aims to exploit the sensing characteristics of CNTs for monitoring applications in bonded joints of dissimilar materials. In previous studies, the sensing capability for monitoring crack propagation with CFRP substrates has been demonstrated, achieving good sensitivity and high capability for defect detection [29-31].

The main objective of this work is to study the effect that the addition of CNTs to the adhesive film has on the mechanical performance, and more specifically, on the lap shear strength (LSS) of the joint when using dissimilar CFRP-metal adherends in comparison to metal-metal and CFRP-CFRP joints, as well as exploring their SHM capabilities.

To achieve this purpose, several single lap shear (SLS) joints are manufactured using aluminium-aluminium and aluminium-CFRP substrates. The LSS and electrical monitoring results are compared to those previously studied for CFRP-CFRP joints by using the same CNT-doped adhesive film [30,31]. In addition, the effect of surface treatment on the metal adherend and its possible influence on the electrical response of the joint is explored. This would be useful to properly characterize the reliability and quality of the joint, something that other conventional SHM techniques are not able to do it.

10.2 Experimental procedure

10.2.1 Adhesive preparation

The adhesive is an FM 300K epoxy-based film with a knit tricot carrier, widely used in structural applications for joining CFRP-CFRP, metal-metal and CFRP-metal substrates. It allows for a better thickness control than other commercial paste adhesives due to its higher viscosity.

CNT addition is achieved by spraying an aqueous CNT dispersion over the adhesive surface. The CNT dispersion was previously optimised [31] using ultrasonication for 20 min in an aqueous solution with the help of a surfactant (sodium-dodecyl-sulfate (SDS)). The CNT/SDS content was set at 0.1/0.25 wt.%, respectively.

10.2.2 Joint manufacturing

The SLS joints of similar and dissimilar adherends (aluminium alloy 7075 and unidirectional CFRP) were manufactured by secondary bonding using a curing cycle, as shown in Table 10.1.

To analyse the influence of the interface between the adhesive and substrate, different surface treatments were carried out: untreated, brushing and grit blasting in the case of the metal substrates and peel-ply in the case of CFRP ones. A summary of the different testing conditions is shown in **Table 10.2**. It is important to note that the data for the CFRP-CFRP joint were extracted from a previous study [31] using the same substrates and CNT-doped adhesive.

Table 10.1: Cure cycle parameters of secondary bonding.

Parameter	First Stage	Second stage
Pressure	Ramp from 0 to 0.6 MPa for 15 min	0.6 MPa for 90 min
Temperature	Ramp from 25 to 175 ºC for 45 min	175 ºC for 60 min

Table 10.2: Summary of different SLS testing conditions.

Material designation	Surface treatment
CFRP-CFRP [31]	Peel-ply CFRP
CFRP-Al GB	Peel-ply CFRP. Grit-blasting Al substrate
CFRP-Al B	Peel-ply CFRP. Brushing with a 120 SiC sandpaper
Al-Al GB	Grit-blasting Al substrates
Al-Al B	Brushing with a 120 SiC sandpaper
Al-Al UN	No surface treatment apart from cleaning

10.2.3 Mechanical and electrical tests

Mechanical tests were carried out in a universal testing machine Zwick Z100. SLS tests were conducted by following the ASTM D5868-01 for both metal-metal and composite-metal joints at a test rate of 1.23 mm/min.

Electrical monitoring was achieved by means of electrical resistance measurements between two electrodes placed on each substrate. In case of Al substrates, the adherend itself was used as the electrode due to its good electrical conductivity. In the case of CFRP ones, due to its higher electrical resistivity, electrodes were made of copper wire and attached with silver ink to the CFRP surface. Then, they were covered by an adhesive layer in order to protect them from environmental influences and to avoid detachment of the electrical contacts. Schematics of the electrode placement are shown in Figure 10.1.

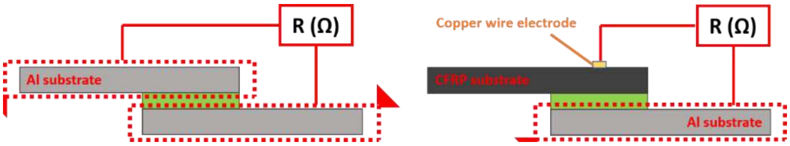

Figure 10.1: Schematics of electrode disposition in Al-Al and CFRP-Al joints.

10.2.4 Microstructural characterization

Microstructural analysis of adhesive joints with different surface treatments was carried out by scanning electron microscopy (SEM) using an S-3400 N apparatus from Hitachi. Transversal sections were properly polished and coated by a thin layer of gold. Several images were taken at different magnifications.

10.3 Results and discussion

10.3.1 Analysis of Al-Al joints

Figure 10.2 summarises the LSS of bonded joints for Al-Al substrates for neat and CNT-doped adhesive films. It is observed that the surface treatment has a significant effect, especially in the case of CNT-doped joints. This is explained because of a better interface between the adhesive and substrate. In this context, grit blasting promotes an optimum surface roughness, giving a higher active surface than brushing or the metal being untreated, making it possible for a better adhesion of the epoxy resin [32].

In the case of CNT-doped joints, the effect of surface treatment is more prevalent, as abovementioned. The untreated substrates show a very low LSS in comparison to both grit-blasted and brushed specimens. It is known that CNT addition induces an enhancement in the mechanical properties of a polymer [33], representing a crucial factor for a good dispersion inside the matrix [34]. In this case, a good CNT dispersion is achieved, as observed in a previous study [31]. Therefore, a possible explanation could be a poor interface between CNTs and the metal substrate, which gives a higher prevalence to the effect of the surface treatment. This poor CNT-metal interaction could also explain the lower values of LSS in comparison to the neat adhesive joints.

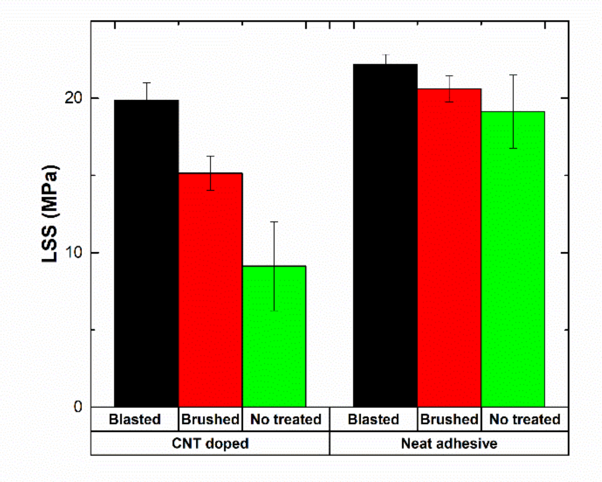

Figure 10.2: LSS of Al-Al joints for different testing conditions.

Figure 10.3 shows the fractured surface of the Al-Al joints. A cohesive failure is observed for GB conditions in both neat and CNT-doped joints. A mixed cohesive-adhesive mode is observed in the brushed condition of the neat Al-Al joint, while a mainly adhesive failure is observed for the rest of the conditions. This observation is in good agreement with the LSS results, which were found to be the lowest in these cases due to the poor metal-CNT/epoxy interfaces.

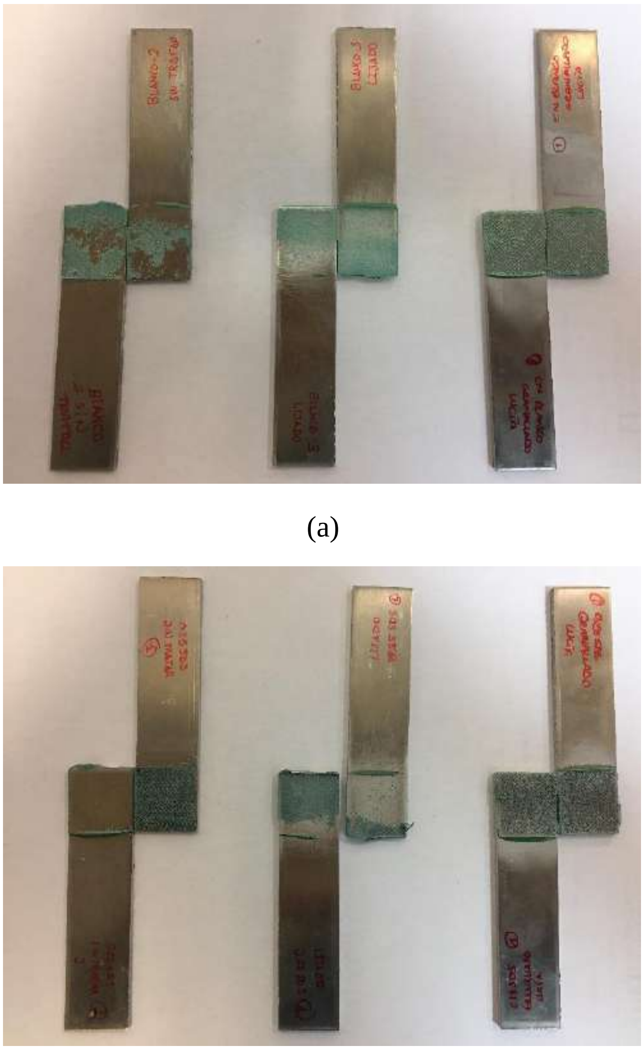

(a)

(b)

Figure 10.3: Fractured surfaces of Al-Al (a) neat and (b) CNT doped joints for (left to right) untreated, B, and GB conditions.

As aforementioned, the final aim of the proposed CNT adhesives is the SHM of bonded joints. In this regard, Figure 10.4 shows an example of electrical sensing curves of CNT-doped joints at SLS tests for the three surface treatment conditions.

An increase in electrical resistance is observed due to the adhesive deformation and crack propagation in the last stages of the SLS test, as reported in other studies [30]. It is observed that both brushed and grit-blasted specimens show an irregular electrical signal (Figure 10.4 (a) and (b), respectively), while the grit-blasted shows a softer one (Figure 10.4 (c)), very similar to those previously observed for CFRP-CFRP [29,30]. This noisy signal can be explained by attending to the interface between the adhesive and substrate. A more irregular interface, which leads to a poor contact, redounds in more unstable changes in the electrical resistance due to the continuous breakage and creation of electrical pathways during the test, as shown in the schematics of Figure 10.5. Therefore, it is possible to establish a correlation between the electrical behaviour and the quality of the joints.

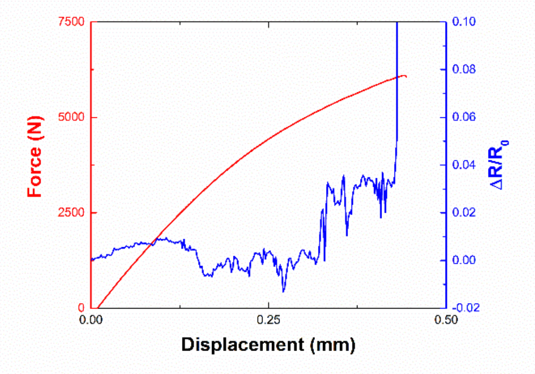

(a)

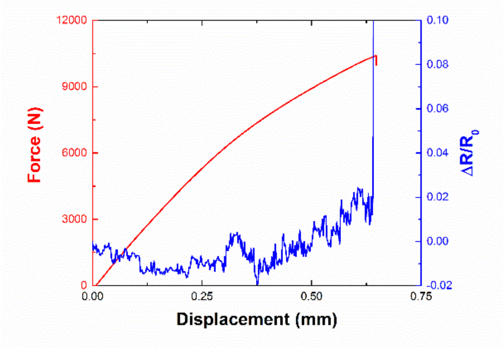

(b)

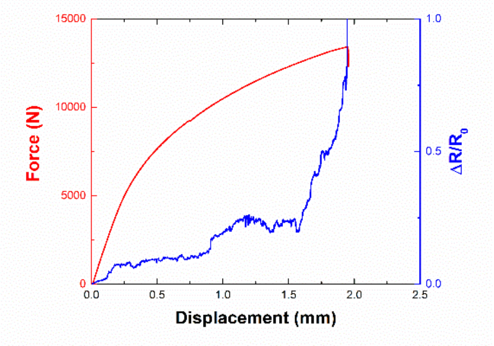

(c)

Figure 10.4: Monitoring electrical curves of SLS tests on Al-Al joints for (a) untreated, (b) brushed and (c) grit-blasted specimens.

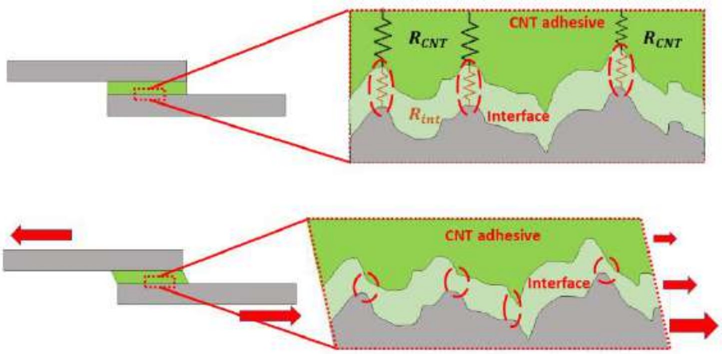

Figure 10.5: Schematics of breakage and creation of electrical pathways during a SLS tests where red circles indicate the preferential electrical paths.

10.3.2 Analysis of dissimilar joints

CFRP-Al joints were tested at two different conditions: brushing and grit blasting of Al surfaces. The untreated condition was not tested in these kinds of joints because of the poor behaviour in Al-Al joints. The results are summarised in Figure 10.6.

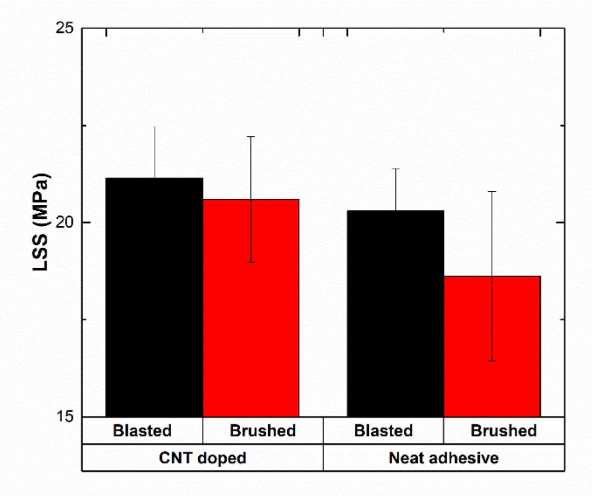

Figure 10.6: LSS of CFRP-Al joints for the neat and CNT doped adhesive films at two different Al surface treatments: brushing and grit blasting.

In this case, CNT addition to the adhesive film seems to have a positive influence on the total strength of the joint. This can be explained by the better interaction between CNTs and the epoxy resin of the CFRP substrate, leading to an overall enhancement of the strength in combination with the strengthening effect of the nanofillers, as commented before. These results are in good agreement with other studies in composite-metal joints with CNT-doped adhesives, where an enhancement in the total strength can be achieved due to a better transfer of the load from the composite to the metal substrate [35,36].

In addition, the fractured surfaces (Figure 10.7) show a mainly cohesive failure for every condition. In the case of brushed surfaces, some areas of adhesive failure can be observed in the metal interface (highlighted in red), which is in good agreement with those previously observed for Al-Al joints.

The electrical behaviour of CNT-doped joints during SLS tests is shown in the graphs of Figure 10.8. As previously observed, the electrical response of the joints highly depends on the quality of the interface. It is noticed that the electrical response significantly changes among specimens in the brushed condition (Figure 10.8 (a) and (b)). This is explained again by the irregular contact surfaces in the metal interface, leading to a more unstable electrical response (Figure 10.5).

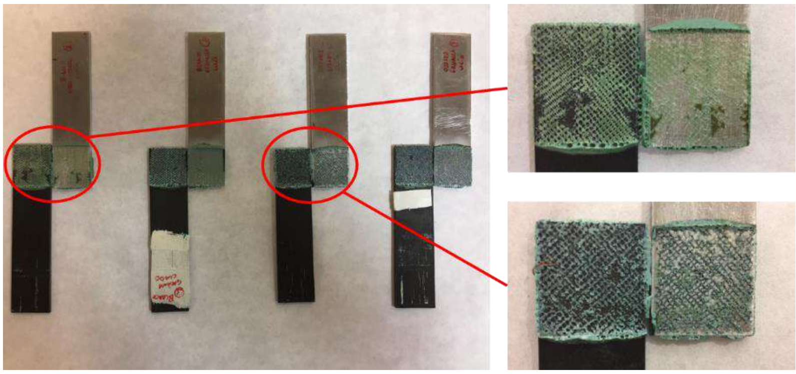

Figure 10.7: Fractured surfaces of CFRP-Al joints for (left to right) neat adhesive at B and GB conditions and CNT adhesive at B and GB conditions.

When analysing the electrical curves for grit-blasted specimens, a more stable and softer evolution of the electrical resistance is observed among specimens (Figure 10.8 (c) and (d)). This is explained by the more regular metal interface achieved by this surface treatment. When comparing to the Al-Al electrical response, it is observed that the electrical behaviour is even more stable and the evolution is softer. The reason for this is the better CNT-composite interaction in the CFRP interface when compared to the metal substrate, in combination with a good load transfer from the CFRP to the metal substrate, making it possible for the creation of more stable electrical pathways along the joint.

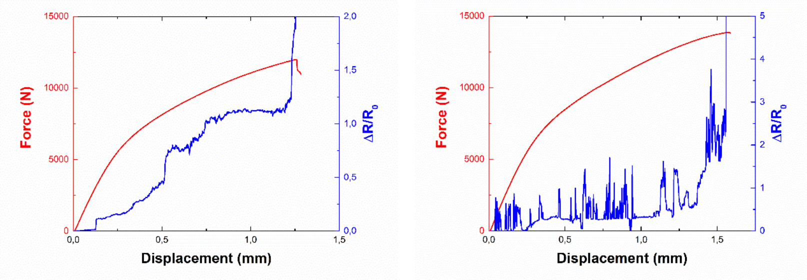

(a) (b)

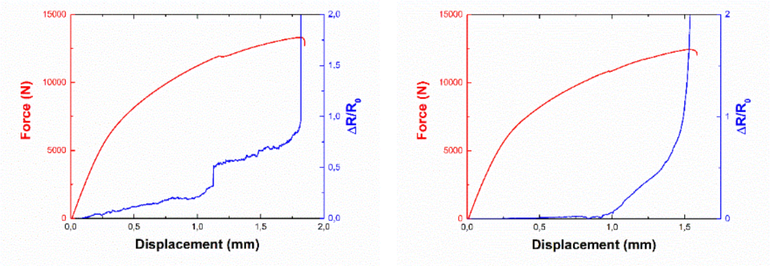

(c) (d)

Figure 10.8: Electrical curves for CNT-doped CFRP-Al joints at SLS tests for (a), (b) brushed and (c) and (d) grit-blasted surface treatments.

10.3.3 Comparison between similar and dissimilar joints

Figure 10.9 shows the LSS of SLS joints for the different tested conditions. The highest values of LSS are achieved in CFRP-CFRP joints, whose data were extracted from a previous study [31], for both neat and CNT-doped adhesive joints. This is explained by two different factors. The first factor is correlated to the better interaction between the CNTs and the composite substrate, causing a strengthening effect on the interface, as stated previously. The second factor is due to the higher stiffness and yield strength of the CFRP substrates in comparison to the aluminium alloy. The higher yield strength of the adherend induces an increase in the total strength of the joint, as stated in several studies [5-7].

When analysing the CFRP-Al and Al-Al joints, two different trends are found for the CNT-doped and neat adhesive joints. On the one hand, neat adhesive joints have a higher LSS for Al-Al joints in comparison to CFRP-Al. This might be surprising at first sight, but it could indicate a better load transfer in the Al-Al joints, making them stronger than CFRP-Al ones, which is in good agreement with other studies using CFRP and Al substrates [6].

On the other hand, CNT-doped joints show a higher LSS value for CFRP-Al joints in comparison to Al-Al ones. As previously commented, the interaction between CNTs and the composite redounds in a good interface between the adhesive and the CFRP substrate, while this interaction is not as good as with the metal substrate. This is in addition to the that fact CNTs promote a better load transfer between substrates, thus causing an increase in the total strength of the joint when compared to neat adhesive joints.

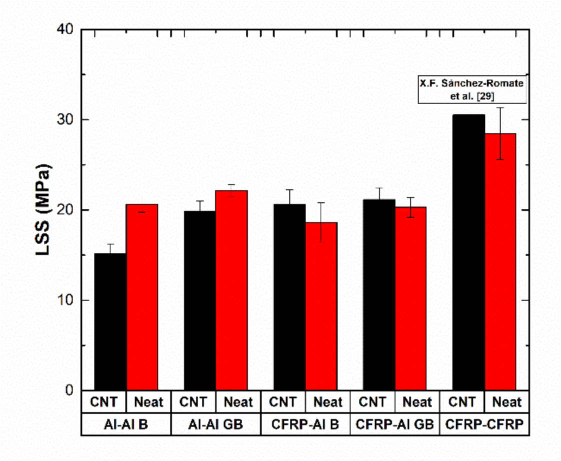

Figure 10.9: Summary of LSS for similar and dissimilar material SLS joints. The data corresponding to CFRP-CFRP joints are extracted from Sánchez et al. [31].

Therefore, the influence of the CNT addition and substrate material has been analysed. The results show a positive influence of the nanofiller when the interaction between them and the substrate is adequate, providing new mechanical paths for load transfer.

Moreover, the electrical properties of bonded joints are also analysed in order to better understand the monitoring capabilities of SLS joints. Table 10.3 summarises the normalised resistance, $\frac{\Delta R}{R_0}$, at displacement at failure for the different SLS tested joints.

The highest variation of electrical resistance is found in the CFRP-Al GB specimens, followed by CFRP-Al B, Al-Al GB and CFRP-CFRP, respectively. The Al-Al B specimen shows only a slight variation of the electrical resistance due to the previously explained unstable behaviour. This high variation in the electrical response for the CFRP-Al GB specimen is explained because of a good contact between the CNT adhesive and the composite interface. This promotes the creation of a homogeneous network of electrical pathways. When subjected to a mechanical load, the electrical resistance increases with strain exponentially due to the tunnelling effect between adjacent nanoparticles [37], as observed in the schematics of Figure 10.10. This fact, in combination with the good load transfer and reasonably good contact with the metal interface, redounds in a more significant change in the electrical resistance.

Table 10.3: Electrical properties at displacement failure for different SLS joints.

Materials	$\boldsymbol{\frac{\Delta R}{R_0}}$	**Displacement at failure (mm)**
CFRP-CFRP [31]	0.635	0.515
CFRP-Al GB	5.905	1.564
CFRP-Al B	1.229	1.228
Al-Al GB	0.854	1,944
Al-Al B	0.025	0.64

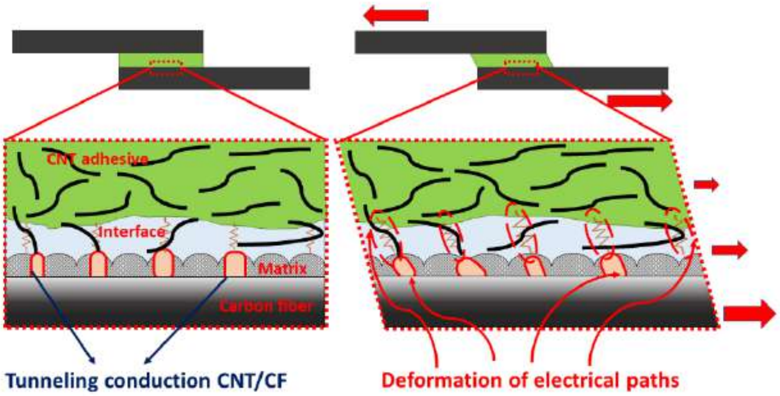

Figure 10.10: Schematics of CNT adhesive-CFRP interface showing the deformation of electrical pathways during SLS test.

The resistance change observed in the CFRP-Al B, Al-Al GB and CFRP-CFRP specimens can be explained in a similar way. In this case, it is important to notice that, although the variation of the normalised resistance is lower in the CFRP-CFRP joint, the displacement at failure is also much lower. This is explained by the fact that Al adherends yielded under higher tension and the rotating angle of the lap joint is also higher than for the CFRP-CFRP joints [5]. Therefore, by defining the sensitivity, S, as the change of the normalised resistance divided by the displacement, d, in mm, $S = \frac{\Delta R/R_0}{d}$, it is observed that for CFRP-CFRP joints, S is equal to 1.23, CFRP-Al B to 1 and Al-Al GB to 0.439. Therefore, the CFRP-CFRP joint is more sensitive to strain than the others. The reason for this is that it has a better interface between the substrate and the CNT adhesive. Its lower sensitivity in comparison to the CFRP-Al GB specimen (3.775) is explained because of the lower tunnelling distance between CNTs due to a lower deformation of the adherends.

10.3.4 Microstructural analysis

Figure 10.11 shows several SEM images of the Al and CFRP substrates for different surface treatments. An irregular distribution of the surface roughness is noticed when observing the Al-B surfaces (Figure 10.11 (a)). Some plain surfaces (Figure 10.11 (b)) and grooves (Figure 10.11 (c)) are observed, inducing, as explained before, an irregular distribution of electrical pathways through the joint, which causes an unstable electrical response. In addition, some weak interfaces are also observed (Figure 10.11 (d)), contributing to the irregular distribution of the electrical network.

However, the Al-GB surfaces show a more uniform roughness (Figure 10.11 (e) and (f)) which leads to an increase in the mechanical properties and forms a much more homogeneous electrical network. No weak interfaces are observed so a good interaction between the adhesive and Al substrate is achieved.

The analysis of CFRP interfaces reveals a good uniformity and no presence of weak bonds (Figure 10.11 (g) and (h)). This fact, in combination with the previously demonstrated good CNT-CFRP interaction, explains their higher mechanical and electrical performance.

Therefore, the analysis of transversal sections confirms the previous results regarding the electrical and mechanical response of the SLS joints.

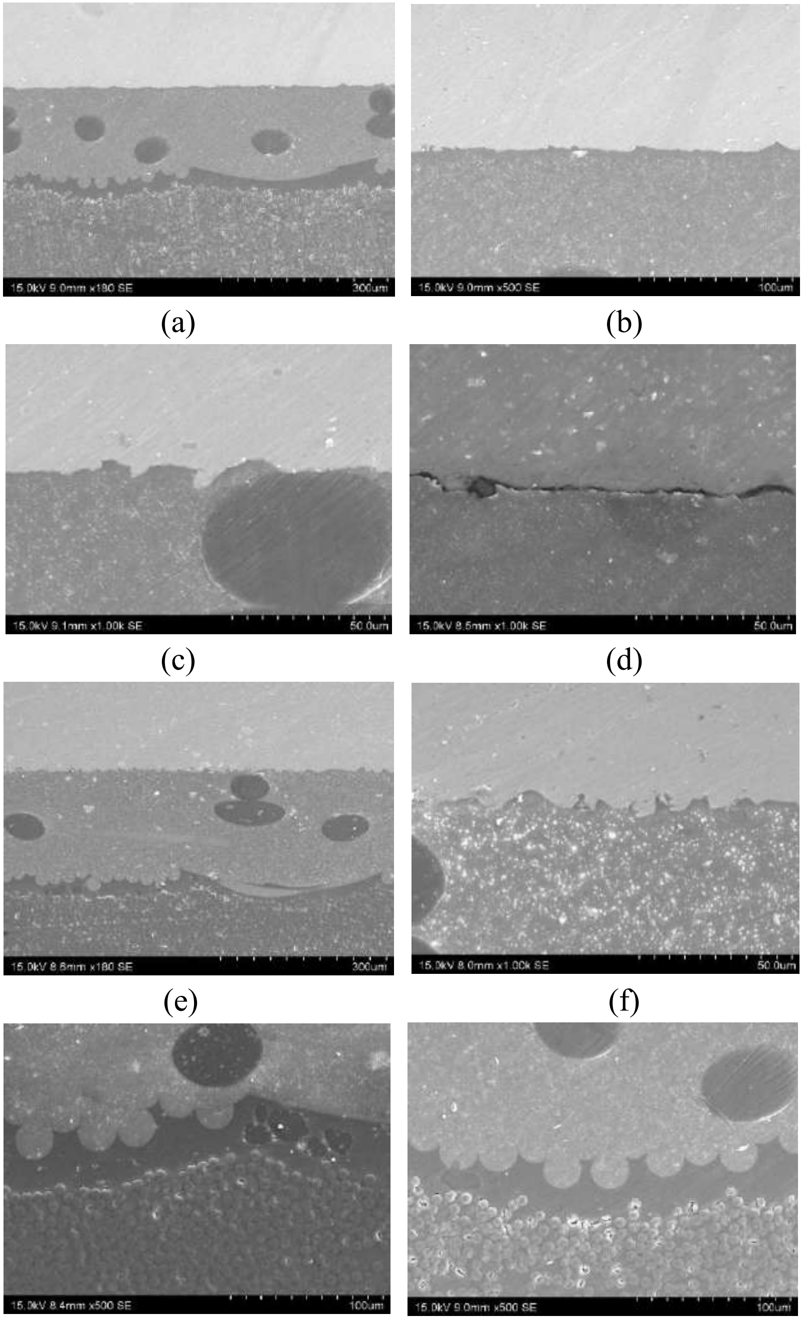

(a) (b)

(c) (d)

(e) (f)

(g) (h)

Figure 10.11: SEM images of transversal sections of the adhesive joints showing (a), (b), (c) and (b) Al-B, (e) and (f) Al-GB and (g) and (h) CFRP interfaces.

10.4 Conclusions

The electrical and mechanical behaviour of multi-material bonded joints using a novel CNT-doped adhesive film has been investigated.

The LSS of Al-Al joints is higher with neat adhesive for every surface treatment condition. This is explained by the poor interaction of CNT with metal substrates, leading to a poor load transfer and, thus, a reduction of the total strength of the joint. In addition to this fact, a higher influence of the surface treatment is observed in the CNT condition.

CFRP-Al joints show a higher LSS for CNT-doped specimens due to the better CNT interaction with the CFRP substrate and a better load transfer from CFRP to the Al substrate, as well as a strengthening effect of CNT inside the adhesive.

When comparing these results to CFRP-CFRP joints from previous studies, a reduction in the LSS is observed, as expected, due to the lower stiffness and strength of the Al substrates in comparison to CFRP ones.

The electrical response shows good agreement with the mechanical behaviour of SLS joints. More unstable measurements have been observed with poorer surface treatments due to the effect that irregular interactions between adhesive and substrate has on the creation and breakage of electrical pathways. A higher sensitivity is observed, thus, for the specimens with more homogeneous surface treatments, such as grit blasting. Therefore, the proposed CNT adhesive film is able to properly monitor SLS tests with dissimilar materials, acting as a powerful tool to evaluate the quality of the joint attending to their electrical response. This highlights the importance and applicability of the proposed technique in comparison to other available SHM methods.

Acknowledgements

This work was supported by the Ministerio de Economía y Competitividad of the Spanish Government [PROJECT MAT2016-78825-C2-1-R] and Comunidad de Madrid regional government [PROJECT 2013/MIT-2862].

10.5 References

[1] Hussey R, Wilson J. Structural Adhesives: Directory and Databook. 1996.

[2] Kim H, Kedward K. Stress analysis of adhesively-bonded joints under in-plane shear loading. J Adhesion 2001;76(1):1-36.

[3] Seong M, Kim T, Nguyen K, Kweon J, Choi J. A parametric study on the failure of bonded single-lap joints of carbon composite and aluminum. Composite Structures 2008;86(1):135-145.

[4] Alves DL, Campilho RDSG, Moreira RDF, Silva FJG, da Silva LFM. Experimental and numerical analysis of hybrid adhesively-bonded scarf joints. International Journal of Adhesion and Adhesives 2018;83:87-95.

[5] Sun G, Liu X, Zheng G, Gong Z, Li Q. On fracture characteristics of adhesive joints with dissimilar materials – An experimental study using digital image correlation (DIC) technique. Composite Structures 2018;201:1056-1075.

[6] Rudawska A. Adhesive joint strength of hybrid assemblies: Titanium sheet-composites and aluminium sheet-composites—Experimental and numerical verification. International Journal of Adhesion and Adhesives 2010;30(7):574-582.

[7] Banea MD, Rosioara M, Carbas RJC, da Silva LFM. Multi-material adhesive joints for automotive industry. Composites Part B: Engineering 2018;151:71-77.

[8] Palaniappan J, Ogin SL, Thorne AM, Reed GT, Crocombe AD, Capell TF, Tjin SC, Mohanty L. Disbond growth detection in composite-composite single-lap joints using chirped FBG sensors. Composites Sci Technol 2008;68(12):2410-2417.

[9] Habib F, Martinez M, Artemev A, Brothers M. Structural health monitoring of bonded composite repairs - A critical comparison between ultrasonic Lamb wave approach and surface mounted crack sensor approach. Composites Part B-Engineering 2013;47:26-34.

[10] Tamborrino R, Palumbo D, Galietti U, Aversa P, Chiozzi S, Luprano VAM. Assessment of the effect of defects on mechanical properties

of adhesive bonded joints by using non destructive methods. Composites Part B: Engineering 2016;91:337-345.

[11] Palaniappan J, Wang H, Ogin SL, Thorne AM, Reed GT, Crocombe AD, Rech Y, Tjin SC. Changes in the reflected spectra of embedded chirped fibre Bragg gratings used to monitor disbonding in bonded composite joints. Composites Sci Technol 2007;67(13):2847-2853.

[12] Flor FR, de Medeiros R, Tita V. Numerical and Experimental Damage Identification in Metal-Composite Bonded Joint. The Journal of Adhesion 2015;91(10-11):863-882.

[13] Crawford A, Droubi MG, Faisal NH. Analysis of Acoustic Emission Propagation in Metal-to-Metal Adhesively Bonded Joints. J Nondestr Eval 2018;37(2):33.

[14] Na WS. Low cost technique for detecting adhesive debonding damage of glass epoxy composite plate using an impedance based non-destructive testing method. Composite Structures 2018;189:99-106.

[15] Ruoff RS, Lorents DC. Mechanical and thermal properties of carbon nanotubes. carbon 1995;33(7):925-930.

[16] Popov VN. Carbon nanotubes: properties and application. Materials Science and Engineering: R: Reports 2004;43(3):61-102.

[17] De Volder MFL, Tawfick SH, Baughman RH, Hart AJ. Carbon Nanotubes: Present and Future Commercial Applications. Science 2013;339(6119):535-539.

[18] Hu N, Masuda Z, Yan C, Yamamoto G, Fukunaga H, Hashida T. The electrical properties of polymer nanocomposites with carbon nanotube fillers. Nanotechnology 2008;19(21):215701.

[19] Khan SU, Pothnis JR, Kim J. Effects of carbon nanotube alignment on electrical and mechanical properties of epoxy nanocomposites. Composites Part A-Applied Science and Manufacturing 2013;49:26-34.

[20] Mostaani F, Moghbeli MR, Karimian H. Electrical conductivity, aging behavior, and electromagnetic interference (EMI) shielding properties of polyaniline/MWCNT nanocomposites. J Thermoplast Compos Mater 2018;31(10):1393-1415.

[21] Cao X, Wei X, Li G, Hu C, Dai K, Guo J, Zheng G, Liu C, Shen C, Guo Z. Strain sensing behaviors of epoxy nanocomposites with carbon nanotubes under cyclic deformation. Polymer 2017;112:1-9.

[22] Arif MF, Kumar S, Gupta TK, Varadarajan KM. Strong linear-piezoresistive-response of carbon nanostructures reinforced hyperelastic polymer nanocomposites. Composites Part A: Applied Science and Manufacturing 2018;113:141-149.

[23] Reddy SK, Kumar S, Varadarajan KM, Marpu PR, Gupta TK, Choosri M. Strain and damage-sensing performance of biocompatible smart CNT/UHMWPE nanocomposites. Materials Science and Engineering: C 2018;92:957-968.

[24] Lim AS, Melrose ZR, Thostenson ET, Chou T. Damage sensing of adhesively-bonded hybrid composite/steel joints using carbon nanotubes. Composites Sci Technol 2011;71(9):1183-1189.

[25] Kang M, Choi J, Kweon J. Fatigue life evaluation and crack detection of the adhesive joint with carbon nanotubes. Composite Structures 2014;108:417-422.

[26] Takeda T, Narita F. Fracture behavior and crack sensing capability of bonded carbon fiber composite joints with carbon nanotube-based polymer adhesive layer under Mode I loading. Composites Science and Technology 2017;146:26-33.

[27] Augustin T, Karsten J, Kötter B, Fiedler B. Health monitoring of scarfed CFRP joints under cyclic loading via electrical resistance measurements using carbon nanotube modified adhesive films. Composites Part A: Applied Science and Manufacturing 2018;105:150-155.

[28] Rose JL. The upcoming revolution in ultrasonic guided waves. 2011;7983:798302.

[29] Sánchez-Romate XF, Sánchez M, García-Nieto C, Molinero J, Jiménez-Suárez A, Güemes A, Ureña A. Structural health monitoring of bonded joints using carbon nanotube doped adhesive films. Eur Workshop Struct Health Monit , EWSHM 2016;4:2450-2455.

[30] Fernández Sánchez-Romate XX, Molinero J, Jiménez-Suárez A, Sánchez M, Güemes A, Ureña A. Carbon Nanotube Doped Adhesive Films for Detecting Crack Propagation on Bonded Joints: A Deeper Understanding of Anomalous Behaviors. ACS applied materials & interfaces 2017.

[31] Sánchez-Romate XF, Jiménez-Suárez A, Molinero J, Sánchez M, Güemes A, Ureña A. Development of bonded joints using novel CNT doped adhesive films: Mechanical and electrical properties. International Journal of Adhesion and Adhesives 2018;86:98-104.

[32] Saleema N, Sarkar DK, Paynter RW, Gallant D, Eskandarian M. A simple surface treatment and characterization of AA 6061 aluminum alloy surface for adhesive bonding applications. Applied Surface Science 2012;261:742-748.

[33] Gojny F, Wichmann M, Kopke U, Fiedler B, Schulte K. Carbon nanotube-reinforced epoxy-compo sites: enhanced stiffness and fracture toughness at low nanotube content. Composites Sci Technol 2004;64(15):2363-2371.

[34] Bai J, Allaoui A. Effect of the length and the aggregate size of MWNTs on the improvement efficiency of the mechanical and electrical properties of nanocomposites - experimental investigation. Composites Part A-Applied Science and Manufacturing 2003;34(8):689-694.

[35] Korayem AH, Li CY, Zhang QH, Zhao XL, Duan WH. Effect of carbon nanotube modified epoxy adhesive on CFRP-to-steel interface. Composites Part B: Engineering 2015;79:95-104.

[36] Konstantakopoulou M, Kotsikos G. Effect of MWCNT filled epoxy adhesives on the quality of adhesively bonded joints. Plastics, Rubber and Composites 2016;45(4):166-172.

[37] Hu N, Karube Y, Yan C, Masuda Z, Fukunaga H. Tunneling effect in a polymer/carbon nanotube nanocomposite strain sensor. Acta Materialia 2008;56(13):2929-2936.

Chapter 11: An Approach to Crack Propagation Monitoring in Skin-Stringer Composite Structures Using Novel Carbon Nanotube Doped Adhesive Films

Xoan F. Sánchez-Romate[a,b,*]*, Ángel Renato Pozo*[a]*, Alberto Jiménez-Suárez*[b]*, María Sánchez*[b]*, Alfredo Güemes*[a] *and Alejandro Ureña*[b]

Submitted to Compos Part B (2019)

[a] Department of Aerospace Materials and Processes, Escuela Técnica Superior de Ingenieros Aeronáuticos, Universidad Politécnica de Madrid, Plaza del Cardenal Cisneros 3, 28040 Madrid, Spain

[b] Materials Science and Engineering Area, Escuela Superior de Ciencias Experimentales y Tecnología, Universidad Rey Juan Carlos, Calle Tulipán s/n, 28933 Móstoles (Madrid), Spain

*Corresponding author: xoan.fernandez.sanchezromate@urjc.es Tel: +34914888252

Skin-stringer sub-elements are manufactured using novel carbon nanotube doped adhesive films in order to detect crack propagation mechanisms during peeling tests by means of electrical measurements. This monitoring tests are combined with SEM analysis of cross-sectional surfaces to detect some manufacturing defects such as lack of compaction due to a low curing pressure. It is observed that the electrical resistance increases with the crack propagation as there is a breakage of electrical pathways. This increase is more prevalent when crack propagation takes places more rapidly as the breakage of conductive is also more significant and it is more prevalent at high test rates. In addition, by simple theoretical estimations, it is possible to know the debonded area, which gives a more accurate idea of how the crack propagates inside the adhesive joint. This estimation of debonded area is compared to the crack patterned area of the fracture surfaces, showing a good agreement. Therefore, this technique proves a significant potential and applicability for crack propagation monitoring of stiffened elements.

Keywords: carbon nanotubes; adhesive joints; composites; stiffened panels; Structural Health Monitoring

11.1 Introduction

The increasingly requirements of aerospace industry make necessary to develop more efficient materials with higher performance and lightweight. For these reasons, composite structures are now attracting the interest of this industry, due to their exceptional mechanical properties and low density in comparison to traditional metallic alloys [1]. In addition, they also show other interesting properties such as good corrosion resistance or radar transparency, making them very useful for many different applications.

Therefore, the higher use of composite materials is associated to an increasingly complexity of composite structures, making necessary the assembly of several components. In this context, the use of adhesive joints for assembly purposes presents many advantages over the bolted connections as they avoid stress concentrations around the holes and lead to weight saving [2,3]. However, they also have many limitations, as their inspection is often very complex and usually requires the disassembly of various components. Thus, it is necessary to develop novel inspection techniques ensuring the reliability of the adhesive joints without increasing maintenance and other additional costs.

The development of proper inspection techniques for composites is a challenging subject, as conventional fiber reinforced polymer composite (FRP) structures also present a wide range of complex failure modes such as fiber breakage, matrix cracking or delamination. For these reasons, the inspection technique must be robust and able to detect and reflect the possible changes due to the presence of defects. To date, there are a lot of research about Fiber Bragg Grating sensors (FBGs) [4-6] and Lamb wave detection among other non-destructive techniques (NDTs) [7-9]. However, most of them often does not give a global overview of the structures, such as FBGs; requires complex analysis techniques, such as Lamb Waves; or implies the implementation of preventive maintenance such as other conventional NDT techniques [10-12]. Therefore, it is necessary to develop an on-line technique for Structural Health Monitoring (SHM) of composite structures addressing the main issues of the existing ones.

In this context, the use of carbon nanoparticles, and more specifically, carbon nanotubes (CNTs) is now increasing since their discovery [13-16]. They have excellent physical properties and their addition to conventional polymer matrixes gives composites new functionalities [17-19] as a substantial enhancement of the electrical conductivity due to the formation of percolating networks inside the material where tunneling transport plays a dominant role [20-22].

The tunneling effect, in combination with the inherent piezoresistivity of CNTs, makes them very useful, thus, for SHM applications [23-27]. It has been observed that the strain monitoring capabilities and sensitivities of these materials are much higher than those reported by conventional metallic strain gauges [28-31]. Moreover, the main advantage of this technique is that the material itself is acting as a sensor, so all the changes in material due to the presence of cracks, delamination, voids, etc. will be reflected by electrical monitoring [32,33].

To date, there are many research on SHM with paste adhesives [34-36], showing the huge potential of CNTs to detect strain and crack propagation mechanisms without compromising the mechanical performance [37-40]. However, most of adhesive joints in aircraft design use films as bonding agent as they allow better thickness control and are easy to handle with. Furthermore, the CNT addition to adhesive films does not involve complex dispersion techniques such as three roll milling, often used to achieve good CNT dispersions on paste adhesives [41,42].

In previous studies, it has been observed that CNT doped adhesive films are properly able to detect crack propagation on bonded joints, showing a high sensitivity. Single Lap Shear and Mode-I tests have been carried out and the electrical response has been correlated to the mechanical performance of the joints [43]. In addition, a detailed study of dispersion influence has been also conducted, showing the influence that dispersion parameters have on the mechanical and electrical performance of the joints [44].

For these reasons, this work intends to go one step further by the analysis of SHM capabilities of CNT doped adhesive films in more complex elements. To achieve that, sub-elements composed by a skin and a stringer have been tested by peeling, while their electrical response has been measured. The aim is to corroborate if the proposed technology for bonded joints is also valid for more complex elements while getting a deeper knowledge about the main failure mechanisms of these kind of sub-elements. In addition, a microstructural study of the joints has been also carried out to identify possible manufacturing and bonding defects. The details of the experimental procedure are shown at the end of the manuscript.

11.2 Experimental procedure

11.2.1 Materials

Nanoparticles used for this study were Multi-wall carbon nanotubes (MWCNTs), supplied by Nanocyl, with a commercial name NC7000. They have an average diameter of 10 nm and a length up to 2 µm.

The adhesive film was a FM300K, supplied by Cytec. It is an epoxy based adhesive with a wide open knit tricot carrier, allowing a better thickness control during curing. It has a mechanical strength of 36.8 MPa and high toughness and elongation.

Stiffened elements (Figure 11.1) were manufactured by co-bonding of a pre-cured T stringer and an uncured flat skin with dimensions of 300 x 150 mm (Figure 11.1 (a)). The material used for the skin was a 2x2 twill CFRP fabric Z19723-ABS5003P-HTA (926) with a layer sequence of [+45/0]s to get a 1.8 mm thickness while the T-stringers were provided by FIDAMC with the geometry shown in Figure 11.1 (b)

11.2.2 Manufacturing process

CNT dispersion (0.1 wt. %) was achieved by means of ultrasonication in an aqueous media, using a horn sonicator during 20 min. To get a better disaggregation of larger agglomerates, a surfactant called SDS (sodium dodecyl sulfate) was used in a 0.25 wt. %. These parameters were previously optimized in other studies [44]. Once CNTs were dispersed, they were sprayed over the adhesive surface using an airbrush at a pressure of 1 bar and 40 cm distance prior to curing.

A manual lay-up process was performed to manufacture the un-cured flat skin with the determined layer sequence. The bonding surface of the pre-cured T stringer was carefully sanded and cleaned with isopropyl alcohol before to manually lay up the doped adhesive layer. Then, the T-stringer was positioned along the flat skin and a vacuum bag process was performed under vacuum conditions. In order to co-bonding the elements the vacuum bag was put into an oven with a standard curing cycle of heating ramp of 2ºC/min and a stabilization step at 180ºC during 150 min.

11.2.3 Electrical tests

Stiffened elements were tested at peeling conditions as shown in the scheme of Figure 11.1 (a) with a load applied in the stringer and a clamping such as shown by the red areas of the schematics and in the actual image of test of Figure 11.1 (d). Test rate was selected at 5 and 10 mm/min in order to study its effect on mechanical properties. The goal was to monitor the crack evolution during these tests by means of electrical measurements.

To achieve these purposes, some electrodes (shown also in the image of Figure 11.1(c)) were attached to both the skin and the stringer to monitor the electrical response through the joint. These electrodes were made of copper wire, attached with silver ink to the substrate surface to have a good electrical contact, and sealed with an adhesive layer to protect them from environment.

In addition to that, the test was recorded by a camera in order to see the approximate crack evolution in the edges of the joint.

11.2.4 Microstructural study

A microstructural study was carried out to better characterize the quality of the CNT adhesive joints, identifying some possible defects during manufacturing. The analysis of transversal joints has been carried out by Scanning electron microscopy (SEM) using a S-3400N apparatus from Hitachi.

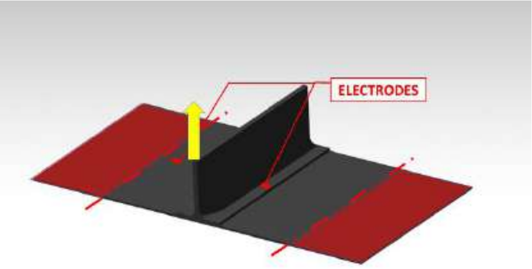

(a)

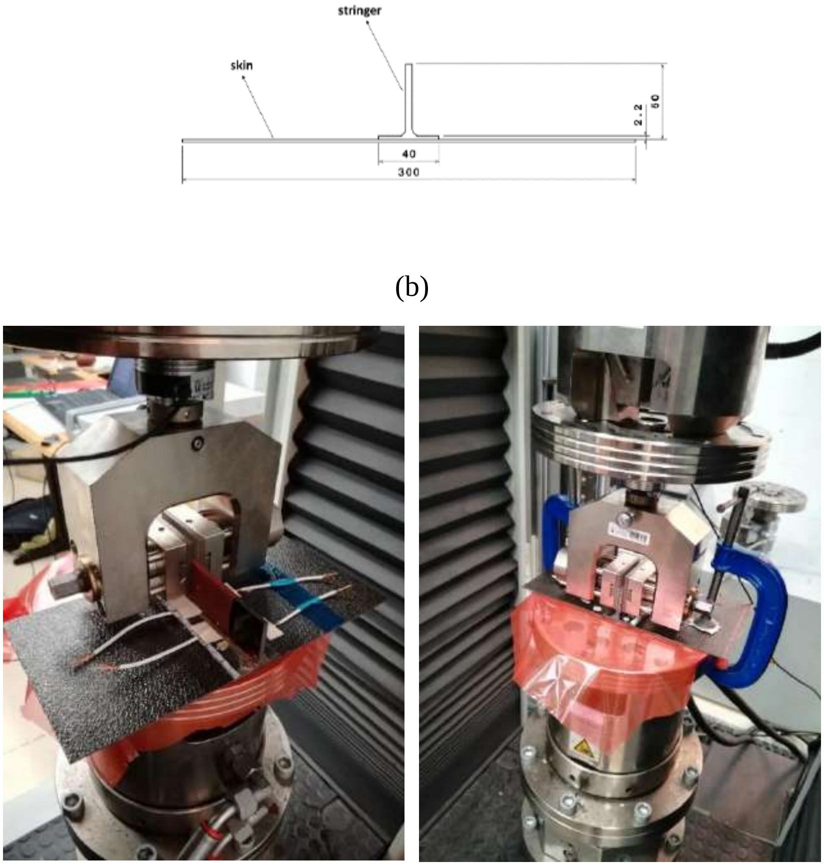

(b)

(c) (d)

Figure 11.1: Schematics of the (a) skin-stringer element with the electrode disposition (yellow arrow indicate the direction of the applied load and red areas the clamped regions) and (b) cross-sectional area with the stringer dimensions (in mm) and (c) image of the actual configuration during the test with (d) the campling system.

11.3 Results and discussion

In this section, the main results of the mechanical testing of stiffened elements are going to be presented and discussed. First of all, a microstructural analysis of bonded joints has been carried out in order to get a deeper knowledge about the possible failure mechanisms that could take place during tests. Then, the electrical response is analyzed during the peeling test. Details of the experimental conditions are shown in the Experimental procedure section at the end of the manuscript.

11.3.1 Microstructural analysis

In addition to that, a microstructural analysis of the bonding line is also carried out in order to better characterize the joint quality and to identify some possible manufacturing defects. For these reasons, a section of the skin-stringer element is cut after manufacturing. Figure 11.2 shows SEM images of the cross-sectional area of the bonded joint between skin and stringer.

Three regions can be distinguished: the CFRP substrate, the interface between adhesive and substrate and the adhesive itself (Figure 11.2 (a)). It differs from previous studies in standard specimens manufactured by secondary bonding [43] where only the adhesive and the substrate can be distinguished. In this case, during the curing process some resin from the adhesive film penetrates the skin promoting the creation of an intermediate region between the adhesive and the substrate (Figure 11.2 (b)). A generally good interface adhesive-substrate is observed along the bonding line. However, some localized porosity is observed in both adhesive joint and, the skin substrate (Figure 11.2 (c)) because of the manufacturing process, carried out at vacuum conditions, inducing a lack of compaction. This porosity can be avoided by the introduction of a higher curing pressure by using an autoclave technology as it induces a higher compaction. Nevertheless, as commented before, the quality and the homogeneity of the adhesive joint is much better than hot-press manufacturing used in previous studies for secondary bonding, where the induced porosity were much more generalized [43].

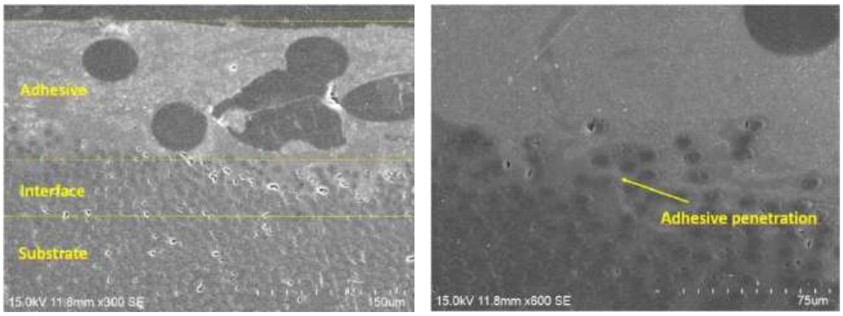

(a) (b)

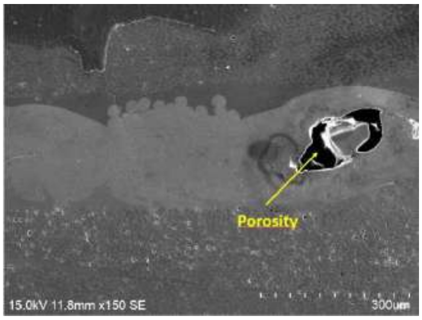

(c)

Figure 11.2: SEM images of the transversal section of the adhesive joint showing (a) the substrate, interface and adhesive regions, (b) the adhesive penetration within the substrate and (c) some localized porosity.

11.3.2 Mechanical testing

Figure 11.3 shows an example of the electromechanical curves obtained during the peeling tests. It is observed that the electrical resistance generally increases during the application of the mechanical load. This general trend is in good agreement with previous results for Mode-I specimens, where the increasing electrical resistance is correlated to crack growth, as it induces a breakage of main electrical pathways along the adhesive joint.

As pointed out for Mode-I testing, different regions can be distinguished depending on the electromechanical behavior of the stiffened element (marked as points 1, 2, 3 and 4 respectively in Figure 11.3): the first one is correlated to the first stages of peeling tests, where no significant crack propagation is taking place through the joint. In this case, the main sensing mechanism is the tunneling effect between adjacent CNTs. Thus, the adhesive deformation causes an increase of the tunneling distance, leading to an electrical resistance growth. However, this increase is not as prevalent as in Tensile or Single Lap Shear tests as the whole joint is not subjected to the same strain level, as observed in the schematics of Figure 11.4.

The second region corresponds to those points where a loss of mechanical strength is observed due to a rapid crack propagation. Here, a sharp increase of the electrical resistance is observed, as there is a sudden breakage of several electrical pathways. The behavior is similar to that observed in previous works for Mode-I standard specimens in the case of stick-slip curves where crack propagation is unstable [43].

Third region can be identified as the areas where crack propagation takes places more softly, as a continuous increase of the mechanical load applied. It is correlated to slight increases of the electrical resistance, as the breakage of electrical pathways is less quick than in the previous region.

Finally, the fourth region corresponds to the last stages of the peeling tests, near final failure, being preceded by a sudden decrease of the load and, thus, a sharp increase of the electrical resistance. These results, therefore, show a general trend that also can be correlated to crack propagation in fatigue tests for SLS specimens, studied in previous research, where the last stages of crack propagation are correlated to significant variations on the electrical response, allowing to anticipate the final failure of the specimen. However, there are some crucial points to be investigated.

The aforementioned instability is often due to high shear rates, inducing an irregular crack propagation along the joint [46,47]. For these reasons, shear rate has been varied in order to see the possible effects that could have in the debonding propagation.

Figure 11.3 (b) shows an example of the electromechanical curve obtained for peeling tests at 5 mm/min shear rate. A similar trend than for the higher shear rate specimen is observed, that is, a general increase of the electrical resistance due to the effect that debonding has on the electrical network through the adhesive. However, some significant differences can be observed when comparing both cases. First of all, a more uniform behavior of both mechanical and electrical curves is observed for low test rates. This is associated to a more uniform crack propagation along the adhesive joint, leading to a softer breakage of electrical paths. Instead of sudden losses of the load, it is noticed many slight drops, correlated to slight increases of the electrical resistance. In addition, in the last stages of testing, the change of the electrical resistance is much lower than in the stick-slip case, leading to a much lower sensitivity. It is important to notice that, before this last stage, the absolute change in the electrical resistance was similar to stick-slip curve (around 70-100 % change approximately). That difference in the last stages could be explained by a more explosive crack propagation at high test rates which can lead to a higher debonded area and, thus, a significant increase of the electrical resistance.

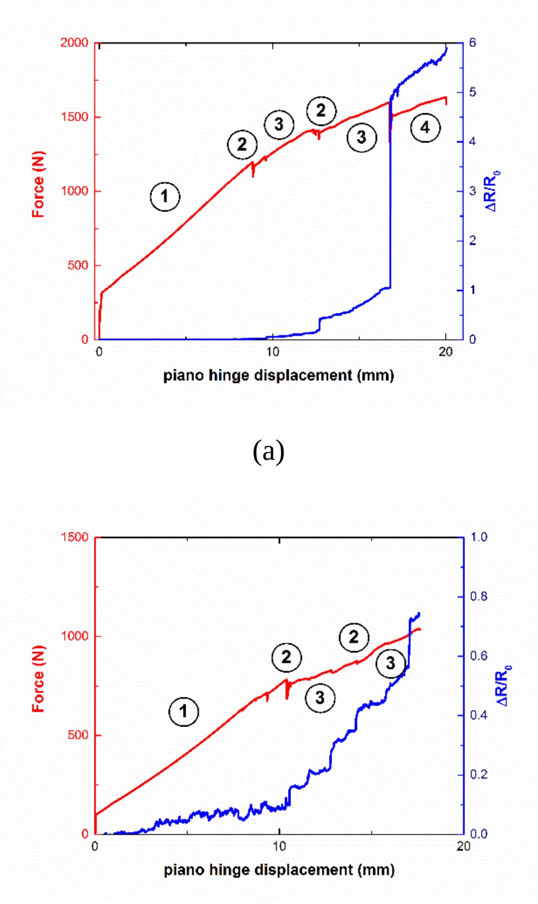

(a)

(b)

Figure 11.3: Electromechanical curves for the stiffened element at (a) 10 mm/min and (b) 5 mm/min test rate.

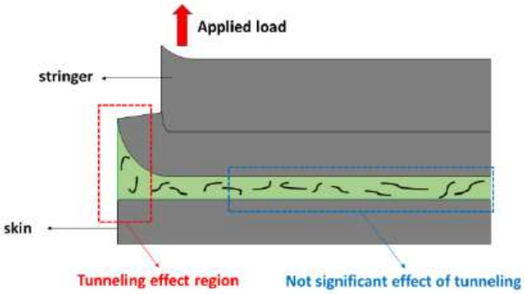

Figure 11.4: Schematics of tunneling distance effect on the adhesive joint at the beginning of the peeling tests.

Therefore, the stated results shed light into how test rate could affect the mechanical behavior at peeling tests. It has been observed that stick-slip behavior is the main prevalent mechanism at high test rates while a more uniform debond propagation is expected when testing at lower test rates. The measured electrical behavior also proves this statement.

However, although some conclusions can be obtained, a further analysis of the main mechanisms involving peeling tests in this kind of sub-elements is still necessary. Therefore, a simple theoretical analysis is carried out.

11.3.3 Theoretical analysis

To analyze the deboding evolution during the peeling tests, a theoretical model, based on previous studies [43], is proposed. By considering the adhesive joint as a parallel circuit of distributed resistances, the total electrical resistance is given by the following expression:

$$\frac{1}{R} = \rho \frac{A_{contact}}{t} \tag{11.1}$$

Being ρ *the resistivity of the reinforced adhesive film*, $A_{contact}$ the area of the bonded joint and t the adhesive thickness.

This formula is valid when there are no manufacturing defects such as porosity due to an irregular pressure distribution, thickness variation due to some overflowing effect or an irregular distribution of CNTs, just to mention few examples. In a previous study, some of these defects were noticed, probably due to a non-homogeneous pressure distribution during curing, causing a gradient of conductivities through the joint [43,45]. In this case, CNT distribution is going to be considered homogeneous and no significant porosity and thickness variation is expected as the pressure distribution is more homogeneous than for Mode-I and SLS specimens, manufactured by hot press.

Thus, the size of the debonded area can be calculated from the value of the electrical resistance, leading to the following formula:

$$\frac{R}{R_0} = \frac{A_0}{A_{contact}} \tag{11.2}$$

Where A_0 and R_0 stand for the initial bonding area and electrical resistance, respectively.

Therefore, it is possible to estimate the debonded area from the measured electrical response during peeling tests. In according to this, Figure 11.5 shows the evolution of the estimated bonding area as a function of displacement for the specimens of 10 and 5 mm/min respectively in correlation with the measured edge crack. As expected, a more unstable decrease of the bonded area is observed at 10 mm/min specimen at the breakage of electrical pathways is also more irregular. By deeply observing the last stages of the peeling tests, it is observed that the value of the bonded area is much lower in than in the case of the 5 mm/min specimen. It implies that the fracture mechanisms are not the same in both cases.

It is observed that for stick-slip curve, the crack reaches the end of the total length of the stringer. However, after that, the electrical resistance still increases. This can be explained by the form in which crack tends to propagate inside the joint. The crack propagation behavior differs from that shown in Mode-I specimens where the crack front is approximately uniform. In this case, the data for the side crack length that was recorded by the camera during the peeling test shows that the crack propagation takes place firstly in the stringer edges where the stress is higher due to the bending effects, as shown in the schematics of Figure 11.5 (a). This debonding first appears at the skin-stringer corner and then starts to propagate through the edges because of a higher stress concentration [48] and inside the adhesive joint, as observed in the schematics of crack propagation of Figures 11.5 (b) and (c). Therefore, in the case of stick-slip specimen (Figure 11.5 (b)), the electrical resistance increases even after reaching the end of the specimen because of the crack propagation inside the joint until failure. This is also clearly seen in the graphs showing the calculated bonding area and the crack length, giving a more accurate analysis of debonding in these skin-stringer elements. The sharp decrease in the bonding area (correlated, thus, to a sharp increase in the electrical resistance) is associated to the final propagation of the crack at the end of the specimen length. In this case, there is an abrupt change in the area as the crack starts to propagate inside the joint, as shown in the region 3 of the schematics of Figure 11.5 (b). The evolution inside the adhesive joint can be described similar to crack propagation in Mode-II [49].

In the case of the 5 mm/min test rate specimen, the crack does not reach the end of the specimen length just before final failure. That, means, accordingly to the schematics of Figure 11.5 (c), that the debonded area is not as larger as in the other case before the final failure propagation. This is in good agreement with the previously estimated results by the theoretical predictions from electrical measurements. This, therefore, explains the differences observed in the sensitivity in the last stages of the peeling test. In addition, a softer evolution of the crack propagation is also observed, being in good agreement also with the previous estimations, as there are not sudden changes in the bonding area due to the crack propagation in the joint.

Figure 11.6 shows an image of the fractured surface of the adhesive joint. A cohesive failure is observed through all the joint, showing a similar pattern than in previous studies for secondary bonding [43,45]. This indicates, as a first sight, a good adhesion in the interface between adhesive and substrate. In addition to that, Figure 11.5 (b) shows the patterned area of the crack. It is observed that, before failure, the crack area is similar to that estimated by the theoretical calculations showed in Figure 11.5 (c).

Therefore, the electrical monitoring of these stiffened elements by the proposed techniques shows a good potential and applicability and allows to get a deeper knowledge about crack propagation mechanisms.

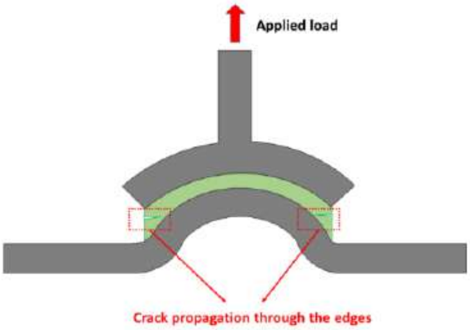
Applied load
Crack propagation through the edges

(a)

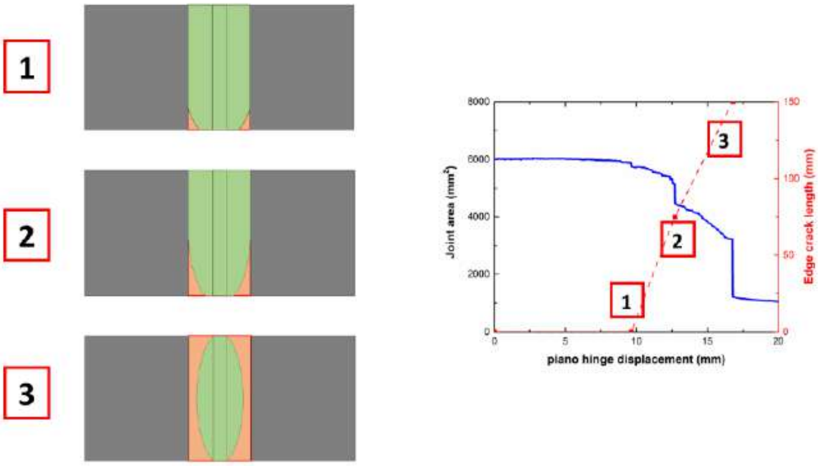
1
2
3
8000
6000
4000
2000
0
Joint area (mm^2)
0
5
10
15
20
piano hinge displacement (mm)
150
100
50
0
Edge crack length (mm)

(b)

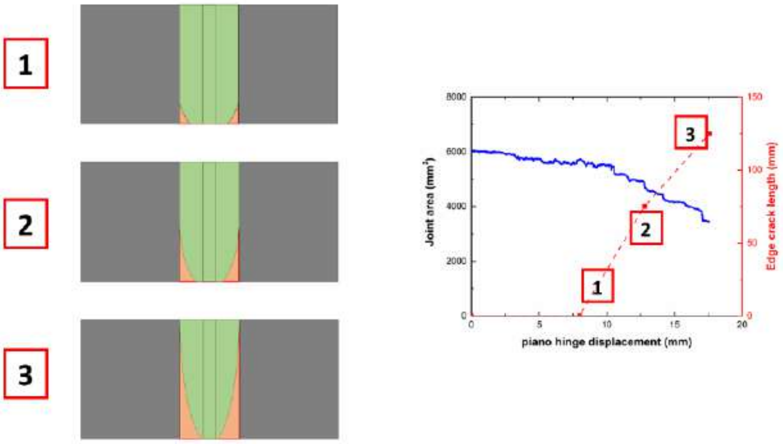

(c)

Figure 11.5: (a) Schematics of crack propagation at initial steps and crack evolution in the stiffened panel and their approximate correlation to the calculated bonding area for (b) 10 and (c) 5 mm/min test rate specimens.

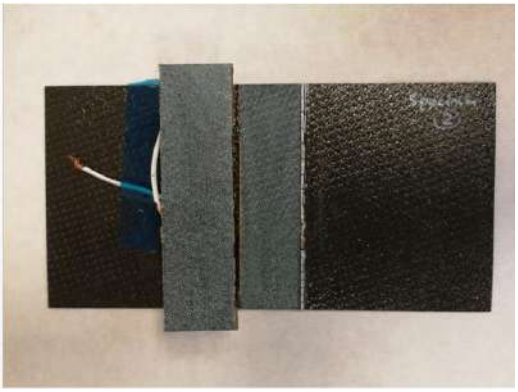

(a)

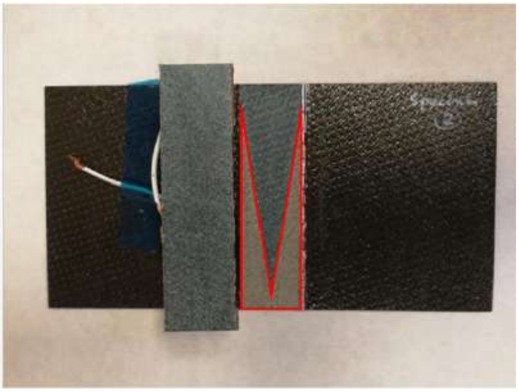

(b)

Figure 11.6: (a) Image of the fracture surface showing (b) the pattern of the crack propagation (highlighted in red).

11.4 Conclusions

Sensing capabilities of CNT reinforced adhesive films on stiffened sub-elements have been studied. For this purpose, peeling tests on skin-stringer elements have been carried out.

It has been observed that the electrical resistance increases with crack propagation, that is, with increasing debonded area. This is due to the breakage of electrical pathways along the joint. It has been also noticed that the electrical response follows a more stable behavior when crack propagation takes places in a more uniform way whereas in the case of unstable debonding propagation, this stick-slip behavior is also reflected in the electrical response by sudden increases of the electrical resistance followed by steadier phases. This instability is more prevalent at high test rates, as proved by experimental analysis. By this way, by measuring the electrical response, it is possible to distinguish between these two types of behaviors.

A simple theoretical approach has been used to get a deeper knowledge about the correlation between mechanical performance and electrical response. The study shows the evolution of the bonded area during peeling tests. By correlating these calculations to the measured crack length by camera, it is possible to know deeper the crack evolution, taking place mainly in the edges and propagating afterwards inside the joint.

Therefore, CNT reinforced adhesive films have demonstrated their capacity to properly detect debonding and crack propagation in this kind of elements. It is also possible to know some interesting features such as the way in which crack propagates inside the joint and how the test rate can affect this mechanical behavior. Thus, this study constitutes a further step in the current investigation on adhesive films, being a promising technique for SHM applications.

Acknowledgements

This work was supported by the Ministerio de Economía y Competitividad of Spanish Government [Project MAT2016-78825-C2-1-R] and Comunidad de Madrid Government [Project P2013/MIT-2862].

11.5 References

[1] Peters ST. Handbook of composites. : Springer Science & Business Media, 2013.

[2] Hussey R, Wilson J. Structural Adhesives: Directory and Databook. : Springer Science & Business Media, 1996.

[3] Kim H, Kedward K. Stress analysis of adhesively-bonded joints under in-plane shear loading. J Adhesion 2001;76:1-36.

[4] Bernasconi A, Carboni M, Comolli L, Galeazzi R, Gianneo A, Kharshiduzzaman M. Fatigue Crack Growth Monitoring in Composite Bonded Lap Joints by a Distributed Fibre Optic Sensing System and Comparison with Ultrasonic Testing. J Adhesion 2016;92:739-57.

[5] Palaniappan J, Wang H, Ogin SL, Thorne AM, Reed GT, Crocombe AD et al. Changes in the reflected spectra of embedded chirped fibre Bragg gratings used to monitor disbonding in bonded composite joints. Composites Sci Technol 2007;67:2847-53.

[6] Bernasconi A, Carboni M, Comolli L. Monitoring of fatigue crack growth in composite adhesively bonded joints using fiber Bragg gratings. Procedia Engineering 2011;10:207-12.

[7] Tamborrino R, Palumbo D, Galietti U, Aversa P, Chiozzi S, Luprano VAM. Assessment of the effect of defects on mechanical properties of adhesive bonded joints by using non destructive methods. Composites Part B: Engineering 2016;91:337-45.

[8] GONCALVES JPM. Application of interface finite elements to three-dimensional progressive failure analysis of adhesive joints. Fatigue & fracture of engineering materials & structures 05;26:479; 479,486; 486.

[9] Yu X, Fan Z, Puliyakote S, Castaings M. Remote monitoring of bond line defects between a composite panel and a stiffener using distributed piezoelectric sensors. Smart Mater Struct 2018;27:035014.

[10] Betz DC, Thursby G, Culshaw B, Staszewski WJ. Structural damage location with fiber Bragg grating rosettes and Lamb waves. Structural Health Monitoring-an International Journal 2007;6:299-308.

[11] Yan G. A Bayesian approach for damage localization in plate-like structures using Lamb waves. Smart Mater Struct 2013;22:035012.

[12] Sherafat MH, Guitel R, Quaegebeur N, Hubert P, Lessard L, Masson P. Structural health monitoring of a composite skin-stringer assembly using within-the-bond strategy of guided wave propagation. Materials & Design 2016;90:787-94.

[13] Iijima S. Helical Microtubules of Graphitic Carbon. Nature 1991;354:56-8.

[14] Popov VN. Carbon nanotubes: properties and application. Materials Science and Engineering: R: Reports 2004;43:61-102.

[15] De Volder MFL, Tawfick SH, Baughman RH, Hart AJ. Carbon Nanotubes: Present and Future Commercial Applications. Science 2013;339:535-9.

[16] Khan U, May P, O’Neill A, Vilatela JJ, Windle AH, Coleman JN. Tuning the mechanical properties of composites from elastomeric to rigid thermoplastic by controlled addition of carbon nanotubes. Small 2011;7:1579-86.

[17] Li J, Ma PC, Chow WS, To CK, Tang BZ, Kim J. Correlations between percolation threshold, dispersion state, and aspect ratio of carbon nanotubes. Advanced Functional Materials 2007;17:3207-15.

[18] Gibson RF. A review of recent research on mechanics of multifunctional composite materials and structures. Composite Structures 2010;92:2793-810.

[19] Ferreira ADBL, Nóvoa PRO, Marques AT. Multifunctional Material Systems: A state-of-the-art review. Composite Structures 2016;151:3-35.

[20] Gao R, Pan Z, Wang Z. Work function at the tips of multiwalled carbon nanotubes. Appl Phys Lett 2001;78:1757-9.

[21] De Vivo B, Lamberti P, Spinelli G, Tucci V, Vertuccio L, Vittoria V. Simulation and experimental characterization of polymer/carbon nanotubes composites for strain sensor applications. J Appl Phys 2014;116:054307.

[22] Sanchez-Romate XF, Jimenez-Suarez A, Sanchez M, Guemes A, Urena A. Novel approach to percolation threshold on electrical conductivity of carbon nanotube reinforced nanocomposites. Rsc Advances 2016;6:43418-28.

[23] Li C, Thostenson ET, Chou T. Sensors and actuators based on carbon nanotubes and their composites: A review. Composites Sci Technol 2008;68:1227-49.

[24] Alamusi, Hu N, Fukunaga H, Atobe S, Liu Y, Li J. Piezoresistive Strain Sensors Made from Carbon Nanotubes Based Polymer Nanocomposites. Sensors 2011;11:10691-723.

[25] Jeong YR, Park H, Jin SW, Hong SY, Lee S, Ha JS. Highly Stretchable and Sensitive Strain Sensors Using Fragmentized Graphene Foam. Advanced Functional Materials 2015;25:4228-36.

[26] Vertuccio L, Guadagno L, Spinelli G, Lamberti P, Zarrelli M, Russo S et al. Smart coatings of epoxy based CNTs designed to meet practical expectations in aeronautics. Composites Part B-Engineering 2018;147:42-6.

[27] García-Macías E, Rodríguez-Tembleque L, Saez A, Ubertini F. Crack detection and localization in RC beams through smart MWCNT/epoxy strip-like strain sensors. Smart Mater Struct 2018.

[28] G.S. Holister ALW. Strain Gauge Technology. London: Elsevier Applied Science, 1982.

[29] Cao J, Wang Q, Dai H. Electromechanical properties of metallic, quasimetallic, and semiconducting carbon nanotubes under stretching. Phys Rev Lett 2003;90:157601.

[30] Cullinan MA, Culpepper ML. Carbon nanotubes as piezoresistive microelectromechanical sensors: Theory and experiment. Physical Review B 2010;82:115428.

[31] DeGraff J, Liang R, Le MQ, Capsal J, Ganet F, Cottinet P. Printable low-cost and flexible carbon nanotube buckypaper motion sensors. Materials & Design 2017;133:47-53.

[32] Hu N, Karube Y, Arai M, Watanabe T, Yan C, Li Y et al. Investigation on sensitivity of a polymer/carbon nanotube composite strain sensor. Carbon 2010;48:680-7.

[33] Heeder NJ, Shukla A, Chalivendra V, Yang S, Park K. Electrical Response of Carbon Nanotube Reinforced Nanocomposites Under Static and Dynamic Loading. Exp Mech 2012;52:315-22.

[34] Mactabi R, Rosca ID, Hoa SV. Monitoring the integrity of adhesive joints during fatigue loading using carbon nanotubes. Composites Sci Technol 2013;78:1-9.

[35] Kang M, Choi J, Kweon J. Fatigue life evaluation and crack detection of the adhesive joint with carbon nanotubes. Composite Structures 2014;108:417-22.

[36] Kim C, Choi J, Kweon J. Defect detection in adhesive joints using the impedance method. Composite Structures 2015;120:183-8.

[37] Gude MR, Prolongo SG, Urena A. Toughening effect of carbon nanotubes and carbon nanofibres in epoxy adhesives for joining carbon fibre laminates. Int J Adhes Adhes 2015;62:139-45.

[38] Li X, Zhang W, Zhai S, Tang S, Zhou X, Yu D et al. Investigation into the toughening mechanism of epoxy reinforced with multi-wall carbon nanotubes. E-Polymers 2015;15:335-43.

[39] Jakubinek MB, Ashrafi B, Zhang Y, Martinez-Rubi Y, Kingston CT, Johnston A et al. Single-walled carbon nanotube–epoxy composites for structural and conductive aerospace adhesives. Composites Part B: Engineering 2015;69:87-93.

[40] Akpinar IA, Gültekin K, Akpinar S, Akbulut H, Ozel A. Research on strength of nanocomposite adhesively bonded composite joints. Composites Part B: Engineering 2017;126:143-52.

[41] Chapartegui M, Markaide N, Florez S, Elizetxea C, Fernandez M, Santamaria A. Curing of epoxy/carbon nanotubes physical networks. Polym Eng Sci 2012;52:663-70.

[42] Aravand M, Lomov SV, Verpoest I, Gorbatikh L. Evolution of carbon nanotube dispersion in preparation of epoxy-based composites: From a masterbatch to a nanocomposite. Express Polymer Letters 2014;8:596-608.

[43] Fernández Sánchez-Romate XX, Molinero J, Jiménez-Suárez A, Sánchez M, Güemes A, Ureña A. Carbon Nanotube Doped Adhesive Films for Detecting Crack Propagation on Bonded Joints: A Deeper Understanding of Anomalous Behaviors. ACS applied materials & interfaces 2017.

[44] Sánchez-Romate XF, Jiménez-Suárez A, Molinero J, Sánchez M, Güemes A, Ureña A. Development of bonded joints using novel CNT doped adhesive films: Mechanical and electrical properties. International Journal of Adhesion and Adhesives 2018;86:98-104.

[45] Sánchez-Romate XF, Sánchez M, García-Nieto C, Molinero J, Jiménez-Suárez A, Güemes A et al. Structural health monitoring of bonded joints using carbon nanotube doped adhesive films. Eur Workshop Struct Health Monit , EWSHM 2016;4:2450-5.

[46] Blackman BRK, Kinloch AJ, Rodriguez Sanchez FS, Teo WS, Williams JG. The fracture behaviour of structural adhesives under high rates of testing. Eng Fract Mech 2009;76:2868-89.

[47] Karac A, Blackman BRK, Cooper V, Kinloch AJ, Sanchez SR, Teo WS et al. Modelling the fracture behaviour of adhesively-bonded joints as a function of test rate. Eng Fract Mech 2011;78:973-89.

[48] Li G, Lee-Sullivan P, Thring R. Nonlinear finite element analysis of stress and strain distributions across the adhesive thickness in composite single-lap joints. Composite Structures 1999;46:395-403.

[49] Blackman BRK, Kinloch AJ, Paraschl M. The determination of the mode II adhesive fracture resistance, G(IIC), of structural adhesive joints: an effective crack length approach. Eng Fract Mech 2005;72:877-97.

Chapter 12: An Approach Using Highly Sensitive Carbon Nanotube Adhesive Films for Crack Growth Detection under Flexural Load in Composite Structures

Xoan F. Sánchez-Romate[a,b,*], *Rocío Moriche*[b,c], *Alberto Jiménez-Suárez*[b], *María Sánchez*[b], *Alfredo Güemes*[a] *and Alejandro Ureña*[b]

Submitted to Compos Struct (2019)

[a] Department of Aerospace Materials and Processes, Escuela Técnica Superior de Ingenieros Aeronáuticos, Universidad Politécnica de Madrid, Plaza del Cardenal Cisneros 3, 28040 Madrid, Spain

[b] Materials Science and Engineering Area, Escuela Superior de Ciencias Experimentales y Tecnología, Universidad Rey Juan Carlos, Calle Tulipán s/n, 28933 Móstoles (Madrid), Spain

[c] Departamento de Ingeniería y Ciencia de los Materiales y del Transporte, Universidad de Sevilla, Avda. Camino de los Descubrimientos, s/n, 41092 Sevilla, Spain

*Corresponding author: xoan.fernandez.sanchezromate@urjc.es Tel: +34914888252

Sensing capabilities of carbon nanotube (CNT) doped adhesive films under bending conditions were investigated. Standard Mode-II coupons and skin-stringer sub-elements were manufactured while their electrical resistance was monitored. Mode-II energy fracture was improved when adding CNTs in comparison to neat adhesive joints due to their toughening effect. Electrical monitoring showed a stable increase of the electrical resistance with crack length with lower sensitivity than Mode-I testing due to a lower crack opening effect. A good agreement was observed by comparing to theoretical estimations, indicating a uniform adhesive distribution inside the joint, confirmed by SEM analysis. Monitoring tests on skin-stringer sub-elements subjected to bending load showed a similar behavior but some sharp increases were observed, especially in the last stages of the test, due to a less uniform adhesive distribution in the central region. Therefore, the proposed technique shows a high potential and applicability for Structural Health Monitoring of composite structures.

Keywords: carbon fiber structures; adhesives; carbon nanotubes; SHM; mechanical properties

12.1 Introduction

Carbon Fiber Reinforced Polymer (CFRP) materials are now of interest because of their high specific as well as some physical properties such as a good corrosion resistance in comparison to conventional metallic alloys. Therefore, the increasing complexity of composite structures has promoted the development of proper assembly techniques.

In this regard, bonded joints present some advantages over bolted connections such as a weight saving and the absence of stress concentrators around the bolt holes (1) but their reliability is not totally ensured by the available inspection techniques. They are mainly based in Fiber Bragg Gratings (FBGs), Ultrasonic Waves or Acoustic Emission systems (2-6). However, their main limitation is that they do not often give a global and complete information about the damage and the obtained signal is sometimes very difficult to analyze and requires complex numerical techniques (7-10). In addition to that, the identification of debonding in adhesive joints is especially difficult and these techniques sometimes do not give a very accurate information about this issue (6, 10).

In this context, carbon nanotubes (CNTs), since the first studies by S. Iijima,(11) have demonstrated a huge potential as they have excellent mechanical and electrical properties (12-15), being suitable for SHM applications by electrical resistance monitoring (16-22).

The CNT capability for SHM applications is based on their piezoresistivity and the tunneling effect between adjacent nanoparticles (23-26), leading to higher gauge factors, defined as the change of the normalized electrical resistance divided by the applied strain, than conventional metallic foils (27, 28). For these reasons they are able to properly identify and quantify some defects such as delaminations or cracks (29, 30).

In previous studies, the effect of CNTs on bonded joints has been investigated by using novel adhesive films sprayed with an aqueous CNT solution (31, 32). This CNT dispersion is done by means of ultrasonication and helped by the addition of a surfactant Sodium-Dodecyl-Sulfate (SDS). Sensing capabilities of CNT doped adhesive films have been demonstrated in Single Lap Shear (SLS) and Mode-I tests. In fact, it has been possible to distinguish between different failure and crack propagation modes by analyzing the electrical response, showing a good agreement and high sensitivity (33).

In this regard, this study aims to analyze the crack propagation under bending conditions on adhesive joints by using the proposed CNT doped adhesive film and their capability for SHM of more complex structures. For that purpose, Mode-II standard specimens and stiffened elements were tested in similar load conditions. The main goal is to get a deeper knowledge about sensing capabilities of CNT doped adhesive films and prove their potential for crack detection in simple sub-elements subjected to more complex load states. Moreover, the comparison between the standard coupons and the sub-elements will give a more complete overview of SHM capabilities of the proposed adhesive films.

In addition to that fact, a simple theoretical model has been proposed to correlate the electrical signal and the mechanical performance of the joints, similar to previous theoretical estimations (33), showing the differences between Mode-I and Mode-II crack propagation. Furthermore, a microstructural characterization of the transversal section and fracture surfaces has been carried out in order to know the adhesive distribution along the joint and identify possible manufacturing defects.

12.2 Experimental procdure

12.2.1 Adhesive preparation

The adhesive used for this study was a FM 300K, supplied by Cytec. It is an epoxy-based adhesive film with a knit tricot carrier typical in aerospace applications for joining CFRP-CFRP and CFRP-metal substrates.

Multi-wall carbon nanotubes (MWCNTs) are supplied by Nanocyl with a commercial name NC7000. They have an average diameter of 10 nm and a length up to 1.5 µm.

The addition of the CNTs to the adhesive film is done by spraying an aqueous CNT dispersion over the adhesive surface at 1 bar. The dispersion is achieved by means of ultrasonication during 20 min, with the help of a surfactant called sodium-dodecyl-sulfate (SDS). CNT and SDS content are fixed at 0.1 and 0.25 wt. %. After that, water is removed by drying the adhesive at 70 ºC during 30 min. All of these parameters are set based on a previous study (32).

12.2.2 Manufacturing of normalized coupons and stiffened elements

Normalized bonded joints are manufactured by secondary bonding in a uniaxial hot press. CFRP substrates are Unidirectional (UD) laminates of 150 × 25 × 3.5 mm3 with a peel-ply surface treatment. Cure cycle conditions are described in Table 12.1. A Teflon of 40 mm is placed at the beginning of the joint to induce the pre-crack for Mode-II testing.

Table 12.1: Cure cycle parameters of secondary bonding.

Parameter	First Stage	Second stage
Pressure	Ramp from 0 to 0.6 MPa during 15 min	0.6 MPa during 90 min
Temperature	Ramp from 25 to 175 ºC during 45 min	175 ºC during 60 min

Stiffened elements are manufactured by secondary bonding of a flat skin of 150 × 300 mm2 with a layer sequence [±45/90/]S and a T-stringer using a vacuum bag as shown in Figure 12.1. The curing temperature was set as previously described in Table 12.1. Secondary bonding is set as the manufacturing technique to directly compare the monitoring tests of the stiffened elements with those obtained from normalized coupons. The pre-crack is made by placing a Teflon insert of 16 mm at the beginning (25 % of the width of the stringer, similar to Mode-II standard coupons, highlighted in red in Figure 12.1).

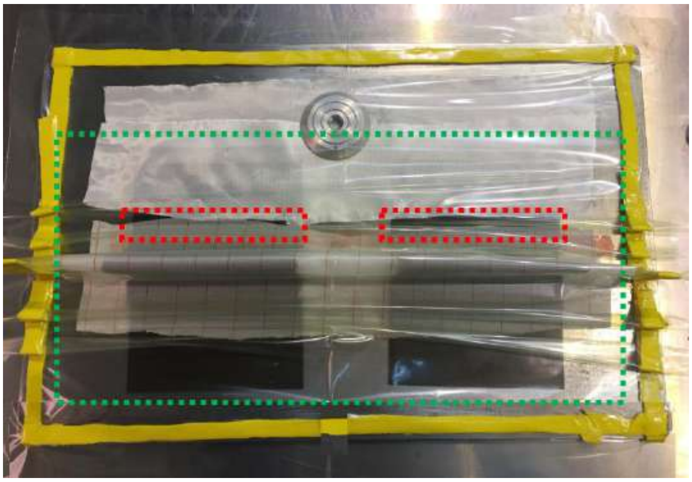

Figure 12.1: Image of the vacuum bag used in the manufacturing of skin-stringer elements. The sub-elements disposition is highlighted in green while the pre-cracked area is marked in red.

12.2.3 Electromechanical and microstructural characterization

Monitoring of both normalized coupons and skin-stringer sub-elements was carried out by means of electrical resistance measurement using a hardware Agilent 34401A.

Electrodes were placed as shown in the schematics of Figure 12.2 and were made of copper wire sealed to the CFRP substrate with silver ink and protected from the environment with an adhesive layer.

Mechanical tests were conducted at a test rate of 1 mm/min in both coupons and sub-elements. In the case of standard coupons, four tests were conducted for each neat and CNT-doped adhesive conditions. Two skin-stringer sub-elements were tested with the CNT-doped adhesive film. One representative example of each condition is shown in the Results and Discussion section.

Microstructural analysis of the transversal sections of normalized coupons and skin-stringer sub-elements was carried out by Scanning Electron Microscopy (SEM) using a S-3400 N apparatus from Hitachi. The samples were coated by a thin layer of gold and SEM images were taken at different magnifications for a better characterization.

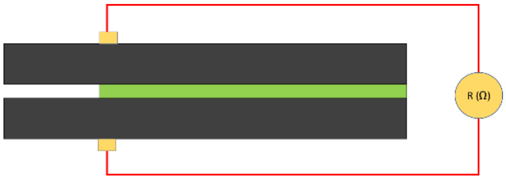

(a)

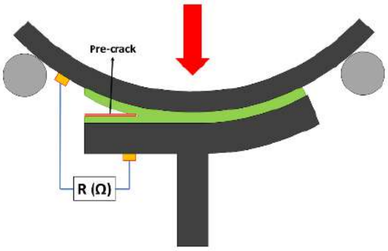

(b)

Figure 12.2: Electrode's disposition in (a) a standard coupon and in (b) a skin-strimger sub-element.

12.3 Results and discussion

This section shows the main results of the electromechanical tests of the CNT doped adhesive joints under bending conditions. Firstly, the mechanical behavior of the Mode-II adhesive joints is analyzed by comparing the fracture energy values of doped and non-doped bonded joints. Simultaneously, the electrical response of the standard Mode-II coupons is also analyzed and compared to the crack propagation through the joint. Then, the most representative results of the sub-elements under bending loading are shown and a comparison with the Mode-II specimen is carried out. Simultaneously, a microstructural study of the bonding line and the fracture surfaces is given.

12.3.1 Mode-II mechanical behavior

By using the Timoshenko beam theory for End Notched Flexure (ENF) test, the specimen compliance ($C = \delta/P$, being δ and P the displacement and the load, respectively) is written as follows:

$$C = \frac{3a^3 + 2L^3}{8E_1Bh^3} + \frac{3L}{10G_{13}Bh} \tag{12.1}$$

Where a is the crack length, L the half length of the span, B and h the width and the thickness of the substrate and $E_1$and G_{13} its longitudinal and shear moduli, respectively,

Therefore, it is possible to calculate the equivalent crack length, a_e from the current specimen compliance by rewriting the Equation (12.1):

$$a_e = \left(\frac{1}{3}\left(\left(C - \frac{3L}{10G_{13}Bh}\right)8E_1Bh^3 - 2L^3\right)\right)^{\frac{1}{3}} \tag{12.2}$$

The strain energy release rate under mode II can be calculated by using the Irvin-Kies equation:

$$G_{II} = \frac{P^2}{2B}\frac{dC}{da} \tag{12.3}$$

Combining the Equations (12.2) and (12.3) it is possible to obtain the G_{II} value:

$$G_{II} = \frac{9P^2{a_e}^2}{16B^2h^3E_1} \tag{12.4}$$

Figure 12.3 shows the mechanical curves of the CNT-doped and neat adhesive joints. Both neat and CNT-doped joints show an expected behavior, in according to other studies (34, 35). The peak load of the force-displacement curve (Figure 12.3 (a)) is slightly higher in the case of CNT-doped bonded joints. By analyzing the $G_{II} - a_e$ curves (also called R-curves) some differences can be observed when adding CNTs to the adhesive film (Figure 12.3 (b)). A slower crack propagation is observed in the CNT-doped sample, leading, thus to a higher value of the fracture energy, around 5 N/mm, in comparison to the neat joints (4.2 N/mm). This enhancement is explained by a good CNT homogeneity, with the absence of larger agglomerates which can induce an embrittlement (32, 36). These results are in good agreement with those observed in Mode-I crack propagation testing (33) and can be explained because of the bridging and toughening effect of CNTs, making the crack propagation along the joint harder (37-39).

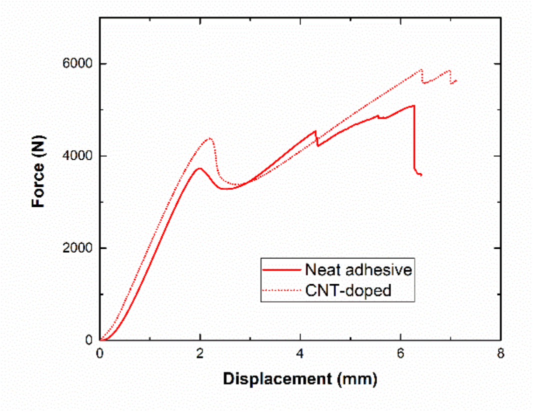

(a)

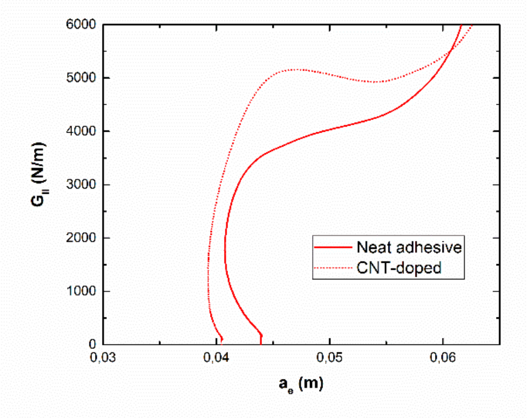

(b)

Figure 12.3: (a) Load-displacement and (b) R-curves of the CNT-doped and neat adhesive Mode-II joints.

Therefore, the CNT addition enhances the fracture energy and leads to a slower crack propagation. As a further step, the huge increase of the electrical conductivity induced by the CNT percolating networks will be used as a method for on-line crack growth monitoring.

12.3.2 Mode-II electromechanical analysis

Figure 12.4 shows an example of the electromechanical behavior of Mode-II standard specimens. By observing the graph of Figure 12.4 (a), it is noticed that there is a sudden increase of the electrical resistance corresponding to the first drop on the mechanical response. This is correlated with the initial crack propagation through the bonded joint in a similar way than previously observed for Mode-I specimens in other studies (33). Then, there is an increase of the electrical resistance until final failure of the specimen due to a continuous breakage of electrical pathways.

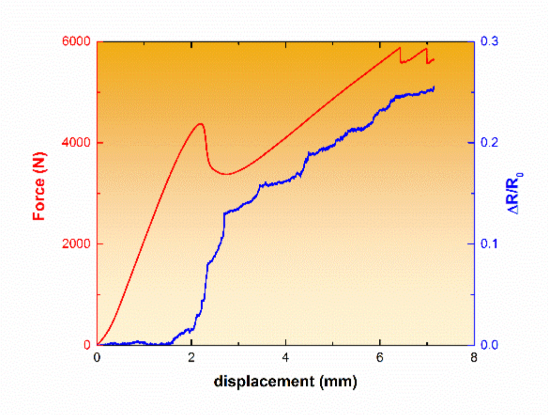

(a)

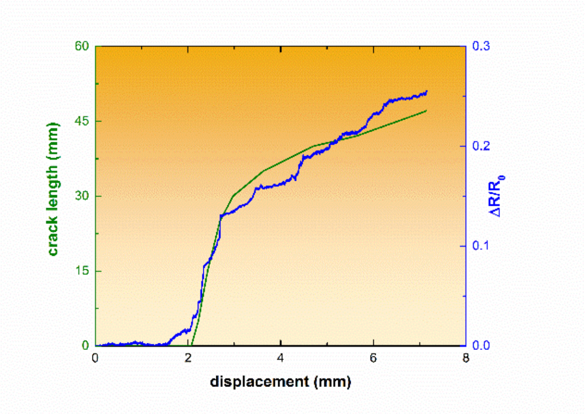

(b)

Figure 12.4: Electromechanical behavior of the Mode-II joints showing (a) the load and (b) crack length to electrical response.

It is important to notice that there is an initial increase of the electrical resistance before crack starts to propagate. This initial increase is associated to the bending effect of the specimens, which induces the adhesive deformation, leading to an increase on the tunneling distance between adjacent CNTs and thus, to an electrical resistance growth. After that, a steady increase of the electrical resistance is observed.

By analyzing the crack propagation and the electrical response, shown in Figure 12.4 (b) it is observed that there is a very good agreement between the crack length and the corresponding measured electrical resistance. It is observed that a faster crack propagation is directly correlated to a higher increase of the electrical resistance as there is a sudden breakage of the electrically conductive pathways.

Figure 12.5 shows the electrical resistance change as a function of the crack length and crack propagation velocity. The crack propagation velocity is calculated from crack length measurements following this formula:

$$v = \frac{\Delta a}{\Delta t} \tag{12.5}$$

Where Δa is the crack length change during a known time interval Δt.

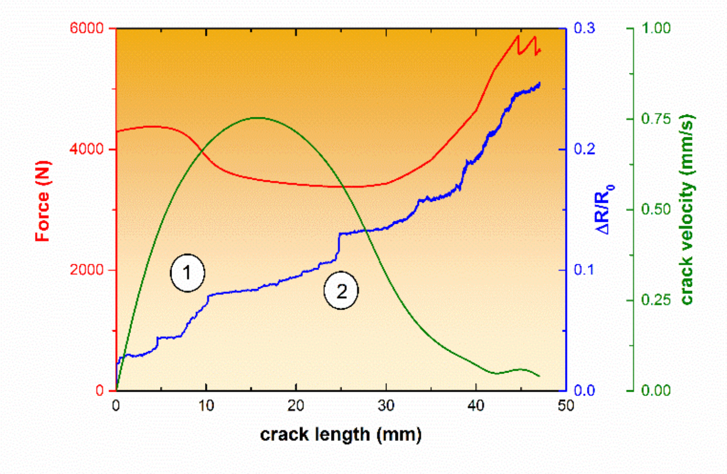

Figure 12.5: Electromechanical response as a function of the crack length.

It is noticed that the increase of the electrical resistance as a function of the crack length is smooth, although some slight sharp increases are also observed (highlighted in the graph as points 1 and 2). These sudden changes are correlated to areas with higher crack propagation velocity and with a sudden drop in the load. This faster crack propagation can be correlated to an irregular crack growth, in a similar way than the stick-slip effect shown in Mode-I testing.

In order to have a deeper knowledge of the electromechanical behavior of the adhesive joints, it is possible to make a first estimation of the electrical response as a function of the crack length. For this purpose, a similar theoretical model than the developed for Mode-I specimens (33) is proposed, given by the following expression valid for an ideal adhesive joint:

$$\frac{\Delta R}{R_0} = \frac{A_0}{A} - 1 = \frac{b \cdot L}{b \cdot (L - a)} - 1 \tag{12.6}$$

Where b and L are the width and the total length of the adhesive joint.

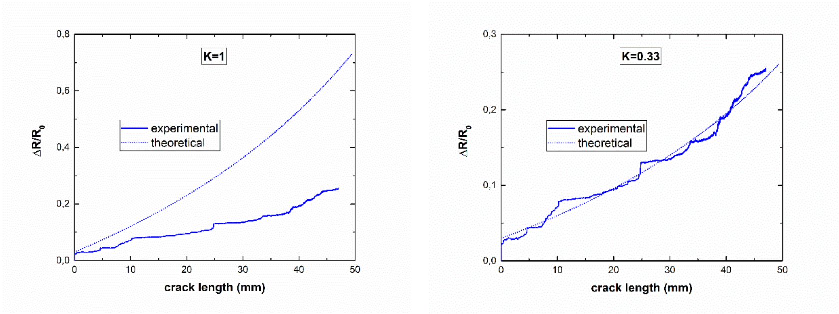

(a) (b)

Figure 12.6: Theoretical predictions and experimental results for (a) K=1 and (b) K=0.33

Figure 12.6 presents the theoretical predictions versus experimental measurements of the electrical resistance. The electrical behavior is found to be similar as there is a steady increase of the electrical resistance. However, the sensitivity, defined as the change of the normalized resistance divided by the crack length, is quite different (Figure 12.6 (a)). It is noticed that the theoretical sensitivity is higher than the experimental one. This can be explained because of the differences between Mode-I and Mode-II crack propagation. In the first case, the crack opening is much more relevant as each substrate moves in an opposite direction (Figure 12.7). However, in the case of Mode-II this effect is less significant as both substrates move in a parallel plane. In addition, there is a relative displacement of the substrate in an opposite way due to the bending effect (34). This implies a lower sensitivity as there is a higher proximity between conductive pathways than in Mode-I crack opening (Figure 12.7). For these reasons, it is necessary to apply a corrective factor, K, taking the lower crack opening effect into account. In this case, the Equation (12.6) will be rewritten as follows:

$$\frac{\Delta R}{R_0} = K \cdot \left(\frac{b \cdot L}{b \cdot (L - a)} - 1 \right) \tag{12.7}$$

The value of K can give a first estimation of this crack opening effect. A value below 1 indicates that the crack is not totally open such as in Mode-I testing. Therefore, after applying the expression of Equation (12.7) with a K coefficient of 0.33, a good agreement with experimental results is observed, as noticed in the dashed line of Figure 12.6 (b). This means that there is no a high opening effect of the crack during the test, and that the adhesive joint does not present significant manufacturing defects such as porosity or thickness variation. Therefore, CNT adhesive distribution can be considered homogeneous along the bonded joint, without sharp increases in the electrical resistance (33). This statement can be confirmed by an analysis of the transversal section and fracture surfaces.

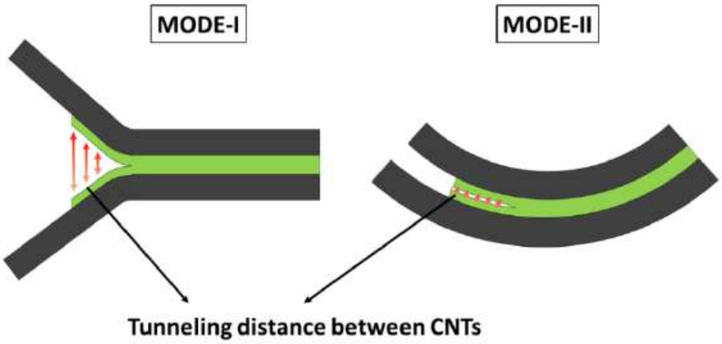

Figure 12.7: Schematics of the crack opening effect on Mode-I (left) and Mode-II (right) showing the differences on CNT tunneling distance (marked as red arrows).

Figure 12.8 shows an image of the fracture surface of the bonded joint. The failure mode is mainly cohesive and the adhesive distribution is similar in both substrates. In addition, a uniform adhesive distribution is observed in the fracture surface along the bonded joint showing no darker bands, in an opposite way than the previously observed results for Mode-I testing (33). This is in good agreement with the electromechanical results, showing a soft crack propagation in contrast to stick-slip behavior where the fracture surfaces usually present a stick-slip pattern (33, 40).

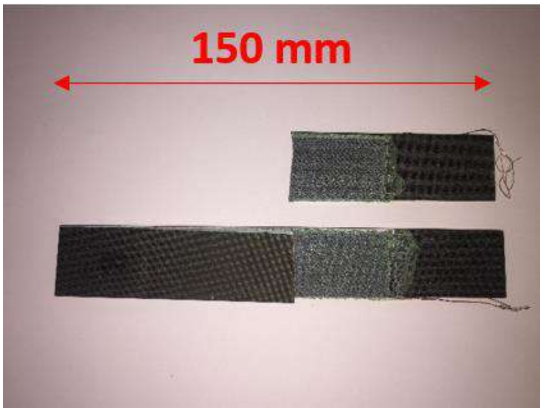

Figure 12.8: Image of the fracture surface of mode-II normalized coupon showing the cohesive failure.

Microstructural characterization reveals a reasonable uniform thickness distribution, ranging from 200-250 µm (Figure 12.9 (a) and (b)). Some voids are observed along the joint. Their presence can be explained by the curing conditions. A uniaxial pressure is applied by using a hot press, inducing an adhesive overflow to the edges and causing a lack of adhesive in several parts of the joint. This can be solved by applying a uniform pressure in every direction, for example by using an autoclave.

In addition to that fact, it is noticed that the interface between the substrate and the adhesive shows a good continuity, leading to a high quality of the interface (Figure 12.9 (c)). A globular distribution of the adhesive is observed in the interface due to the peel-ply surface treatment (Figure 12.9 (d)), which induces a controlled roughness.

Therefore, the proposed method has proved its applicability for crack propagation monitoring under bending conditions in standard coupons. Thus, in order to further investigate the adhesive monitoring capabilities under bending loading, the electromechanical response of skin-stringer sub-elements is going to be analyzed.

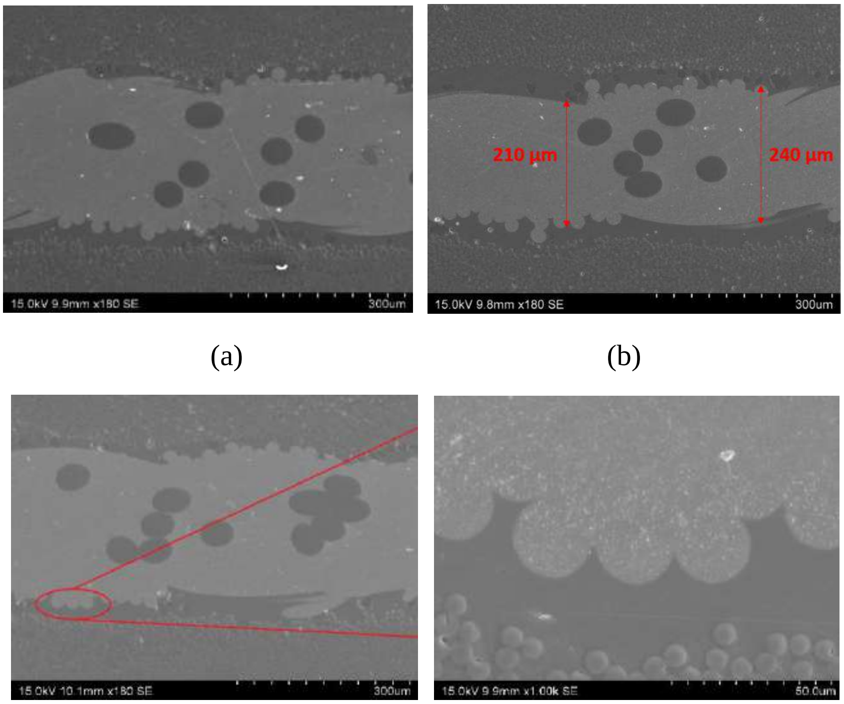

(a) (b)

(c) (d)

Figure 12.9: SEM images of transversal area of the CNT-doped mode-II normalized joints showing the (a), (b) thickness uniformity, (c) the globular distribution of the adhesive (highlighted in red) and (d) the adhesive interface in detail.

12.3.3 Skin-stringer bending analysis

Figure 12.10 shows an example of the electromechanical response of the skin-stringer sub-element when subjected to flexure load. In a similar way to mode-II normalized coupon test, the electrical resistance increases with crack propagation due to the breakage of the electrical pathways. It is observed that when the crack reaches the middle point of the stringer, that is, 17 mm, (Figure 12.10 (b)) the variation of electrical resistance is about 20 %, showing a similar sensitivity than in the coupon tests. This is also explained by the way in which electrical pathways are breaking during the test.

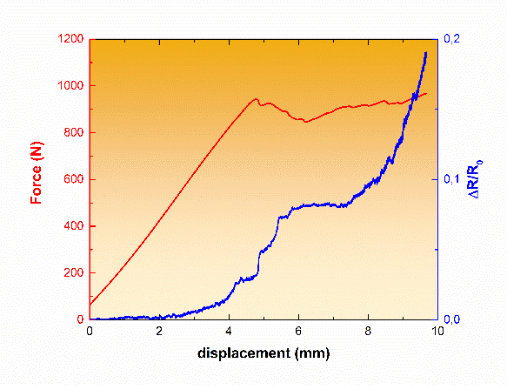

(a)

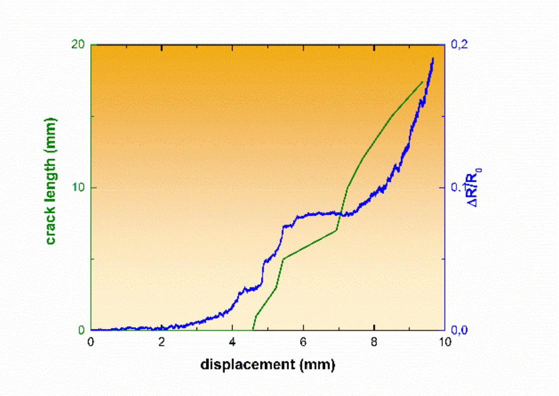

(b)

Figure 12.10: Electrical response of the skin-stringer element as a function of (a) the grip displacement and (b) the crack length.

The electrical resistance of the specimen, supposing that the conductivity of the CFRP substrates is much higher than the adhesive and, thus, this contribution to the electrical resistance can be negligible, can be defined by the following expression:

$$\Delta R = \Delta R_{crack} + \Delta R_{bending} \tag{12.8}$$

Where ΔR is the variation of total resistance of the specimen and ΔR_{crack} and $\Delta R_{bending}$ the resistance change due to the crack propagation and the bending effect, respectively.

The mechanical behavior of the specimen is described in the schematics of Figure 12.11. The region where crack propagates shows a similar behavior than in Mode-I testing with a crack opening. Therefore, the contribution due to ΔR_{crack} is higher than in the case of normalized coupons, that is $\Delta R_{crack_{stiffned}} > \Delta R_{crack_{coupon}}$. On the other hand, there is more prevalent compressive effects in the adhesive layer when looking the region where there is no crack propagation due to the higher thickness of the stiffened element. This compression effects leads to a reduction in the tunneling distance between adjacent nanoparticles leading to a reduction of $R_{bending}$ in comparison to mode-II tests where the adhesive layer is placed near the neutral axis and, thus, the variation of $R_{bending}$ is approximately zero, that is, $R_{bending_{stiffened}} < R_{bending_{coupon}}$. Therefore, the variation of the electrical resistance, $\Delta R_{stiffned}$, during the bending tests, when applying Equation (12.8) is similar to mode-II normalized tests, ΔR_{coupon}.

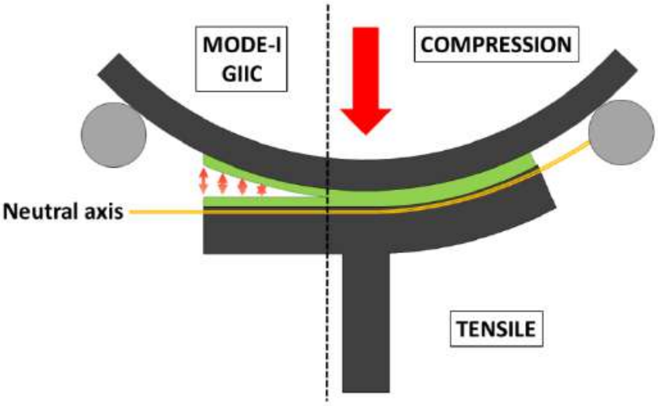

Figure 12.11: Schematics of mechanical force effect on crack opening and mechanical behavior of skin-stringer element.

Moreover, Figure 12.12 shows the variation of the electrical and mechanical response as a function of the crack length and crack propagation velocity. There are slight differences that can be attributed to a more complex strain distribution in the skin-stringer element than in the mode-II normalized coupons, requiring a deeper theoretical analysis. However, it can be noticed that there is a good agreement between the expected electrical response, calculated by using the expression of Equation (12.7) (dash lines), with the same correction factor K=0.33, and the measured one during the test. Some differences are found in the last stages of the bending test, probably due to a more irregular adhesive distribution inside the joint. Therefore, the proposed method shows a good applicability also in more complex elements such as stiffened panels.

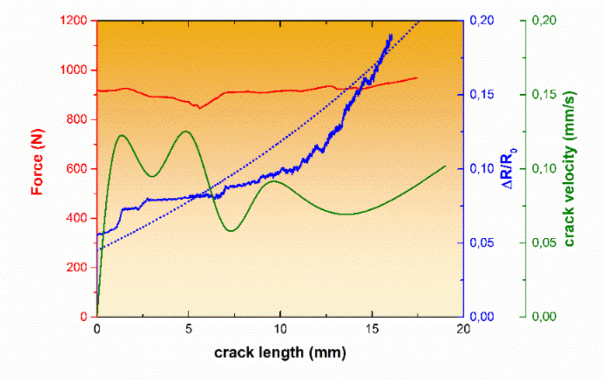

Figure 12.12: Electromechanical response of the skin-stringer element as a function of the crack length.

The analysis of fracture surfaces (Figure 12.13) of the skin-stringer sub-elements reveals a good uniformity of the adhesive distribution and a mainly cohesive failure, in a similar way to the previously described normalized coupons, justifying again the softer evolution of the electrical resistance in comparison to mode-I tests.

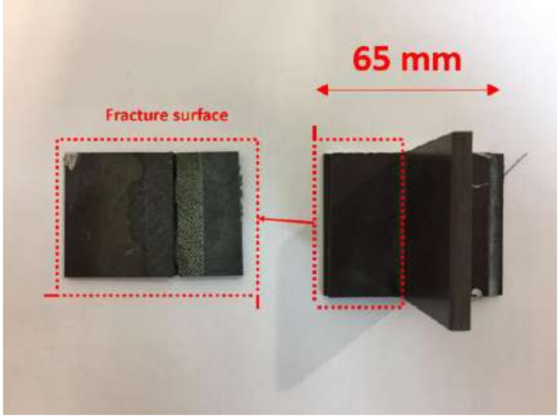

Figure 12.13: Image of the fracture surfaces of skin-stringer sub-element.

Figure 12.14 shows several SEM images of the transversal section of the T and web regions. The peel-ply treatment of the stringer face results in a better interface than in the skin side, treated by brushing, where crack trends to propagate preferentially (Figure 12.14 (a)). The typical globular distribution of the adhesive due to the peel-ply roughness is also observed in a similar way than to mode-II coupons. In this case, the thickness distribution of the adhesive joint is not as uniform as at coupon level due to the stiffener effect. Therefore, a lower thickness is observed in the central area (around 130 µm, as observed in Figure 12.14 (b)) in comparison to the web region around 190 µm, as observed in Figure 12.14 (c)) where the effect of the stiffener weight is not as prevalent. This would explain the sharper evolution of the electrical resistance in the last stages of the test due to a breakage of prevalent pathways in the central region of the stiffener. The crack opening is observed to be more significant in the web region (Figure 12.14 (d)). However, the crack end is narrow (Figure 12.14 (e)) and several crack-bridging is observed (Figure 12.14 (f)), which induces a not completely breakage of electrical pathways, leading to lower values of resistance and sensitivity, as commented before. In addition, some localized voids are observed inside the adhesive joint (Figure 12.14 (d) and (e)). In this case, these voids are identified as some porosity induced by the vacuum conditions during curing, leading to a lack of compaction.

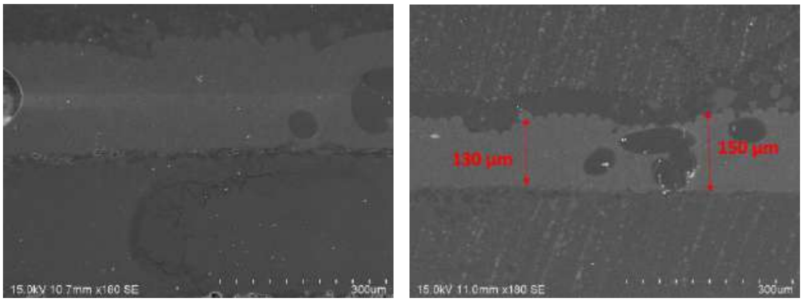

(a) (b)

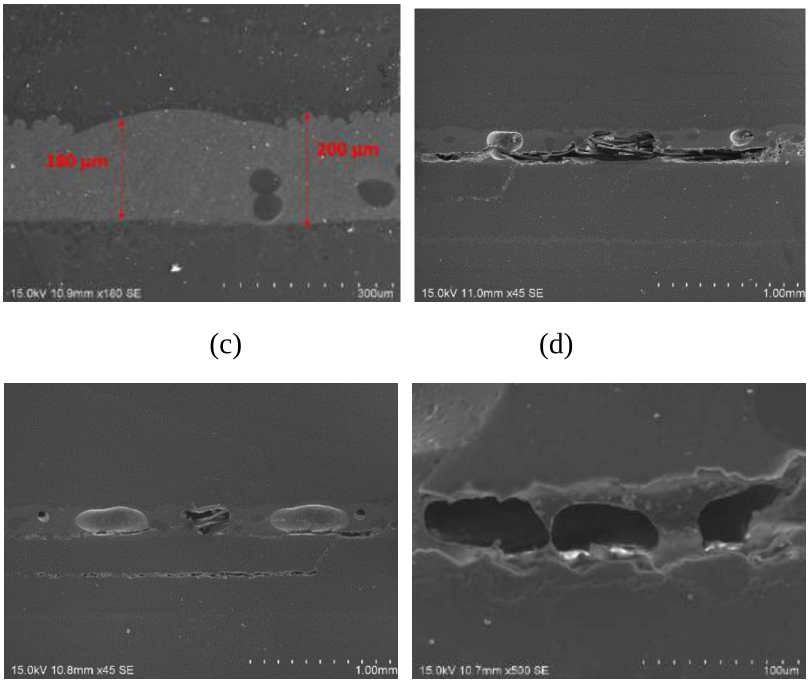

(c) (d)

(e) (f)

Figure 12.14: SEM images of the transversal section of the skin-stringer sub-element showing (a) the adhesive interface, the adhesive thickness in the (b) T and (c) web regions, the crack opening (d), (e) and bridging (f) in the joint.

12.4 Conclusions

Mode-II crack propagation monitoring capabilities of CNT doped adhesive films have been investigated at coupon and at sub-element level.

The electrical resistance increases with crack propagation as there is a breakage of electrical pathways. This variation differs from mode-I testing where the sensitivity is much higher, because of the effect of crack opening. In addition to that, the change of the electrical resistance does not show sharp increases and arrest phases due to a stable crack growth and a good adhesive homogeneity.

In addition, an enhancement of G_{IIC} is observed when comparing to non-doped adhesive joints due to the toughening effect of the carbon nanotubes, leading to a slower crack propagation.

Moreover, bending tests were also conducted in skin-stringer sub-elements. A similar electrical response has been observed. In this case, there is two opposite effects affecting the electrical behavior: the higher resistance changes due to crack opening and the compressive state due to bending loads.

Microstructural analysis reveals a good uniformity in the adhesive thickness distribution in case of standard coupons. Skin-stringer elements show a lower adhesive thickness in central region of the T-stringer, resulting in a more prevalent breakage of electrical pathways in the last stages of the tests. In addition, there are presence of voids due to adhesive overflow in normalized coupons and a general porosity due to a lack of compaction in the skin-stringer elements.

Therefore, the proposed technology has proved its potential and applicability for monitoring CFRP bonded joints subjected to bending conditions at coupon and sub-element level being a promising technique for SHM applications on composite structures.

Acknowledgements

This work was supported by the Ministerio de Economía y Competitividad of Spanish Government [PROJECT MAT2016-78825-C2-1-R] and Comunidad de Madrid regional government [PROJECT 2013/MIT-2862].

Data statement

The raw/processed data required to reproduce these findings cannot be shared at this time due to technical or time limitations. It will be made available on request.

12.5 References

[1] Hussey R, Wilson J. Structural Adhesives: Directory and Databook. 1996.

[2] Palaniappan J, Ogin SL, Thorne AM, Reed GT, Crocombe AD, Capell TF, Tjin SC, Mohanty L. Disbond growth detection in composite-composite single-lap joints using chirped FBG sensors. Composites Sci Technol 2008;68(12):2410-2417.

[3] Bernasconi A, Carboni M, Comolli L. Monitoring of fatigue crack growth in composite adhesively bonded joints using fiber Bragg gratings. Procedia Engineering 2011;10:207-212.

[4] Malinowski P, Wandowski T, Ostachowicz W. The use of electromechanical impedance conductance signatures for detection of weak adhesive bonds of carbon fibre–reinforced polymer. Structural Health Monitoring 2015;14(4):332-344.

[5] Sherafat MH, Guitel R, Quaegebeur N, Hubert P, Lessard L, Masson P. Structural health monitoring of a composite skin-stringer assembly using within-the-bond strategy of guided wave propagation. Mater Des 2016;90:787-794.

[6] Tamborrino R, Palumbo D, Galietti U, Aversa P, Chiozzi S, Luprano VAM. Assessment of the effect of defects on mechanical properties of adhesive bonded joints by using non destructive methods. Composites Part B: Engineering 2016;91:337-345.

[7] Froggatt M, Moore J. High-spatial-resolution distributed strain measurement in optical fiber with Rayleigh scatter. Appl Opt 1998;37(10):1735-1740.

[8] Basri R, Chiu W. Numerical analysis on the interaction of guided Lamb waves with a local elastic stiffness reduction in quasi-isotropic composite plate structures. Composite structures 2004;66(1):87-99.

[9] Palaniappan J, Wang H, Ogin SL, Thorne AM, Reed GT, Crocombe AD, Rech Y, Tjin SC. Changes in the reflected spectra of embedded chirped fibre Bragg gratings used to monitor disbonding in bonded composite joints. Composites Sci Technol 2007;67(13):2847-2853.

[10] Habib F, Martinez M, Artemev A, Brothers M. Structural health monitoring of bonded composite repairs - A critical comparison between ultrasonic Lamb wave approach and surface mounted crack sensor approach. Composites Part B-Engineering 2013;47:26-34.

[11] Iijima S. Helical Microtubules of Graphitic Carbon. Nature 1991;354(6348):56-58.

[12] Ruoff RS, Lorents DC. Mechanical and thermal properties of carbon nanotubes. carbon 1995;33(7):925-930.

[13] Xie S, Li W, Pan Z, Chang B, Sun L. Mechanical and physical properties on carbon nanotube. Journal of Physics and Chemistry of solids 2000;61(7):1153-1158.

[14] Popov VN. Carbon nanotubes: properties and application. Materials Science and Engineering: R: Reports 2004;43(3):61-102.

[15] Gan L, Dong M, Han Y, Xiao Y, Yang L, Huang J. Connection-improved conductive network of carbon nanotubes in the rubber crosslink network. ACS applied materials & interfaces 2018.

[16] Li C, Thostenson ET, Chou T. Sensors and actuators based on carbon nanotubes and their composites: A review. Composites Sci Technol 2008;68(6):1227-1249.

[17] Hu N, Karube Y, Arai M, Watanabe T, Yan C, Li Y, Liu Y, Fukunaga H. Investigation on sensitivity of a polymer/carbon nanotube composite strain sensor. Carbon 2010;48(3):680-687.

[18] Gao L, Chou T, Thostenson ET, Zhang Z, Coulaud M. In situ sensing of impact damage in epoxy/glass fiber composites using percolating carbon nanotube networks. Carbon 2011;49(10):3382-3385.

[19] Cao X, Wei X, Li G, Hu C, Dai K, Guo J, Zheng G, Liu C, Shen C, Guo Z. Strain sensing behaviors of epoxy nanocomposites with carbon nanotubes under cyclic deformation. Polymer 2017;112:1-9.

[20] Datta S, Neerukatti RK, Chattopadhyay A. Buckypaper embedded self-sensing composite for real-time fatigue damage diagnosis and prognosis. Carbon 2018;139:353-360.

[21] Khashaba UA. Static and fatigue analysis of bolted/bonded joints modified with CNTs in CFRP composites under hot, cold and room temperatures. Composite Structures 2018;194:279-291.

[22] Boztepe S, Liu H, Heider D, Thostenson ET. Novel carbon nanotube interlaminar film sensors for carbon fiber composites under uniaxial fatigue loading. Composite Structures 2018;189:340-348.

[23] Alamusi, Hu N, Fukunaga H, Atobe S, Liu Y, Li J. Piezoresistive Strain Sensors Made from Carbon Nanotubes Based Polymer Nanocomposites. Sensors 2011;11(11):10691-10723.

[24] Loyola BR, Zhao Y, Loh KJ, La Saponara V. The electrical response of carbon nanotube-based thin film sensors subjected to mechanical and environmental effects. Smart Mater Struct 2013;22(2):025010.

[25] Sanli A, Benchirouf A, Mueller C, Kanoun O. Piezoresistive performance characterization of strain sensitive multi-walled carbon nanotube-epoxy nanocomposites. Sensors and Actuators A-Physical 2017;254:61-68.

[26] Reddy SK, Kumar S, Varadarajan KM, Marpu PR, Gupta TK, Choosri M. Strain and damage-sensing performance of biocompatible smart CNT/UHMWPE nanocomposites. Materials Science and Engineering: C 2018;92:957-968.

[27] Cao J, Wang Q, Dai H. Electromechanical properties of metallic, quasimetallic, and semiconducting carbon nanotubes under stretching. Phys Rev Lett 2003;90(15):157601.

[28] Cullinan MA, Culpepper ML. Carbon nanotubes as piezoresistive microelectromechanical sensors: Theory and experiment. Physical Review B 2010;82(11):115428.

[29] Loyola BR, La Saponara V, Loh KJ, Briggs TM, O'Bryan G, Skinner JL. Spatial Sensing Using Electrical Impedance Tomography. Ieee Sensors Journal 2013;13(6):2357-2367.

[30] Tallman TN, Gungor S, Wang KW, Bakis CE. Tactile imaging and distributed strain sensing in highly flexible carbon nanofiber/polyurethane nanocomposites. Carbon 2015;95:485-493.

[31] Garcia C, Sanchez M, Urena A, Rams J. Carbon Nanotubes for Assessing the Structural Integrity of Composite Bonded Joints with Film Adhesives. Structural Health Monitoring 2015: System Reliability for Verification and Implementation, Vols.1 and 2 2015:2169-2176.

[32] Sánchez-Romate XF, Jiménez-Suárez A, Molinero J, Sánchez M, Güemes A, Ureña A. Development of bonded joints using novel CNT doped adhesive films: Mechanical and electrical properties. International Journal of Adhesion and Adhesives 2018;86:98-104.

[33] Fernández Sánchez-Romate XX, Molinero J, Jiménez-Suárez A, Sánchez M, Güemes A, Ureña A. Carbon Nanotube Doped Adhesive Films for Detecting Crack Propagation on Bonded Joints: A Deeper Understanding of Anomalous Behaviors. ACS applied materials & interfaces 2017.

[34] Fernandes RMRP, Chousal JAG, de Moura MFSF, Xavier J. Determination of cohesive laws of composite bonded joints under mode II loading. Composites Part B-Engineering 2013;52:269-274.

[35] Fernandes RL, de Moura MFSF, Moreira RDF. Effect of moisture on pure mode I and II fracture behaviour of composite bonded joints. International Journal of Adhesion and Adhesives 2016;68:30-38.

[36] Burkholder GL, Kwon YW, Pollak RD. Effect of carbon nanotube reinforcement on fracture strength of composite adhesive joints. J Mater Sci 2011;46(10):3370-3377.

[37] Hsieh TH, Kinloch AJ, Taylor AC, Kinloch IA. The effect of carbon nanotubes on the fracture toughness and fatigue performance of a thermosetting epoxy polymer. J Mater Sci 2011;46(23):7525-7535.

[38] Gude MR, Prolongo SG, Urena A. Toughening effect of carbon nanotubes and carbon nanofibres in epoxy adhesives for joining carbon fibre laminates. Int J Adhes Adhes 2015;62:139-145.

[39] Li X, Zhang W, Zhai S, Tang S, Zhou X, Yu D, Wang X. Investigation into the toughening mechanism of epoxy reinforced with multi-wall carbon nanotubes. E-Polymers 2015;15(5):335-343.

[40] Ashcroft IA, Hughes DJ, Shaw SJ. Mode I fracture of epoxy bonded composite joints: 1. Quasi-static loading. Int J Adhes Adhes 2001;21(2):87-99.

CHAPTER 13: RESULTS AND DISCUSSION

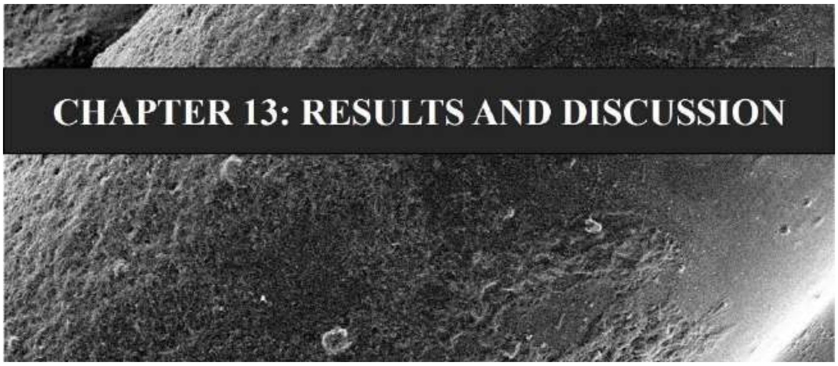

Chapter 13: Results and Discussion

In this chapter, a brief discussion about the published and submitted journal papers is shown addressing the main objectives of the proposed Thesis. Firstly, electromechanical properties of CNT reinforced nanocomposites are discussed and a brief explanation of the proposed theoretical model to get a deeper knowledge of this type of materials is stated. Then, SHM applicability of CNT doped adhesive films for strain sensing and crack propagation monitoring on standard coupon and skin-stringer sub-elements are demonstrated.

13.1 Electrical modelling of CNT based nanocomposites

Electrical properties of CNT doped nanocomposites have been deeply analyzed and a novel theoretical model has been proposed in order to properly correlate mechanical to electrical behavior.

To achieve this purpose, a first approach to percolation threshold has been given in order to analyze the influence of CNT geometry and distribution inside the material depending on the different dispersion techniques and CNT contents. Then, a global model correlating the electrical conductivity to strain sensing capabilities has been developed by taking the agglomeration degree of nanoparticles into account. In this context, several parameters have been defined and adjusted to experimental measurements. By this way, a deeper understanding of electrical behavior of nanocomposites has been obtained.

13.1.1 Novel approach to percolation threshold on CNT nanocomposites

Percolation threshold (PT) is defined as the critical volume fraction where an insulating material becomes electrically conductive. As previously stated, it depends mainly on the CNT geometry and other aspects such as the degree of dispersion and nanoparticle entanglement. There are several studies correlating the PT of CNT nanocomposites with these aspects [76,137,138] but they do not usually offer a deep analysis of how dispersion procedure affects the CNT distribution inside the material and how it is influencing the electrical properties of nanocomposites.

In fact, the proposed novel approach to percolation threshold lays under the basis of the one proposed by J. Li et al. [75] where the dispersion procedure and its influence over the CNT dispersion inside the material is correlated with the PT of nanocomposites. They concluded that PT (θ_{PT}) is mainly dominated both by the aspect ratio, that is, the length divided by the diameter and the ratio of dispersed to aggregated CNTs as shown in the following formula:

$$\theta_{PT} = \frac{\xi \varepsilon \pi}{6} + \frac{(1-\xi)27\pi d^2}{4l^2} \qquad (13.1)$$

Where ξ is the volume fraction of agglomerated CNTs, ε is the localized volume content, which is the fraction of material occupied by CNTs in an agglomerate, *d* and *l* the diameter and length of CNTs, respectively.

Therefore, by applying Equation (13.1) it is possible to estimate the electrical conductivity, σ, by using a widely known scaling power law:

$$\sigma = (\theta - \theta_{PT})^t \sigma_0 \qquad (13.2)$$

Where θ is the volume content of CNTs, σ_0 a parameter depending on the aspect ratio of CNTs and *t* an empirical parameter that usually ranges from 1.3 to 2 for a 2D/3D nanoparticle distribution.

The main limitation of the approach of J. Li et al. is that they do not take waviness and entanglement factors into account.

In this approach, a novel concept of percolation threshold has been defined, called equivalent percolation threshold. For this purpose, PT is considered as a function of waviness and agglomeration parameters but also depends on the CNT content. That is, there is a dynamic approach to PT. For example, the degree of entanglement of CNT dispersion varies with nanoparticle content and, thus, it would lead to a different PT.

The novel definition of PT is based on the idea that CNTs are considered in a 3D random distribution when agglomerated and in a 2D distribution when well dispersed, as they are oriented in the flow direction, that is, the x-y plane. This is explained under the basis that higher agglomeration degree leads to a more randomly distribution of CNTs [139]. Therefore, Equation (10.1) is rewritten by taking the orientation parameters into account:

$$\theta_{PT} = \frac{\xi \varepsilon \pi}{6} + \frac{(1-\xi)\pi}{4\left(\frac{1}{\sqrt{2}} - \frac{\sqrt{3}-\sqrt{2}}{\sqrt{6}}\xi\right)^3 \Lambda^2} \qquad (13.3)$$

Where Λ denotes the aspect ratio (l/d) of the CNTs.

By applying this formula and estimating the number of CNTs in an agglomerate, it is possible to calculate the PT as a function of CNT content.

Therefore, the paper introduces two different concepts for the PT: the statistical, where CNTs are considered straight, and the equivalent one, where other factors such as waviness can be taken into account and are affected by CNT content and dispersion procedure due to the different interactions between adjacent nanoparticles.

The equivalent PT will be different depending on the CNT content, as the CNT interactions will lead to a variation of the CNT waviness and agglomeration parameters. For this reason, it is necessary to go deeper into waviness effects, by defining a waviness factor as the ratio between the actual length of the CNTs and the effective one, as defined in the schematics of Figure 13.1:

$$\lambda = L_{eff}/L \qquad (13.4)$$

By this way, the paper proposes to define an equivalent carbon nanotube with the same volume than the actual one and the effective length due to CNT waviness, as shown in the schematics of Figure 13.1.

$$L_{eff} = 4\sqrt{\left(\frac{L}{4}\right)^2 - a^2} \qquad (13.5)$$

Where L and L_{eff} are the actual and the effective CNT length and a the amplitude of the waviness.

The new effective aspect ratio Λ_{eff} is defined as the effective length, defined in Figure 13.1 divided by the effective CNT diameter, stated in the following formula:

$$d_{eff} = \sqrt{\frac{L}{L_{eff}}}d \qquad (13.6)$$

Thus, Equation (13.3) will be rewritten by taking the effective aspect ratio into account:

$$\theta_{PT} = \frac{\xi^2\pi}{6} + \frac{(1-\xi)\pi}{4\left(\frac{1}{\sqrt{2}} - \frac{\sqrt{3}-\sqrt{2}}{\sqrt{6}}\xi\right)^3 {\Lambda_{eff}}^2} \qquad (13.7)$$

Where $\xi = \varepsilon$ to simplify the calculations.

Therefore, the expression of Equation (13.7) will lead to a different PT depending on dispersion procedure and nanoparticle content as it both will affect the CNT geometry and distribution inside the nanocomposite.

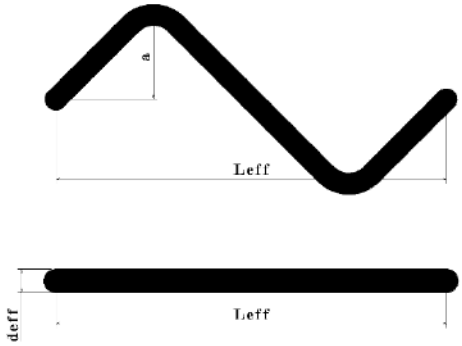

Figure 13.1: Schematics of actual (upper) and equivalent (lower) carbon nanotube for the model.

To validate this model, several experimental measurements using different dispersion techniques, toroidal stirring and three roll milling, as well as different CNT contents were carried out. Here, it is very important to know how dispersion procedure exactly affects the CNT geometry. The breakage effect induced by the shear forces involved in the different dispersion procedures can be estimated depending on the CNT aspect ratio and viscosity of the resin [140].

A parametric study was carried out showing the effect of CNT waviness, aspect ratio and content on PT and electrical conductivity (Figure 13.2**¡Error! No se encuentra el origen de la referencia.** (a)). It was concluded that equivalent percolation threshold increases with CNT waviness due to a reduction in the effective aspect ratio. Moreover, CNT waviness has also a negative effect on the electrical conductivity (Figure 13.2 (b)) with a more prevalent effect at lower CNT contents. This is explained because the reduction in the effective aspect ratio could lead to an equivalent PT above the actual content, being not the material electrically conductive.

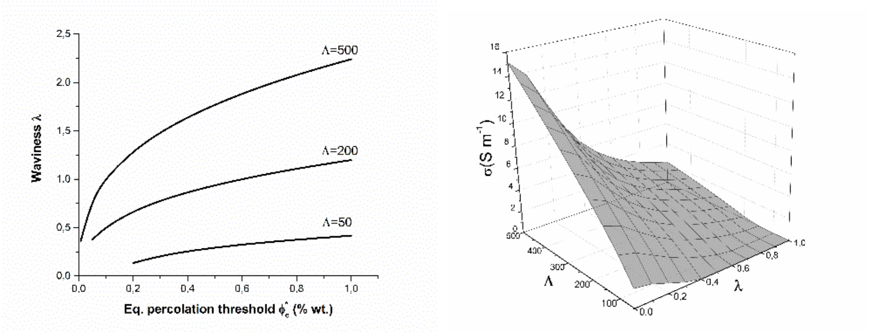

(a) (b)

Figure 13.2 (a) Estimated PT as a function of waviness depending on CNT aspect ratio and (b) effect of geometry parameters on electrical conductivity of nanocomposites.

The experimental measurements of the electrical conductivity showed a good agreement with theoretical estimations. The main conclusion is that CNT waviness increases with CNT content, as shown in Figure 13.3 (a). This is explained because at higher contents, CNTs tend to be agglomerated, inducing higher interactions between them [141]. The calculated CNT waviness was compared to experimental one by image analysis of TEM/SEM images of CNT dispersion, showing a good agreement (Figure 13.3 (b)). In addition to that, three roll milling has proved to be a better dispersion technique to reduce CNT entanglement although it leads to a higher breakage effect that explains the lower values of electrical conductivity. The amino-functionalization of CNTs also leads to a higher entanglement by causing local distortions along the radial direction of the nanotubes [142,143].

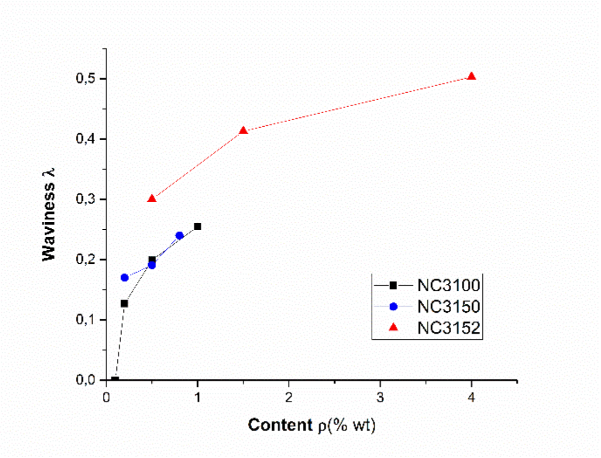

(a)

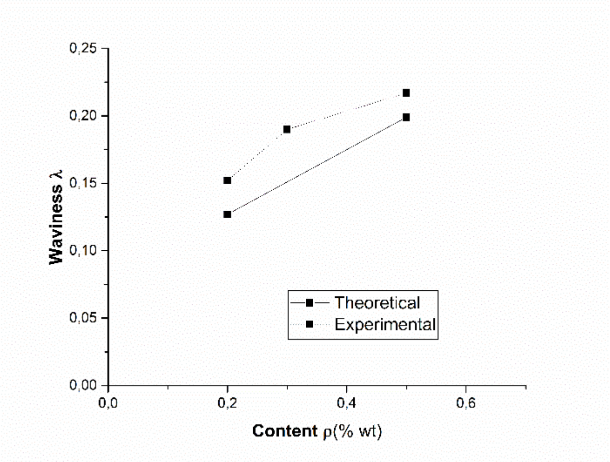

(b)

Figure 13.3 (a) Estimation of waviness ratio as a function of content and CNT type and (b) comparison with experimental measurements by TEM image analysis.

Therefore, the equivalent PT also increases with CNT content following a proportional law, as shown in Figure 13.4. The effective aspect ratio, calculated based on the waviness ratio of the CNTs, in combination with the estimated equivalent percolation threshold, would allow to calculating the electrical conductivity of CNT based nanocomposites.

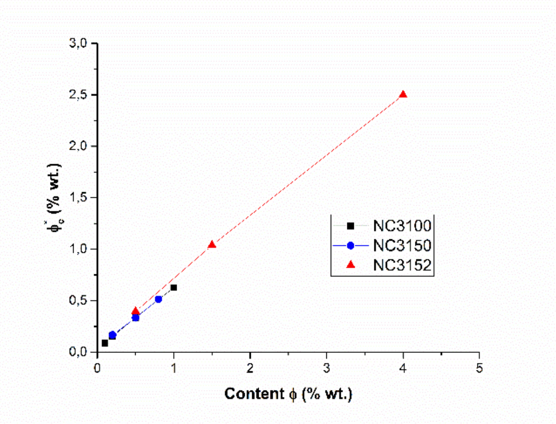

Figure 13.4: Equivalent PT as a function of CNT content.

This model can be used in two opposite directions: to calculating electrical conductivity knowing the CNT geometry and distribution from TEM/SEM analysis or to estimating CNT waviness and distribution from electrical conductivity measurements knowing the dispersion procedure parameters.

In this context, an additional work to that published has been carried out to prove the potential of the proposed theoretical model. Here, the aim is to have a deeper knowledge of how the involved shear forces in dispersion procedures can affect electrical properties of CNTs. To achieve this purpose, three roll milling was selected as dispersion technique and several electrical conductivity measurements were conducted for different CNT contents by adjusting the gap distance between rolls, maintaining the speed rotation at 250 rpm.

Figure 13.5 shows the electrical conductivity measurements for the different tested conditions. At lower contents, it is observed that the electrical conductivity increases by reducing the gap between rolls while at higher contents, there is an optimum value of gap distance where the electrical conductivity is the highest. This apparently anomalous behavior is explained by the influence of two effects acting in opposite senses: on the one side, the CNT breakage due to the higher shear forces involved because of the gap reduction and, on the other side, a better CNT dispersion due to a higher effectiveness of three roll milling procedure. The CNT breakage is more prevalent at higher contents where the interactions between nanoparticles are higher while the improvement of the CNT dispersion is more pronounced at lower contents, explaining the differences observed in the electrical conductivity.

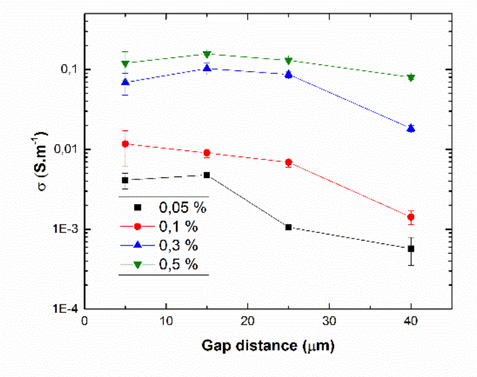

Figure 13.5: Electrical conductivity measurements as a function of gap distance between rolls.

The theoretical model can be used to get a deeper knowledge of CNT distribution in the nanocomposite. By applying the formula of Equation (13.7), it is possible to calculate the CNT waviness as a function of the gap distance, summarized in the graph of Figure 13.6.

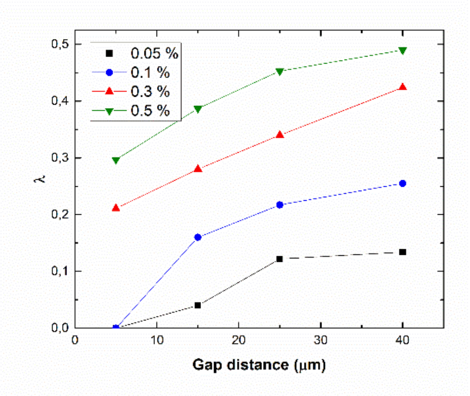

Figure 13.6: Estimated waviness ratio as a function of gap distance in three roll milling process.

It is shown that CNT waviness decreases with a reduction in the gap distance. This is explained by the stretching effect of three roll milling process [144]. In addition to that, waviness ratio increases with CNT content due to the previously commented higher CNT agglomeration and entanglement. As observed in the previous study, the sensitivity of the proposed theoretical model is very high near the percolation threshold as small variations on the geometry can drastically affect the electrical conductivity, so it is possible to obtain results that are not very realistic. For these reasons, the estimation of waviness ratio at 0.05 and 0.1 wt. % 5 µm as well as at 0.05 wt. % 15 µm gap distance can be probably inaccurate. Nevertheless, the previous statements about the influence of dispersion procedure on CNT waviness are still valid.

On the other hand, Figure 13.7 shows the value of the mean aggregate size. A reduction in the mean aggregate size is observed with lower gap distances. This is explained because of a better CNT dispersion, trending to homogenize the CNT distribution thorough the whole nanocomposite. Obviously, the higher the CNT content, the higher the mean aggregate size, due to a higher tendency of CNT to be as agglomerates. This is in good agreement with our previous statements.

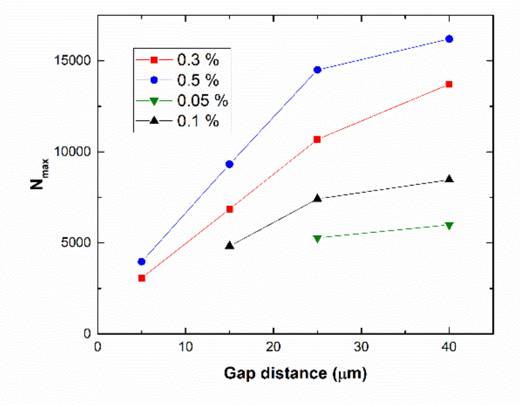

Figure 13.7: Mean aggregate size as a function of three roll milling process parameters.

Moreover, the theoretical model has been used to estimate the waviness ratio of CNTs accordingly to different research studies, summarized in Figure 13.8. It is observed that waviness ratio increases with CNT content in every case, as expected, following a similar trend. Table 10.2 shows the aspect ratio of the straight CNTs in each study. When comparing the geometrical information about CNTs with the calculated waviness ratio among the different studies, a higher entanglement is observed with CNT aspect ratio as well as for amino-functionalized nanoparticles. This is in good agreement with the results of our previous study, where the larger CNTs showed a higher entanglement.

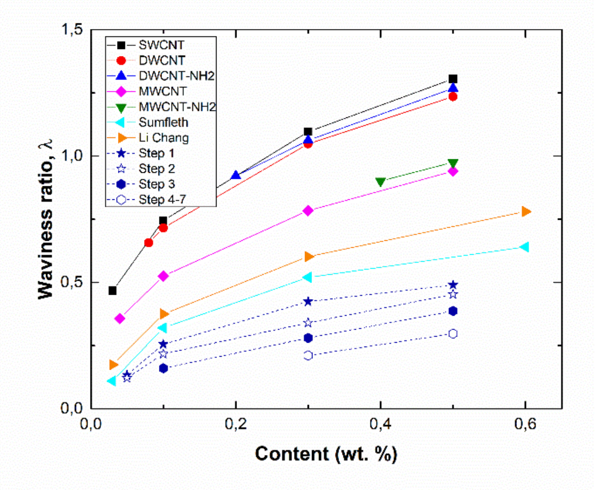

Figure 13.8: Estimated waviness ratio as a function of CNT content for the present study and other research.

Therefore, the model shows a good potential and applicability for correlating CNT structure and distribution to electrical properties of nanocomposites. It can be used as a first approach to better understanding the effect of dispersion procedure on the final properties of the material, but do not offer a complete global overview of it and cannot be used for strain sensing purposes as it does not take tunneling mechanisms into account. For these reasons, an evolution of the theoretical model has been also proposed taking the interactions between CNTs and how they affect electrical properties of the whole nanocomposites into account.

13.1.2 Critical parameters affecting electrical conductivity and strain sensing capabilities on CNT nanocomposites

The influence of dispersion procedure on CNT electromechanical properties has been widely investigated. In a similar way than for studying the variation of PT depending on CNT distribution, a novel theoretical model lying in the basis of the previously developed is proposed. The main difference is that it takes the tunneling mechanisms and possible interactions between nanoparticles into account. Therefore, it can be used to determine the sensing behavior in strain monitoring applications.

CNT electrical network is affected by the effect of three different electrical mechanisms, as shown in the schematics of Figure 13.9: the intrinsic electrical conductivity, the electrical resistance between two CNTs in direct contact, and the tunneling transport between two adjacent CNTs. The first one depends on the intrinsic electrical conductivity, which is known and the CNT geometry. Contact resistance is calculated by applying the formula of S. Gong et al. [99] by taking the transmission probability function, *T*, and number of conducting channels, *M*, into account. Moreover, the tunneling resistance is estimated by applying the previously commented formula by J.G. Simmons et al. [77] and more deeply analyzed by N. Hu et al. [102]. Therefore, the total resistance will be estimated as follows:

$$R_T = R_{CNT} + R_{contact} + R_{tunnel}$$

$$R_{CNT} = \frac{1}{\sigma_{CNT}} \cdot \frac{l}{A}$$

$$R_{contact} = \frac{h}{e^2} \cdot \frac{1}{MT} \qquad (13.8)$$

$$R_{tunnel} = \frac{h^2 t}{Ae^2\sqrt{2m\varphi}} exp\left(\frac{4\pi t}{h}\sqrt{2m\Phi}\right)$$

Where *A* and *t* are the tunneling contact area and distance, respectively; *h* the Planck's constant; *m* and *e* the electron mass and charge, respectively and Φ the height barrier of the epoxy matrix.

To date, most of studies suppose that CNT are randomly distributed inside the nanocomposite, but they do not often take the CNT dispersion degree into account. However, it plays an important role, as previously demonstrated, in electrical properties of the material by affecting the CNT geometry and, thus, percolation threshold of nanocomposite. Therefore, it must be taken into account to estimate their strain sensing capabilities.

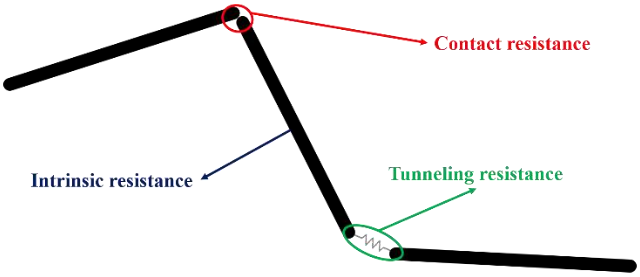

Figure 13.9: Schematics of tunneling and contact mechanisms on electrical conductivity of CNTs.

Three parameters determining the dispersion state are defined: one defined as the fraction of agglomerated CNTs, ξ_a, the second one defined as the fraction of well dispersed CNTs, ξ_d, and the last one defined as the volume fraction of the material where there are not conductive paths because of a high separation between adjacent nanoparticles, called non-percolating region, ξ_n.

The proposed model supposes an electrical network as shown in Figure 13.10 where three different electrical pathways are defined accordingly to agglomerated, well-dispersed and non-percolated regions. The electrical resistance of the agglomerated is given by $R_{CNT} + R_{contact}$ of Equation (13.8), being mainly dominated by the intrinsic and contact resistance of CNTs. The resistance of the well-dispersed area is given, however, by R_{tunnel} while the resistance of the non-percolated area will be considered infinite. Therefore, by using the electrical network defined in the schematics of Figure 13.10 the total resistance of the nanocomposite can be calculated accordingly to the following formula:

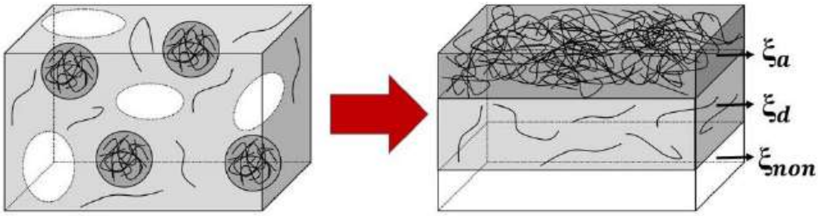

Figure 13.10: Schematics of actual dispersion state (left) and equivalent block distribution in the model (right).

$$\frac{1}{R} = \xi_a \cdot \frac{1}{R_a} + \xi_d \cdot \frac{1}{R_d} + \underbrace{\xi_{non} \cdot \frac{1}{R_\infty}}_{\sim 0} \quad \rightarrow \quad R = \frac{R_a R_d}{(\xi_d R_a + \xi_a R_d)} \qquad (13.9)$$

The calculation of R will allow to estimate the total electrical conductivity of the nanocomposite by using the following expression:

$$\sigma = \frac{L}{R \cdot A} = \frac{L_{eq}}{R \cdot {L_{eq}}^2} = \frac{1}{R \cdot L_{eq}} = \frac{1}{L_{eq}} \cdot \frac{(\xi_d R_a + \xi_a R_d)}{R_a R_d} \qquad (13.10)$$

The main difference between the present model and the equivalent percolation one is that the first one takes tunneling mechanisms into account so it is possible to estimate the variation of resistance due to strain. Electrical response at a given strain is given by the following expression:

$$\frac{\Delta R}{R_0} = \frac{\frac{R_a R_d}{(\xi_d R_a + \xi_a R_d)}}{\frac{R_{a0} R_{d0}}{(\xi_d R_{a0} + \xi_a R_{d0})}} - 1$$

$$(13.11)$$

$$= \frac{R_a R_d}{R_{a0} R_{d0}} \cdot \left(\frac{\xi_d R_{a0} + \xi_a R_{d0}}{\xi_d R_a + \xi_a R_d} \right) - 1$$

Where the subscript 0 indicates the initial values, that is, when no strain is applied in the material.

Here, one of the most critical aspects is the inter-particle distance (IPD) estimation. IPD basically depends on the volume content of nanoparticles.

Based on T. Takeda et al. [145] supposition, IPD is correlated to the number of particles per unit volume by following a power law:

$$t_d = t_0 \left(\frac{\theta_0}{\theta}\right)^{\alpha} \qquad (13.12)$$

Where θ and $\theta_0$are the current volume fraction at the CNT content at percolation threshold, respectively and t_0 is the tunnelling distance at percolation threshold.

It is known that, at maximum package content, the IPD is equal to the minimum distance between nanoparticles, called Van der Waals distance, fixed at 0.34 nm. On the other hand, IPD at percolation threshold is given by the maximum distance at which there is an electrical tunneling transport between two adjacent nanoparticles, determined at 1.4 nm by C. Li et al. [79]. The critical volume fraction at percolation threshold can be estimated from Equation (13.3).

Therefore, by knowing the IPD at two different CNT contents, the expression of Equation (10.11) is totally defined:

$$t_0 \left(\frac{\theta_0}{\theta_m}\right)^{\alpha} = d_w \quad \rightarrow \quad \alpha = \frac{ln\left(\frac{d_{wd}}{t_0}\right)}{ln\left(\frac{\theta_0}{\theta_m}\right)} \qquad (13.13)$$

$$\theta_m = \frac{\pi}{6} \quad (max.package\ factor\ of\ a\ sphere)$$

Being d_{wd} the Van der Waals distance and θ_m the volume fraction at maximum package content.

Once determined IPD, tunneling resistance can be calculated and, thus, the electrical conductivity and sensitivity of CNT nanocomposites. Hence, a parametric study of the proposed model has been carried out to analyze the influence of the agglomeration parameters.

Firstly, the correlation between IPD and aggregate parameters with gauge factor has been analyzed. One of the most interesting conclusions is that the maximum sensitivity is not achieved at the highest value of IPD, as observed in Figure 13.11 (a), however it depends on aggregate parameters. In fact, there is an optimum IPD value where the GF is the maximum depending on the aggregate ratio, defined as the volume fraction of agglomerate region divided by the well-dispersed area. This is physically explained because a higher aggregate ratio imply a more prevalence of agglomerates inside the material and, thus, the main conducting mechanisms take place in the agglomerated area. Therefore, if IPD value is very high the contribution of the well-dispersed area to the electrical conductivity of the nanocomposite, when applying Equation (13.9) would be negligible, as the value of tunneling resistance will be too high.

Secondly, the influence of aggregate parameters to electrical conductivity has been also analyzed at different CNT contents. It has been shown that at lower contents, the electrical conductivity depends mainly on the volume fraction of the agglomerated area (Figure 13.11 (b)). This is explained because IPD of well-dispersed area is higher and, thus, the aggregates constitute the main electrical pathways inside the material. However, at higher contents, there is an increasing dominance of well-dispersed region, as stated in Figure 13.11 (c), due to a reduction of the IPD.

To analyze the influence of dispersion procedures, CNT nanocomposites were manufactured at several conditions by three roll milling, toroidal stirring and a combination of both techniques. The experimental results, summarized in Figure 13.12 (a), showed that electrical conductivity is slightly higher when using toroidal stirring. This was previously explained by the homogenization effect induced by the 3D flow of toroidal stirring which has a positive effect in opposition to the breakage effect of three roll milling due to higher shear forces involved. However, the effect of dispersion procedure on electrical sensitivity, shown in Figure 13.12 (b), is quite more difficult due to the complex interactions between nanoparticles inside the material. It was determined at low strain levels to avoid breakage mechanisms [146]. Therefore, the proposed model has been used to better understand the sensing mechanisms inside the material.

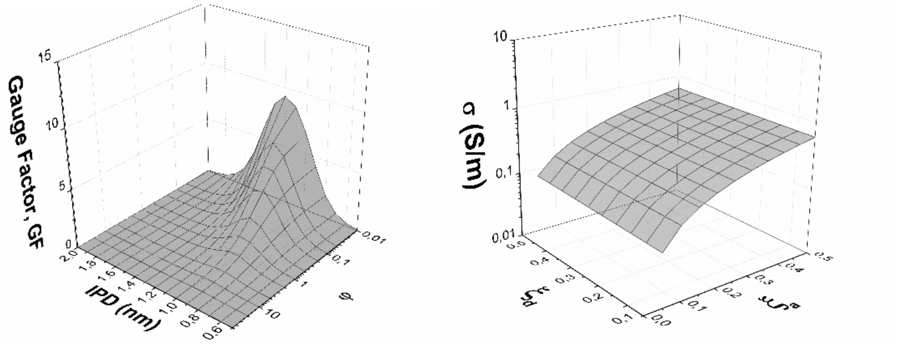

(a) (b)

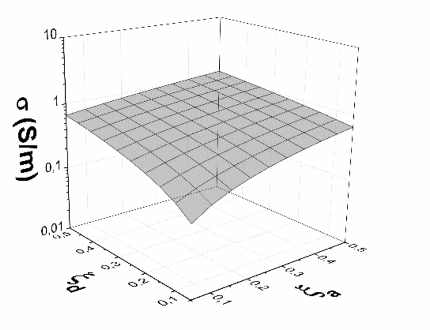

(c)

Figure 13.11: Theoretical estimations of (a) GF as a function of IPD and aggregate ratio and electrical conductivity as a function of aggregate parameters at (b) 0.1 and (c) 0.5 wt. % CNT content.

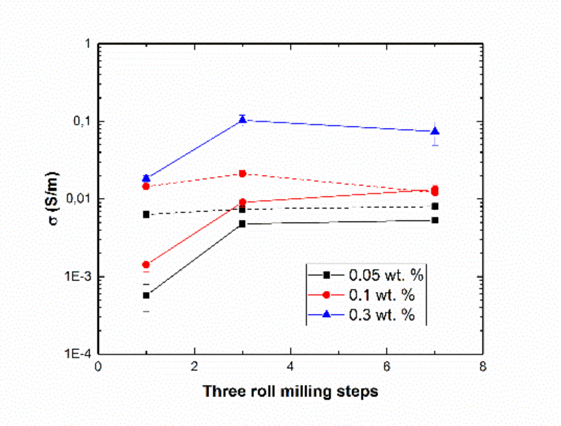

(a)

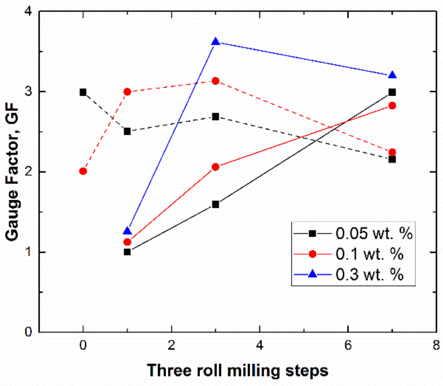

(b)

Figure 13.12: (a) Electrical conductivity and (b) GF measurements of different samples manufactured by three roll milling (solid lines) and three roll milling + toroidal stirring (dash lines).

By applying the formulas of Equations (13.10) and (13.11) knowing the electrical conductivity and GF as well as dispersion procedure, it is possible to obtain the aggregate parameters for each sample. It is observed that the aggregate ratio is significantly reduced when introducing the toroidal stirring method at lower three roll milling steps. This is explained again by the homogenization effect of 3D flow which is more prevalent in sensing capabilities than the disaggregation effect of three roll milling shear forces at high gap distances. However, at higher three roll milling steps, there are not significant differences in both electrical and sensing capabilities when adding an additional toroidal stirring step and, thus, the aggregation parameters are very similar. In this case, the effect of three roll milling process is enough to ensure a good CNT dispersion inside the material so, an additional toroidal stirring step do not significantly enhance the dispersion. This statement is confirmed by a TOM analysis of CNT/epoxy mixture where an enhancement of the dispersion is observed at lower three roll milling steps and no drastic differences are observed at higher three roll milling steps. FEG-SEM images of fractured surface also confirm this evidence with the presence of higher aggregates at lower three roll milling steps and a uniform CNT distribution when including the toroidal stirring step.

A map of dispersion procedures and their influence on the electromechanical properties of nanocomposites has been also shown as a function of aggregate parameters (Figure 13.13), allowing to understanding the effect of CNT content and dispersion procedure on the quality of dispersion inside the material. Higher contents lead to a poorer CNT dispersion inside the material and a higher effect of the dispersion procedure on the CNT distribution due to a more prevalent disaggregation of main agglomerates.

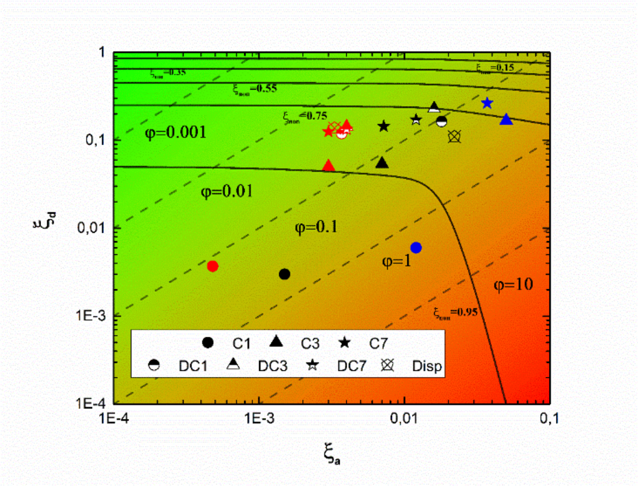

Figure 13.13: Map of dispersion procedures as a function of aggregate parameters where the red and green areas indicate a poor/good dispersion, respectively.

FEG-SEM images of fracture surfaces of nanocomposites under cryogenic conditions also confirm the previous statements, as shown in Figure 13.14. Samples without toroidal stirring process and lower three roll milling cycles showed a highly irregular CNT distribution with the presence of larger aggregates (Figure 13.14 (a) and (b)). When including an additional toroidal stirring step, CNT dispersion is highly improved as well as there is a prevalent breakage of larger agglomerates. CNT dispersion was found to be very similar for high-steps three roll milling samples (Figure 13.14 (c) and (d)).

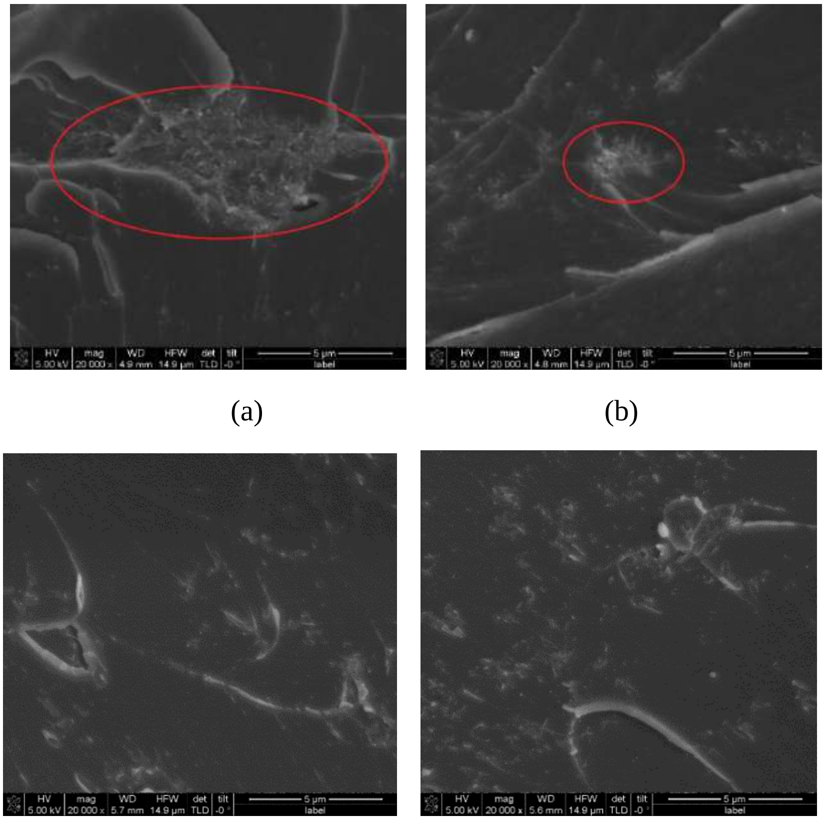

(a) (b)

(c) (d)

Figure 13.14: FEG-SEM images of fracture surfaces for (a) C1, (b) C3, (c) C7 and (d) DC7 conditions.

Thus, the model shed light into how dispersion procedure really affects electrical properties of CNT nanocomposites and highlights the difficulty of establishing adequate statements only under the basis of experimental measurements.

The proposed models apply to CNT/epoxy bulk nanocomposites at tensile loading where a 3D CNT distribution is considered. However, it is important to also analyze the influence that geometry of specimen can have in the strain sensing capabilities. For these reasons, another study highlighting the differences on electromechanical behavior between bulk nanocomposites and multifunctional coatings for damage sensing. That is, the difference between a 3D and 2D CNT distribution on sensing properties.

13.1.3 Strain sensing behavior of CNT/epoxy materials: from bulk nanocomposites to sensitive coatings

Bulk nanocomposites and strain sensitive coatings were manufactured. The idea was to compare their electrical response to mechanical strain to better understand the role of CNT distribution inside the material on sensing purposes. MWCNTs were dispersed by toroidal stirring which has been proved as a simple technique that offers high electrical sensitivities as commented before. Both bulk materials and coatings were tested under tensile and bending conditions to have a better overview of electromechanical properties.

Electrical curve at tensile load shows important differences between bulk nanocomposite and sensitive coatings (Figure 13.15). The most important is that GF is much higher in the case of coatings. The reason lies in the fact that breakage of electrical pathways is more prevalent in thin films than in bulk nanocomposites [80,147]. It means that there is a more accused exponential effect of electrical resistance increase with applied strain, leading to higher values of sensitivity. This can be explained because of the increase of tunneling distance due to a higher percolation threshold in a 2D system [148].

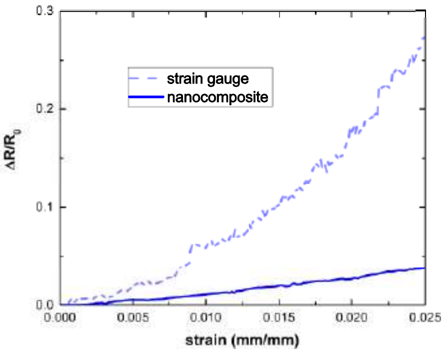

Figure 13.15: Variation of normalized resistance at tensile tests for strain gauges and bulk nanocomposites.

In addition to that fact, bending tests were also conducted to evaluate the global electromechanical response of the material. It has been observed that the sensitivity is much lower when comparing to tensile tests, as expected (Figure 13.16 (a)). This is explained by the effect of compressive-tensile equivalent area during test, as shown in the schematics of Figure 13.16 (b). It means that tensile area is also affected by compressive effects leading to a decrease of the electrical resistance variation during test. These results are in good agreement with other studies for CNP nanocomposites subjected to bending loads [91].

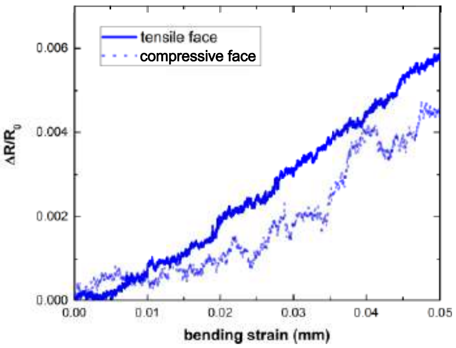

(a)

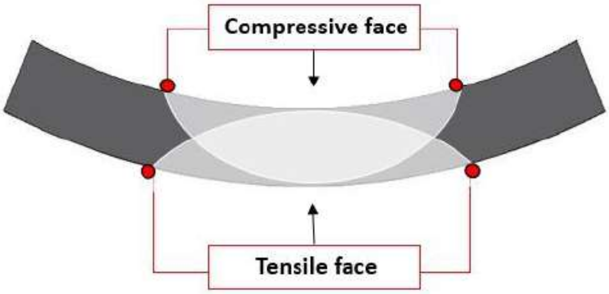

(b)

Figure 13.16: (a) Electromechanical measurements of bulk nanocomposites at bending load and (b) schematics of influence area during the test.

When comparing sensitive coatings to bulk nanocomposites, an increase of GF is observed again. In this case, tensile subjected face is not affected by compressive effects as the substrate used for this test is not electrically conductive and thus, the variation of electrical resistance due to tunneling effects is higher. On the other hand, there is a more significant decrease of the electrical resistance in the compressive-subjected face, as shown in Figure 13.17.

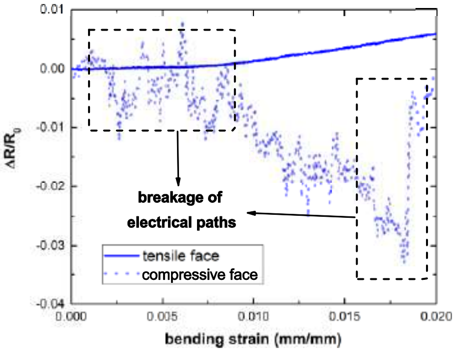

Figure 13.17: Variation of the normalized resistance in strain gauges at tensile (solid lines) and compressive (dashed ones) subjected faces.

Multifunctional coatings were also tested to evaluate their sensitivity to damage detection. To achieve this purpose, an electrical network comprising the whole coating was set, as shown in the electrode disposition schematics of Figure 13.18. After that, several defects were induced and their corresponding electrical resistance variation was measured. An increase of electrical resistance was observed with crack length due to the breakage of electrical pathways. This variation was more prevalent in the channels directly affected by the defect, but also some changes were observed in the adjacent channels due to the influence region effect. This allows to create a conductivity map during the test, by interpolating the electrical resistance measurements of each electrical channel, as shown in Figure 13.19, proving the huge sensitivity of the proposed technique. Here, the conductivity changes associated to the presence of defects allows to have a complete mapping of the structure.

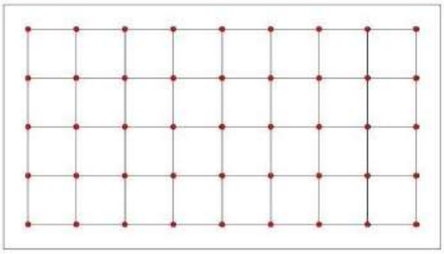

Figure 13.18: Schematics of electrode disposition in sensitive coatings.

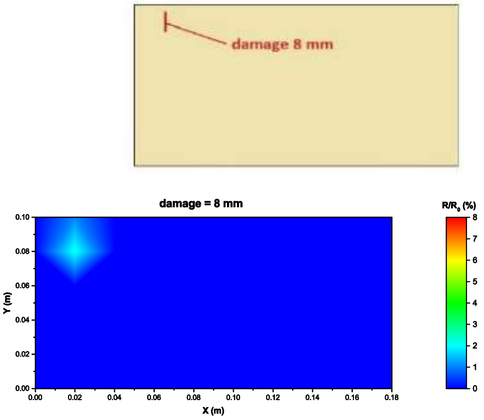
damage 8 mm
damage = 8 mm
Y (m)
0.10
0.08
0.06
0.04
0.02
0.00
X (m)
0.00
0.02
0.04
0.06
0.08
0.10
0.12
0.14
0.16
0.18
R/R$_0$ (%)
8
7
6
5
4
3
2
1
0

(a)

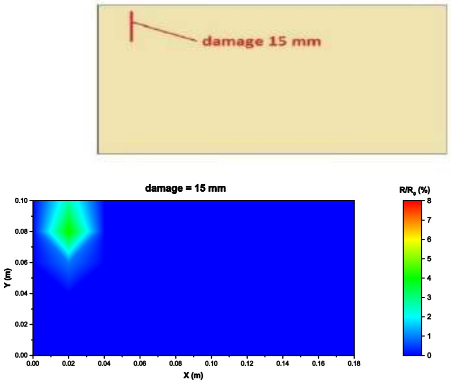
damage 15 mm
damage = 15 mm
Y (m)
0.10
0.08
0.06
0.04
0.02
0.00
X (m)
0.00
0.02
0.04
0.06
0.08
0.10
0.12
0.14
0.16
0.18
R/R$_0$ (%)
8
7
6
5
4
3
2
1
0

(b)

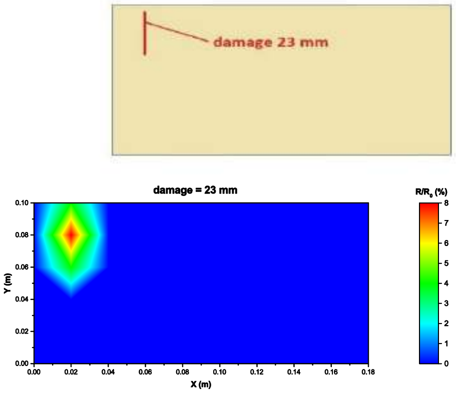

(c)

Figure 13.19: Schematic of defect induced (above) and their corresponding 2D electrical resistance mapping (below) for (a) 8 mm, (b) 15 mm and (c) 23 mm damage length.

Therefore, a complete understanding of electromechanical properties of CNT nanocomposites has been achieved in terms of theoretical estimations and experimental measurements from bulk nanocomposites to multifunctional coatings for damage sensing, proving the high potential and applicability of the proposed nanocomposites for strain sensing and damage detection.

13.2 Strain sensing and crack propagation capabilities of adhesive joints at coupon level

The previous analysis allows to get a global overview of sensing properties of CNT nanocomposites, studying the influence of dispersion procedures and how CNT interactions affect the electromechanical response of the material. Now, the addition of CNTs on adhesive joints for strain sensing and crack propagation purposes is studied.

The main novelty of the present work is the use of adhesive films instead of paste adhesives. As commented before, there is some research in paste adhesives, however, SHM capabilities of adhesive films, which are widely used in aircraft and other industries, remain to be investigated. This study is focused on investigating sensing and crack propagation mechanisms from coupon to sub-element level.

13.2.1 Mechanical and electrical properties of CNT doped adhesive joints

A detailed mechanical and electrical study of SLS joints was carried out in order to select the adequate dispersion parameters for an optimum behavior.

In this regard, ultrasonication was selected as dispersion technique. The reason lies in the fact that, due to the precured state of the adhesive films, spraying was set as an adequate technique for doping the adhesive films. Therefore, it was necessary to previously disperse the CNTs in a low viscosity media, such as distilled water or acetone and, thus, it was not possible to use other dispersion techniques such as three roll milling or toroidal stirring where a higher viscosity of the media is needed.

Nevertheless, the dispersion quality of ultrasonication has been proved to be very good. As commented before, this technique involves the use of the most aggressive disaggregation forces leading to the breakage of larger agglomerates and even the CNTs themselves [57,149]. For these reasons the degree of CNT dispersion is very high with the absence of large agglomerates. Therefore, the aggregate ratio of CNTs is expected to be very low and, based on the previous proposed model, the electrical sensitivity will be higher.

In this context, there are two crucial parameters affecting the dispersion state of CNTs: sonication time and surfactant content. The first one has a prevalent effect on CNT disaggregation and breakage and, thus, on their mechanical and electrical properties [150]. The second one is used to improve the dispersion quality by disaggregating the larger agglomerates. In our case, surfactant was selected as sodium dodecyl sulfate (SDS) based on a previous research [122]. It has an amphiphilic behavior showing a hydrophobic radical attached to the CNT and other free hydrophilic one [151].

Sonication time was varied from 0 to 120 min to study its effect on CNT dispersion state. It was observed that, without using sonication, only manually mixed, there is a high entanglement of CNTs appearing mainly as agglomerates (Figure 13.20 (a)). This would induce a detriment on mechanical properties acting the aggregates as stress concentrators. At 20 min sonication time, a much better dispersion is observed, with lower entanglement and higher disaggregation of agglomerates (Figure 13.20 (b)). However, no significant differences are observed when increasing the sonication time (Figure 13.20 (c)) as the breakage of larger agglomerates takes places during the first stages of dispersion process. In fact, accordingly to T. Roll et al. [149] the mean agglomerate size scales with time as following:

$$s(t) \sim t^{-1/\lambda} \tag{13.14}$$

Where s is the mean aggregate size and λ an homogeneity index, empirically obtained.

Therefore, with very large sonication times, the aggregate size is not significantly changing.

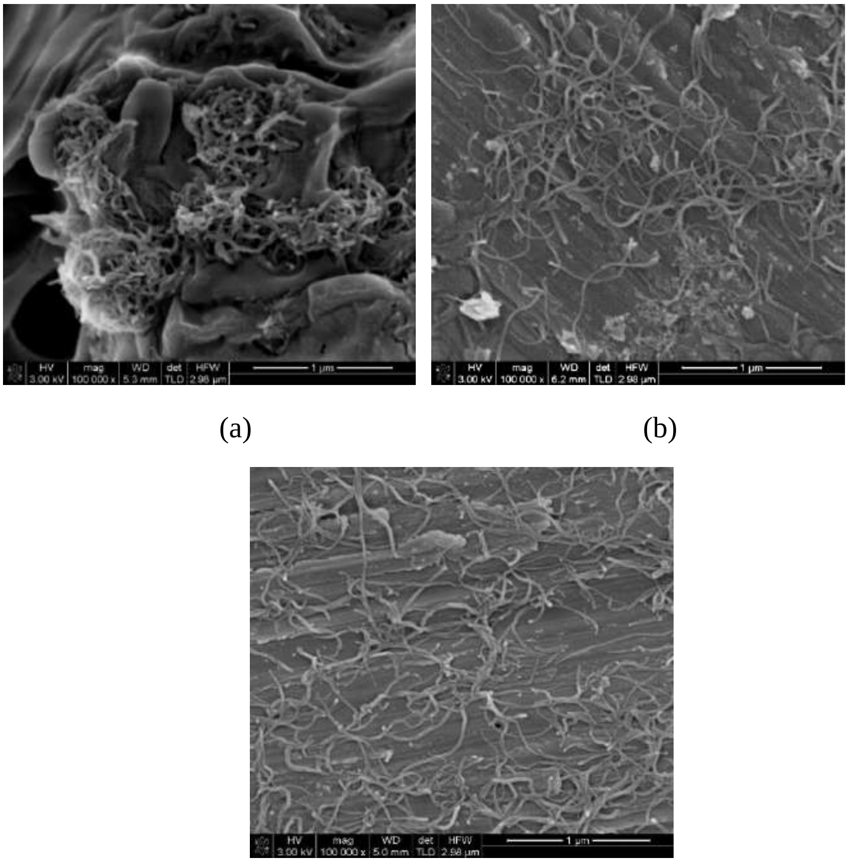

(a) (b)

(c)

Figure 13.20: FEG-SEM images of CNT dispersion at (a) 0, (b) 20 and (c) 120 min sonication time.

However, in terms of CNT breakage A. Lucas et al. [152] observed a drastic reduction of the average length distribution of MWCNTS in the first 5 hours of sonication. It was previously stated that a significant breakage of CNTs lead to a lower aspect ratio of nanoparticles and, thus, PT is increased. For these reasons, and accordingly with FEG-SEM images of CNT dispersion, 20 min sonication was selected as the optimum condition for dispersing the nanoparticles.

On the other hand, the effect of SDS was evaluated attending to the mechanical properties of SLS joints. Firstly, their effect on CNT distribution was also evaluated. In fact, samples without SDS showed a high CNT agglomeration and entanglement (Figure 13.21 (a)) while a 0.25 wt. % SDS content induces a higher disaggregation of main agglomerates and reducing the CNT entanglement (Figure 13.21 (b)), having, thus, at a first sight, a good influence on CNT dispersion.

To evaluate the effect of SDS on lap shear strength (LSS) of adhesive joints, CNT dispersions with different SDS contents were tested: 0, 0.1, 0.25 and 1 wt. %. It was shown that LSS is significantly affected by SDS content (Figure 13.22 (a)). At lower SDS contents, up to 0.25 wt. %, an increase of LSS is observed when increasing the SDS fraction. This is explained by an enhancement of the CNT dispersion inside the adhesive joint, leading to a better distribution of nanoparticles and, thus, a better mechanical performance. However, for 1 wt. % SDS content, a significant decrease of the LSS was observed, even below the joint without surfactant. This is due to the presence of the surfactant itself that could have, when added at high quantities, a negative effect on the mechanical properties of the epoxy adhesive.

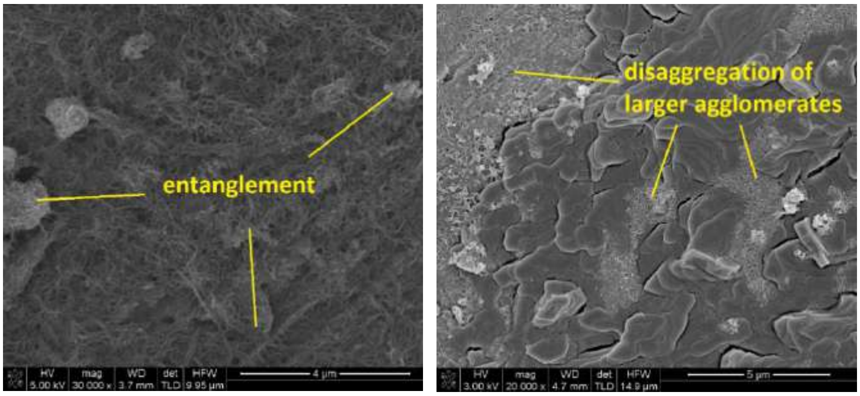

(a) (b)

Figure 13.21: FEG-SEM images of samples (a) without SDS and (b) with a 0.25 wt. % SDS content.

Electrical properties of SLS joints were also evaluated as a function of SDS content, showing significant differences, as shown in Figure 13.22 (b). Electrical resistivity decreases with SDS content up to 0.25 wt. %. This is explained by a better CNT distribution and the homogenization effect induced by the SDS addition. However, at 1 wt. % SDS content, an increase was noticed due to a larger steric stabilization as well as larger distance between adjacent CNTs [153].

Moreover, adhesive joints, as well as most of structural materials, are usually exposed to aggressive conditions, such as humidity or heat. In this context, as commented before, the influence of SDS can be very significative due to its amphiphilic behavior, so it could affect the ageing behavior of the joints. For this reason, an analysis of the surfactant and CNT addition influence on SLS under ageing conditions has been carried out as well as their SHM capabilities were also explored.

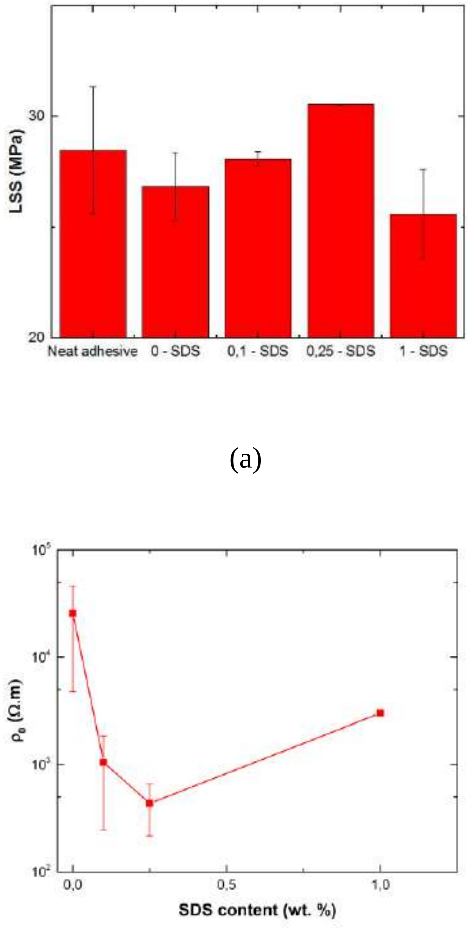

(a)

(c)

Figure 13.22: (a) LSS of adhesive joints and (b) electrical resistivity as a function of SDS content.

13.2.1.1 Ageing behavior of SLS joints

SLS joints were immersed in distilled water at 60ºC, in a similar way than observed in other studies [154]. The idea was to reproduce some aggressive environmental conditions to analyze the electromechanical behavior of the SLS joints with the proposed adhesive film to demonstrate their capabilities for structural bonding.

Firstly, water uptake measurements in bulk CNT adhesives were carried out by varying SDS content: 0, 0.25 and 1 wt. % and compared to neat resin condition. Simultaneously, DSC measurements were also carried out to evaluate glass transition temperature, *Tg*, of the different tested conditions to better explain the ageing mechanisms.

The results showed a relatively similar water uptake behavior for the different tested conditions (Figure 13.23). In this context, two opposite effects can be found: on the one side, the amphiphilic effect of SDS trending to increase the water absorption due to the hydrophilic radical and, on the other side, the presence of CNTs, improving the barrier properties and leading to a water uptake reduction, as shown in the schematics of Figure 13.24. Here, the better the CNT dispersion, the higher the barrier properties due to a more uniform distribution of nanoparticles inside the material. Therefore, as explained before, higher SDS contents improve the CNT dispersion but their amphiphilic behavior is more prevalent, leading to similar water uptake results for every case. When comparing to neat adhesive, no drastic differences are observed due to the previous commented effects.

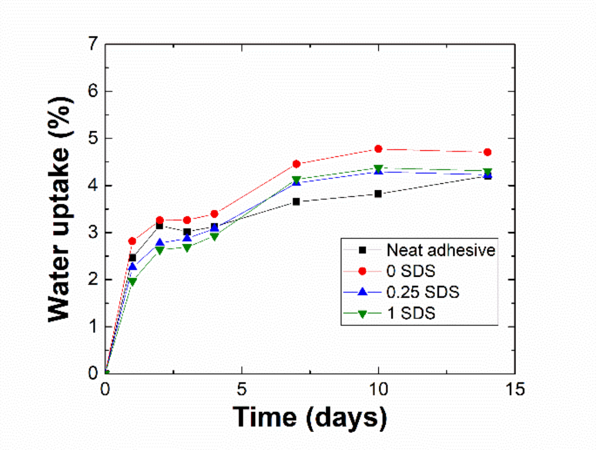

Figure 13.23: Water uptake measurements for in-bulk samples as a function of SDS content.

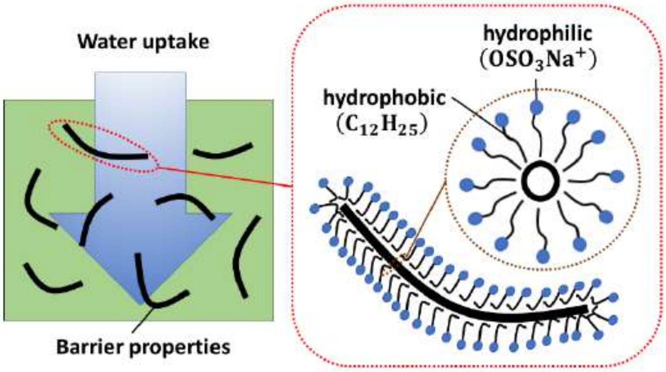

Figure 13.24: Influence of CNT dispersion and amphiphilic behavior of SDS on water uptake.

Therefore, at a first sight, it seems that the addition of CNTs could not have significant influence on water uptake of SLS joints. However, they can induce some changes in the epoxy crosslinking. In fact, when observing Tg measurements by DSC technique, shown in Table 13.1, it is observed that the addition of surfactant, on the one side, implies a drastic reduction of the Tg in the 1st scanning, due to a higher plasticization effect. A similar behavior is observed when comparing CNT doped to neat ones at aged and non-aged conditions. Whereas the neat joints do not show a significant decrease of the Tg, in case of CNT ones, a drastic reduction is observed, explained, again, by a higher plasticization effect.

Table 13.1: Glass transition temperature for different in-bulk conditions.

Condition	Non-aged T_g (ºC)		2-week aged T_g (ºC)	
	1st scanning	2nd scanning	1st scanning	2nd scanning
Neat adhesive	117.0	146.0	115.5	146.0
0.00 SDS	144.0	148.0	119.0	146.0
0.25 SDS	148.5	149.5	118.0	148.5
1.00 SDS	146.0	147.5	109.0	149.5

When comparing the mechanical curves of SLS joints, some interesting facts were observed. On the one side, there is an initial reduction of the LSS value for one-month aged samples and then an increase at 2 months aged samples in almost every case as shown in Figure 13.25 (a). This can be explained by the effect that water absorption has when interacting with polymer chains. In fact, the presence of water induces a plasticization step (Figure 13.25 (b)) due to the creation of weak hydrogen bonds inside the polymer. However, at increasing ageing times, the hydrogen bonds could transform into chemical connections within the polymer network, inducing a secondary crosslinking of the epoxy [155]. It induces a stiffening effect, explaining the LSS recovery of 2 months aged samples. This situation, nevertheless, is quite different in case of CNT doped sample without surfactant. Here, CNT distribution is very poor and, thus, it induces an embrittlement effect due to the presence of aggregates. Secondary crosslinking does not help to toughening the adhesive and, indeed, leads to a higher embrittlement, which explains the drastic reduction of the LSS value for 2 months aged specimens.

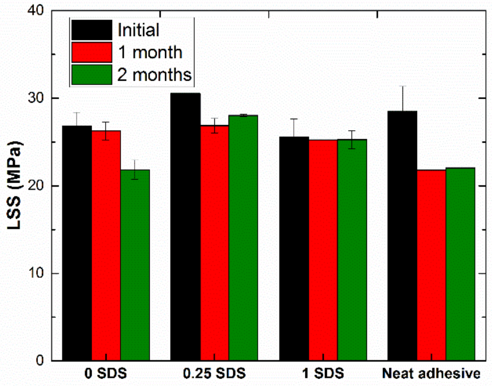

(a)

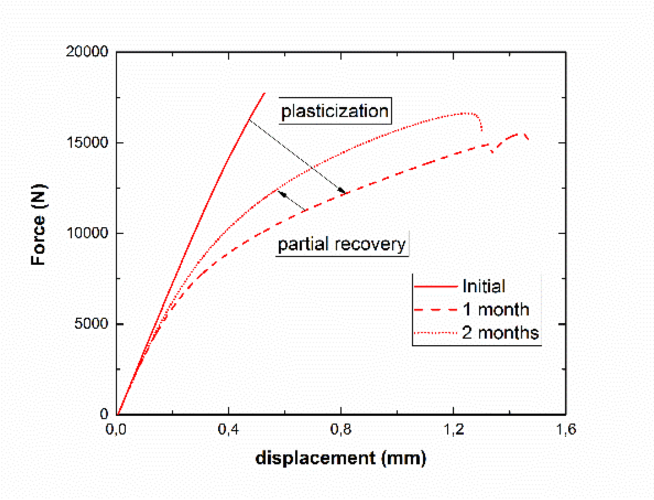

(b)

Figure 13.25: (a) LSS values and (b) mechanical behavior of SLS joints depending on the ageing time.

As commented before, electrical resistance of SLS joints was simultaneously measured during the mechanical tests. The electrical response showed a good agreement with that previously observed for SLS testing for non-aged specimens. Here, the sensitivity is much higher as the displacement increases due to higher plasticization effect.

In this context, it is particularly interesting to analyze the electrical response based on the previous proposed model. As stated before, the variation of electrical resistance can be due to the combination of two different effects: the adhesive deformation and the presence of damage due to crack nucleation and propagation. The damage accumulation is more prevalent for ductile materials as there is a higher crack nucleation and coalescence. Moreover, the electrical resistance change due to adhesive deformation can be estimated by applying the expression of Equation (13.8). As the precise CNT content inside the adhesive joint is unknown, the initial tunneling resistance is estimated by adjusting the value to the initial measured electrical resistance. By this way, the difference between the theoretical electrical response and the measured through the entire SLS tests will give us the damage accumulation of the adhesive joint.

Here, it is observed that non-aged specimens do not barely show damage accumulation during the test as the fracture is mainly brittle (Figure 13.26 (a)). However, the aged specimens showed an increasing damage accumulation effect with displacement (Figure 13.26 (b) and (c)) due to the mentioned before plasticization effect, which leads to crack nucleation and propagation during the test. SEM images confirms the previous statements. The non-aged specimens showed a more brittle fracture, with smooth surfaces (Figure 13.27 (a)). However, the aged specimens showed a more prevalent plasticization effect with the presence of adhesive plastic deformation (arrowed areas of Figure 13.27 (b) and (c)). The neat adhesive joints showed a similar facture behavior.

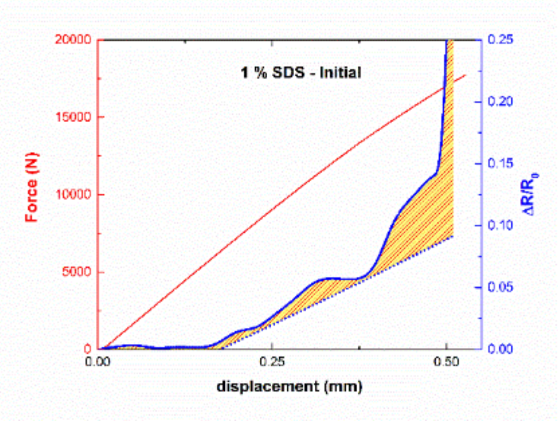

(a)

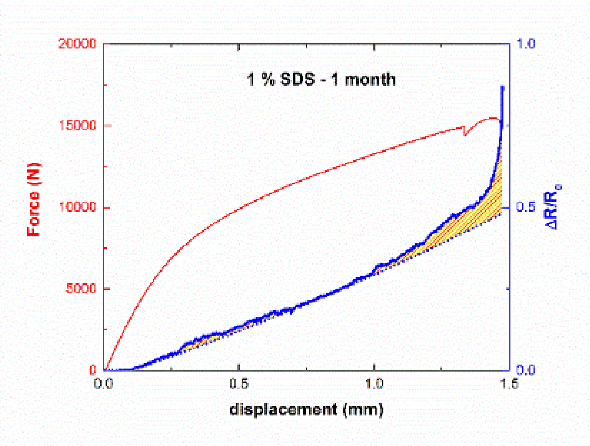

(b)

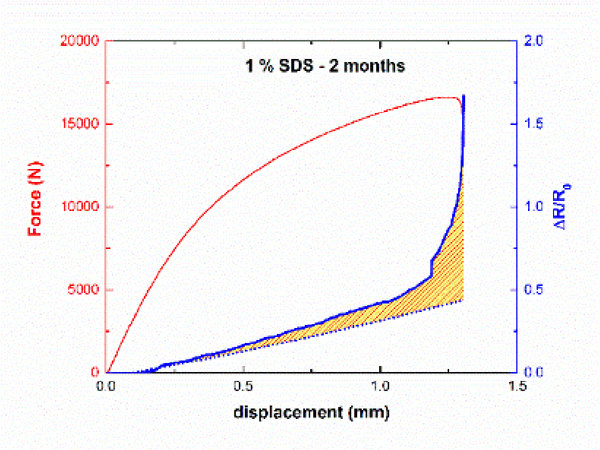

(c)

Figure 13.26: Electromechanical curves of (a) non-aged, (b) 1 month and (c) 2 month aged samples.

Therefore, as a first estimation, several issues about damage accumulation can be stated by investigating the electrical response, giving a deeper understanding of ageing mechanisms.

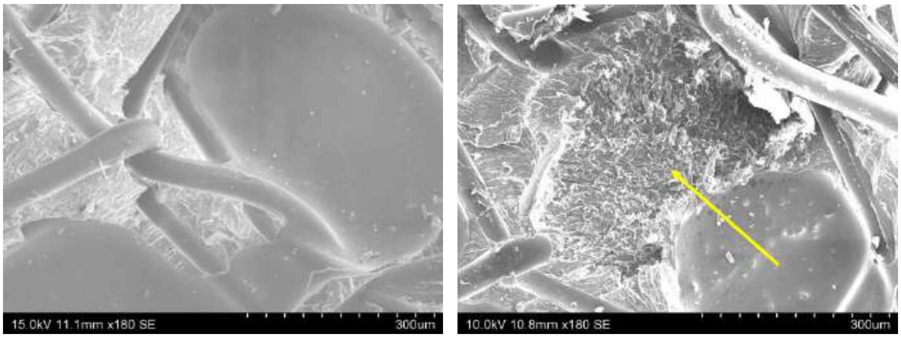

(a) (b)

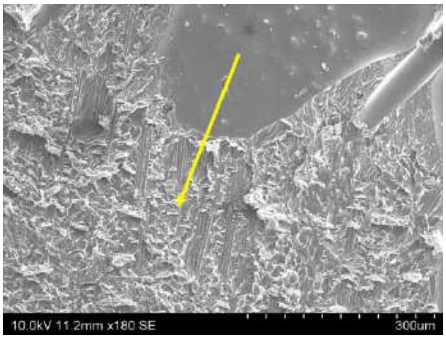

(c)

Figure 13.27: SEM images of fracture surfaces of (a) non-aged, (b) 1 month and (c) 2 month aged specimens showing ductile fracture mechanisms (yellow arrows).

13.2.1.2 Mode-I and Mode-II fracture energy mechanical tests

Therefore, accordingly to CNT dispersion analysis and mechanical properties, it was concluded that the optimum conditions were the CNT doped adhesive with 0.25 wt. % SDS content at 20 min sonication. Thus, for crack propagation and strain sensing purposes as well as skin-stringer sub-elements, it will be selected as the process condition.

Moreover, the effect of CNT addition on mechanical properties was also evaluated for Mode-I and Mode-II energy fracture tests. These types of testing allow to have an understanding of how crack propagates inside the joint and how it is affected because of the addition of CNTs.

Mode-I adhesive fracture energy, G_{IC}, was calculated under the theory of corrected beam developed by B. Blackman et al. [156]:

$$G_{IC} = \frac{3P\delta}{2B(a + |\Delta|)} \cdot \frac{1}{N} \qquad (13.15)$$

Where P is the applied load, δ the piano hinge displacement, B the specimen width, a the crack length and $|\Delta|$ and N two correction factors depending on the ratio of displacement divided by the applied load, also called, compliance.

It has been observed that the mean value of G_{IC} for CNT doped joints is slightly higher than that obtained for neat ones, although the difference is not very prevalent (Figure 13.28). This is explained because CNTs have a toughening and crack bridging effect on the adhesive. This enhancement, however, is not very significant probably because of the negative effect that SDS could have on the epoxy adhesive, in a similar way than for SLS joints. In every case, the failure mode was identified as cohesive, which means that an adequate surface treatment has been carried out.

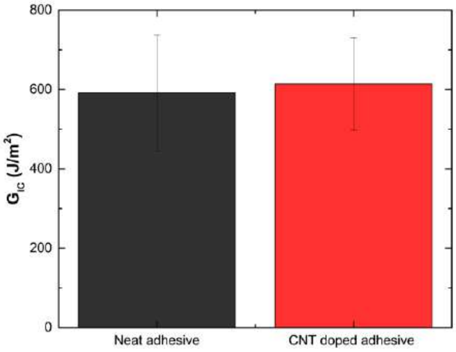

Figure 13.28: GIC values of neat and CNT doped CFRP adhesive joints.

Mode-II fracture energy was calculated by using the Irvin-Kies equation where compliance, $C = \delta/P$, is obtained from Timoshenko beam theory for end notched flexure tests.

$$C = \frac{3a^3 + 2L^3}{8E_1Bh^3} + \frac{3L}{10G_{13}Bh} \qquad (13.16)$$

Being a the crack length, B, h and L the specimen width, thickness and span, E_1 and G_{13} the longitudinal and shear moduli of the substrate, respectively.

Therefore, it is possible to estimate Mode-II fracture energy, G_{II}, of the adhesive joints:

$$G_{IIC} = \frac{9P^2{a_e}^2}{16B^2h^3E_1} \qquad (13.17)$$

It was shown that the peak load in the force-displacement curve of CNT doped joints is slightly higher than the neat ones. By analyzing the R-curves, shown in Figure 13.29, correlating the fracture energy with crack length, a slower crack propagation is observed for CNT doped specimens with higher G_{IIC} values (5 to 4.2 N/mm). This indicates a good homogeneity of CNT distribution along the adhesive joint which induces a toughening effect on the adhesive in a similar way than previously observed for Mode-I specimens. This fact difficulties the crack propagation through the joint.

Therefore, once analyzed mechanical properties at different load states and proved the electrical conductivity of adhesive joints strain sensing and crack propagation monitoring tests were carried out to evaluate their potential in SHM applications, which is, indeed, the main objective of the present work.

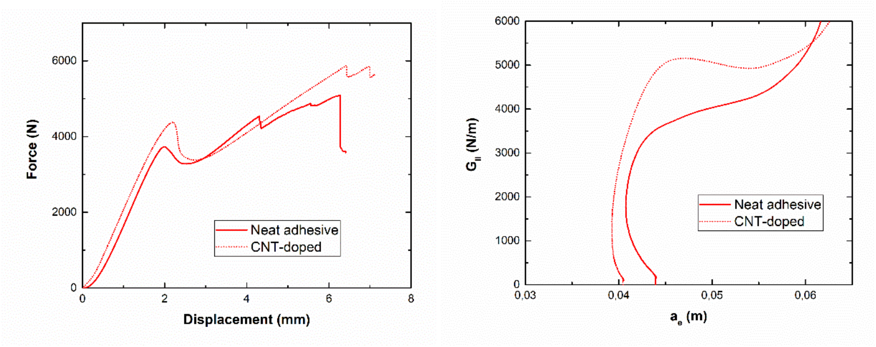

(a) (b)

Figure 13.29: (a) Load-displacement and (b) R-curves for neat and CNT-doped (dashed lines) adhesive joints.

13.2.2 Crack propagation monitoring in SLS, Mode-I and Mode-II joints

Electrical behavior of adhesive joints was monitored under SLS testing conditions. An increase of electrical resistance was observed with displacement with a very prevalent exponential behavior (Figure 13.30 (a)). This is explained by the combination of two effects inside the adhesive joint: on the one side, the adhesive deformation leading to an increase of tunneling distance and thus, an increase of tunneling resistance and, on the other side, the rapid crack propagation in the last stages of the SLS test as shown in the schematics of Figure 13.30 (b). This rapid crack nucleation and propagation induces a sudden breakage of electrical pathways explaining the sharp increase of the electrical resistance in the last stages of the test.

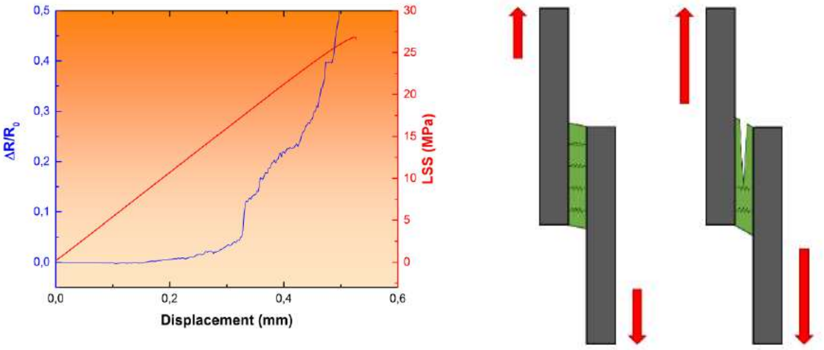

(a) (b)

Figure 13.30: (a) Electrical response of SLS and (b) schematics indicating the electrical breakage during the test.

The electrical response of SLS joints gives a first estimation of the high sensitivity of the proposed CNT adhesive, but it does not offer a complete information about sensing properties for crack propagation monitoring as crack propagates in a very sudden way. Therefore, a deeper analysis of Mode-I and Mode-II monitored tests has been carried out.

Crack propagation in Mode-I tests can follow a uniform trend or an unstable behavior, following a stick-slip pattern. In the first case, the mechanical curve shows a stable decrease of the load with crack length while in the second one, there are sudden drops of the load correlated to rapid crack propagation inside the joint and arrest phases in the regions where this propagation is stopped. This different behavior is also observed in the fracture surfaces of the joint where the adhesive shows a stick-slip pattern.

When comparing the electrical response of the two situations, significantly differences were observed. Specimens with a more uniform crack propagation show a more stable increase of the electrical resistance (Figure 13.31 (a)), as the breakage of electrical pathways due to crack propagation is more uniform. However, when observing stick-slip specimens a more unstable increase of the electrical resistance is noticed (Figure 13.31 (b)). There are sharp increases of the electrical resistance corresponding to sudden drops in the mechanical performance (point 3 in the graph), that is, in those regions where crack rapidly propagates. Then, the increase of mechanical load due to crack stoppage is correlated to arrest phases in the electrical response (points 2).

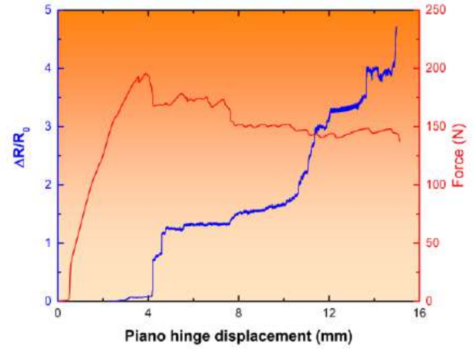

(a)

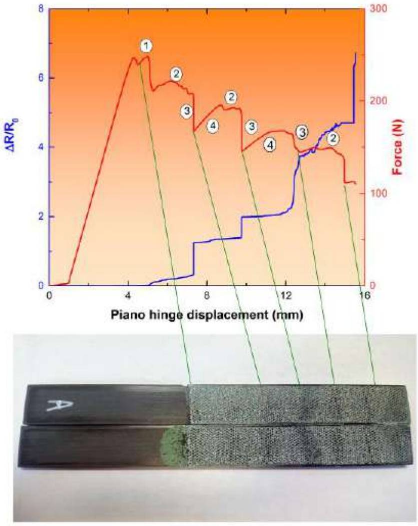

(b)

Figure 13.31: Electromechanical curves of Mode-I specimens showing (a) a uniform trend and a (b) stick-slip pattern.

This good agreement between electrical and mechanical response highlights a potential use for crack propagation monitoring purposes. However, a deeper theoretical analysis is needed to properly establish the correlations between electrical and mechanical behavior. For this reason, a simple theoretical model is proposed.

A first approach is to modelling the adhesive joint as an electrical circuit with parallel pathways. The equivalent resistance is calculated supposing that CNTs are uniformly distributed along the joint and the adhesive thickness is constant through the total length:

$$R = \rho \cdot \frac{l}{A} \qquad (13.18)$$

Being l and A the thickness and cross-sectional area of CNT adhesive and ρ the resistivity.

When crack propagates through the joint, it induces a breakage of electrical pathways so the total resistance can be estimated as follows:

$$\frac{1}{R} = \frac{1}{\rho} \int_{x_a}^{x_0} \frac{b \cdot dx}{l} \qquad (13.19)$$

Where x_0 and x_a are the initial and current crack length, respectively.

Therefore, the electrical resistance is inversely proportional to the bonded area. It means that, in an ideal situation, the electrical resistance should follow a uniform trend with crack length. This is observed when uniform crack propagation takes places, however, in the stick-slip case, there are significant differences between the expected and measured electrical response. More specifically, the highest significant differences are observed in the areas where crack propagates in a sudden way.

The main limitation of Equations (13.18) and (13.19) is that adhesive is considered totally homogeneous. However, manufacturing defects play an important role in mechanical but also electrical properties of adhesive joints. This manufacturing defects can be due to an excessive adhesive overflowing during curing. In fact, when observing profilometry images of fracture surfaces, shown in Figure 13.32, there is a lack of adhesive in the areas where crack propagates rapidly (Figure 13.32 (b)) and, thus, the adhesive distribution is heterogenous inside the adhesive joint.

To capture these effects, adhesive joint will be divided in blocks with different electrical properties (Figure 13.33 (a)). The areas where crack propagates in a sudden way, due to a lack of adhesive and, thus, a reduction in the adhesive thickness would have a higher electrical conductivity so they will be prevalent electrical pathways:

$$\frac{1}{R} = \sum_{i=0}^{n} \frac{1}{\rho_i} \cdot \frac{b \cdot x_i}{l} = \sum_{i=0}^{n} \frac{1}{R_i} \qquad (13.20)$$

Where the subscript i denotes each one of the different blocks in which adhesive joint has been divided.

When increasing d, $d = \rho_i/\rho_0$, parameter, a coefficient of electrical conductivity of rapid crack propagation areas divided by the conductivity of arrest regions, a sharper increase of the electrical resistance is observed (Figure 13.33 (b)), showing the previously noticed stick-slip behavior. Therefore, a deeper understanding of stick-slip phenomenon is understood by analyzing the electrical response of the joints.

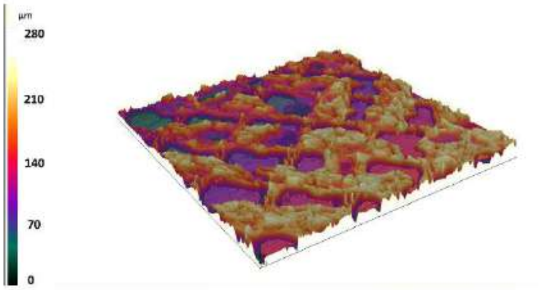

(a)

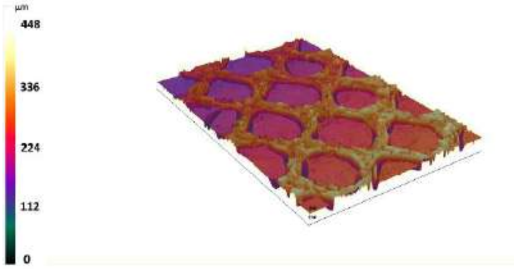

(b)

Figure 13.32: Profilometry images of fracture surfaces indicating areas with (a) high presence and (b) lack of adhesive.

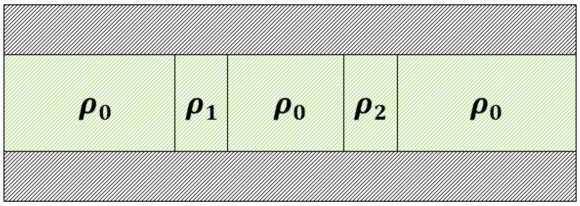

(a)

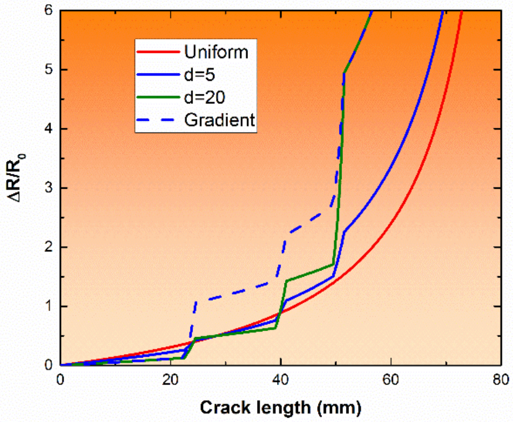

(b)

Figure 13.33: (a) Schematics of block-equivalent electrical circuit and (b) electromechanical estimations as a function of *d* parameter.

Moreover, the effect of damage in the mechanical and electrical response of the joint was also investigated. To achieve this purpose, several artificial defects were induced by using a solid release agent (Teflon). Figure 13.34 shows the electromechanical response of the bonded joint. It is observed that there are sudden drops of the mechanical force corresponding to sharp increases of the electrical resistance, in a similar way than in previously observed stick-slip curves [109]. The sudden drops of the force correspond to areas where crack propagates rapidly inside the adhesive, inducing a sudden breakage of electrical pathways. This prevalent stick-slip pattern is because Teflon inserts cause a complete discontinuity between the adhesive and the substrate.

In this case, there is a reduction on the applied load while crack is propagating through a section of the adhesive joint and it takes places in a sudden way (sudden drops of the mechanical resistance marked as point 1 on Figure 13.34). Then, after passing through the adhesive area, the crack founds a discontinuity (marked as point 2 of Figure 13.34) so a higher force is needed to promote the crack propagation again through the next section of the adhesive joint (marked as point 3 of Figure 13.34) where the crack propagates rapidly again. The small variation of the electrical resistance when the mechanical load increases (point 3) is explained because of an increase of tunneling distance between adjacent nanoparticles due to the adhesive deformation, inducing a decrease of electrical conductivity [102]. This electromechanical response is repeated in each section of the adhesive joint, as also observed in the schematics of Figure 13.34. Therefore, it can be noticed that a total discontinuity induces a less uniform mechanical response and, thus, a more unstable electrical behavior.

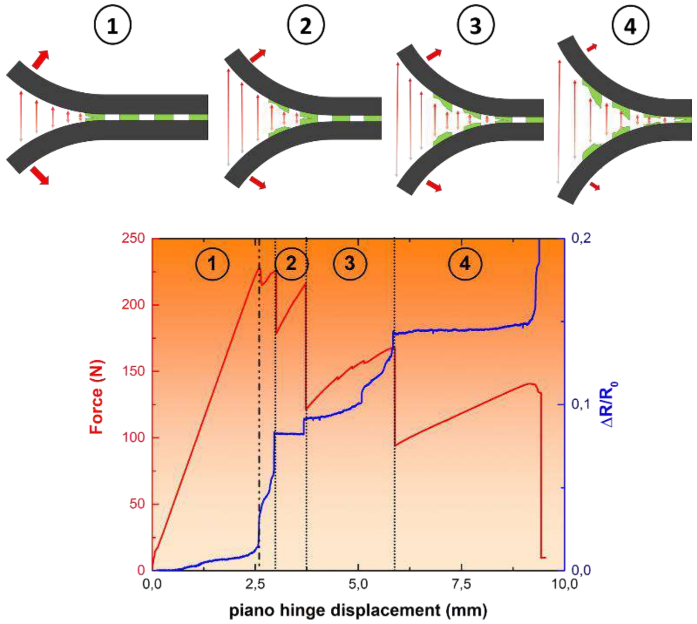

Figure 13.34: Electromechanical response of damaged specimen showing the correlation between crack propagation and mechanical behavior.

A similar electrical response is observed when analyzing Mode-II specimens, shown in Figure 13.35. Here, there are two contributions to electrical resistance: the adhesive deformation due to bending of specimen and the breakage of conducting paths due to crack propagation, where a good agreement between electrical and mechanical response is observed (Figure 13.35 (b)). The first effect can be neglected as the CNT adhesive layer is placed near the neutral axis, so not significant deformation is expected and, thus, the variation of electrical resistance due to tunneling mechanisms is too small. The second one can be modelled in the same way than Mode-I testing, with the electrical resistance being inversely proportional to bonded area. However, some differences when comparing the electrical properties of Mode-I and Mode-II specimens are observed.

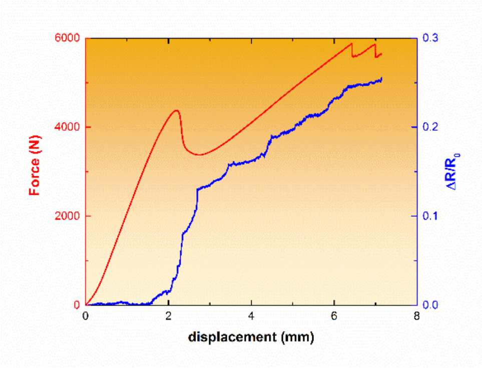

(a)

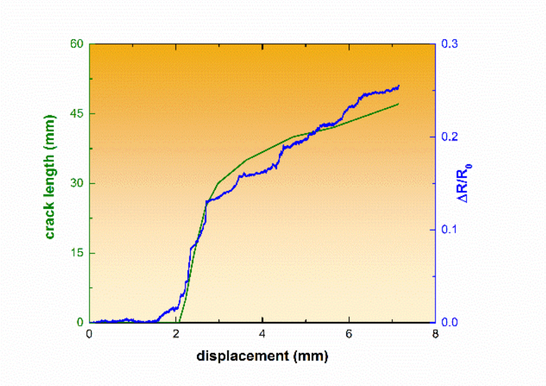

(b)

Figure 13.35: Electromechanical response of Mode-II specimens (a) as a function of the load and (b) crack length.

The first one is that the sensitivity in Mode-II specimens is much lower. This is explained due to the crack opening effect. In Mode-I testing crack is wide open while in Mode-II testing there is a slippage effect of the two adherents leading to a narrower crack front, and thus, the breakage of electrical pathways is not as prevalent as in Mode-I tests. Therefore, in order to take this effect into account, the expression of Equation (13.19) can be modified by applying a corrective factor, K:

$$\frac{\Delta R}{R_0} = K \cdot \left(\frac{b \cdot L}{b \cdot (L-a)} - 1\right) \tag{13.21}$$

The value of *K* can be determined accordingly to experimental measurements. In this case, when K=0.33 a very good agreement between predicted and measured electrical properties as a function of crack length was achieved, as shown in Figure 13.36.

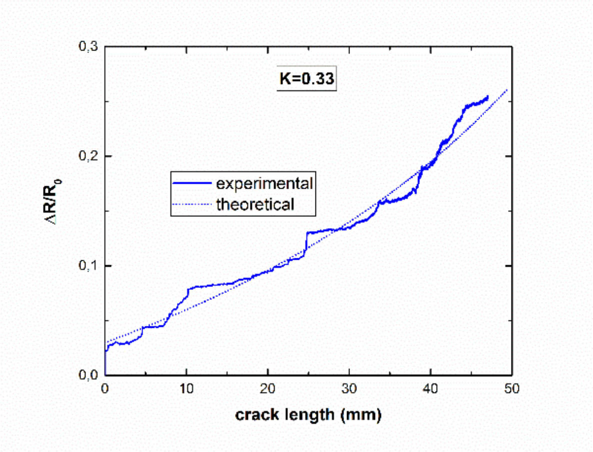

Figure 13.36: Experimental and theoretical electrical response for a K value of 0.33.

The second difference with Mode-I testing is that the increase of electrical resistance was more stable with no presence of stick-slip effects. In every case the fracture surface shows a very homogeneous adhesive distribution through the whole joint, so no significant manufacturing defects were detected. The measured electromechanical response of the sample also proved this statement.

SEM images of adhesive joints showed a relatively homogeneous adhesive thickness through the whole joint (Figure 13.37 (a) and (b)). In addition to that, it is generalized observed the presence of voids through the entire adhesive. This is explained by the effect of pressure during curing. In fact, hot-press do not induce an homogeneous pressure distribution through the sample, as it is applied in one axis. Therefore, it can lead to an adhesive overflowing and, thus, the lack of adhesive inside the joint (Figure 13.37 (c)). In this context, however, no differences between the CNT doped and neat adhesive joints were observed.

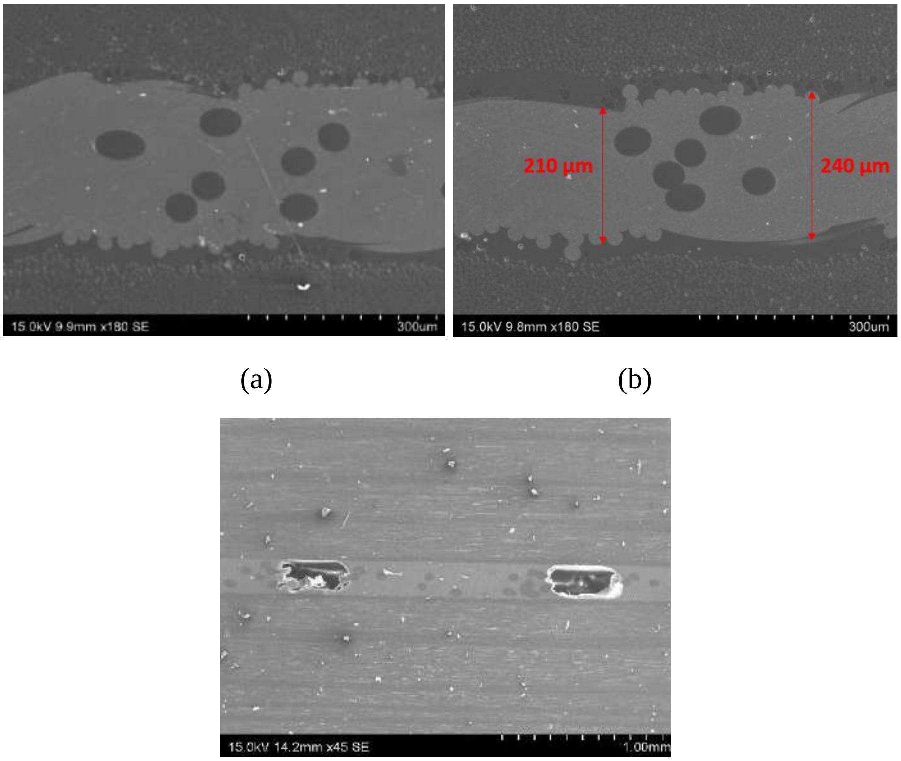

(a) (b)

(c)

Figure 13.37: SEM images of Mode-II transversal sections showing (a), (b) thickness distribution and (c) presence of voids.

Therefore, CNT doped adhesive films have proved to be a good alternative for joining CFRP materials with an increase of the mechanical properties for both SLS, Mode-I and Mode-II loading tests. Their sensing and crack propagation monitoring capabilities have been demonstrated under quasi-static load conditions. Thus, they show a promising potential and applicability for SHM purposes. However, it is necessary to explore more realistic scenarios. In fact, structural components are usually subjected to dynamic loads. For these reasons, it is very important to analyze their fatigue behavior and explore their crack propagation monitoring capabilities under these dynamic conditions.

13.2.3 Crack propagation monitoring of CNT adhesive joints under fatigue loading

Neat and CNT doped adhesive joints were tested under fatigue conditions. These experiments were carried out in a research stay at Dipartimento di Meccanica of Politecnico di Milano. Here, the most important issue is the experimental set-up, showing some differences when comparing to experimental procedure at quasi-static loading, as stated in the Methods section. The reason lies in the fact that, due to the dynamic conditions of the load, a high acquisition frequency device is needed in order to properly capture the complete evolution of the electrical response in a single cycle. Therefore, *Agilent* hardware cannot be used as it offers a maximum acquisition frequency of 10 Hz, which is exactly the same as the load frequency during the fatigue test. Instead, a *NI9234* module from *National Instruments* was used. In this case, voltage was acquired instead of electrical resistance and, thus, a power supply with an integrated circuit to maintain the current constant was needed. By this way, the changes in the voltage are due only to changes in the electrical resistance of the specimen, in a similar way than for quasi-static tests.

Crack length was determined by using a portable microscope camera *Dino-Lite* AM413ZTA at several fatigue cycles. The optical approach for crack growth monitoring has been explored in other studies using a Digital Image Correlation (DIC) technique, showing very accurate results [130]. Therefore, this study will be focused on comparing the measurements of the crack propagation to the electrical response of the specimen.

Electrical results, thus, were recorded for several CNT doped specimens with the optimum SDS conditions (0.25 wt. %) as shown in Figure 13.38 (a). It was observed that there is a good agreement between electrical signal and mechanical behavior. By focusing on a single cycle, an expected electrical behavior was found similar to that shown for a SLS quasi-static test, with an increase of the electrical resistance with the applied mechanical load. Then a decrease is observed when decreasing the mechanical force, reaching the initial value of resistance (Figure 13.38 (b)). Although the mechanical load was applied by following a sinusoidal waveform, the electrical response seems to be more linear. This is explained by the exponential dependence of the resistance with the applied strain due to the effect of tunneling mechanisms.

When observing the overall behavior as a function of time, that is, fatigue cycles, a general increase of the electrical resistance is observed (Figure 13.39 (a)). This is explained because of the crack propagation during the fatigue tests.

Once damage is appearing inside the adhesive joint there is an irreversible breakage of electrical pathways, meaning that the baseline of electrical resistance also increases. This statement is confirmed when representing the electrical response versus measured crack length (Figure 13.39 (b)). Here, three regions can be distinguished: the first one (I) with a slight variation of the electrical response corresponding to the region where crack is not propagating through the edges of the joint (Figure 13.39 (c)). In this case, this slight variation can be associated to the presence of some microcavities which start to appear and then coalesce in a similar way than observed in other studies [133]. The second one (II) is associated to the initial stages of crack propagation, where a more significant increase of the electrical resistance is also observed and the last one (III) corresponds to the last crack propagation until final failure of the joint. Here, as expected, the variation of the electrical resistance is much more significant.

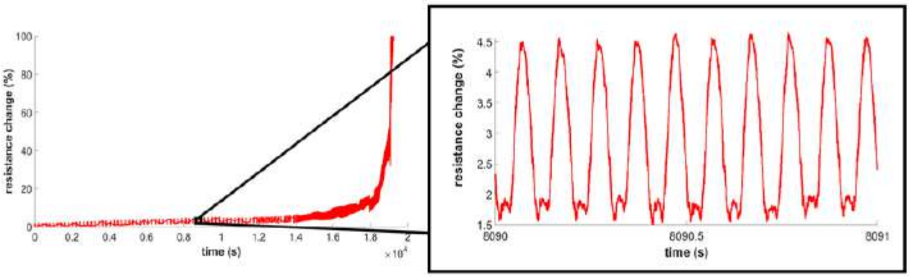

(a) (b)

Figure 13.38: Electrical response (a) as a function of number of cycles and (b) detailed response of a 10 cycle window.

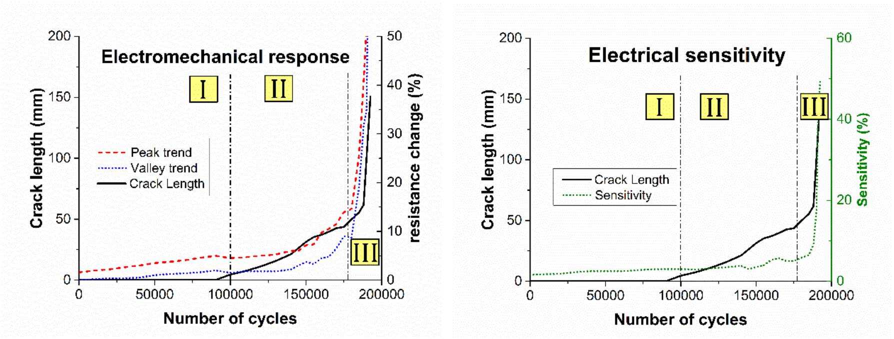

(a) (b)

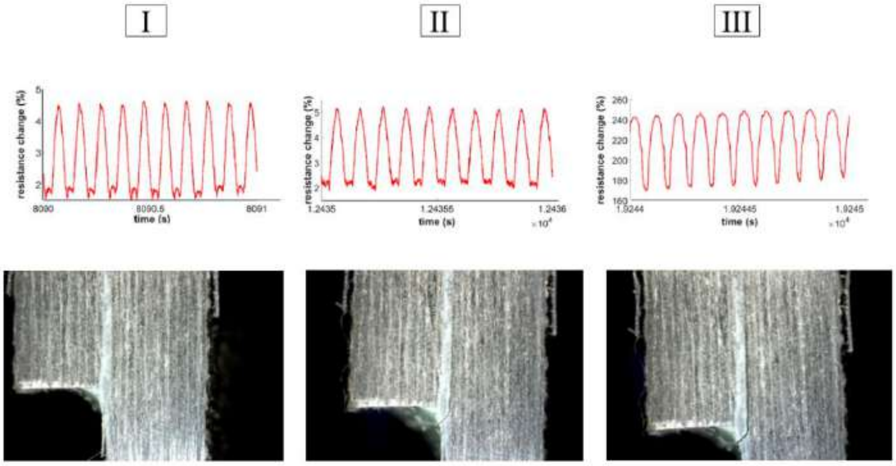

(c)

Figure 13.39: Electromechanical response of fatigue joints showing (a) the electrical behavior as a function of number of cycles, (b) crack length and (d) detailed response at several regions.

Apart from the baseline changing of the electrical resistance, it is particularly interesting to focus on the change of the resistance in a single cycle. It was observed that the electrical sensitivity, defined as the change of the normalized resistance in a single cycle, increases significantly, especially in the last stages of fatigue test. This is explained by a higher shear stress involved in the joint due to the presence of the crack as well as a higher deformation adhesive. These changes in the strain field of the adhesive joint not only induces a change in the sensitivity but also in the shape of the electrical signal. For this reason, it is interesting to represent the cross-correlation, *xcorr*, of a 10 cycles window as a function of the number of cycles with respect to a baseline signal window at the beginning of the test, as observed in the graph of Figure 13.40. By this way, it is easier to observe the changes in the signal shape with increasing debonding area, due to the previously commented facts.

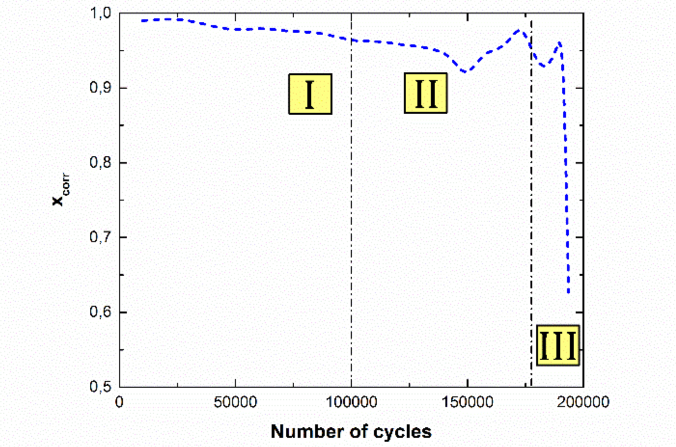

Figure 13.40: Variation of xcorr parameter as a function of number of cycles.

A good agreement between electrical response and crack propagation was observed in every case. More specifically, some specimens showed a more prevalent stick-slip effect with a less uniform crack propagation with fatigue cycles. This was also noticed in the electrical response with a sharper increase of the electrical resistance. Therefore, the proposed methods show a good potential for detecting crack growth in fatigue conditions with a very high resolution. In fact, much higher sensitivity was observed when comparing to mechanical response, as shown in Figure 13.41.

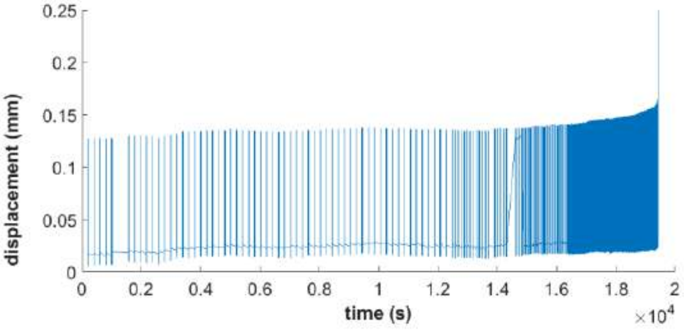

Figure 13.41: Displacement as a function of the number of cycles during fatigue testing.

For a deeper investigation on fatigue monitoring capabilities, simple theoretical calculations were carried out to estimate the cracked area. To achieve this purpose, a similar model than previously developed for Mode-I and Mode-II test was used, by comparing the actual resistance with the initial one, where no cracked area is supposed to be:

$$\frac{\Delta R}{R_0} = \frac{R}{R_0} - 1 = \frac{A_0}{A} - 1 \qquad (13.22)$$

The evolution of the estimated cracked area as a function of the crack shape gives a deeper understanding of how crack is propagating inside the joint as shown in Figure 13.42. A higher ratio of crack area vs crack length implies a that crack is propagating mainly inside the joint and not only through the edges. The opposite situation indicates a crack propagation mainly through the edges.

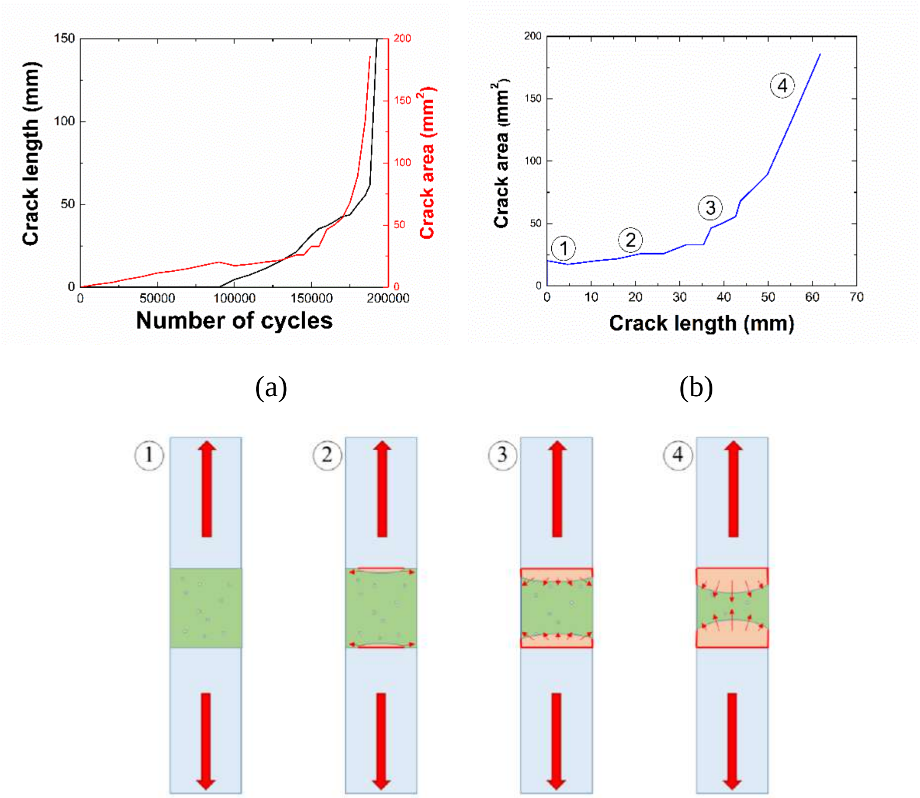

(a)

(b)

(c)

Figure 13.42: Measured crack length (a) as a function of number of cycles, (b) represented versus crack area and (c) evolution of bonded area during the test based on theoretical estimations.

It was observed that the ratio of the cracked area divided by crack length is increasing during the test. This is explained because crack initiation usually takes places in the edges where higher shear stresses are involved [157]. Once crack starts to propagate, it induces a change in the shear stress field and it starts to propagate inside the joint, explained by a higher ratio area/length of the crack. This is in good agreement with other studies analyzing the distribution of shear stresses inside the joint in a SLS fatigue test [158].

In addition to that fact, the analysis of fracture surfaces allows to estimating the cracked area inside the joint in the last stages of the test, as shown in Figure 13.43, indicating that crack propagation took place inside the joint once initiated in the edges, as predicted by our theoretical estimations. In this case, the shape of the crack is not symmetric. This fact can be explained due to an irregular distribution of porosity inside the joint which can induce a prompt failure in the lower fillet.

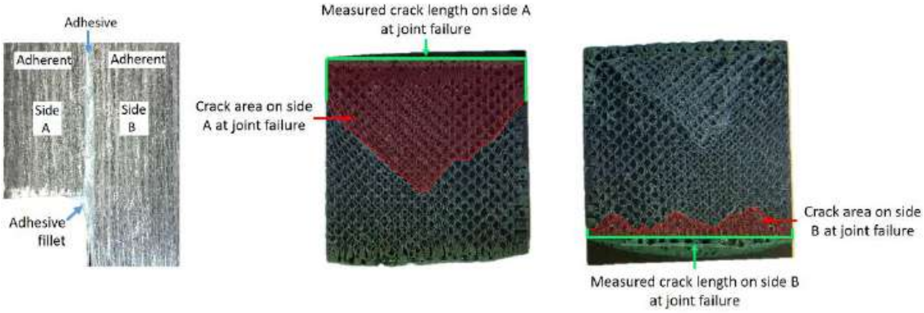

Figure 13.43: Image of fracture surface showing the estimated crack shape in the last stages of the test.

Therefore, due to all the aforementioned reasons, and especially because its higher sensitivity when comparing to the mechanical response as well as its high repeatability, the proposed technique shows a huge potential and applicability for crack propagation under fatigue conditions.

13.2.4 Joints between dissimilar materials

As stated before, the increasing complexity of structures, which usually involves different materials, makes it necessary the development of joining techniques between them. For this reason, a first study exploring the mechanical and monitoring capabilities of CNT doped adhesive films applied to joints between dissimilar materials: a 7075 aluminum alloy (Al) and CFRP; was carried out.

Two configurations were tested under SLS conditions: Al-Al and Al-CFRP and the influence of surface treatment of the metallic substrate was also investigated. Therefore, three substrate conditions were analyzed: no surface treatment (UT), brushing (B) with a 120 SiC sand paper and grit-blasting (GB).

From the mechanical point of view, some differences were observed when comparing the LSS of Al-Al to Al-CFRP joints, as shown in Figure 13.44.

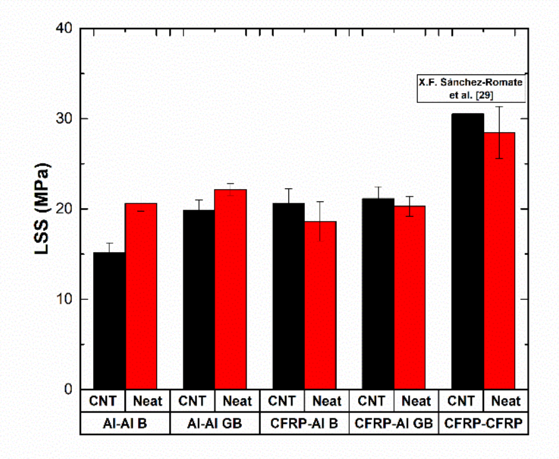

Figure 13.44: LSS value of Al-Al, CFRP-CFRP and CFRP-Al joints under different tested conditions.

Al-Al joints showed a significant dependence on surface treatment, especially in case of CNT doped adhesive. For both neat and CNT doped adhesive joints the samples without any surface treatment showed the lowest LSS due to a poor interface between adhesive and substrate. In this case, the addition of CNTs had a very negative effect. This was explained due to a poorer interaction between CNTs and Al surface, leading to a lubricating effect on the adhesive surface. For brushed specimens, LSS increase was too prevalent, especially in the case of CNT doped joints. The reason lies in the fact that surface roughness improves the adhesion in the interface area. Because of the poorer mechanical performance of the untreated CNT joints, this effect is more significant in this case. Finally, grit-blasting condition showed the best performance for both neat and CNT doped joints. The creation of an active surface in the adherent improves the interfacial adhesion, thus, strengthening the joint [159]. In every surface treatment condition a decrease of the mechanical properties is observed with the addition of CNTs, although at GB condition, the mechanical detriment was the lowest.

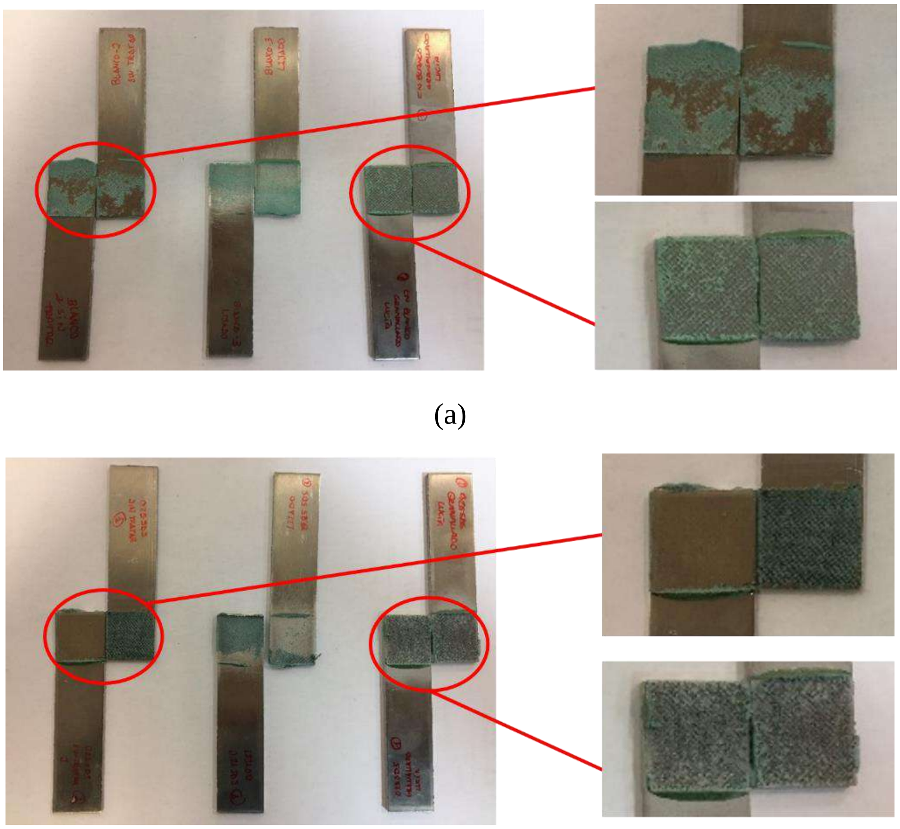

(a)

(b)

Figure 13.45: Images of fracture surfaces of (a) neat and (b) CNT doped adhesive Al-Al joints with (red circles) fracture areas highlighted.

The analysis of fracture surfaces allows to better understanding the mechanical performance of the bonded joints (Figure 13.45). An adhesive failure was found in both untreated specimens. However, at brushing condition, the failure mode was mainly cohesive in case of neat joints while mainly adhesive or mixed in case of CNT doped ones, which showed a poorer mechanical performance. At GB condition, both neat and CNT doped joints showed a mainly cohesive failure.

In case of CFRP-Al joints, the dependence on the surface treatment was not so prevalent as in Al-Al ones. Here, there was no untreated conditions due to the extremely poor behavior showed in metal to metal joints. Here, LSS was higher for both B and GB conditions with the addition of CNTs. This is explained due to a good load transferring between substrates, which is enhance with the presence of CNTs, as also observed in other studies [131,132]. The highest performances were obtained, as expected, at GB conditions due to the creation of an active surface in the metal as previously stated. In this case, the analysis of fracture surfaces (Figure 13.46) revealed a mixed adhesive-cohesive mode in B condition for the neat joints while the rest of conditions showed a mainly cohesive failure, which was in good agreement with the mechanical performance of the joints. It is important to point out that LSS value of dissimilar joints is higher than Al-Al ones due to the higher stiffness and strength of the CFRP substrate which plays an important role in the total strength of the joint [124,125].

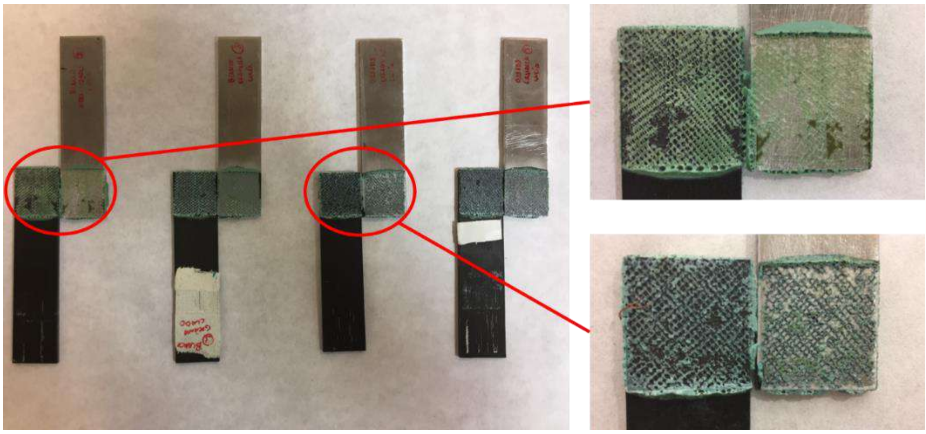

Figure 13.46: Images of fracture surfaces of CFRP-Al joints for (left to right) neat B, GB and CNT doped B, GB conditions.

Simultaneously to mechanical testing, the electrical response of SLS joints was also measured, in order to explore the SHM capabilities of dissimilar joints. Here, as stated in Methods section, the whole Al substrate acts as an electrode itself while the copper wire configuration was used in case of CFRP substrates.

Electrical measurements showed some differences with respect to CFRP-CFRP curves. By analyzing Al-Al electromechanical curves, it is observed that the electrical response varies depending on the surface treatment conditions due to changes in the way the joints fail. Untreated and brushed specimens showed a very unstable response, with a noisy signal (Figure 13.47 (a) and (b)). This is due to the poor interface between adhesive and substrate, leading to the creation and breakage of electrical pathways during the test, as shown in the schematics of Figure 13.48. Therefore, this is translated into an irregular electrical signal. However, there is a softer electrical response in the GB condition (Figure 13.47 (c)). Here, as shown in the fracture surface, the interface adhesive-substrate is much better, and therefore, there is no creation and breakage of electrical pathways during the test.

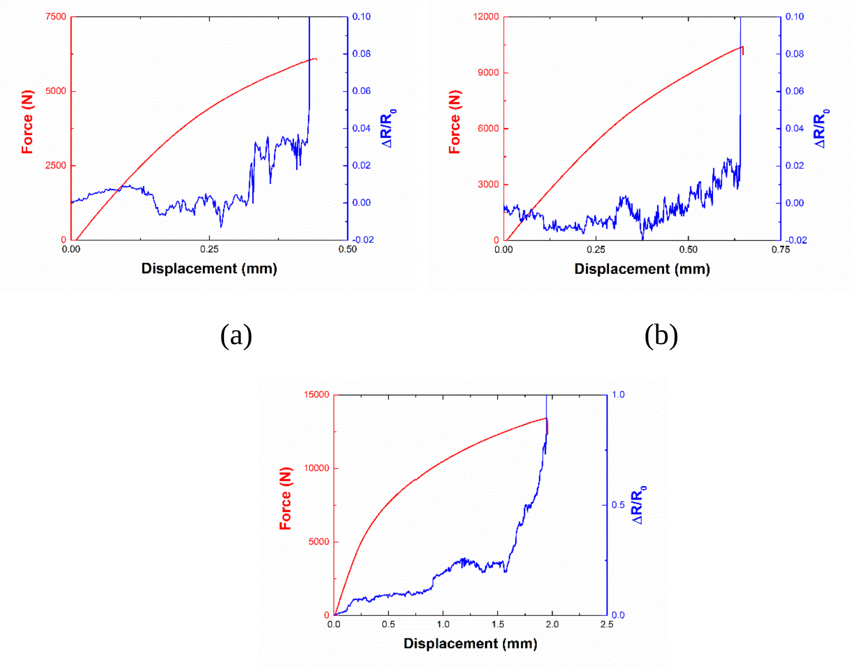

(a) (b)

(c)

Figure 13.47: Electrical response of Al-Al joints for (a) untreated, (b) B and (c) GB conditions.

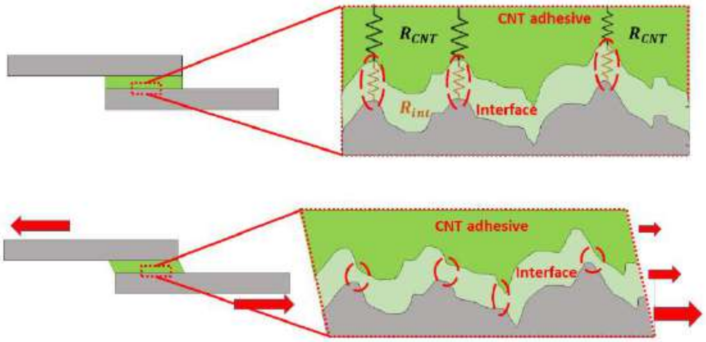

Figure 13.48: Schematics of creation and breakage of electrical pathways during a SLS test.

Dissimilar joints showed a similar electromechanical response (Figure 13.49) with a very unstable increase of the electrical resistance in the brushed condition, where a mixed cohesive-adhesive failure was observed and a less noisy signal in case of GB condition, where a cohesive failure was found. Here, the effect of surface treatment is very similar that the previously observed in Al-Al joints with the respective creation and breakage of electrical pathways during the test. Therefore, the proposed technique can be useful to evaluate the quality of the interface in metal to metal and metal to CFRP SLS joints.

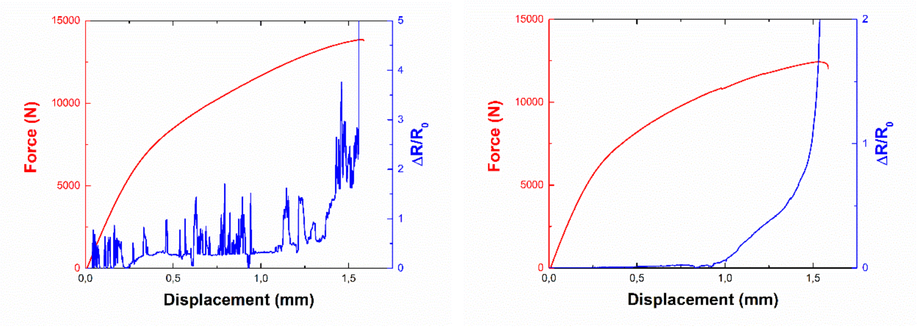

(a) (b)

Figure 13.49: Electrical response of CFRP-Al joints for (a) B and (b) GB conditions.

These results can be confirmed by analyzing the sensitivity during the SLS tests, which is defined as the change of the normalized resistance divided by the displacement. Here, the lowest sensitivities were obtained in those joints with a poor surface treatment due to the negative effect of continuous creation and breakage of electrical pathways. The highest sensitivities were achieved for the GB condition on dissimilar joint, which is in good agreement with the mechanical and microstructural results, showing the best performances in this case. Sensitivity is even higher than CFRP-CFRP despite its lower performance. It can be explained by the higher yielding effect of the Al substrate, leading to higher adhesive deformation and thus, a more prevalence on the tunneling resistance effect.

SEM images of the transversal section showed a good adhesive distribution through the joint. Brushed samples showed the presence of smooth surfaces (Figure 13.50 (a) and (b)) in combination with some abrasion peaks (Figure 13.50 (c)), leading to a more irregular roughness distribution. In addition to that, some samples showed interface defects and discontinuities (Figure 13.50 (d)) due to poorer adhesion properties between the adhesive and substrate. However, GB conditions showed a uniform distribution of substrate roughness (Figure 13.50 (e) and (f)) due to a more strict control of the processing parameters. This would explain the poorer performance of the brushed joints when comparing to grit-blasting. In case of CFRP samples, the typical globular roughness of pee-ply treatment is observed with no presence of discontinuities or interface defects (Figure 13.50 (g) and (h)). That implies a good adhesion between substrate and adhesive, leading to better mechanical properties. Thus, it can be concluded that surface treatment has a prevalent effect on mechanical and electrical properties of the bonded joints, being necessary an optimum roughness distribution on the adherent surface to achieve the best mechanical performances.

Therefore, SHM applicability of the proposed technique has been widely proved in joints of dissimilar materials. However, as mentioned before, the aim of the work is the applicability of the proposed CNT adhesive film in structural applications. Therefore, once analyzed and demonstrated their SHM capabilities as well as their good mechanical properties at coupon level, several tests at skin-stringer sub-elements will be carried out to explore the actual potential of the proposed techniques.

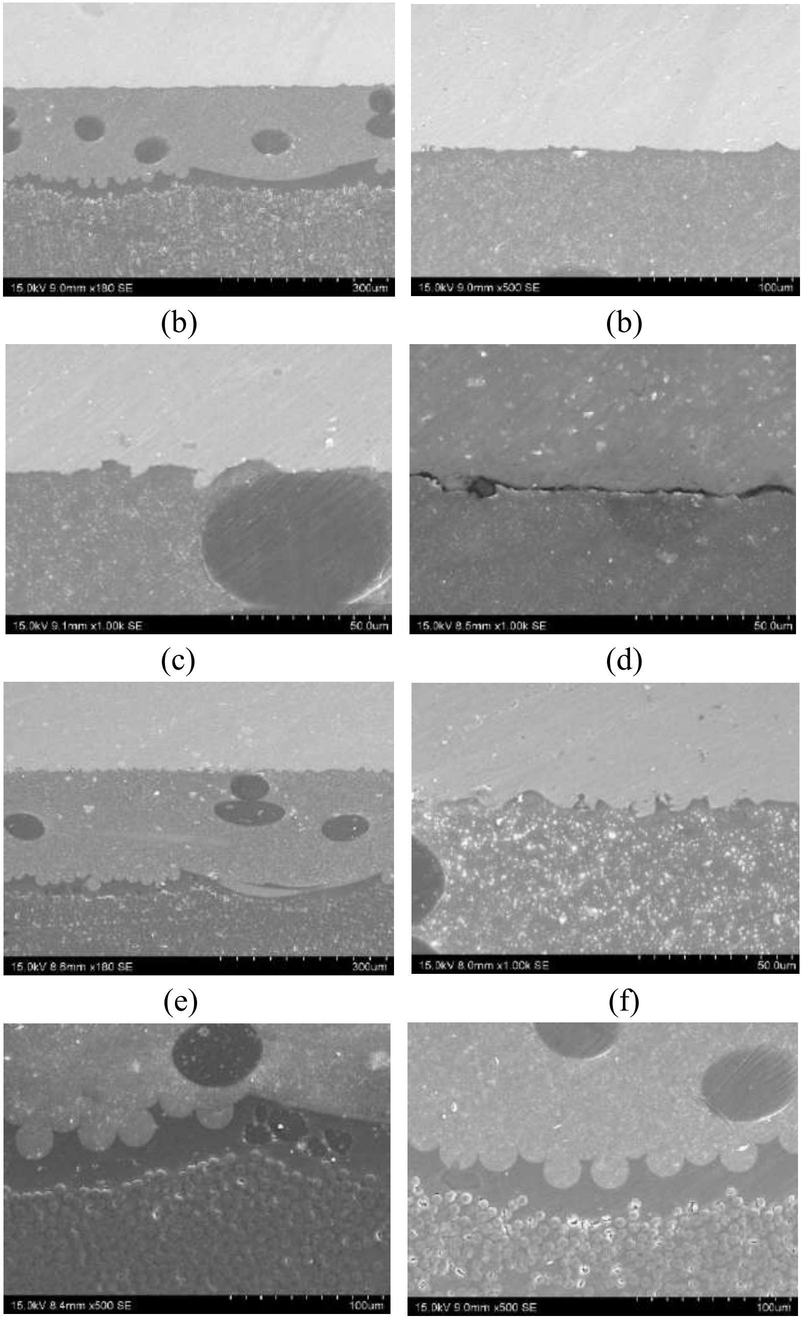

(b) (b)

(c) (d)

(e) (f)

(g) (h)

Figure 13.50: SEM images of transversal section showing (a-d) B condition, (e,f) GB condition and (g,h) peel-ply treatment.

13.3 Skin-stringer sub-elements

Skin-stringer sub-elements have been manufactured by two different techniques, as mentioned in Methods section: co-bonding and secondary bonding. Co-bonding is defined as the process of joining a pre-cured substrate to an uncured one while on secondary bonding, both substrates are precured. In the first case, curing cycle is determined by the curing characteristics of substrates while in the second one, curing cycle is given by the adhesive, which is the only non-cured element.

To demonstrate SHM capabilities of CNT adhesive films, skin-stringer sub-elements were tested under two different load conditions: peeling and bending, similar to Mode-I and Mode-II tests at coupon level, respectively. Although the first one is not a realistic scenario of loading type for skin-stringer elements, it is very useful to observe the crack propagation monitoring capabilities of the proposed adhesives. The second one is more realistic and complex failure mode and is useful to go further on SHM applicability.

13.3.1 Crack propagation monitoring at peeling tests

Several skin-stringer sub-elements were subjected to peeling conditions. The load was applied at the end of the stringer element while the skin was clamped. The aim is to observe the evolution of the electrical response with crack propagation and compare it with the electromechanical behavior on Mode-I coupons to demonstrate the robustness of the method.

It was observed that electrical resistance increases during the peeling test (Figure 13.51) as expected due to crack propagation and, thus, breakage of electrical pathways. In a similar way than Mode-I coupon testing, there is a slight increase of the electrical resistance due to adhesive deformation in the region where crack starts to propagate. Then, a sharp increase is observed, corresponding to a sudden drop of the mechanical load and, thus, a rapid crack propagation inside the joint. After that, a more stable increase of the electrical resistance is observed due to a slower and more stable crack propagation as noticed also in the mechanical response.

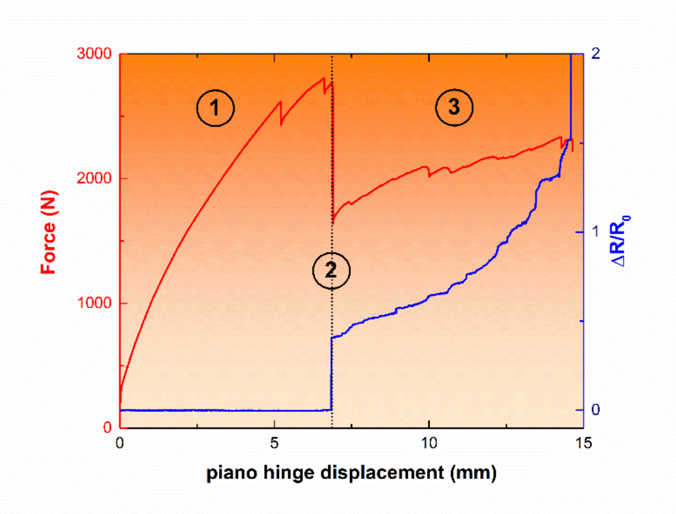

Figure 13.51: An example of electromechanical response on skin-stringer sub-elements subjected to peeling load where 1 denotes the first stages, 2 the sudden initial crack propagation and 3 the crack evolution during the test.

The main difference with Mode-I coupon tests is the way in which crack propagates inside the joint. In the first case, the crack front is almost straight and perpendicular to the crack propagation. However, in case of skin-stringer sub-elements, as not initial Teflon insert is placed, crack propagation is more complex. Due to a higher stress concentration in the edges of the joint [157], the crack initiates in this area. Then, it starts to propagate inside the joint through the central region of the stringer. Depending on the joint strength and loading conditions, there can be an opening of the crack in the area where the load is applied and then a propagation similar to Mode-I coupon tests (Figure 13.52 (a)) or the crack can propagate through the whole stringer edges and then growing inside the joint until final failure (Figure 13.52 (b)).

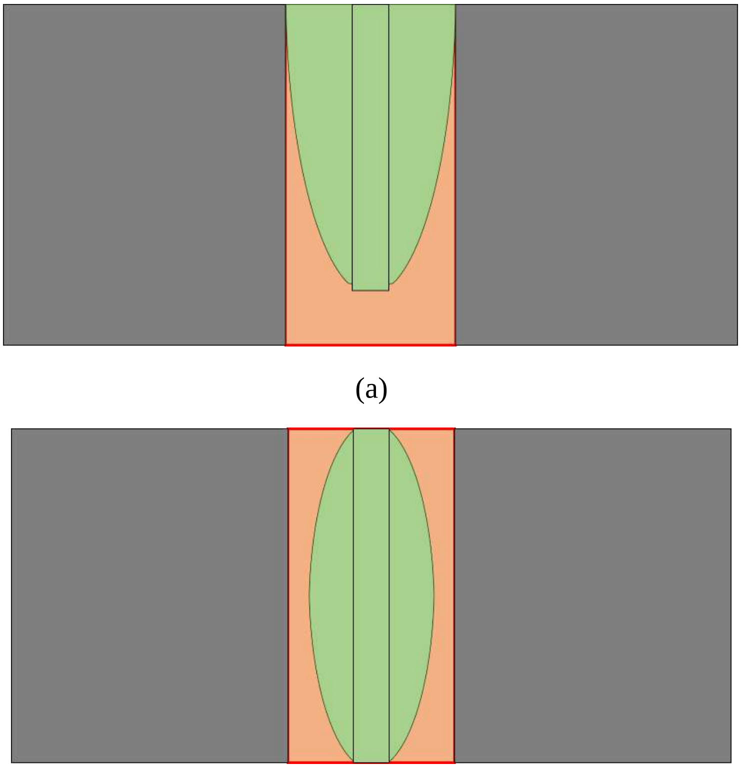

(a)

(b)

Figure 13.52: Crack propagation mechanisms in skin-stringer elements (a) in case of a Mode-I similar behavior and (b) crack propagation through the edges.

The different crack propagation mechanisms will affect, obviously, the electrical response during the peeling test. In this way, Figure 13.53 summarizes the electrical response correlated with crack propagation inside the joint for the different cases. The first one (Figure 13.53 (a)) shows an initial sharp increase of the electrical resistance. It corresponds to a region where crack propagates in a very sudden way. In fact, when observing the crack length measured during the test, it was observed that it propagates through the whole stringer length very rapidly, corresponding to the sudden drop in the mechanical response, then a softer evolution of the electrical resistance is observed as crack grows in a more uniform way. The second case (Figure 13.53 (b) and (c)) corresponds to a slower crack propagation through the edges. Here, a softer evolution of the electrical resistance is observed once crack starts to propagate. Then, depending on the failure mechanisms, a sharp increase of the electrical resistance can be observed if crack reaches the entire stringer length prior to failure (Figure 13.53 (b)), where a softer increase of the electrical resistance is noticed in the last stages of the test (Figure 13.53 (c)).

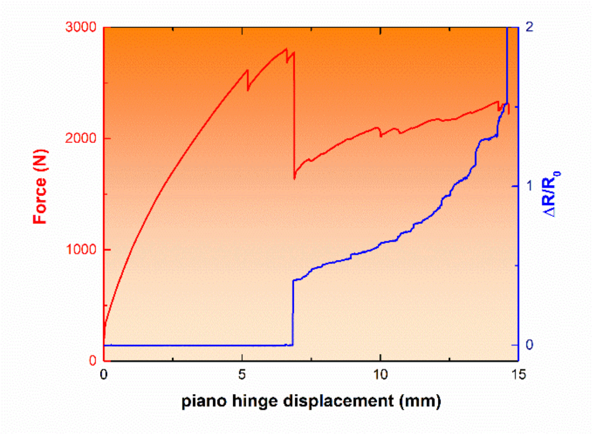

(a)

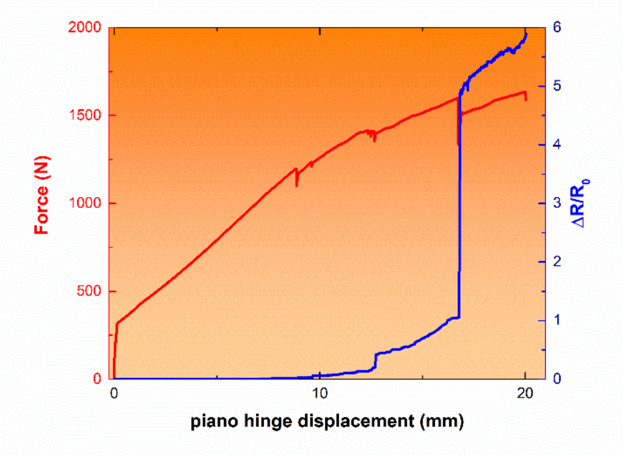

(b)

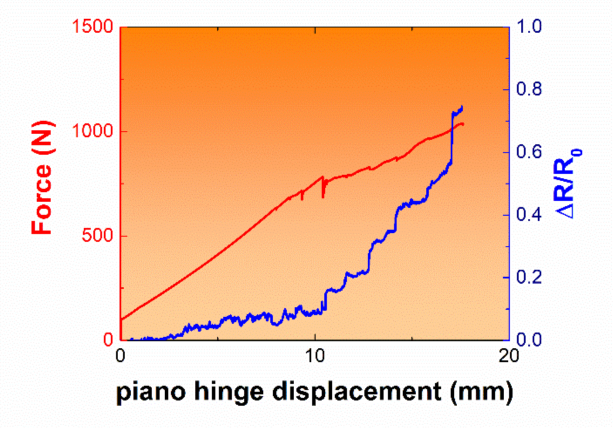

(c)

Figure 13.53: Electromechanical curves of skin-stringer elements indicating (a) a fast crack propagation through the edges, (b) a slower crack propagation when crack reaches and (c) does not reach the end of the stringer.

Therefore, electrical resistance monitoring is in a very good agreement with mechanical response and crack propagation mechanisms. In addition to that, as well as in Mode-I tests, some skin-stringer elements with artificial defects were also tested to corroborate the SHM potential of the proposed technique.

In this context, two types of artificial defects were induced: one with a liquid release agent and the other with a solid agent such as a Teflon insert, following the same pattern.

Electromechanical curves show an apparent similar behavior, but, by in detail analyzing them, some slight differences can be observed. Electrical response of the liquid agent damaged specimen shows a more uniform behavior (Figure 13.54 (a)) than Teflon insert one (Figure 13.54 (b)). This is explained by the interfacial strength and the way in which crack propagates in both cases.

The liquid agent does not induce a complete discontinuity in the interface between adhesive and substrate, it simulates a kissing bond, that is, a weak interface. However, Teflon inserts induces a total discontinuity in the adhesive joint, as shown in the damaged specimens of Mode-I and, thus, a total disruption of electrical pathways. Therefore, crack propagation is softer in the case of liquid release agent, as also observed in other studies [109]. Thus, this is reflected in a sharper and more unstable electrical response for the Teflon specimen. By deeply analyzing the electromechanical curves, an excellent agreement between the electrical and mechanical response is observed, which each drop of the mechanical load corresponding to a sharp increase of the electrical resistance.

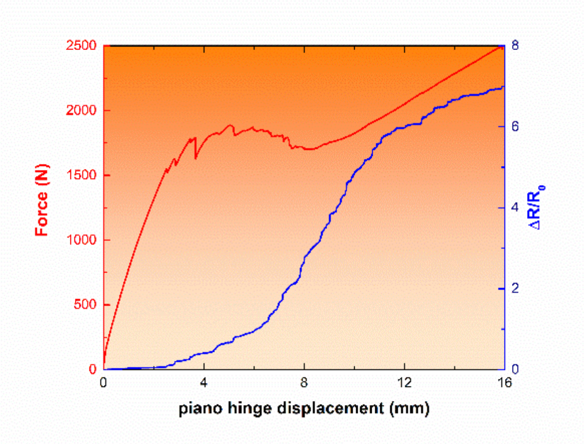

(a)

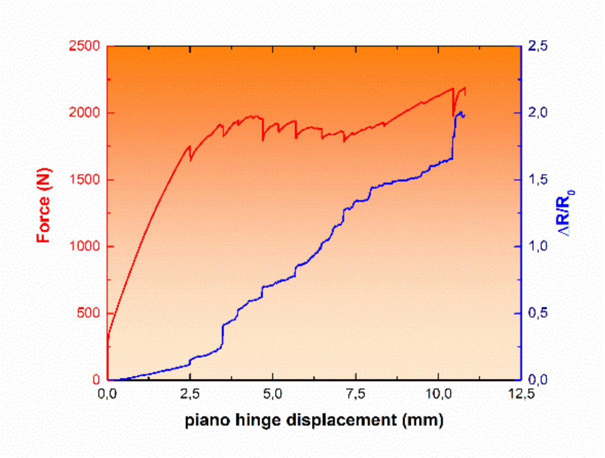

(b)

Figure 13.54: Electromechanical response of (a) liquid agent and (b) Teflon insert skin-stringer specimens.

The analysis of the fracture surfaces of skin-stringer elements reveals the main crack propagation mechanisms until final failure in a similar way than observed before for fatigue testing, which a mainly crack propagation thorugh the edges of the stringer as shown in the schematics of Figure 13.52. They showed a mainly cohesive failure for most of conditions although mixed adhesive-cohesive failures were also observed in some elements.

In addition to that, the results of the proposed technique were compared to other SHM available methods, such as AU guided waves and Electromechanical Impedance (EIM) technique. The aim was to evaluate the main advantages of CNT adhesive when comparing to these methods, as well as to have a double checked with different SHM techniques. These tests were conducted during a research stay at Universität Siegen and the results were presented and published in the EWSHM 2018 conference proceedings.

As commented in Methods section, one actuator and two sensors were placed in the skin-stringer elements: the actuator was placed in the skin while the two sensors were placed in both skin, making the skin-skin channel and stringer web region, making the skin-stringer channel. Figure 13.55 shows a waterfall diagram of the AU response in both the skin-skin (a) and stringer-skin (b) channels. It is observed that the signal amplitude increases through the peeling test in the skin-skin, while it decreases in the skin-stringer channel. It means that when crack reaches a propagation path between sensor and actuator, there is a transfer of the energy amplitude. That happens in both channel seen in the first incoming bursts (red circle). A decrease is observed in the skin-stringer signal as there is no longer a direct path between the skin and the stringer. The opposite effect, therefore, takes place in the skin-skin channel, where a sudden increase of the energy amplitude is observed. The same effect occurs earlier (purple circle, crack starts growing) and later (green circle, crack length ≈ 100%) within the measurement).

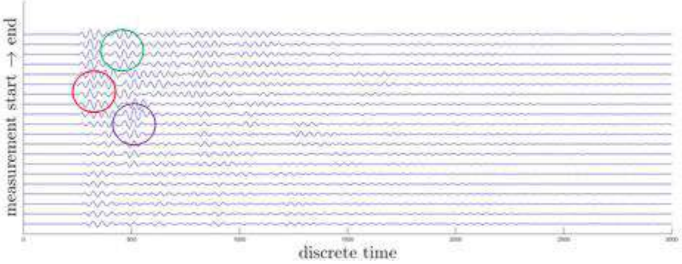

(a)

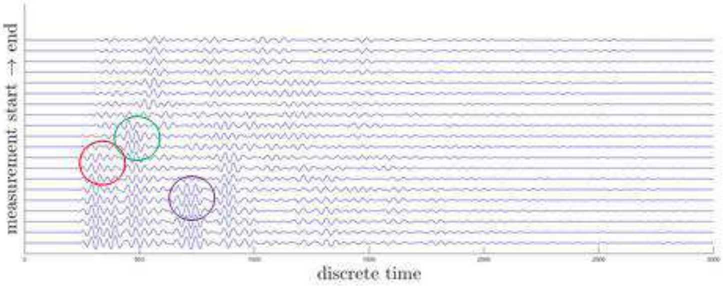

(b)

Figure 13.55: Waterfall diagram showing the evolution of the energy amplitude of AU system for (a) skin-skin and (b) skin-stringer wave propagation channels.

In the consideration of the signals under energetic aspects with progressive measuring duration, both sensors initially show a drop in the energy in the signal, as shown in Figure 13.56. This effect can be attributed to the deflection of the plate. When the crack propagation reaches approximately 30%, a change in the behavior of the signals-energy curves shows up, in a similar way to the waterfall diagrams and a crack propagation becomes recognizable.

The AU-system can detect the crack, by the change of the energy-flow, at approximately 45mm. In this context, the overlap between the deflection of the plate and crack propagation makes it difficult to detect crack initiation and it is only possible to detect extensive damage.

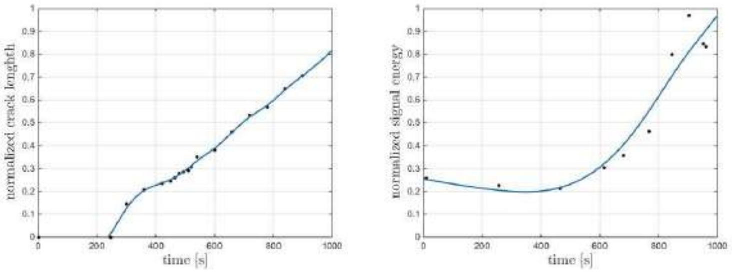

(a) (b)

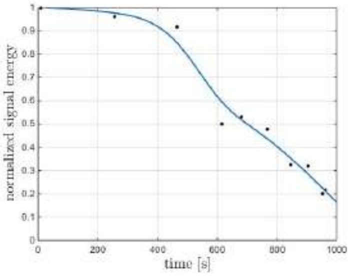

(c)

Figure 13.56: Trajectories of the (a) crack propagation and the energy levels of the (b) skin-skin and (c) skin-stringer signals (right).

Concerning EMI measurements, the complex electrical admittance of the piezoelectric transducer, which is the inverse of the electro-mechanical impedance, depends on mechanical impedance of the monitored structure and the piezoelectric transducer. Accordingly, Figure 13.57 shows the susceptance as a function of the frequency at different moments of the peeling tests. Therefore, the changes in the mechanial performance of the sub-elements would result in changes in the susceptance as observed in Figure 13.57. However, these changes are not so prevalent. Only small shifts and changing amplitudes can be seen in the first resonance/antiresonance range. While the specimen is subjected to the load, no change in the signal is seen (comparison baseline to start) as desired, since crack propagation can be observed without cross-sensitivities to loadings. Nevertheless, the resolution of crack propagation seems to be low since we investigate first changes after the 13th measure, being these changes constant until the end of the test.

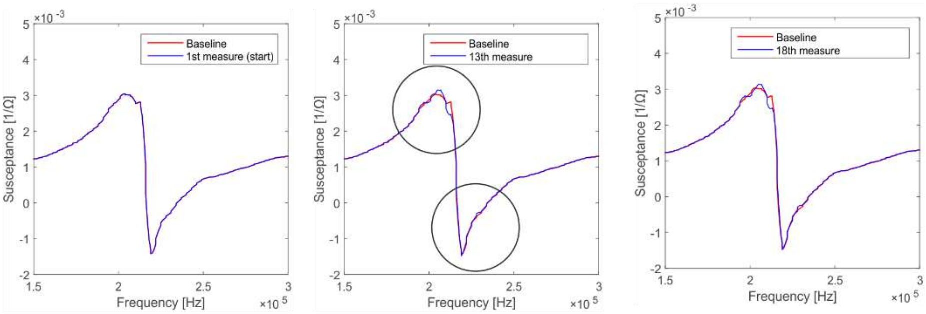

Figure 13.57: EMI measurements with time indicating the variation of susceptance with crack length.

Therefore, the SHM capabilities of the proposed technique seems to be very promising, with a much higher sensitivity and detectability of crack propagation mechanisms in skin-stringer sub-elements than AU and EIM techniques. Proven that, skin-stringer sub-elements were also tested under more complex load conditions such as bending, in a similar way than Mode-II coupon tests.

13.3.2 SHM of skin-stringer elements under bending load

Skin-stringer elements were subjected to bending load to further explore on SHM capabilities of the proposed adhesive films. In this case, a pre-crack was initiated near the edge of the stringer through the whole joint, as explained before in Methods section. This experimental configuration was set-up based in other research [160].

Electrical response of skin-stringer sub-elements, shown in Figure 13.58, is similar to that observed in Mode-II coupons. An increase of electrical resistance with displacement is observed. However, some differences can be noticed. The first one is the crack propagation mechanisms taking place in the skin-stringer elements. In fact, the change of the normalized resistance when the crack reaches the middle point of the stringer is about 20 %, similar to that previously obtained for Mode-II specimens. As mentioned before, in Mode-II coupons, adhesive is place near the neutral axis, that is, the adhesive deformation can be neglected and, thus, the electrical response depends mainly on breakage of electrical pathways due to crack propagation. In addition, there is not crack opening effect due to the slippage of adherents during the test, leading to lower sensitivities than Mode-I testing. However, the mechanisms in skin-stringer elements are slightly different.

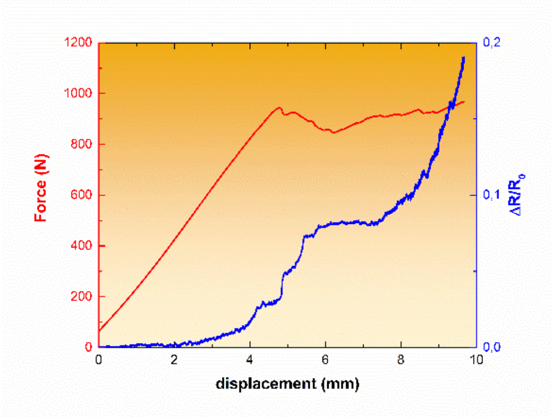

Figure 13.58: Electrical response as a function of applied mechanical load.

Here, there are two opposite effects: on the one side, the adhesive is not placed in the neutral axis, as the skin thickness is lower than stringer. Therefore, there are compression effects inside the joint, leading to a decrease of the electrical resistance [147]. On the other side, there is a much more significant crack opening effect, due to the separation of skin and stringer, as shown in the schematics of Figure 13.59, leading, thus, to a more prevalent increase of the electrical response due to this effect. The combination of these two effects leads to a similar sensitivity than those previously observed for Mode-I coupon tests.

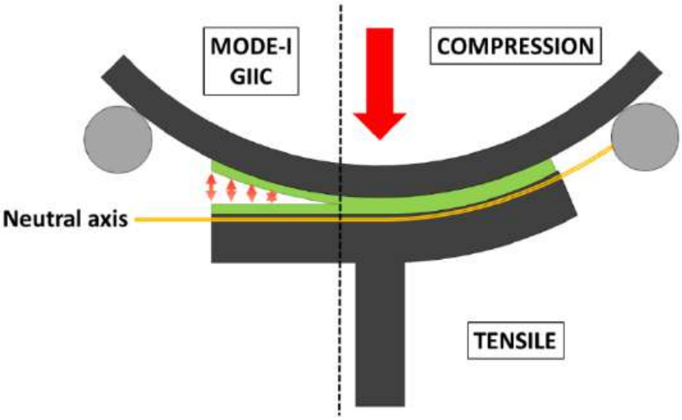

Figure 13.59: Schematics of crack growth during Mode-II skin-stringer tests.

Moreover, when observing the electrical response as a function of the crack length (Figure 13.60 (a)), there are also some differences with Mode-II samples. Here, the crack propagation velocity is less uniform, showing an increase up to a maximum in the initial stages of the crack propagation and then a decrease until it reaches the middle point (Figure 13.60 (b)). These differences are attributed to a more complex strain field in this type of specimen so a deeper analysis would be necessary.

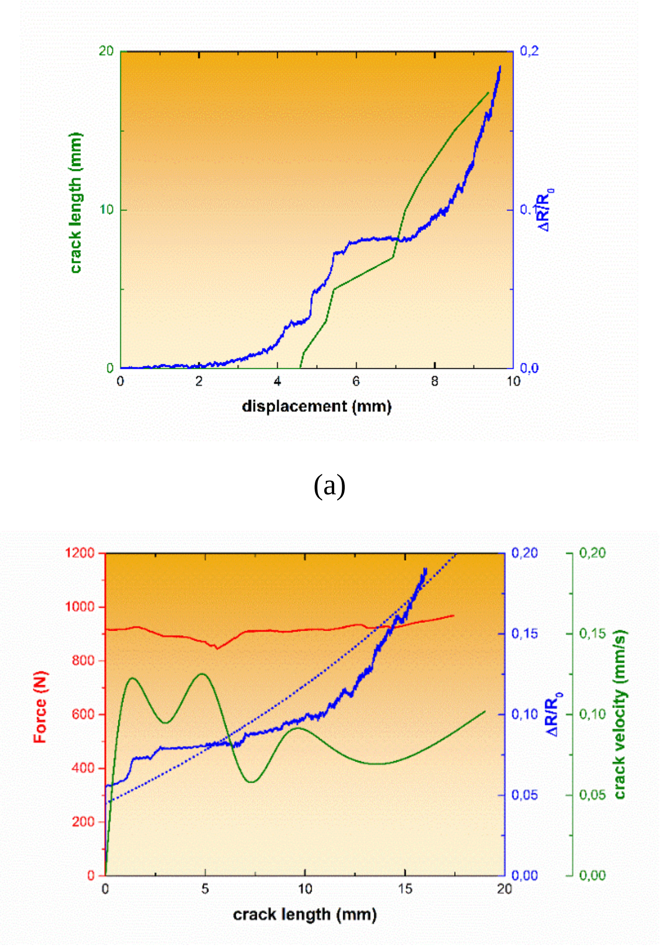

(a)

(b)

Figure 13.60: Electrical response of Mode-II skin-stringer elements (a) as a function of crack length and (b) crack propagation velocity.

The analysis of fracture surfaces showed a mainly cohesive failure with a uniform adhesive distribution and no presence of stick-slip patterns, being in good agreement with the electrical response. SEM images of the transversal sections showed the typical globular roughness due to peel-ply treatment in the stringer side. However, the adhesive thickness is not constant through the whole joint. This is explained by the stringer effect during curing, as shown in the schematics of Figure 13.61. In fact, the stringer region (Figure 13.62 (a) and (b)) shows a lower thickness than the web region (Figure 13.62 (c) and (d)). This would explain the sharper increase of the electrical resistance in the last stages of the monitoring tests, due to a breakage of more prevalent electrical pathways in the stringer region. In addition to that, some defects can be also observed such as localized porosity (Figure 13.62 (e)) or lack of adhesive due to the low curing pressure, inducing a poor adhesive compaction. Moreover, the crack bridging effect can be observed near the crack end in the middle point of T-stringer (Figure 13.62 (f)).

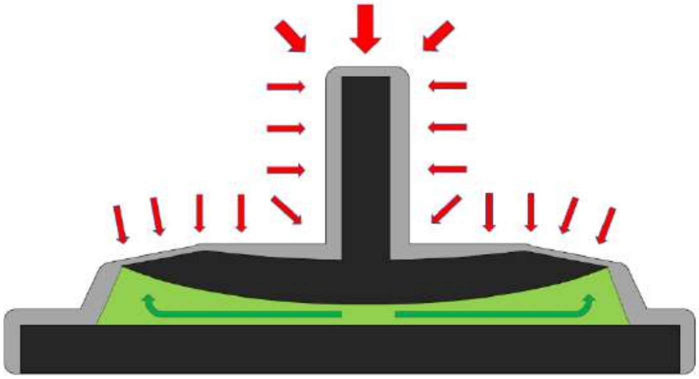

Figure 13.61: Schematics of pressure distribution during curing.

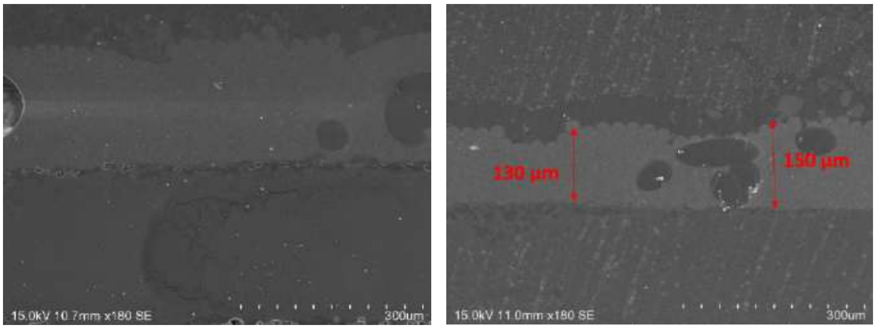

(a) (b)

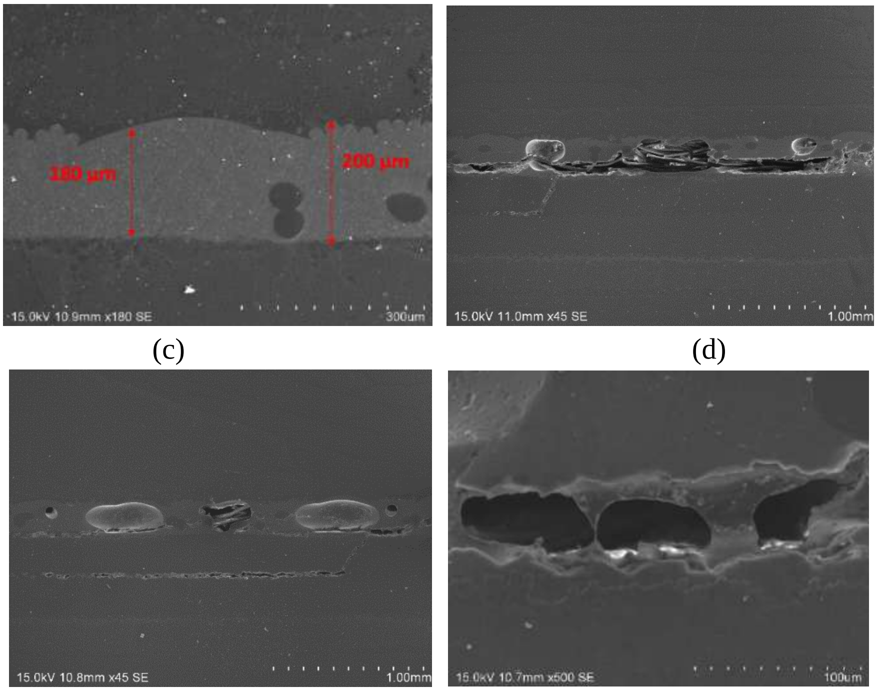

(c) (d)

(e) (f)

Figure 13.62: SEM images of transversal sections of (a,b) T-stringer region, (c,d) web region and (e) showing the crack propagation and (f) bridging effect.

The measured electrical response, as well as the good agreement with mechanical behavior, proves the excellent capabilities of the proposed adhesive films for crack propagation monitoring in skin-stringer sub-elements even in a more complex load state.

Therefore, from coupon and sub-element test, SHM capabilities of the CNT adhesive films have been widely demonstrated. They have proved to be a good alternative to other NDT and SHM techniques such as guided waves or electromechanical impedances for bonded joints without suffering any significant detriment on their mechanical properties.

CHAPTER 14-15: CONCLUSIONS & FUTURE WORK

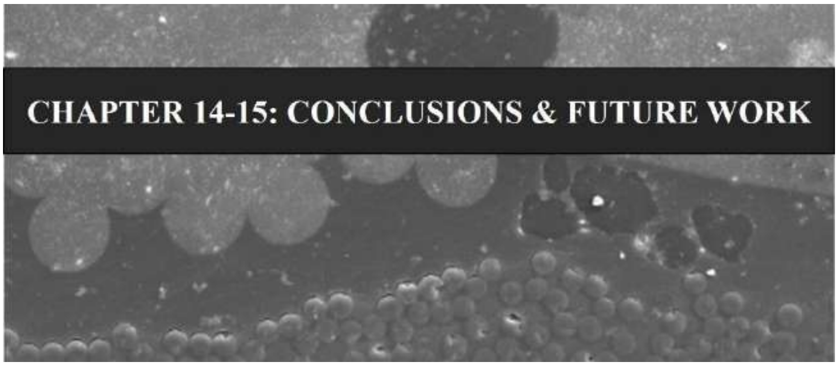

Chapter 14: Conclusions

Electromechanical and sensing capabilities of CNT/epoxy composites have been widely investigated in the present study. First, a theoretical model analyzing the influence of dispersion technique on sensitivity of CNT doped nanocomposites has been proposed. Then, a practical application on adhesive joints for monitoring the health of a structure has been widely explored.

14.1 Electrical characterization of nanocomposites

From electromechanical point of view, several CNT nanocomposites were manufactured under different CNT loadings and dispersion procedures to deeply analyze the effect of dispersion technique and CNT distribution in the electrical properties of this type of materials. The main conclusions are stated as follows:

- Dispersion procedure plays a dominant role on electrical and sensing capabilities of CNT nanocomposites as it affects CNT distribution and, therefore, nanoparticle interactions inside the material.
- The influence of CNT geometry on electrical properties has been evaluated. An equivalent percolation threshold model has been proposed by taking CNT waviness into account. It was found that percolation threshold increases with CNT waviness due to a reduction in their effective aspect ratio.
- Waviness ratio was found to be higher for larger and amino-functionalized CNTs due to a larger distortion effects. In addition to that fact, a decrease of waviness was found in three roll milling

technique due to the stretching effect of shear forces involved during the dispersion procedure.

- Electromechanical sensitivity of CNT nanocomposites was studied by the definition of three dispersion parameters: the volume fraction of agglomerated CNTs, the well-dispersed one and non-percolated area, defining the dispersion state of the material.
- Inter-particle distance was determined as the average distance between adjacent particles based on the maximum package Van der Waals distance and percolating tunneling distance. It was found that there is an optimum value of Inter-particle distance where the highest sensitivity is achieved due to the combined effect of the aggregated to well-dispersed CNT regions.
- A better dispersion state leads to a higher GF due to the prevalence of tunneling mechanisms of well-dispersed area over the intrinsic non-variant mechanisms of aggregated CNTs. In this context, toroidal stirring was found to be a good dispersion procedure to achieve high GF due to a more prevalent homogenization effect induced by the 3D flow during dispersion.
- Electrical sensitivity of CNT strain gauges was found to be much higher than the equivalent bulk nanocomposites. This is explained by an increasing percolation threshold for 2D random distribution in comparison to 3D one, leading to higher values of tunneling distance and thus, a more prevalent exponential effect of the tunneling resistance. Electrical monitoring at bending load showed the relevance of compressive-tensile effects during loading leading to much lower values of sensitivity than at tensile testing.

Therefore, a complete understanding of the role of CNT geometry and distribution on electromechanical properties of nanocomposites has been achieved, allowing to select the optimum dispersion procedure depending on the desired behavior.

14.2 Crack propagation and sensing capabilities of CNT adhesive joints

SHM capabilities of CNT reinforced adhesive films were deeply investigated at coupon and skin-stringer sub-element level by exploring the mechanical and electrical properties of SLS, Mode-I and Mode-II under static and dynamic conditions. In this framework, the main conclusions are the following:

- A slight increase of the Lap Shear Strength was observed due to the strengthening effect of CNTs. The optimum surfactant condition was found at 0.25 wt. % where a good CNT dispersion is achieved without a detrimental mechanical effect of surfactant.
- Mode-I and Mode-II fracture energy were found to be slightly higher for CNT doped adhesive films due to the bridging and toughening effect of CNTs.
- Ageing tests revealed a similar behavior for neat and CNT doped adhesive joints. This is explained by the combination of two opposite effects: on the one side, the amphiphilic behavior of surfactant, leading to higher water uptake and, on the other side, the better barrier properties of CNTs leading to a lower water absorption
- Electrical resistance shows a pronounced exponential increase at Single Lap Shear tests due to the combined effect of tunneling resistance variation due to deformation and the breakage of electrical pathways because a catastrophic failure in the last stages of the test. In ageing tests, it is possible to make a first estimation about damage accumulation associated to a plasticization effect of epoxy resin by comparing the expected to the measured electrical response.
- A high sensitivity was observed for crack propagation in Mode-I and Mode-II tests. In fact, attending to electrical response, it is possible to distinguish between stick-slip behavior, where a sharper evolution of electrical resistance is observed and a more uniform crack propagation, where the electrical response is much more stable.
- Crack propagation capabilities under fatigue conditions were also demonstrated. A high repeatability among consecutive cycles was observed. By analyzing the whole fatigue testing, three regions of crack propagation can be distinguished attending the electrical response: a first one where there is a slight variation of the baseline due to crack and microcavities nucleation, a second one where crack starts to propagate and, thus, electrical base changes more prevalently and the last one, accordingly to crack propagation until failure, where a sharper increase of the electrical resistance is observed.
- SHM of skin-stringer elements showed a similar behavior than observed before at coupon level. At peeling test, an increase of the electrical resistance is observed accordingly to Mode-I crack propagation, with sharper increases corresponding to faster crack

propagation inside the joint. At bending loads, the electromechanical behavior was comparable to Mode-II crack propagation test.

- The comparison with other existing techniques such as guided waves and electromechanical impedance showed a higher sensitivity of the proposed CNT adhesive films for crack detection and monitoring.

Therefore, the proposed CNT doped adhesive film has demonstrated a huge potential and applicability for SHM applications on CFRP and metal-metal structures, addressing some of the main concerns of other available inspection techniques.

Chapter 15: Future works

In the light of the results of the present work, there are several lines of action that can be developed in the future. They can be divided in two main topics, in the same way that this Thesis: electrical modeling of nanocomposites and SHM of bonded joints. Some of them are now being investigated.

15.1 Electrical modeling of nanocomposites

i. Selection of an optimum dispersion technique based on the proposed model by exploring other methods such as sonication where a very good dispersion can be achieved.
ii. Adaptation of the model proposed for CNTs to 2D particles such as graphene or graphene nanoplatelets, where the tunneling mechanisms are slightly different.
iii. Modeling electrical properties of strain gauges by adapting the equivalent percolation model to a 2D random distribution
iv. Establishing a correlation between electrical and thermal properties of nanocomposites by proposing a novel model identifying the main conducting mechanisms. In this context, some studies are now being developed with promising results.
v. Exploring thermomechanical properties such as Joule effect for a better understanding between nanoparticle distribution and nanocomposite self-heating properties.

15.2 Reinforced adhesive films

i. A more detailed analysis of mechanical properties of CNT doped adhesive joints is needed. In this context, it is being deeply explored the influence of artificial defects and manufacturing processes on standard coupon properties.
ii. Studying the electromechanical properties of other conductive nanoparticles. In this regard, sensing and crack propafation monitoring capabilities of GNPs are now being explored due to their very high electrical sensitivity.
iii. Exploring joints with dissimilar materials at sub-element levels by combining a metal skin with a CFRP stringer and vice-versa to deeply analyze their electromechanical properties.
iv. Investigating fatigue capabilities at Mode-I and Mode-II load states as well as at sub-element level. In this context, a new collaboration with Politecnico di Milano is being explored.
v. Studying monitoring capabilities at a component level, such as an stiffened panel or even a torsion box. The aim will be to demonstrate SHM capabilities of this type of adhesive films in a real structure. Now, these capabilities are being investigated within the framework of *Fuselage* program, a collaboration with Airbus.
vi. Analyzing the possibility of applying this type of material to other structures such as sandwich panels, where the assessment of defects is very critical.

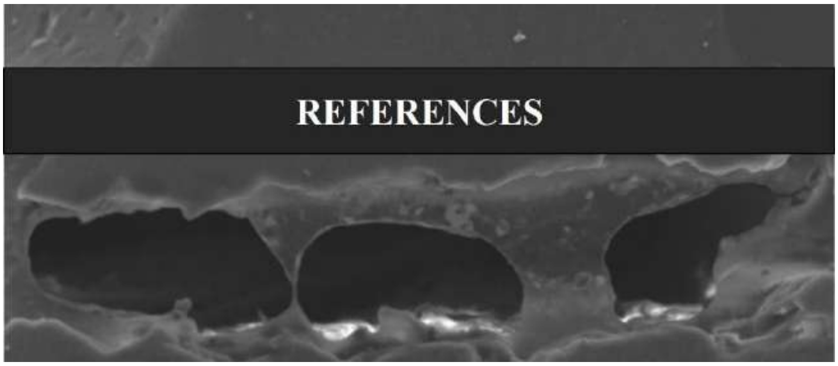

REFERENCES

References

[1] Peters ST. Handbook of composites. 2013.

[2] Taub AI, Krajewski PE, Luo AA, Owens JN. The evolution of technology for materials processing over the last 50 years: The automotive example. JOM 2007;59(2):48-57.

[3] Mangino E, Carruthers J, Pitarresi G. The future use of structural composite materials in the automotive industry. Int J Veh Des 2007;44(3-4):211-232.

[4] Garces JM, Moll DJ, Bicerano J, Fibiger R, McLeod DG. Polymeric nanocomposites for automotive applications. Adv Mater 2000;12(23):1835-1839.

[5] Shanyi D. Advanced composite materials and aerospace engineering [J]. Acta Materiae Compositae Sinica 2007;1:000.

[6] Grimshaw MN, Grant CG, Diaz JML. Advanced technology tape laying for affordable manufacturing of large composite structures. 2001:2484-2494.

[7] Lubin G. Handbook of composites. 2013.

[8] Miller TC, Chajes MJ, Mertz DR, Hastings JN. Strengthening of a steel bridge girder using CFRP plates. J Bridge Eng 2001;6(6):514-522.

[9] Schnerch D, Rizkalla S. Flexural strengthening of steel bridges with high modulus CFRP strips. J Bridge Eng 2008;13(2):192-201.

[10] Daniel IM, Ishai O, Daniel IM, Daniel I. Engineering mechanics of composite materials. 1994;3.

[11] Hussey R, Wilson J. Structural Adhesives: Directory and Databook. 1996.

[12] Sorrentino L, Polini W, Bellini C, Parodo G. Surface treatment of CFRP: influence on single lap joint performances. International Journal of Adhesion and Adhesives 2018;85:225-233.

[13] Prolongo S, Gude M, Del Rosario G, Ureña A. Surface pretreatments for composite joints: study of surface profile by SEM image analysis. J Adhes Sci Technol 2010;24(11-12):1855-1867.

[14] Johnson WS, Butkus LM. Designing for the durability of bonded structures. 1996;1:147-160.

[15] Davis M, Bond D. Principles and practices of adhesive bonded structural joints and repairs. International Journal of Adhesion and Adhesives 1999;19(2):91-105.

[16] Abbott S. Adhesion science: principles and practice. 2015.

[17] Elhannani M, Madani K, Legrand E, Touzain S, Feaugas X. Numerical analysis of the effect of the presence, number and shape of bonding defect on the shear stresses distribution in an adhesive layer for the single-lap bonded joint; Part 1. Aerospace Science and Technology 2017;62:122-135.

[18] Elhannani M, Madani K, Chama Z, Legrand E, Touzain S, Feaugas X. Influence of the presence of defects on the adhesive layer for the single-lap bonded joint—Part II: Probabilistic assessment of the critical state. Aerospace Science and Technology 2017;63:372-386.

[19] Trask RS, Hallett SR, Helenon FMM, Wisnom MR. Influence of process induced defects on the failure of composite T-joint specimens. Composites Part A: Applied Science and Manufacturing 2012;43(4):748-757.

[20] Heidarpour F, Farahani M, Ghabezi P. Experimental investigation of the effects of adhesive defects on the single lap joint strength. Int J Adhes Adhes 2018;80:128-132.

[21] Ribeiro FMF, Campilho RDSG, Carbas RJC, da Silva LFM. Strength and damage growth in composite bonded joints with defects. Composites Part B: Engineering 2016;100:91-100.

[22] Balageas D. Introduction to structural health monitoring. Structural health monitoring 2006:13-43.

[23] Chandrasekaran S, Chitambaram T. Health monitoring of offshore structures using wireless sensor network: experimental investigations. 2016;9804:980416.

[24] Ho D, Lee P, Nguyen K, Hong D, Lee S, Kim J, Shin S, Yun C, Shinozuka M. Solar-powered multi-scale sensor node on Imote2 platform for

hybrid SHM in cable-stayed bridge. Smart Structures and Systems 2012;9(2):145-164.

[25] Ramos LF, Masciotta M, Lourenço PB, Vasta M. SHM of a Masonry Chimney after a Lightning Accident. 2013:740-747.

[26] Rytter A. Vibrational based inspection of civil engineering structures 1993.

[27] Speckmann H, Henrich R. Structural Health Monitoring (SHM)-Overview on Airbus Activities. WCNDT, Aug 2004.

[28] Bernasconi A, Carboni M, Comolli L. Monitoring of fatigue crack growth in composite adhesively bonded joints using fiber Bragg gratings. Procedia Engineering 2011;10:207-212.

[29] Frieden J, Cugnoni J, Botsis J, Gmuer T. Low energy impact damage monitoring of composites using dynamic strain signals from FBG sensors - Part I: Impact detection and localization. Composite Structures 2012;94(2):438-445.

[30] Frieden J, Cugnoni J, Botsis J, Gmür T. Low energy impact damage monitoring of composites using dynamic strain signals from FBG sensors–Part II: Damage identification. Composite Structures 2012;94(2):593-600.

[31] Riccio A, Di Caprio F, Camerlingo F, Scaramuzzino F, Gambino B. Positioning of Embedded Optical Fibres Sensors for the Monitoring of Buckling in Stiffened Composite Panels. Applied Composite Materials 2013;20(1):73-86.

[32] Minakuchi S, Takeda N, Takeda S, Nagao Y, Franceschetti A, Liu X. Life cycle monitoring of large-scale CFRP VARTM structure by fiber-optic-based distributed sensing. Composites Part A: Applied Science and Manufacturing 2011;42(6):669-676.

[33] Sierra-Pérez J, Torres-Arredondo MA, Güemes A. Damage and nonlinearities detection in wind turbine blades based on strain field pattern recognition. FBGs, OBR and strain gauges comparison. Composite Structures 2016;135:156-166.

[34] Sherafat MH, Guitel R, Quaegebeur N, Hubert P, Lessard L, Masson P. Structural health monitoring of a composite skin-stringer assembly using within-the-bond strategy of guided wave propagation. Mater Des 2016;90:787-794.

[35] Giurgiutiu V. Lamb wave generation with piezoelectric wafer active sensors for structural health monitoring. Smart Structures and Materials 2003 2003;5056:111-122.

[36] Su Z, Ye L, Lu Y. Guided Lamb waves for identification of damage in composite structures: A review. Journal of Sound and Vibration 2006;295(3):753-780.

[37] Rose JL. The upcoming revolution in ultrasonic guided waves. 2011;7983:798302.

[38] Crawford A, Droubi MG, Faisal NH. Analysis of Acoustic Emission Propagation in Metal-to-Metal Adhesively Bonded Joints. J Nondestr Eval 2018;37(2):33.

[39] Di Sante R. Fibre optic sensors for structural health monitoring of aircraft composite structures: Recent advances and applications. Sensors 2015;15(8):18666-18713.

[40] Ladpli P, Kopsaftopoulos F, Chang F. Estimating state of charge and health of lithium-ion batteries with guided waves using built-in piezoelectric sensors/actuators. Journal of Power Sources 2018;384:342-354.

[41] Iijima S. Helical Microtubules of Graphitic Carbon. Nature 1991;354(6348):56-58.

[42] Popov VN. Carbon nanotubes: properties and application. Materials Science and Engineering: R: Reports 2004;43(3):61-102.

[43] Jacobsen R, Tritt T, Guth J, Ehrlich A, Gillespie D. Mechanical properties of vapor-grown carbon fiber. Carbon 1995;33(9):1217-1221.

[44] Wong EW, Sheehan PE, Lieber CM. Nanobeam mechanics: Elasticity, strength, and toughness of nanorods and nanotubes. Science 1997;277(5334):1971-1975.

[45] Yu MF, Lourie O, Dyer MJ, Moloni K, Kelly TF, Ruoff RS. Strength and breaking mechanism of multiwalled carbon nanotubes under tensile load. Science 2000;287(5453):637-640.

[46] Kim P, Shi L, Majumdar A, McEuen PL. Thermal transport measurements of individual multiwalled nanotubes. Phys Rev Lett 2001;87(21):215502.

[47] Gojny F, Wichmann M, Köpke U, Fiedler B, Schulte K. Carbon nanotube-reinforced epoxy-composites: enhanced stiffness and fracture toughness at low nanotube content. Composites Sci Technol 2004;64(15):2363-2371.

[48] Gojny FH, Wichmann MH, Fiedler B, Schulte K. Influence of different carbon nanotubes on the mechanical properties of epoxy matrix composites–a comparative study. Composites Sci Technol 2005;65(15-16):2300-2313.

[49] Wichmann MH, Sumfleth J, Gojny FH, Quaresimin M, Fiedler B, Schulte K. Glass-fibre-reinforced composites with enhanced mechanical and electrical properties–benefits and limitations of a nanoparticle modified matrix. Eng Fract Mech 2006;73(16):2346-2359.

[50] Davis DC, Wilkerson JW, Zhu J, Ayewah DO. Improvements in mechanical properties of a carbon fiber epoxy composite using nanotube science and technology. Composite Structures 2010;92(11):2653-2662.

[51] Young RJ, Kinloch IA, Gong L, Novoselov KS. The mechanics of graphene nanocomposites: A review. Composites Sci Technol 2012;72(12):1459-1476.

[52] Jimenez-Suarez A, Campo M, Sanchez M, Romon C, Urena A. Influence of the functionalization of carbon nanotubes on calendering dispersion effectiveness in a low viscosity resin for VARIM processes. Composites Part B-Engineering 2012;43(8):3482-3490.

[53] Jiménez-Suárez A, Campo M, Gaztelumendi I, Markaide N, Sánchez M, Ureña A. The influence of mechanical dispersion of MWCNT in epoxy matrix by calendering method: Batch method versus time controlled. Composites Part B: Engineering 2013;48:88-94.

[54] Chapartegui M, Markaide N, Florez S, Elizetxea C, Fernandez M, Santamaria A. Curing of epoxy/carbon nanotubes physical networks. Polym Eng Sci 2012;52(3):663-670.

[55] Aravand M, Lomov SV, Verpoest I, Gorbatikh L. Evolution of carbon nanotube dispersion in preparation of epoxy-based composites: From a masterbatch to a nanocomposite. Express Polymer Letters 2014;8(8):596-608.

[56] Ahmadi-Moghadam B, Taheri F. Effect of processing parameters on the structure and multi-functional performance of epoxy/GNP-nanocomposites. J Mater Sci 2014;49(18):6180-6190.

[57] Hennrich F, Krupke R, Arnold K, Stuetz JAR, Lebedkin S, Koch T, Schimmel T, Kappes MM. The mechanism of cavitation-induced scission of single-walled carbon nanotubes. J Phys Chem B 2007;111(8):1932-1937.

[58] Pagani G, Green MJ, Poulin P, Pasquali M. Competing mechanisms and scaling laws for carbon nanotube scission by ultrasonication. Proc Natl Acad Sci U S A 2012;109(29):11599-11604.

[59] Huang YY, Terentjev EM. Dispersion of Carbon Nanotubes: Mixing, Sonication, Stabilization, and Composite Properties. Polymers 2012;4(1):275-295.

[60] Moriche R, Prolongo SG, Sánchez M, Jiménez-Suárez A, Sayagués MJ, Ureña A. Morphological changes on graphene nanoplatelets induced during dispersion into an epoxy resin by different methods. Composites Part B: Engineering 2015;72:199-205.

[61] Moisala A, Li Q, Kinloch I, Windle A. Thermal and electrical conductivity of single-and multi-walled carbon nanotube-epoxy composites. Composites Sci Technol 2006;66(10):1285-1288.

[62] Allaoui A, Bai S, Cheng H, Bai J. Mechanical and electrical properties of a MWNT/epoxy composite. Composites Sci Technol 2002;62(15):1993-1998.

[63] Martin C, Sandler J, Windle A, Schwarz M, Bauhofer W, Schulte K, Shaffer M. Electric field-induced aligned multi-wall carbon nanotube networks in epoxy composites. Polymer 2005;46(3):877-886.

[64] Potts JR, Dreyer DR, Bielawski CW, Ruoff RS. Graphene-based polymer nanocomposites. Polymer 2011;52(1):5-25.

[65] Ghaleb Z, Mariatti M, Ariff Z. Properties of graphene nanopowder and multi-walled carbon nanotube-filled epoxy thin-film nanocomposites for electronic applications: the effect of sonication time and filler loading. Composites Part A: Applied Science and Manufacturing 2014;58:77-83.

[66] Prolongo S, Moriche R, Jiménez-Suárez A, Sánchez M, Ureña A. Advantages and disadvantages of the addition of graphene nanoplatelets to epoxy resins. European Polymer Journal 2014;61:206-214.

[67] Bauhofer W, Kovacs JZ. A review and analysis of electrical percolation in carbon nanotube polymer composites. Composites Sci Technol 2009;69(10):1486-1498.

[68] Sandler J, Kirk J, Kinloch I, Shaffer M, Windle A. Ultra-low electrical percolation threshold in carbon-nanotube-epoxy composites. Polymer 2003;44(19):5893-5899.

[69] Hu N, Masuda Z, Fukunaga H. Prediction of electrical conductivity of polymer filled by carbon nanotubes. 2007.

[70] Yu A, Itkis ME, Bekyarova E, Haddon RC. Effect of single-walled carbon nanotube purity on the thermal conductivity of carbon nanotube-based composites. Appl Phys Lett 2006;89(13):133102.

[71] Moriche R, Sánchez M, Jiménez-Suárez A, Prolongo SG, Ureña A. Electrically conductive functionalized-GNP/epoxy based composites: From nanocomposite to multiscale glass fibre composite material. Composites Part B: Engineering 2016;98:49-55.

[72] Moriche R, Sanchez M, Jimenez-Suarez A, Prolongo SG, Urena A. Strain monitoring mechanisms of sensors based on the addition of graphene nanoplatelets into an epoxy matrix. Composites Sci Technol 2016;123:65-70.

[73] He F, Lau S, Chan HL, Fan J. High dielectric permittivity and low percolation threshold in nanocomposites based on poly (vinylidene fluoride) and exfoliated graphite nanoplates. Adv Mater 2009;21(6):710-715.

[74] Stankovich S, Dikin DA, Dommett GH, Kohlhaas KM, Zimney EJ, Stach EA, Piner RD, Nguyen ST, Ruoff RS. Graphene-based composite materials. Nature 2006;442(7100):282.

[75] Li J, Ma PC, Chow WS, To CK, Tang BZ, Kim J. Correlations between percolation threshold, dispersion state, and aspect ratio of carbon nanotubes. Advanced Functional Materials 2007;17(16):3207-3215.

[76] Li J, Kim J. Percolation threshold of conducting polymer composites containing 3D randomly distributed graphite nanoplatelets. Composites Sci Technol 2007;67(10):2114-2120.

[77] Simmons JG. Generalized formula for the electric tunnel effect between similar electrodes separated by a thin insulating film. J Appl Phys 1963;34(6):1793-1803.

[78] Thostenson ET, Chou T. Carbon nanotube networks: Sensing of distributed strain and damage for life prediction and self healing. Adv Mater 2006;18(21):2837-+.

[79] Li C, Thostenson ET, Chou T. Dominant role of tunneling resistance in the electrical conductivity of carbon nanotube-based composites. Appl Phys Lett 2007;91(22):223114.

[80] Hu N, Karube Y, Arai M, Watanabe T, Yan C, Li Y, Liu Y, Fukunaga H. Investigation on sensitivity of a polymer/carbon nanotube composite strain sensor. Carbon 2010;48(3):680-687.

[81] De Vivo B, Lamberti P, Spinelli G, Tucci V, Vertuccio L, Vittoria V. Simulation and experimental characterization of polymer/carbon nanotubes composites for strain sensor applications. J Appl Phys 2014;116(5):054307.

[82] Alamusi, Hu N, Fukunaga H, Atobe S, Liu Y, Li J. Piezoresistive Strain Sensors Made from Carbon Nanotubes Based Polymer Nanocomposites. Sensors 2011;11(11):10691-10723.

[83] Grammatikos SA, Paipetis AS. On the electrical properties of multi scale reinforced composites for damage accumulation monitoring. Composites Part B-Engineering 2012;43(6):2687-2696.

[84] Cao X, Wei X, Li G, Hu C, Dai K, Guo J, Zheng G, Liu C, Shen C, Guo Z. Strain sensing behaviors of epoxy nanocomposites with carbon nanotubes under cyclic deformation. Polymer 2017;112:1-9.

[85] Wang M, Zhang K, Dai X, Li Y, Guo J, Liu H, Li G, Tan Y, Zeng J, Guo Z. Enhanced electrical conductivity and piezoresistive sensing in multi-wall carbon nanotubes/polydimethylsiloxane nanocomposites via the construction of a self-segregated structure. Nanoscale 2017;9(31):11017-11026.

[86] Robert C, Feller JF, Castro M. Sensing Skin for Strain Monitoring Made of PC-CNT Conductive Polymer Nanocomposite Sprayed Layer by Layer. Acs Applied Materials & Interfaces 2012;4(7):3508-3516.

[87] Loyola BR, Zhao Y, Loh KJ, La Saponara V. The electrical response of carbon nanotube-based thin film sensors subjected to mechanical and environmental effects. Smart Mater Struct 2013;22(2):025010.

[88] Reddy SK, Kumar S, Varadarajan KM, Marpu PR, Gupta TK, Choosri M. Strain and damage-sensing performance of biocompatible smart CNT/UHMWPE nanocomposites. Materials Science and Engineering: C 2018;92:957-968.

[89] Tallman TN, Gungor S, Wang KW, Bakis CE. Tactile imaging and distributed strain sensing in highly flexible carbon nanofiber/polyurethane nanocomposites. Carbon 2015;95:485-493.

[90] Loh KJ, Hou T, Lynch JP, Kotov NA. Carbon Nanotube Sensing Skins for Spatial Strain and Impact Damage Identification. J Nondestr Eval 2009;28(1):9-25.

[91] Moriche R, Sanchez M, Prolongo SG, Jimenez-Suarez A, Urena A. Reversible phenomena and failure localization in self-monitoring GNP/epoxy nanocomposites. Composite Structures 2016;136:101-105.

[92] Chiacchiarelli LM, Rallini M, Monti M, Puglia D, Kenny JM, Torre L. The role of irreversible and reversible phenomena in the piezoresistive behavior of graphene epoxy nanocomposites applied to structural health monitoring. Composites Sci Technol 2013;80:73-79.

[93] Eswaraiah V, Balasubramaniam K, Ramaprabhu S. Functionalized graphene reinforced thermoplastic nanocomposites as strain sensors in structural health monitoring. Journal of Materials Chemistry 2011;21(34):12626-12628.

[94] Eswaraiah V, Balasubramaniam K, Ramaprabhu S. One-pot synthesis of conducting graphene-polymer composites and their strain sensing application. Nanoscale 2012;4(4):1258-1262.

[95] Cao J, Wang Q, Dai H. Electromechanical properties of metallic, quasimetallic, and semiconducting carbon nanotubes under stretching. Phys Rev Lett 2003;90(15):157601.

[96] Cullinan MA, Culpepper ML. Carbon nanotubes as piezoresistive microelectromechanical sensors: Theory and experiment. Physical Review B 2010;82(11):115428.

[97] Bao W, Meguid S, Zhu Z, Meguid M. Modeling electrical conductivities of nanocomposites with aligned carbon nanotubes. Nanotechnology 2011;22(48):485704.

[98] Bao W, Meguid S, Zhu Z, Pan Y, Weng G. A novel approach to predict the electrical conductivity of multifunctional nanocomposites. Mech Mater 2012;46:129-138.

[99] Gong S, Zhu Z, Haddad E. Modeling electrical conductivity of nanocomposites by considering carbon nanotube deformation at nanotube junctions. J Appl Phys 2013;114(7):074303.

[100] Wang Y, Weng GJ, Meguid SA, Hamouda AM. A continuum model with a percolation threshold and tunneling-assisted interfacial conductivity for carbon nanotube-based nanocomposites. J Appl Phys 2014;115(19):193706.

[101] Jangam S, Raja S, Maheswar Gowd BU. Influence of multiwall carbon nanotube alignment on vibration damping of nanocomposites. J Reinf Plast Compos 2016;35(8):617-627.

[102] Hu N, Karube Y, Yan C, Masuda Z, Fukunaga H. Tunneling effect in a polymer/carbon nanotube nanocomposite strain sensor. Acta Materialia 2008;56(13):2929-2936.

[103] Rahman R, Servati P. Effects of inter-tube distance and alignment on tunnelling resistance and strain sensitivity of nanotube/polymer composite films. Nanotechnology 2012;23(5):055703.

[104] Kuronuma Y, Takeda T, Shindo Y, Narita F, Wei Z. Electrical resistance-based strain sensing in carbon nanotube/polymer composites under tension: Analytical modeling and experiments. Composites Sci Technol 2012;72(14):1678-1682.

[105] Panozzo F, Zappalorto M, Quaresimin M. Analytical model for the prediction of the piezoresistive behavior of CNT modified polymers. Compos Part B: Eng 2017;109:53-63.

[106] Hicks J, Behnam A, Ural A. A computational study of tunneling-percolation electrical transport in graphene-based nanocomposites. Appl Phys Lett 2009;95(21):213103.

[107] Wang W, Jayatissa AH. Computational and experimental study of electrical conductivity of graphene/poly(methyl methacrylate) nanocomposite using Monte Carlo method and percolation theory. Synth Met 2015;204:141-147.

[108] Wang Y, Shan JW, Weng GJ. Percolation threshold and electrical conductivity of graphene-based nanocomposites with filler agglomeration and interfacial tunneling. J Appl Phys 2015;118(6):065101.

[109] Takeda T, Narita F. Fracture behavior and crack sensing capability of bonded carbon fiber composite joints with carbon nanotube-based polymer adhesive layer under Mode I loading. Composites Science and Technology 2017;146:26-33.

[110] Kang M, Choi J, Kweon J. Fatigue life evaluation and crack detection of the adhesive joint with carbon nanotubes. Composite Structures 2014;108:417-422.

[111] Mactabi R, Rosca ID, Hoa SV. Monitoring the integrity of adhesive joints during fatigue loading using carbon nanotubes. Composites Sci Technol 2013;78:1-9.

[112] Lim AS, Melrose ZR, Thostenson ET, Chou T. Damage sensing of adhesively-bonded hybrid composite/steel joints using carbon nanotubes. Composites Sci Technol 2011;71(9):1183-1189.

[113] Gude MR, Prolongo SG, Gomez-del Rio T, Urena A. Mode-I adhesive fracture energy of carbon fibre composite joints with nanoreinforced epoxy adhesives. Int J Adhes Adhes 2011;31(7):695-703.

[114] Gude MR, Prolongo SG, Urena A. Toughening effect of carbon nanotubes and carbon nanofibres in epoxy adhesives for joining carbon fibre laminates. Int J Adhes Adhes 2015;62:139-145.

[115] Vietri U, Guadagno L, Raimondo M, Vertuccio L, Lafdi K. Nanofilled epoxy adhesive for structural aeronautic materials. Composites Part B-Engineering 2014;61:73-83.

[116] Akpinar IA, Gültekin K, Akpinar S, Akbulut H, Ozel A. Research on strength of nanocomposite adhesively bonded composite joints. Composites Part B: Engineering 2017;126:143-152.

[117] Meguid S, Sun Y. On the tensile and shear strength of nano-reinforced composite interfaces. Mater Des 2004;25(4):289-296.

[118] Burkholder GL, Kwon YW, Pollak RD. Effect of carbon nanotube reinforcement on fracture strength of composite adhesive joints. J Mater Sci 2011;46(10):3370-3377.

[119] Wernik JM, Meguid SA. On the mechanical characterization of carbon nanotube reinforced epoxy adhesives. Mater Des 2014;59:19-32.

[120] Jojibabu P, Jagannatham M, Haridoss P, Ram GDJ, Deshpande AP, Bakshi SR. Effect of different carbon nano-fillers on rheological properties and lap shear strength of epoxy adhesive joints. Composites Part A-Applied Science and Manufacturing 2016;82:53-64.

[121] Adams RD, Adams RD, Comyn J, Wake WC, Wake W. Structural adhesive joints in engineering. 1997.

[122] Garcia C, Sanchez M, Urena A, Rams J. Carbon Nanotubes for Assessing the Structural Integrity of Composite Bonded Joints with Film Adhesives. Structural Health Monitoring 2015: System Reliability for Verification and Implementation, Vols.1 and 2 2015:2169-2176.

[123] Ureña A, García-Nieto C, Sánchez-Romate XF, Rams J, Sánchez M. Smart behaviour of CNT modified adhesive films for carbon fiber composite repair. Conf Smart Struct Mater , SMART Int Conf Smart Mater Nanotechnol in Eng , SMN 2017;2017-January:66-76.

[124] Rudawska A. Adhesive joint strength of hybrid assemblies: Titanium sheet-composites and aluminium sheet-composites—Experimental and numerical verification. International Journal of Adhesion and Adhesives 2010;30(7):574-582.

[125] Banea MD, Rosioara M, Carbas RJC, da Silva LFM. Multi-material adhesive joints for automotive industry. Composites Part B: Engineering 2018;151:71-77.

[126] Ribeiro TEA, Campilho RDSG, da Silva LFM, Goglio L. Damage analysis of composite–aluminium adhesively-bonded single-lap joints. Composite Structures 2016;136:25-33.

[127] Tsouvalis NG, Karatzas VA. An investigation of the tensile strength of a composite-to-metal adhesive joint. Applied Composite Materials 2011;18(2):149-163.

[128] Seong M, Kim T, Nguyen K, Kweon J, Choi J. A parametric study on the failure of bonded single-lap joints of carbon composite and aluminum. Composite Structures 2008;86(1):135-145.

[129] Alves DL, Campilho RDSG, Moreira RDF, Silva FJG, da Silva LFM. Experimental and numerical analysis of hybrid adhesively-bonded scarf joints. International Journal of Adhesion and Adhesives 2018;83:87-95.

[130] Sun G, Liu X, Zheng G, Gong Z, Li Q. On fracture characteristics of adhesive joints with dissimilar materials – An experimental study using digital image correlation (DIC) technique. Composite Structures 2018;201:1056-1075.

[131] Korayem AH, Li CY, Zhang QH, Zhao XL, Duan WH. Effect of carbon nanotube modified epoxy adhesive on CFRP-to-steel interface. Composites Part B: Engineering 2015;79:95-104.

[132] Konstantakopoulou M, Kotsikos G. Effect of MWCNT filled epoxy adhesives on the quality of adhesively bonded joints. Plastics, Rubber and Composites 2016;45(4):166-172.

[133] Moriche R, Jiménez-Suárez A, Sánchez M, Prolongo SG, Ureña A. Sensitivity, influence of the strain rate and reversibility of GNPs based multiscale composite materials for high sensitive strain sensors. Composites Science and Technology 2018;155:100-107.

[134] Yu J, Grossiord N, Koning CE, Loos J. Controlling the dispersion of multi-wall carbon nanotubes in aqueous surfactant solution. Carbon 2007;45(3):618-623.

[135] Rastogi R, Kaushal R, Tripathi SK, Sharma AL, Kaur I, Bharadwaj LM. Comparative study of carbon nanotube dispersion using surfactants. J Colloid Interface Sci 2008;328(2):421-428.

[136] Quaresimin M, Ricotta M. Fatigue behaviour and damage evolution of single lap bonded joints in composite material. Composites Sci Technol 2006;66(2):176-187.

[137] Li J, Östling M. Conductivity scaling in supercritical percolation of nanoparticles–not a power law. Nanoscale 2015;7(8):3424-3428.

[138] Kale S, Sabet FA, Jasiuk I, Ostoja-Starzewski M. Effect of filler alignment on percolation in polymer nanocomposites using tunneling-percolation model. J Appl Phys 2016;120(4):045105.

[139] Cueto E, Monge R, Chinesta F, Poitou A, Alfaro I, Mackley MR. Rheological modeling and forming process simulation of CNT nanocomposites. International journal of material forming 2010;3(2):1327-1338.

[140] Yamamoto S, Matsuoka T. Dynamic simulation of flow-induced fiber fracture. Polymer Engineering & Science 1995;35(12):1022-1030.

[141] Jam J, Pourasghar A, Kamarian S. Effect of the aspect ratio and waviness of carbon nanotubes on the vibrational behavior of functionally graded nanocomposite cylindrical panels. Polymer Composites 2012;33(11):2036-2044.

[142] Veloso MV, Souza Filho A, Mendes Filho J, Fagan SB, Mota R. Ab initio study of covalently functionalized carbon nanotubes. Chemical physics letters 2006;430(1-3):71-74.

[143] Milowska K, Birowska M, Majewski JA. Mechanical and electrical properties of carbon nanotubes and graphene layers functionalized with amines. Diamond and Related Materials 2012;23:167-171.

[144] Prolongo S, Jimenez-Suarez A, Moriche R, Ureña A. In situ processing of epoxy composites reinforced with graphene nanoplatelets. Composites Sci Technol 2013;86:185-191.

[145] Takeda T, Shindo Y, Kuronuma Y, Narita F. Modeling and characterization of the electrical conductivity of carbon nanotube-based polymer composites. Polymer 2011;52(17):3852-3856.

[146] Shindo Y, Kuronuma Y, Takeda T, Narita F, Fu S. Electrical resistance change and crack behavior in carbon nanotube/polymer composites under tensile loading. Composites Part B-Engineering 2012;43(1):39-43.

[147] Fernberg S, Joffe R, Nilsson G, AB SS. Strain and damage sensing during loading of carbon nanotube doped composites. 2009.

[148] Li J, Ma P, Sze C, Kai T, Tang B, Kim JK. Percolation threshold of polymer nanocomposites containing graphite nanoplatelets and carbon nanotubes. 2007.

[149] Frømyr TR, Hansen FK, Olsen T. The Optimum Dispersion of Carbon Nanotubes for Epoxy Nanocomposites: Evolution of the Particle Size Distribution by Ultrasonic Treatment. Journal of Nanotechnology 2012.

[150] Montazeri A, Khavandi A, Javadpour J, Tcharkhtchi A. An investigation on the effect of sonication time and dispersing medium on the Mechanical properties of MWCNT/epoxy nanocomposites. Advances in Materials and Processing Technologies Ii, Pts 1 and 2 2011;264-265:1954-1959.

[151] Song Y, Wang F, Guo G, Luo S, Guo R. Amphiphilic-Polymer-Coated Carbon Nanotubes as Promoters for Methane Hydrate Formation. Acs Sustainable Chemistry & Engineering 2017;5(10):9271-9278.

[152] Lucas A, Zakri C, Maugey M, Pasquali M, Van Der Schoot P, Poulin P. Kinetics of nanotube and microfiber scission under sonication. The Journal of Physical Chemistry C 2009;113(48):20599-20605.

[153] Chiang TH, Liu C, Lin Y. The effect of an anhydride curing agent, an accelerant, and non-ionic surfactants on the electrical resistivity of graphene/epoxy composites. J Appl Polym Sci 2015;132(20):41975.

[154] Weiss J, Voigt M, Kunze C, Sanchez JEH, Possart W, Grundmeier G. Ageing mechanisms of polyurethane adhesive/steel interfaces. Int J Adhes Adhes 2016;70:167-175.

[155] Prolongo SG, Gude MR, Urena A. Water uptake of epoxy composites reinforced with carbon nanofillers. Composites Part A-Applied Science and Manufacturing 2012;43(12):2169-2175.

[156] Blackman BRK, Kinloch AJ, Paraschi M, Teo WS. Measuring the mode I adhesive fracture energy, GIC, of structural adhesive joints: the results of an international round-robin. Int J Adhes Adhes 2003;23(4):293-305.

[157] Anyfantis KN, Tsouvalis NG. Loading and fracture response of CFRP-to-steel adhesively bonded joints with thick adherents - Part II: Numerical simulation. Composite Structures 2013;96:858-868.

[158] Bernasconi A, Carboni M, Comolli L, Galeazzi R, Gianneo A, Kharshiduzzaman M. Fatigue Crack Growth Monitoring in Composite Bonded Lap Joints by a Distributed Fibre Optic Sensing System and Comparison with Ultrasonic Testing. J Adhesion 2016;92(7-9):739-757.

[159] Saleema N, Sarkar DK, Paynter RW, Gallant D, Eskandarian M. A simple surface treatment and characterization of AA 6061 aluminum alloy surface for adhesive bonding applications. Applied Surface Science 2012;261:742-748.

[160] Krueger R, Cvitkovich MK, O'Brien TK, Minguet PJ. Testing and analysis of composite skin/stringer debonding under multi-axial loading. J Composite Mater 2000;34(15):1263-1300.

List of Figures

List of Tables

JOURNAL PAPERS

i. ***Exploring the mechanical and sensing capabilities of multi-material bonded joints with carbon nanotube-doped adhesive films.*** X.F. Sánchez-Romate, L. Baena, A. Jiménez-Suárez, M. Sánchez, A. Güemes and A. Ureña, *Under review*

ii. ***An approach to crack propagation in skin-stringer composite structures using novel carbon nanotube adhesive films.*** X.F. Sánchez-Romate, A.R. Pozo, A. Jiménez-Suárez, M. Sánchez, A. Güemes and A. Ureña, *Submitted to journal*

iii. ***An approach using highly sensitive carbon nanotube adhesive films for crack growth detection under flexural load in composite structures.*** X.F. Sánchez-Romate, R. Moriche, A. Jiménez-Suárez, M. Sánchez, A. Güemes and A. Ureña, *Under review*

iv. ***Electrical monitoring as a novel route to understanding the ageing mechanisms of carbon nanotube-doped adhesive films.*** X.F. Sánchez-Romate, A. Jiménez-Suárez, M. Sánchez, S.G. Prolongo, A. Güemes and A. Ureña, *Under review*

v. ***Fatigue crack growth identification in bonded joints using carbon nanotube doped adhesive films.*** X.F. Sánchez-Romate, C. Sbarufatti, M. Sánchez, A. Bernasconi, D. Scaccabarozzi, S. Cinquemani, A. Güemes and A. Ureña, *Under review*

vi. ***Critical parameters of carbon nanotube reinforced composites for structural health monitoring applications: empirical results versus theoretical predictions.*** X.F. Sánchez-Romate, J. Artigas, A. Jiménez-Suárez, M. Sánchez, A. Güemes and A. Ureña. Composites Science and Technology 181; 44-53 (2019)

vii. ***Development of bonded joints using novel CNT doped adhesive films: mechanical and electrical properties.*** X.F. Sánchez-Romate, A. Jiménez-Suárez, J. Molinero, M. Sánchez, A. Güemes and A. Ureña. International Journal of Adhesion and Adhesives 86; 98-104 (2018)

viii. ***Carbon nanotube-doped adhesive films for detecting crack propagation on bonded joints: a deeper understanding of anomalous***

behaviors. X.F. Sánchez-Romate, A. Jiménez-Suárez, J. Molinero, M. Sánchez, A. Güemes and A. Ureña. ACS Applied Materials & Interfaces 9; 43267-43274 (2017)

ix. ***Highly sensitive strain gauges with carbon nanotubes: from bulk nanocomposites to multifunctional coatings for damage sensing.*** X.F. Sánchez-Romate, R. Moriche, A. Jiménez-Suárez, M. Sánchez, S.G. Prolongo, A. Güemes and A. Ureña. Applied Surface Science 424; 213-221 (2017)

x. ***Novel approach to percolation threshold on electrical conductivity of carbon nanotube reinforced nanocomposites.*** X.F. Sánchez-Romate, A. Jiménez-Suárez, M. Sánchez, A. Güemes and A. Ureña. RSC Advances 6; 43418-43428 (2016)

CONFERENCE CONTRIBUTIONS

i. 15-21st July 2018: 26th Annual International Conference on Composites/Nano Engineering ICCE 26, Paris (France). Oral Presentation: ***Study of Crack Propagation Mechanisms of Skin-Stringer Sub-elements Joined with Carbon Nanotube Adhesive Films***. X. F. Sánchez-Romate, M. Sánchez, A. Jiménez-Suárez, A. Güemes, A.R. Pozo, A. Ureña

ii. 10-13th July 2018: 9th European Workshop on Structural Health Monitoring EWSHM 2018, Manchester (United Kingdom). Oral Presentation***: Crack Propagation Monitoring with Carbon Nanotube Doped Adhesive Films on Skin-Stringer Sub-elements***. X. F. Sánchez-Romate, A. R. Pozo, V. Yokaribas, J. Kathol, A. Jiménez-Suárez, R. Moriche, M. Sánchez, C-P. Fritzen, A. Güemes, A. Ureña

iii. 1-5th July 2018: 12th International Conference on Advanced Computational Engineering and Experimenting ACE-X 2018, Amsterdam (Netherlands). Oral Presentation: ***Addition of Carbon Nanotubes to Adhesive Hybrid Aluminium/CFRP Joints with SHM Properties***. A. Jiménez-Suárez, X. F. Sánchez-Romate, S. G. Prolongo, M. Sánchez, A. Güemes, A. Ureña

iv. 12-14th September 2017: 11th International Workshop on Structural Health Monitoring IWSHM 2018, Standford (United States). Oral Presentation: ***On the Dynamic Acquisition of Electrical Signals for Structural Heatlh Monitoring of Carbon Nanotube Doped Composites***. C. Sbarufatti, X. F. Sánchez-Romate, S. Cinquemani, D. Scaccabarozzi, F. Libonatti, A. Güemes, A. Ureña

v. 3-6th July 2017: 11th International Conference on Advanced Computational Engineering and Experimenting (ACE-X 2017), Viena (Austria). Oral Presentation: ***Ageing Effect on Electrical and Mechanical Properties of CFRP Bonded Joints Using CNT Doped Adhesive Films***. X. F. Sánchez-Romate, A. Jiménez-Suárez, M. Sánchez, A. Güemes, A. Ureña

vi. 5-8th June 2017: 8th ECCOMAS Thematic Conference on Smart Materials and Structures, Madrid (Spain). Oral Presentation: ***Crack propagation monitoring of bonded joints with novel carbon nanotube***

doped adhesive films. X. F. Sánchez-Romate, C. Sbarufatti, M. Sánchez, A. Bernasconi, D. Scaccabarozzi, A. Güemes, A. Ureña

vii. 5-8th June 2017: 8th ECCOMAS Thematic Conference on Smart Materials and Structures, Madrid (Spain). Oral Presentation: ***Smart Behavior of CNT modified adhesive films for carbon fiber composite repair***. A. Ureña, C. García-Nieto, X.F. Sánchez-Romate, J. Rams, M. Sánchez

viii. 21-23th May 2017: XII Congreso Nacional de Materiales Compuestos (MATCOMP 2017), San Sebastián (Spain). Oral Presentation: ***Comportamiento Multifuncional de Películas de Adhesivo Modificadas con CNT para Reparaciones en Materiales Compuestos***. C. García-Nieto, X.F. Sánchez-Romate, M. Sánchez, A. Ureña

ix. 25-29th March 2017: SPIE Smart Structures/NDE 2017, Portland (United States). Oral Presentation: ***Monitoring of Impact Dynamics on Carbon Nanotube Multiscale Glass Fiber Composites by Means of Electrical Measurements***. X. F. Sánchez-Romate, C. Sbarufatti, D. Scaccabarozzi, S. Cinquemani, A. Jiménez-Suárez, A. Güemes, A. Ureña

x. 12-14th September 2016: 8th International Conference on Advanced Nanomaterial AEM 2016, Guildford (United Kingdom). Oral Presentation: ***High-Sensitivity Strain Gauges with Carbon Nanotube Doped Expoxy Films***. X. F. Sánchez-Romate, R. Moriche, A. Jiménez-Suárez, M. Sánchez, S.G. Prolongo, A. Güemes, A. Ureña

xi. 5-8th July 2016: 8th European Workshop on Structural Health Monitoring 2016, Bilbao (Spain). Oral Presentation: ***Structural Health Monitoring of Bonded Joints Using Carbon Nanotube Doped Adhesive Films***. X. F. Sánchez-Romate, M. Sánchez, C. García-Nieto, J. Molinero, A. Jiménez-Suárez, A. Güemes, A. Ureña

xii. 5-8th July 2016: 8th European Workshop on Structural Health Monitoring 2016, Bilbao (Spain). Poster Presentation: ***Influence of Process Parameters on Gauge Factor of CNT-Epoxy based Strain Sensors***. X. F. Sánchez-Romate, M. Sánchez, J. Artigas, A. Jiménez-Suárez, A. Güemes, A. Ureña

xiii. 3-6th July 2016: 10th International Conference on Advanced Computational Engineering and Experimenting ACE-X 2016, Split (Croatia). Oral Presentation: ***The Key-Role of Nanoreinforcements in New Multifunctional Adhesives***. A. Jiménez-Suárez, R. Moriche, X. F. Sánchez-Romate, S.G. Prolongo, A. Ureña

xiv. 3-6th July 2016: 10th International Conference on Advanced Computational Engineering and Experimenting ACE-X 2016, Split (Croatia). Poster Presentation: ***Effect of the Addition of Carbon Nanotubes to an Adhesive Film***. X. F. Sánchez-Romate, A. Jiménez-Suárez, M. Sánchez, A. Güemes, A. Ureña

Escuela Técnica Superior de Ingeniería Aeronáutica y del Espacio
Departamento de Materiales y Producción Aeroespacial

“DEVELOPMENT OF A MULTIFUNCTIONAL COMPOSITE STRUCTURE WITH SELF-SENSING PROPERTIES”

Autor:

Xoan Xosé Fernández Sánchez-Romate

Directores:

Jesús Alfredo Güemes Gordo

Alejandro Ureña Fernández

Madrid, 2019